Fingering instabilities in gravity and surfactant-related thin film flows

Joseph Victor Goddard

June 2015

Submitted in partial fulfilment of the requirements of the degree of

Doctor of Philosophy

Keele University

School of Computing and Mathematics

In loving memory of Malcolm Goddard

whose thirst for knowledge inspired my own.

Acknowledgements

I would like to thank my supervisor, Dr. Shailesh Naire, for the patient guidance, encouragement and advice he has provided throughout my time as his student. I have been extremely lucky to have a supervisor who cared so much about my work and who was so thoroughly fascinated by the subject. He pushed me when I needed to be pushed and showed huge amount of belief in my ability as a Mathematician. Thank you to my Rich, Ahmed and Wayne whose discussions helped me formulate my ideas fully.

I must express my gratitude to Camilla, my fiancée, for her continued support and encouragement. I was continually amazed by her willingness to proof read countless pages of meaningless mathematics. Now that this is finished you no longer have to listen to my incoherent mathematical mutterings. I would like to thank the teachings of both my parents who first inspired my love of science. To my brothers whose endless teasing about my obsession with mathematics drove my obsession even more. Thank you to Kate for correcting my atrocious spelling and thank you to Ella for hours of entertainment. I am hugely grateful to a wonderful teacher, Hazel Duggan,

who really helped me cultivate my ability and love for the subject. I am forever indebted. Completing this work would have been all the more difficult were it not for the support and friendship provided by the other members of the School of Computing and Mathematics. I am indebted to them for their help. Also thank you to the sports teams I have managed for the escapism that I occasionally need to vent frustration. Finally, I would like to thank ESPRC and Keele University's Acorn funding, not only for providing the funding which allowed me to undertake this research, but also for giving me the opportunity to attend conferences and meet so many interesting people.

Abstract

Thin-film fluid flows are central to a number of biological, industrial and chemical applications and processes. Thin films driven by external forces are highly susceptible to instabilities leading to the break-up of the film into fingering-type patterns. These fingering-type patterns are usually undesirable as they lead to imperfections and dry spots. This behaviour has motivated theoreticians to try to understand the behaviour of the flow and the mechanisms by which these instabilities occur.

This work focuses on modelling the dynamics of a thin viscous droplet spreading down an inclined pre-wetted plane due to gravity and surfactant-related effects. We use high resolution numerical simulations combined with analytical solutions to describe the influence of different competing physical effects on the spreading behaviour. We also obtain the spreading and thinning rates for the droplet based on fluid and surfactant conservation arguments where a power-law behaviour is not assumed *a priori*. In particular, a quasi-steady similarity solution is obtained for one-dimensional flow at the leading edge of the droplet. A linear stability analysis shows that this base state is linearly unstable to long-wavelength perturbations in the transverse direction. This

suggests that the onset of the fingering instabilities originate from this region. The influence of surfactant, particularly, the Marangoni effect is shown to increase the growth rate and band of unstable wavenumbers compared to gravity-driven spreading alone. Moreover, with the addition of insoluble surfactant it is shown that this region is linearly unstable for all inclination angles. This is in contrast to gravity-driven spreading where it has been shown that there is a threshold angle below which this region is linearly stable. Stability criteria are obtained in the small wave number limit. For gravity-driven spreading, capillary effects are shown to be responsible for the instability in this limit as reported by previous studies. The Marangoni effect is shown to be behind this instability at small inclination angles and in the small wave number limit when surfactant effects are included. Two-dimensional simulations undertaken here support the linear stability results and are useful in exploring the nonlinear stability of the flow.

Contents

List of Figures

Chapter 1

Introduction

Thin fluid films are omnipresent in nature and their flow is important in a wide range of biological, industrial and chemical applications and processes where the understanding of the physics behind their spreading is of great importance. They are used in many simple applications ranging from paint coating and drying and rain droplets flowing down a window to more complicated industrial processes such as dip coating, production of contact lenses. Myers [49, 50] provides a nice review of these applications. Thin-film flows are also used in the production of computer components [57]. Thin films also have many biological applications, such as, in the formation of tear films and within the thin mucus layer coating the walls of mammalian lungs. The mucus layer plays a vital role in trapping small particles of toxic material and therefore stopping them from entering the airways. They also play an important function in stabilising the lung. Thin-film flow can occur on a length scale much larger than the examples

cited above. In geophysical and environmental engineering thin-film flows occur in mudslides and lava flow [6, 22].

The above applications have provided motivation for a substantial amount of research to be undertaken within this area of fluid dynamics. Thin-film flow consists of a stretch of liquid bounded either by two solid substrates (e.g. lubricating oil between bearings) or one solid substrate and one free surface (e.g. a rain droplet or sheet flowing down a windscreen) or between two free surfaces (e.g. a soap film). The area of research conducted as part of this thesis is related to a thin film bounded by one solid substrate with the main driving force being gravity. However, as the film thins, surface tension effects becomes more prominent. Surface tension is defined as 'The tension of the surface film of a liquid caused by the attraction of the particles in the surface layer by the bulk of the liquid, which tends to minimise surface area' [19]. Surface tension is a measure of the strength of intermolecular forces of attraction between the molecules that lie on the surface. Surface tension of a fluid is often constant, however, it can be altered due to, for example, heating of the fluid which induces thermo-capillary effects or, alternatively, the addition of surfactants. Surfactants (surface-active-agents) are chemicals that, when present in low concentration, adsorb on the liquid-air interface and lower the surface tension there [53]. Surfactants are amphiphiles, i.e., chemicals that possess both a hydrophobic (water 'hating') functional group and a hydrophilic (water 'loving') functional group. This means that the hydrophilic head is soluble and typically remains within the bulk of the fluid whereas the hydrophobic tail wishes to

remain outside the main bulk of the fluid. Not all surfactants are insoluble and can therefore be characterised by their solubility from insoluble (where the surfactant is only found on the liquid-air interface) to highly soluble (where the surfactant exists on the interface as well as in the main bulk of the fluid). When surfactants are present in high concentration they clump together and form spherical type structures known as 'micelles'. As surfactants lower surface tension locally, non-uniformities in surfactant concentration lead to surface tension gradients. Fluid is drawn by these surface tension gradients and is called the Marangoni effect and the ensuing flow is referred to as Marangoni flow [40].

Surfactants have been used in many aspects of technology and industry to control the wetting properties of liquids due to their ability to modify surface tension. They are used in detergents (in the form of fatty acids), crop spraying, coating processes and oil recovery. Surfactants also occur naturally, for example in the mammalian lung as briefly aforementioned. They reduce the surface tension within the liquid lining the airways, which assists in preventing the collapse of the smaller airways [23, 24]. In the lungs of premature infants the quantity of surfactant produced is insufficient as the lungs are under-developed. This leads to a respiratory distress syndrome which is treated by surfactant replacement therapy (SRT). SRT involves delivering artificial surfactant into the lung exogenously and orientating the infant to ensure that the surfactant coats the airways as uniformly as possible.

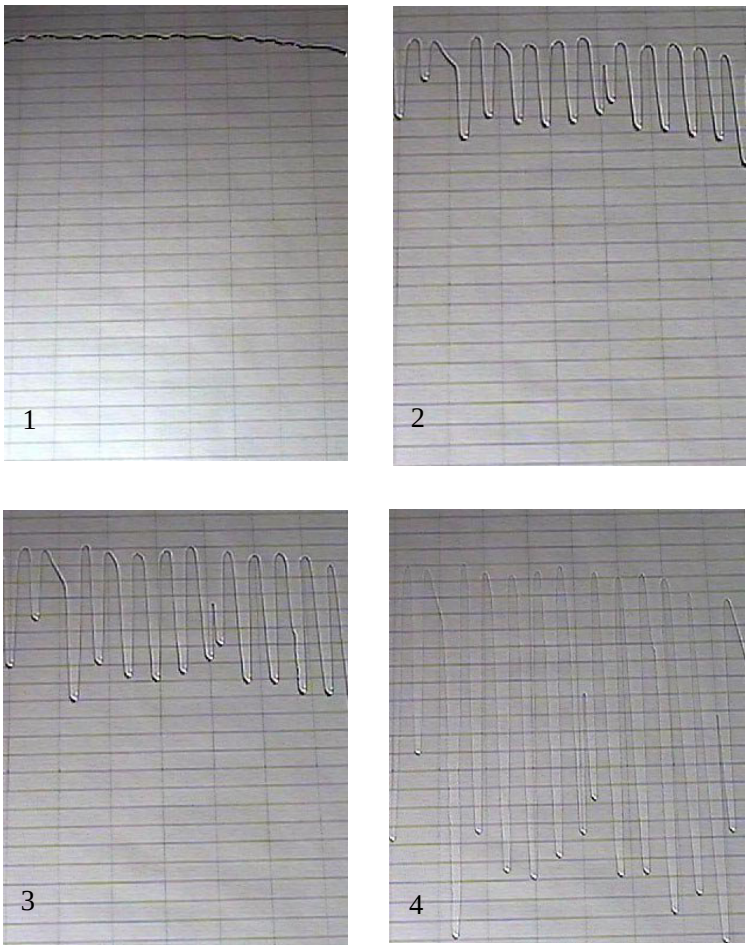

Figure 1.1: Photographs of a liquid sheet flowing down an inclined plane at various times (increasing from top left to bottom right). An initially uniform sheet breaks up into fingers. Reproduced from experiments by Kondic [34].

Thin films also exhibit intriguing instabilities that form under different conditions, resulting in the formation of a range of striking patterns. This provides extra motivation to theoreticians to understand the formation of these instabilities. The flow of a droplet or sheet spreading down an inclined substrate develops a fingering instability as shown in panels 1-4 in Fig. 1.1. A simple example of this is observed when rainwater flows down the windscreen of a car. An experiment into the spreading of

a droplet or sheet down an inclined plane was first conducted by Huppert [27] and then built on by Silvi and Dussan [58]. They observed that an initially uniform flow breaks up into fingers due to any perturbations in the flow or substrate irregularities. Other patterns such as 'saw tooth'-like patterns have also been observed experimentally [58, 27, 33]. 'Saw tooth' instabilities are generally visible at shallow angles of inclination but, as the angle of inclination is increased, the instabilities look more like fingers shown in Fig. 1.1 with the sides of the fingers almost parallel. These fingering instabilities are usually undesirable in many applications as they lead to dry areas and imperfections. For example, one would prefer to uniformly coat a wall with paint and not see fingers for obvious reasons. Therefore understanding their mechanisms and how to suppress them will enable their prevention. A completely different fingering instability is observed in the case when surfactant is present. Figure 1.2 shows an experiment by Afsar-Siddiqui and co-workers where a fluid droplet laden with surfactant spreads on a horizontal plane [3, 4, 5]. In contrast to the fingering instability observed during gravity-driven spreading, the fingers here are more dramatic (often referred to as 'dendritic') and are of a much smaller length scale. Gravity-driven fingering has a lengthscale of centimetres or meters compared to the millimetre scale observed in surfactant-driven fingering. The mechanism behind this fingering is believed to be due to the Marangoni effect. This is related to surface tension gradients at the air-liquid interface created by non-uniformities in surfactant concentration there as they are advected along by the underlying liquid film flow. This fingering behaviour was first observed by Marmur and Lelah [41] and a significant amount of experimental work has

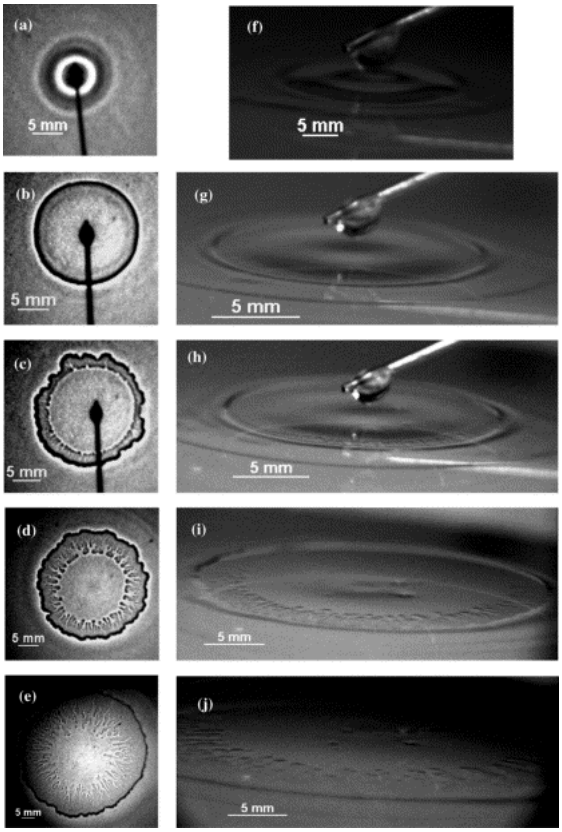

Figure 1.2: The development of fingering-type patterns in a surfactant laden drop. Reproduced experiments a paper by Afsar-Siddiqui *et al.* [3].

been done by several researchers [3, 4, 5]. These works show that at surfactant concentrations below a critical surfactant level, stable spreading occurs. However, above this critical concentration, fingering behaviour like the one shown in Fig. 1.2, is observed [3]. For a detailed review of this see Asafar-Siddiqui *et al.* [2]. As the angle of inclination is increased from the horizontal slightly, the effects of gravity will begin to compete with that due to surfactant. However, if the angle of inclination is too large, gravity will dominate. To the best of our knowledge, there are no experiments for surfactant and gravity-driven spreading on inclined planes to describe these competing effects.

Mathematical modelling enables us to describe real-world phenomena using mathematical concepts. It aids us in understanding the mechanisms behind the phenomena. The governing equations for the flow of viscous Newtonian fluids (viscous fluid stress is proportional to the local strain rate) are given by the Navier-Stokes equations,

$$\rho\left(\frac{\partial \boldsymbol{u}^*}{\partial t} + \boldsymbol{u}^* \cdot \nabla \boldsymbol{u}^*\right) = -\nabla^* P^* + \rho^* \boldsymbol{g}^* + \mu^* \nabla^{*2} \boldsymbol{u}^*, \tag{1.1}$$

$$0 = \nabla^* \cdot \boldsymbol{u}^*, \tag{1.2}$$

where P^* is the fluid pressure, ρ^* is the fluid density, μ^* is the fluid viscosity, $\boldsymbol{g}^*$ is the acceleration due to gravity and $\boldsymbol{u}^*$ is the fluid velocity vector. We assume slow viscous flow in the following analysis so inertial terms on the LHS are neglected. This is the same as taking a small Reynolds number. The convective-diffusion equation for insoluble surfactant transport was derived by Stone [60] and built upon by Wong *et al.* [67]:

$$\frac{\partial \Gamma^*}{\partial t} + \nabla_s^* \cdot (\Gamma^* \boldsymbol{u}_s^*) + \Gamma^* (\nabla_s^* \cdot \boldsymbol{n}^*)(\boldsymbol{u}^* \cdot \boldsymbol{n}^*) = D_s^* \nabla_s^{*2} \Gamma^*, \tag{1.3}$$

where Γ^* in the surfactant concentration, $\boldsymbol{u}_s^*$ is the surface velocity, D_s^* is the surfactant diffusivity, $\boldsymbol{n}^*$ is the unit outward normal at the interface and ∇_s^* is a surface divergence operator. Theoretical modelling of fluid mechanics problems applies the 'no slip' boundary condition at the liquid-solid interface (e.g. on the substrate) [1]. This sets the velocity of the fluid on the solid substrate equal to the velocity of the substrate.

For a stationary substrate we have

$$\boldsymbol{u}^* = 0. \tag{1.4}$$

At the free surface (fluid-air interface) the kinematic condition is applied. This states that fluid particles that lie on the interface must always remain on the interface. This implies that

$$\frac{D}{Dt^*}\left[z^* - h^*(x^*, y^*, t^*)\right] = 0, \tag{1.5}$$

where the free surface is represented by $z^* = h^*(x^*, y^*, t^*)$ and D/Dt^* is the total derivative. The final boundary condition which is applied is the surface stress condition [55],

$$-(T_1^* - T^*) \cdot \boldsymbol{n}^* = 2R^*\sigma^*\boldsymbol{n}^* - \nabla_s\sigma^*, \tag{1.6}$$

where T_1^* and T^* are the stress tensors in the air and fluid, respectively, R^* is the radius of curvature of the free surface and σ^* is the surface tension. The normal surface stress balances the surface curvature and the tangential surface stress is zero when surface tension is constant. However when surfactants are introduced surface tension is no longer constant and is a function of surfactant concentration. Here, tangential surface stress balances changes in the surface tension. Finally, when surfactant is present we need an equation of state to relate surfactant concentration to the surface tension. Many different equations of states can be used. The linear equation of state is valid for

dilute surfactant concentration [17] and is used in many similar problems [12, 15]. The equation of state is chosen for simplicity to implement, however, there are others that are also used, particularly at higher surfactant concentrations. A couple of examples of adsorption isotherms are Langmuir [37] and Frumkin [20] (an extension of Langmuir) which are nonlinear and applicable to soluble surfactants.

When there is moving contact line (where the liquid, solid and air interfaces intersect), relevant in many spreading problems, imposing a no slip condition at the solid substrate leads to a non-integrable stress singularity. Physically, this amounts to applying an infinite force at the contact line in order to move it [11, 26]. This is referred to as the contact line paradox. Various regularisations have been proposed to remedy this. These are:

(i) allowing the liquid to 'slip' on the solid substrate (referred to as the 'slip' condition). The so-called Navier condition proposed by Navier [51], is widely used which assumes that the tangential fluid velocity relative to a substrate is proportional to the tangential stress applied at the substrate. The constant of proportionality is referred to as a slip length which is empirically determined. This condition was first used in the context of thin-film-flow theory by Greenspan [21]. Once a choice of slip model is made a boundary condition at the contact line needs to be imposed. Greenspan [21] proposed that the speed of the contact line is related to the contact angle. A contact line condition generally used is the so called Tanner's Law [61] which states the contact line speed is proportional to

the cube of the contact angle.

(ii) assuming that the solid substrate is pre-wetted with a precursor liquid film. Incorporating a precursor film, such that the spreading front of the droplet only has 'effective' or 'apparent' contact with the precursor film, allows the 'no slip' boundary condition to be still imposed without being contradictory.

This area remains highly contentious. We will therefore follow the last regularisation and assume that the spreading is always over a pre-existing precursor film. This is due to the simplicity in its implementation in comparison to the other regularisations.

Within the modelling of thin liquid films, it is typical to use lubrication or long-wavelength theory. The main characterising factor of thin film flows is the small aspect ratio (i.e., the length of the film , L (say), is much greater than its thickness, H (say)). This is the key factor in lubrication theory. An expansion of the governing equations and boundary conditions in terms of the small aspect ratio, $\epsilon = H/L$, and then neglecting the higher order terms enables one to reduce the governing equations and boundary conditions. However depending on the system studied or the physical effects that one wishes to explore higher order terms may be included. An example of which is capillary (or surface tension)effects whose suppression would mathematically turn the problem into a singular perturbation problem. Lubrication theory is generally employed to describe several aspects of the thin-film flow problems to predict the evolution of the free surface (for a nice review see Oron, Davis and Bankoff [52]).

The above modelling ideas have been used to theoretically describe many problems in

thin-film fluid dynamics. The thesis focuses on the spreading dynamics and stability of a viscous fluid droplet laden with an insoluble surfactant down an inclined pre-wetted substrate. The spreading of a viscous droplet or fluid sheet due to gravity alone has been studied extensively over the past 30 years. The key studies investigating the spreading dynamics of a droplet of constant volume were discussed by Huppert [27], Troian *et al.* [63] and Hocking [25]. These studies have shown that the existence of a multi-region locally self-similar structure, particularly at late-time (see Fig. 2.8). This problem was first studied by Huppert [27] who identified a similarity solution for the droplet height, $h \sim \sqrt{x}$ (where h is the droplet height and x is the distance in the flow direction), where the horizontal component of gravity is the dominant spreading mechanism. This work was extended, particularly, by Troian *et al.* [63] and Hocking [25] who identified the existence of short transition regions at the leading and trailing edges of the spreading droplet. In these transition regions, capillary effects are important and are comparable to the horizontal component of gravity. The transition region at the leading edge of the droplet is characterised by a family of quasi-steady solution parametrised by the ratio of the downstream precursor film thickness and the droplet height far upstream of this region. These solutions accommodate a bulge in the droplet height referred to as the capillary ridge. Troian *et al.* [63] and Hocking [25] also performed a linear stability analysis of this region to transverse perturbations by extracting the growth of these perturbations to a 'frozen' in time base state represented by a particular solution curve in the family of quasi-steady solutions. This type of linear stability analysis is typical of such spreading problems where the base state is typically non-uniform and time-

dependant and assumes that the perturbations grow on a much quicker timescale than the evolving base state. They showed that this region is linearly unstable to a fingering instability with a well-defined maximum growth rate and wavenumber. Hocking [25] also showed that the droplet increases in length like $t^{1/3}$ and thins like $t^{-1/3}$ at time t.

It is worth noting that the solution structure at the leading edge of the spreading droplet is similar to a model problem of a fluid sheet spreading down an inclined pre-wetted plane from a constant flux source first studied by Bertozzi and Brenner [8]. They showed the existence of a travelling wave solution whose structure is described by a boundary-value-problem. They also analysed the stability of this travelling wave solution and showed it to be linearly unstable to small amplitude transverse perturbations. They performed a small wavenumber analysis to obtain a stability criterion which shows that the capillary ridge is necessary for the instability. They also showed that there is a critical angle beyond which the flow is linearly stable. This contradicts what is observed experimentally as fingering-type instabilities are shown to occur a all inclination angles above the horizontal. It has been postulated by Bertozzi and Brenner [8] that a possible explanation for this is that infinitesimally small perturbations that are present initially, particularly at the contact line, have a growth rate similar to the evolution of the flow. The transient growth of these perturbations could result in the contact line becoming unstable leading to the development of the fingering instabilities. Spaid and Homsy [59] were interested in the spreading of a viscoelastic fluid sheet down an inclined plane. They have compared the effects of a precursor film and

slip condition at the moving contact line on the spreading dynamics and subsequent fingering instabilities. They found that the results are similar, particularly when the precursor film thickness is made sufficiently thin.

Two-dimensional numerical studies have focused upon the stability of a thin viscous fluid film flowing down an inclined plane due to gravity from a constant flux source. Schwartz [54] focussed on the case of a completely wetting fluid and showed the evolution of the instability into triangular-shaped patterns. Kondic and Deiz [35, 36] revisited the problem and showed that by varying the inclination angle the shape of the fingering instabilities and the surface coverage varied considerably. Decreasing the angle of inclination resulted in saw-tooth, or triangular-type patterns being observed. As the angle of inclination was increased the fingers were more rounded with parallel sides. This gave quantitative agreement to the experimental work undertaken by Huppert [27] and Jerrett and de Bruyn [33]. To the best of our knowledge, there are no studies on two-dimensional numerical simulations of a droplet of constant volume spreading gown an inclined plane due to gravity.

In comparison, the theoretical study of surfactant-driven spreading is still relatively young, and has only developed over the past 20 years. Surfactant-driven droplet spreading on horizontal pre-wetted surfactant free substrate has been the focus of several experimental and theoretical studies [31, 29, 42, 43, 44, 45, 62] mainly to better understand the the dendritic fingering instability observed near the drop's edge (see Fig. 1.2). Troian *et al.* [62] first investigated theoretically the one-dimensional

flow structure which included a propagating fluid front ahead of the leading edge of the spreading bulk droplet. The initial surfactant concentration gradients that exists between the droplet and the surfactant-free precursor film causes fluid to be 'sucked' from the precursor film resulting in these Marangoni driven fluid front. Jensen and Grotberg [30] showed how an insoluble surfactant monolayer spreading on an initially planar film can be described using a variety of similarity solution (see also Jensen [28]). In particular for a planar geometry, they showed that a fluid front similar to that mentioned above increases in length like $t^{1/3}$ at time t.

Troian *at al.* [62] also proposed qualitatively a physical mechanism giving rise to the observed fingering. Identifying an 'adverse mobility gradient' (between the bulk droplet and precursor film) they suggested an analogy with the viscous fingering in a Hele-Shaw cell where more mobile (less viscous) displaces a less mobile (more viscous) one.

Warner *et al.* [65] examined the stability of a surfactant-laden droplet spreading over a surfactant free precursor film using two coupled nonlinear partial differential equations for the evolution of the film thickness and the surfactant concentration. Their 1-D simulations revealed a structure broadly similar to that described by Troian [62], with the bulk droplet connecting to the fluid front via an ultra-thin film. The severe thinning of the droplet resulting in the formation of an ultra-thin film is due to the fluid being sucked into the fluid front by the Marangoni effect. Their numerical solutions showed the fluid front to spread like $t^{1/3}$ with the solution structure following the similarity solution described by Jensen and Grotberg [30] for a planar geometry.

They also showed the examined the stability of their 1-D solution to small amplitude transverse perturbations using a transient growth analysis for spatially non-uniform and time dependent base states where the growth of perturbations is measured by a suitable norm. Their stability analysis showed sustained growth of disturbances concentrated around the edge of the droplet (it's so-called 'effective' contact line). They also performed 2-D computations that showed fingering patterns resembling those seen in experiments.

More recently, Jensen and Naire [32] built on the work by Warner *et al.* by exploiting high-resolution numerical simulations to describe the late-time multi-region asymptotic structure of the spatially 1-D spreading flow. They were able to obtain similarity solutions for each of these regions by using asymptotic analysis using which the spreading and thinning rates were determined. In particular, they were able to show that the local solution of the drop's 'effective' contact line can be described using the Landau-Levich equation. They examined the linear stability of this region to transverse perturbations and showed it to be linearly unstable with a well defined maximum growth rate and wavelength. Using long-wavelength asymptotics, they derived a stability criterion which revealed the de-stabilising influence of surfactant via the Marangoni effect.

Only a few studies have examined theoretically the spreading of drops on inclined planes including surfactant [12, 13, 14, 15, 46, 47, 48]. Gravity and surfactant related effects were first studied by Edmonstone *et al.* [12, 13, 14, 15]. They investigated, as we will, the spreading of thin viscous droplet laden with insoluble surfactant down

an inclined pre-wetted plane. Their 1-D numerical simulations showed the bulk fluid droplet with a capillary ridge at its leading edge. Ahead and behind the leading and trailing edges of the spreading droplet, respectively, there are fluid fronts driven by the Marangoni effect. They used transient growth analysis to explore the stability of their 1-D solution to small amplitude transverse perturbations. They found that the flow is linearly unstable with sustained growth of disturbances concentrated near the droplets leading edge 'effective' contact line. They also showed that by increasing the angle of inclination destabilises the flow further. This research was built upon to include surfactant solubility effects [14] which included an addition equation for the surfactant transport in the fluid bulk. They showed that solubility effects add to the destabilising influence of surfactants. There have also been continuing interest in the climbing of a surfactant-laden film against the influence of gravity [14, 46, 47, 48]. Mavromoustaki *et al.* [46, 47, 48] investigated this problem under both constant volume and flux conditions. They obtained the power-law time dependence of the fluid film climbing against the influence of gravity. They also explored the linear and non-linear stability of the of the flow using linear stability analysis and two dimensional simulations. They found that the surfactant concentration gradient behind the leading edge 'effective' contact line was important in the development of the fingering instability.

It is worth noting that the local solution at the leading edge of the surfactant spreading droplet of constant volume is similar to the model problem of a fluid sheet laden with surfactant spreading down an inclined pre-wetted plane from a constant flux source.

This configuration has been studied by Levy an Shearer [38] who showed the existence of travelling wave solutions. They expanded upon this research to include surface tension effects that show the existence of a capillary ridge at the leading edge of the spreading film [39].

To the best of my knowledge there are no experimental studies of a surfactant-laden droplet spreading down a pre-wetted inclined plane. We believe that the interaction between gravity and surfactant-related effects are important in several applications, particularly these related to the lung airways described previously. Moreover, mathematically describing the transition between the two distinct fingering patterns is also of interest to us. Hence, this motivates the research conducted in this thesis.

The outline of this thesis is as follows. Chapter 2 explores the one dimensional or base state flow of a viscous fluid droplet down an inclined pre-wetted plane. We obtain an equation for the evolution free surface (represented by a nonlinear partial differential equation) from the Navier-Stokes equations neglecting inertial terms and using lubrication theory. We then use high-resolution numerics to obtain the 1-D numerical solution for the evolution of the spreading droplet. We discuss the effect that variations in the parameters have on the flow of the droplet. The one dimensional numerical simulations reveal a multi-region self similar solution structure at late time. We divide the solution structure into regions that have different dominant physical effects and are characterised by key variables describing the evolution of each region. We then derive approximate solutions for each region by reducing the governing PDE

to an ODE which can be solved either numerically or analytically. We finally derive an ODE model for the key variables to obtain the spreading and thinning rates. Although most of the results for this problem have already been obtained in previous works, the methodology followed here is new and novel and forms the basis when investigating the spreading of a fluid droplet of constant volume laden with insoluble surfactant in Chapter 4.

Chapter 3 discusses the two-dimensional stability to small amplitude transverse perturbations of the time dependent base-states obtained in Chapter 2. We undertake a linear stability analysis of the 'effective' contact line at the leading edge of the droplet. We also undertake two-dimensional simulations to validate the linear stability analysis as well as a paramateritic study to understand the influence of key parameters on the fingering instability. This approach is undertaken as it allows for the physical mechanism of the growth of the perturbations to be fundamentally understood. Using the approach of the transient growth of optimum perturbations allows one to obtain an understanding of the relevant physics involved in the growth of the perturbations however one is unable to obtain a stability criterion for the flow.

Chapter 4 discuss the spreading of a viscous droplet due to gravity and surfactant-related effects. We obtain a coupled pair of partial differential equations for the evolution of the free surface of the droplet and the surfactant concentration from the Navier-Stokes equations and the surfactant transport equation obtained by Stone [60] and using lubrication theory and a linear equation of state. We then use high-resolution

numerical simulations to obtain the 1-D numerical solutions for the evolution of the spreading droplet and surfactant concentration. We discuss the effect that variations in the parameters have on the flow of the droplet. The one-dimensional simulations reveal a multi-region self-similar structure at late time. We divide the numerical solution into regions that have different dominant physical effects and are characterised by key variables describing the evolution of each region. We then derive approximate solutions for each region by reducing the governing PDEs to ODEs which can be either solved numerically or analytically depending on the region. We finally derive a differential algebraic system of equations for the key variables to obtain the time evolution of the characteristic variables numerically and analytically.

Chapter 5 discusses the two-dimensional stability of the flow to small amplitude transverse perturbations to the base-states obtained in Chapters 4. We undertake a linear stability analysis of the 'effective' contact line at the leading edge of the droplet. We also undertake two-dimensional simulations to validate the linear stability analysis as well as a parameteritic study to understand the influence that the variables have on the fingering behaviour.

We draw conclusions and present future work in Chapter 5. We analyse the main findings of this thesis and describe the natural extension to the work undertaken.

Chapter 2

Viscous fluid droplet spreading down an inclined pre-wetted plane: base state.

In this chapter we will consider the spreading of a thin viscous droplet, of constant volume, down an inclined pre-wetted plane. We will derive the evolution equations for the droplet height using the lubrication approximation. We use high-resolution numerics to provide an insight into the important physical mechanisms. Asymptotic analysis is used to obtain approximate solutions based on the dominant physical mechanisms in each region. The spreading and thinning rates are naturally obtained from our asymptotic analysis and are not assumed to be known *a priori*.

2.1 Mathematical formulation

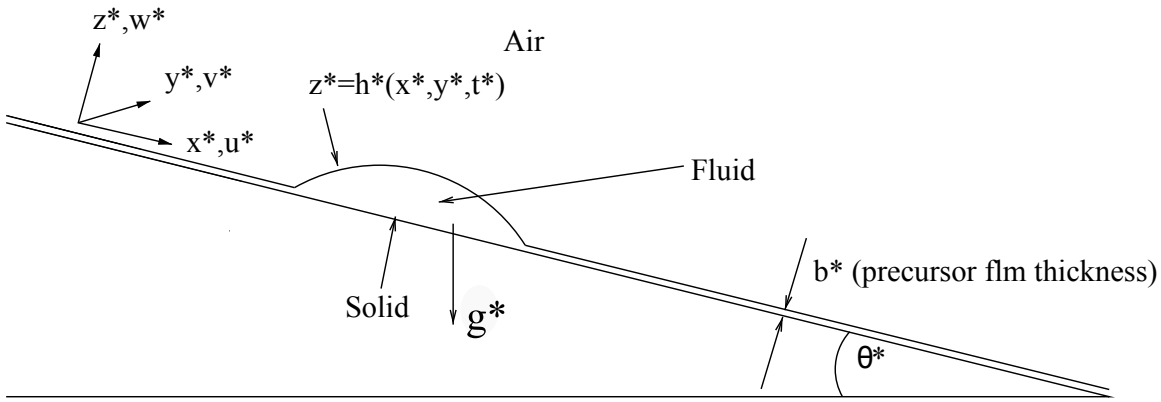

Figure 2.1: Schematic representation of the model studied.

Consider the spreading of a thin fluid droplet, of constant volume, down an inclined plane. The fluid has viscosity μ^*, density ρ^* and surface tension σ^*. The plane is pre-wetted with a thin precursor film of thickness b^*. We choose a Cartesian co-ordinate system (x^*, y^*, z^*) with x^* and y^* along the plane, and z^* along the thickness of the drop. θ is the angle of inclination. The velocities in the x^*, y^*, z^* directions are given by u^*, v^*, w^*, respectively. The free surface is given by $z^* = h^*(x^*, y^*, t^*)$ and the fluid-solid interface is at $z^* = 0$. All starred variables are dimensional.

2.1.1 Governing equations

The equations of motion in the bulk fluid are given by the Stokes equations,

$$0 = -\nabla^* P^* + \rho^* \boldsymbol{g}^* + \mu^* \nabla^{*2} \boldsymbol{u}^*, \tag{2.1}$$

$$0 = \nabla^* \cdot \boldsymbol{u}^*. \tag{2.2}$$

Eqs.(2.1), (2.2) represent conservation of momentum and mass, respectively. The fluid in the bulk is assumed to be very slow viscous flow, so inertial effects have been neglected in Eq. (2.1). In Eq. (2.1), $\boldsymbol{u}^* = (u^*, v^*, w^*)$ is the fluid velocity and P^* is the fluid pressure relative to atmospheric pressure. Without loss of generality, we take the pressure in the air to be zero. The gravitational acceleration, $\boldsymbol{g}^* = (g^* \sin(\theta), 0, -g^* \cos(\theta))$, where g^* is the magnitude of gravitational acceleration. We assume that both the fluid viscosity μ^* and its density ρ^* are constant.

2.1.2 Boundary conditions

On the fluid-solid interface, $z^* = 0$, the no slip boundary condition is applied. This states that the velocity of fluid on the solid equals the velocity of the solid itself. Hence

$$u^* = v^* = w^* = 0, \text{ at } z^* = 0. \tag{2.3}$$

On the free surface, $z^* = h^*(x^*, y^*, t^*)$, which is also referred to as the fluid-air interface the boundary conditions are less well known. Scriven [55] describes this interface as a 'two dimension molecular world analogous to the three dimensional system'. The boundary condition is prescribed by a stress balance at the free surface. This can be written as

$$-(T_1^* - T^*) \cdot \boldsymbol{n}^* = 2R^* \sigma \boldsymbol{n}^*, \tag{2.4}$$

where $T_1^* = -P_1^*$, is the stress tensor in the air phase, which is assumed to be inviscid. P_1^* is the air pressure. Since pressure is measured relative to atmospheric pressure, without loss of generality, $P_1^* = 0$. $T^* = -P^*I + \boldsymbol{\tau}^*$ is the stress tensor in the fluid phase, where P^* is the liquid pressure, $\boldsymbol{\tau}^* = \mu^*(\nabla \boldsymbol{u}^* + \nabla \boldsymbol{u}^{*T})$ is the viscous component of the stress tensor and I is the identity tensor. σ^* is the surface tension at the air liquid interface. σ^* is constant since the free surface is assumed to be free of any contaminants. $2R^*$ is the mean curvature of the surface and $\boldsymbol{n}^*$ is the unit outward normal to the surface (pointing out of the liquid).

The unit outward normal to the surface $z^* = h^*(x^*, y^*, t^*)$ is

$$\boldsymbol{n}^* = \nabla^* \cdot (z^* - h^*(x^*, y^*, t^*)) = \frac{1}{\sqrt{h_{x^*}^{*2} + h_{y^*}^{*2} + 1}} \left(-h_{x^*}^*, -h_{y^*}^*, 1\right). \tag{2.5}$$

The two unit tangents to the free surface, $z^* = h^*(x^*, y^*, z^*)$ are

$$\boldsymbol{t_1^*} = \frac{1}{\sqrt{h_{x^*}^{*2} + 1}} \left(1, 0, {h^*}_{x^*}\right), \tag{2.6}$$

$$\boldsymbol{t_2^*} = \frac{1}{\sqrt{h_{x^*}^{*2} + h_{y^*}^{*2} + 1}\sqrt{h_{x^*}^{*2} + 1}} \left(-h_{x^*}^* h_{y^*}^*, h_{x^*}^{*2} + 1, h_{y^*}^*\right). \tag{2.7}$$

The mean curvature of the surface is $2R^* = \nabla_s^* \cdot \boldsymbol{n^*}$, where ${\nabla^*}_s = (I - \boldsymbol{n^* n^*}) \cdot \nabla^*$ is the surface gradient operator [16]. This is analogous to the gradient operator ∇^*. Using the above, the curvature of the free surface can be written as,

$$2R^* = \frac{h_{x^*x^*}^*(-h_{y^*}^{*2} - 1) + h_{y^*y^*}^*(-h_{x^*}^{*2} - 1) + 2h_{x^*}^* h_{y^*}^* h_{x^*y^*}^*}{(h_{x^*}^{*2} + h_{y^*}^{*2} + 1)^{\frac{3}{2}}}. \tag{2.8}$$

The normal component of the stress balance at the free surface (Eq. (2.4)) is

$$h_{x^*}^{*^2}(P^* - 2\mu u_{x^*}^*) - 2\mu h_{x^*}^* h_{y^*}^*(v_{x^*}^* + u_{y^*}^*) + 2h_{x^*}^*\mu(w_{x^*}^* + u_{z^*}^*) + 2\mu h_{y^*}^{*^2}(w_{y^*}^* + v_{z^*}^*) +$$

$$h_{y^*}^{*^2}(P^* - 2\mu v_{y^*}^*) + P^* - 2\mu w_{z^*}^*$$

$$= -\frac{h_{x^*x*}^*(h_{y^*}^{*^2} + 1) + h_{y^*y^*}^*(h_{x^*}^{*^2} + 1) - 2h_{x^*}^* h_{y^*}^* h_{x^*y^*}^*}{(h_{x^*}^{*^2} + h_{y^*}^{*^2} + 1)^{\frac{1}{2}}}\sigma. \tag{2.9}$$

The two tangential components of Eq. (2.4) are

$$2\mu h_{x^*}^*(u_{x^*}^* - w_{z^*}^*) + \mu(h_{x^*}^{*^2} - 1)(w_{x^*}^* + u_{z^*}^*) + \mu h_{y^*}^*(v_{x^*}^* + u_{y^*}^*)$$

$$+\mu h_{x^*}^* h_{y^*}^*(v_{z^*}^* + w_{y^*}^*) = 0, \tag{2.10}$$

$$2\mu h_{y^*}^*(h_{x^*}^{*^2}(v_{y^*}^* - u_{x^*}^*) - w_{z^*}^* + v_{y^*}^*) + \mu h_{x^*}^*(h_{x^*}^{*^2} + 1 - h_{y^*}^{*^2})(v_{x^*}^* + u_{y^*}^*)$$

$$+2\mu h_{y^*}^* h_{x^*}^*(w_{x^*}^* + u_{z^*}^*) + \mu(h_{y^*}^{*^2} - h_{x^*}^{*^2} - 1)(w_{y^*}^* + v_{z^*}^*) = 0. \tag{2.11}$$

The final boundary condition at $z^* = h^*(x^*, y^*, t^*)$ is the kinematic condition. This states that fluid particles that lie on the interface must always remain on the interface. This implies that

$$\frac{D}{Dt^*}\left[z^* - h^*(x^*, y^*, t^*)\right] = 0 \text{ or}$$

$$\frac{\partial}{\partial t^*}(z^* - h^*(x^*, y^*, t^*)) + \boldsymbol{u}_s^* \cdot \boldsymbol{\nabla}^*(z^* - h^*(x^*, y^*, t^*)) = 0. \tag{2.12}$$

Here $\boldsymbol{u_s^*} = (u_s^*, v_s^*, w_s^*)$ is the velocity vector at the free surface, given by $(u_s^*, v^*{}_s, w^*{}_s) = (u^*|_{z^*=h^*(x^*,y^*,*t)}, v^*|_{z^*=h^*(x^*,y^*,*t)}, w^*|_{z^*=h^*(x^*,y^*,*t)})$. Hence the kinematic condition on

the interface can be written as

$$-h^*_{t^*} + (u^*_s, v^*_s, w^*_s) \cdot (-h^*_{x^*}, h^*_{y^*}, 1) = -h^*_{t^*} - u^*_s h^*_{x^*} - v^*_s h^*_{y^*} + w^*_s = 0. \tag{2.13}$$

Hence,

$$h^*_{t^*} = -u^*_s h^*_{x^*} - v^*_s h^*_{y^*} + w^*_s. \tag{2.14}$$

2.1.3 Nondimensionalisation

We nondimensionalise the equations based on length scales H^*, L^*, a characteristic drop thickness (e.g. the initial drop height) and length (e.g. the initial drop length), respectively, a characteristic speed $U^* = (\rho^* g^* \sin(\theta) {H^*}^2)/\mu^*$ (balancing viscous forces with the horizontal component of gravity), a characteristic pressure $P^* = (\mu^* U^* L^*)/{H^*}^2$ (pressure gradient balancing viscous forces) and a characteristic time $T^* = L^*/U^*$. Typical values along with fluid properties are shown in Table 2.1. Hence we nondimensionalise the variables as

$$\begin{aligned}(x, y) = \frac{(x^*, y^*)}{L^*}, (z, h) = \frac{(z^*, h^*)}{H^*}, (u, v) = \frac{(u^*, v^*)}{U^*}, w = \frac{w^*}{\epsilon U^*},\\ P = \frac{\epsilon H^* P^*}{\mu U^*}, t = \frac{t^* U^*}{L^*}, \epsilon = \frac{H^*}{L^*}.\end{aligned} \tag{2.15}$$

Here, ϵ is the aspect ratio, which is typically much less than one for these problems. It is worth mentioning that there is an intrinsic length scale $h^* = (\sigma^*/(\rho^* g^*))^{1/2}$, referred to

as the capillary length scale. This is the length scale over which surface tension balances gravity and is much less than 1 for most liquids. Other nondimensionalizations have been used (e.g. see Kondic [34] and Hocking [25]). We prefer to use the above, but the final form of the equations are similar. Substituting the above dimensionless variables

Physical quantities	Typical value
Viscosity, μ^* (for silicon oil)	0.5 kg/ms
Surface tension, σ^* (for silicon oil)	0.0021 N/m
Density, ρ^* (for silicon oil)	960 kg/m^3
Characteristic Height, H^*	0.001m
Characteristic Length, L^*	0.01m
Characteristic speed, $U^* = \frac{\rho^* g^* \sin(\theta) H^{*2}}{\mu^*}$	0.02 m/s
Characteristic pressure, $P^* = \frac{\mu^* U^* L^*}{H^{*2}}$	100 kg/(m s^2)
Characteristic time, $T^* = \frac{L^*}{U^*}$	0.05 s
Capillary lengthscale, $(\frac{\sigma^*}{\rho^* g^*})^{1/2}$	10^{-4}m

Table 2.1: Typical values of the dimensional quantities.

into the fluid bulk equations and boundary conditions produces a set of dimensionless equations

$$u_x + v_y + w_z = 0, \tag{2.16}$$

$$-P_x + \epsilon^2 u_{xx} + \epsilon^2 u_{yy} + u_{zz} + 1 = 0, \tag{2.17}$$

$$-P_y + \epsilon^2 v_{xx} + \epsilon^2 v_{yy} + v_{zz} = 0, \tag{2.18}$$

$$-P_z + \epsilon^4 w_{xx} + \epsilon^4 w_{yy} + \epsilon^2 w_{zz} - \epsilon \cot(\theta) = 0. \tag{2.19}$$

On the free surface, $z = h(x, y, t)$, the nondimensionalized normal stress balance is

$$\frac{1}{\epsilon^2 h_x^2 + \epsilon^2 h_y^2 + 1}[P(\epsilon^2 h_x^2 + \epsilon^2 h_y^2 + 1) - \epsilon^4 h_x^2 u_x - 2\epsilon^4 h_x h_y (v_x - u_y) + 2\epsilon^2 h_x (\epsilon^2 w_x + u_z)$$

$$+2\epsilon^3(\epsilon^2 w_y + v_z) - 2\epsilon^3 h_y^2 v_y + 2\epsilon^2 w_x] =$$
$$-Ca\frac{h_{xx}(1+\epsilon^2 h_y^2) + h_{yy}(1+\epsilon^2 h_x^2) - 2\epsilon^2 h_y h_x h_{xy}}{(\epsilon^2 h_x^2 + \epsilon^2 h_y^2 + 1)^{\frac{3}{2}}}. \tag{2.20}$$

Where Ca= $(\epsilon^3\sigma^*)/(\mu^* U^*)$, is the capillary number and is assumed $O(1)$. The nondimensional tangential interfacial stress boundary conditions are

$$2\epsilon^2 h_x(u_x + w_z) + (\epsilon^2 h_x^2 - 1)(\epsilon^2 w_x + u_z) + \epsilon^2 h_y(v_x + u_y) + \epsilon^2 h_x h_y(v_z + \epsilon^2 w_y) = 0 \tag{2.21}$$

$$2\epsilon^2 h_y(\epsilon^2 h_x^2(v_y - u_x) - w_z + v_y) + \epsilon^2 h_x(\epsilon^2 h_x^2 - \epsilon^2 h_y^2 - 1)(v_x + u_y) + 2\epsilon^2 h_y h_x(\epsilon^2 w_x + u_z)$$
$$+(\epsilon^2 h_y^2 - \epsilon^2 h_x^2 - 1)(\epsilon^2 w_y + v_z) = 0. \tag{2.22}$$

The nondimensional kinematic condition is,

$$h_t + h_x u|_{z=h(x,y,t)} + h_y v|_{z=h(x,y,t)} - w|_{z=h(x,y,t)} = 0. \tag{2.23}$$

The no slip boundary condition on $z = 0$ in dimensionless form is

$$u = v = w = 0. \tag{2.24}$$

2.1.4 Lubrication theory

Eqs. (2.16-2.24) can be simplified using the fact that the aspect ratio $\epsilon \ll 1$. The equations obtained at leading order in ϵ are referred to as a long wavelength or lubrication approximation. We seek solutions in the form of a regular perturbation expansion in

powers of ϵ^2 as

$$(u, v, w, P, h) = (u_0, v_0, w_0, P_0, h_0) + \epsilon^2(u_1, v_1, w_1, P_1, h_1) + ... \tag{2.25}$$

Substituting this series into Eqs. (2.16-2.24) gives, at leading order, in the fluid

$$\begin{aligned} u_{0x} + v_{0y} + w_{0z} &= 0, & (2.26)\\ -P_{0x} + u_{0zz} + 1 &= 0, & (2.27)\\ -P_{0y} + v_{0zz} &= 0, & (2.28)\\ -P_{0z} - D(\theta) &= 0, & (2.29) \end{aligned}$$

where $D(\theta) = \epsilon \cot(\theta)$, and is assumed $O(1)$. We include this effect at leading order even though it is of order ϵ. At $z = h_0(x, y, t)$ we have

$$\begin{aligned} h_{0t} + h_{0x}u_0 + h_{0y}v_0 - w_0 &= 0, & (2.30)\\ -Ca(h_{0xx} + h_{0yy}) &= P_0, & (2.31)\\ u_{0z} &= 0, & (2.32)\\ v_{0z} &= 0. & (2.33) \end{aligned}$$

At $z = 0$ the leading order no slip boundary condition is

$$u_0 = v_0 = w_0 = 0. \tag{2.34}$$

We now follow a sequence of steps to reduce Eqs. (2.26-2.34) to a single evolution equation for $h_0(x, y, t)$. Integrating Eq. (2.29) with respect to z and applying Eq. (2.31), we obtain the leading order equation for pressure,

$$P_0 = D(\theta)(h_0 - z) - Ca(h_{0xx} + h_{0yy}). \tag{2.35}$$

Differentiating the above equation with respect to x and substituting it into Eq. (2.27) gives

$$u_{0zz} = -1 + D(\theta)h_{0x} - Ca(h_{0xxx} + h_{0yyx}). \tag{2.36}$$

Integrating with respect to z twice and applying the two boundary conditions for u_0 in Eqs. (2.32, 2.34) gives

$$u_0 = [Ca(h_{0xxx} + h_{0yyx}) - D(\theta)h_{0x} + 1]\left[h_0 z - \frac{z^2}{2}\right]. \tag{2.37}$$

To obtain the equation for v_0, we differentiate Eq. (2.35) with respect to y then substitute it into Eq. (2.28). Integrating the resulting equation with respect to z twice and applying the boundary conditions for v_0 in Eqs. (2.33, 2.34) gives,

$$v_0 = [Ca(h_{0xxy} + h_{0yyy}) - D(\theta)h_{0y}]\left[h_0 z - \frac{z^2}{2}\right]. \tag{2.38}$$

Differentiating Eqs. (2.37, 2.38) with respect to x and y, respectively, and substituting

it into Eq. (2.26) gives on integration with respect to z,

$$\begin{aligned} w_0 = &-[Ca(h_{0xxx} + h_{0yyx}) - D(\theta)h_{0x} + 1]_x \left(h_0 \frac{z^2}{2} - \frac{z^3}{6} \right) \\ &-[Ca(h_{0xxx} + h_{0yyx}) - D(\theta)h_{0x} + 1]h_{0x} \frac{z^2}{2} \\ &-[(Cah_{0xxy} + h_{0yyy}) - D(\theta)h_{0y}]_y \left(h_0 \frac{z^2}{2} - \frac{z^3}{6} \right) \\ &-[Ca(h_{0xxy} + h_{0yyy}) - D(\theta)h_{0y}]h_{0y} \frac{z^2}{2}. \end{aligned} \tag{2.39}$$

Finally substituting the expressions for the velocities into the kinematic condition produces an equation for the evolution of the free surface. This can be written in compact form as

$$h_{0t} + \nabla \cdot \left[Ca \frac{{h_0}^3}{3} \nabla \nabla^2 h_0 - D(\theta) \frac{h_0^3}{3} \nabla h_0 \right] + \left[\frac{h_0^3}{3} \right]_x = 0. \tag{2.40}$$

We have thus reduced the problem to a single parabolic PDE for the evolution of the free surface due to fluid fluxes driven by surface tension (second term) vertical gravity (third term) and horizontal gravity (fourth term). The evolution equation is characterized by two parameters the typical values of which are provided in Table 2.2.

In the next section we seek 1D solutions of Eq. (2.40) by assuming that h only varies in the x-direction with no dependence in y. This will provide the base state whose linear stability in the transverse y direction will be investigated in Chapter 4.

Nondimensional quantities	Typical value
ϵ	0.1
$Ca = \frac{\epsilon^3 \sigma^*}{\mu^* U^*}$	2.23×10^{-3}
$D(\theta)$	$0 \leq D(\theta) \leq \infty$

Table 2.2: Typical values for the dimensionless parameters calculated using values in Table 2.1.

2.2 1D drop spreading: numerical results.

We first consider the spreading of the droplet in the x-direction with no variation in the y-direction. The 1D version of Eq. (2.40) is then given by

$$h_t + Q_x = 0; \; Q = \left[Ca \frac{h^3}{3} h_{xxx} - D(\theta) \frac{h^3}{3} h_x + \frac{h^3}{3} \right]. \tag{2.41}$$

This partial differential equation are suplimented by four boundary conditions, which are,

$$h = b, \;\; h_x = 0 \;\; \text{at} \;\; x = \pm L, \tag{2.42}$$

where $b \ll 1$ is the precursor film thickness and L is an arbitrary length. This characterises a flat precursor film far upstream and downstream of the spreading droplet. The initial conditions are chosen as: (see Fig. 2.2)

$$h(x,0) = (1 + b - x^2)[H(1-x) - H(-1-x)] + b[H(x-1) + H(-1-x)], \tag{2.43}$$

where $H(x)$ is the Heaviside function. The initial condition for the fluid droplet

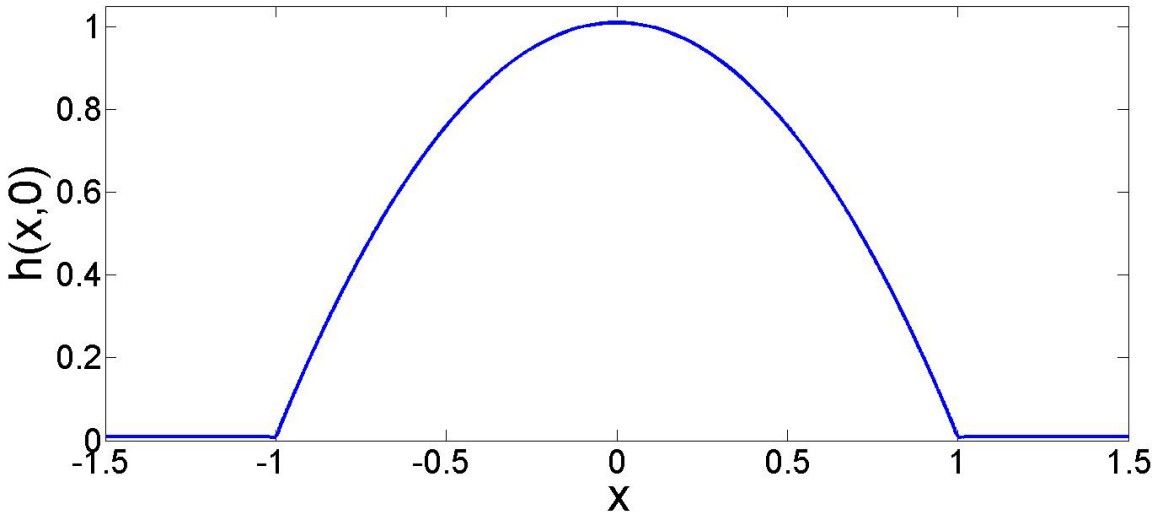

Figure 2.2: The initial shape of the droplet

assumes a parabolic shape connecting to a precursor film ahead and behind it. We seek the time evolution of the free surface keeping the precursor thickness, capillary number and inclination angle θ fixed. We will compute numerical simulation varying these parameters to understand the influence they have on the spreading of the droplet. We first discretise the spatial derivatives in Eq. (2.41) keeping the time derivative continuous. We define a forward difference and backward difference by,

$$h_{x,i} = \frac{h_{i+1} - h_i}{\Delta x}, \quad h_{\tilde{x},i} = \frac{h_i - h_{i-1}}{\Delta x}, \tag{2.44}$$

respectively, where $h_i = h(x_i, t)$, $i = 0, 1, ..., N$. N is the number of discretisation points and Δx is the grid size. Using these forward and backward differences we can discretise Eq. (2.41) such that,

$$h_{t,i} + \left[Ca\ a(h_{i+1}, h_i) h_{\tilde{x}\tilde{x}\tilde{x},i} - \hat{D}(\theta) a(h_{i+1}, h_i) h_{\tilde{x},i}\right]_x + \left[\frac{h_i^3}{3}\right]_{\tilde{x}} = 0, \tag{2.45}$$

where,

$$a(h_{i+1}, h_i) = \frac{h_{i+1}^3 + h_i^3}{6}, \tag{2.46}$$

so that these are second order approximations hence Eq. (2.45) are second order accurate. The finite difference scheme used in the above discretisation uses a 5-point stencil. This has the advantage of a smaller bandwidth (in comparison a 7-point stencil using the standard centred-difference scheme) while still maintaining second order accuracy. This scheme is commonly used in thin film problems (see [34, 38]). Our numerical scheme employed a fixed and spatially uniform grid. We used implicit timestepping and validated convergence using grid refinement. The resulting differential equations are solved using the ODE solver ODE15i [56] in Matlab. The overall features of the flow are as reported by Huppert [27], Troian *et al.* [63] and Hocking [25].

Figure 2.3 shows the late time evolution ($t = 10^2 - 2 \times 10^3$) of the droplet height h for $\theta = 90^o$, $Ca = 10^{-3}$ and $b = 10^{-2}$. Inspection of this figure reveals there are several main features of the droplet. The first is the main bulk droplet spreading under the influence of horizontal gravity. Towards the leading edge of the spreading droplet is a short region in which horizontal gravity balances capillary forces. This region contains the so-called capillary ridge where there is an abrupt jump in fluid height as the main bulk connects onto the precursor film ahead of the fluid droplet. Ahead of the fluid droplet the precursor film remains undisturbed. At the trailing edge of the droplet is another small transition region where capillary forces balance gravity.

Figure 2.4 compares the droplet height h for $t = 2 \times 10^3$. The parameter values are: $Ca = 10^{-3}$, $b = 10^{-2}$, $\theta = 90°$ (dashed line), $\theta = 60°$ (dotted line) and $\theta = 3°$ (solid line). We can see that the overall droplet height remains unchanged, except for the amplitude of the capillary ridge which decreases as the angle of inclination θ (see inset Fig. 2.4).

Figure 2.5 the droplet height h at $t = 2 \times 10^3$, with $\theta = 90^o$ and $b = 10^{-2}$. The solid line shows the fluid where $Ca = 10^{-3}$ and dashed line $Ca \approx 0$. The case where $Ca = 0$ would lead to a a shock to form which would not be resolved numerically. We can see that the overall droplet height remains unchanged, except within short regions such as the capillary ridge shown in insets in Fig. 2.5. Therefore the solutions obtained, downstream of the trailing edge of the droplet are robust for a variety of parameters and persist at late-late times.

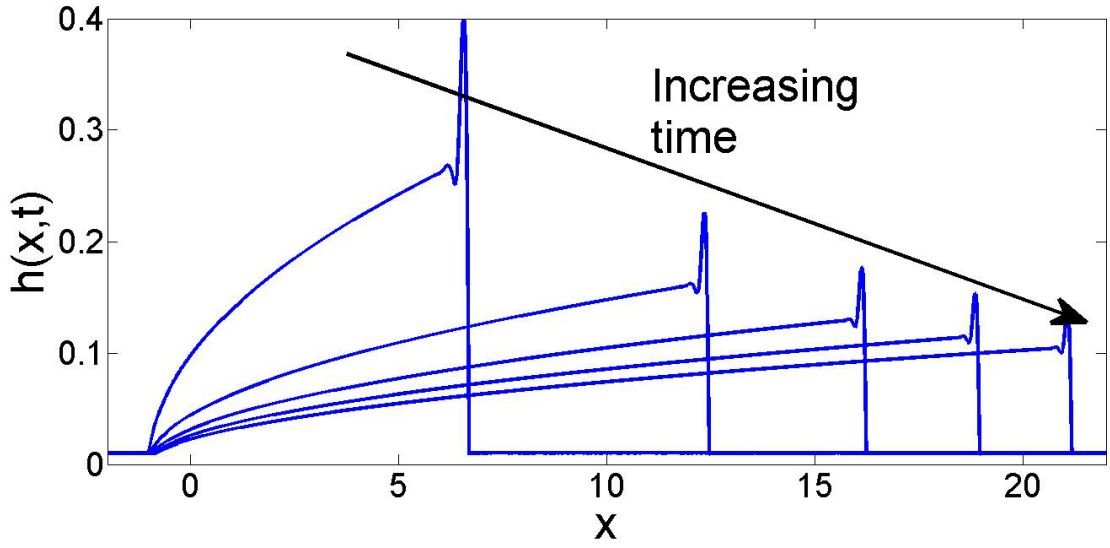

Figure 2.3: The evolution of the spreading droplet angle of inclination $\theta = 90^o$, $b = 10^{-2}$ and $Ca = 10^{-3}$ for $t = 100, 500, 1000, 1500, 2000$.

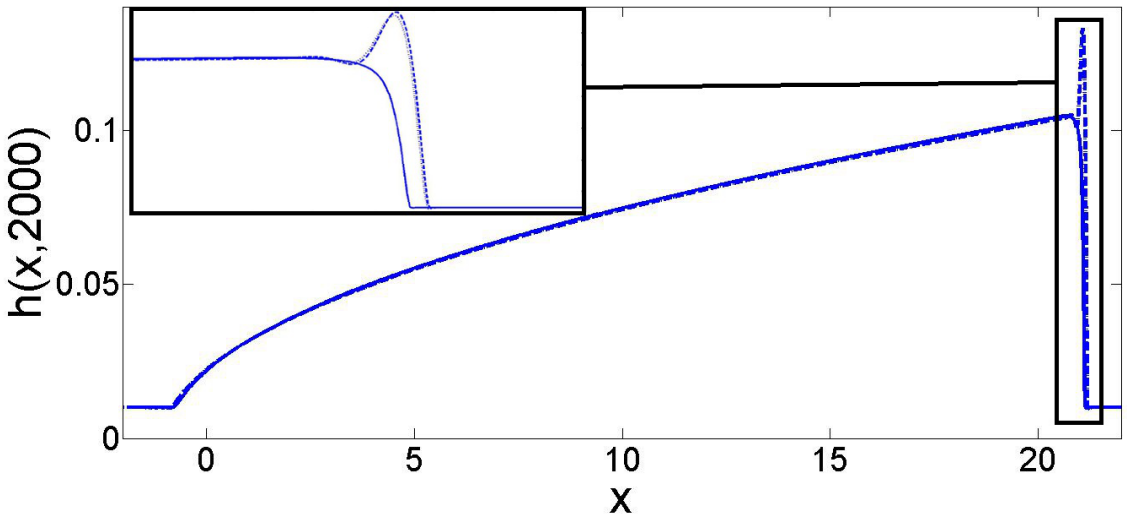

Figure 2.4: Comparing the droplet height h for $t = 2 \times 10^3$. The parameter values are: $Ca = 10^{-3}$, $b = 10^{-2}$, $\theta = 90^o$ (dashed line), $\theta = 60^o$ (dotted line) and $\theta = 3^o$ (solid line).

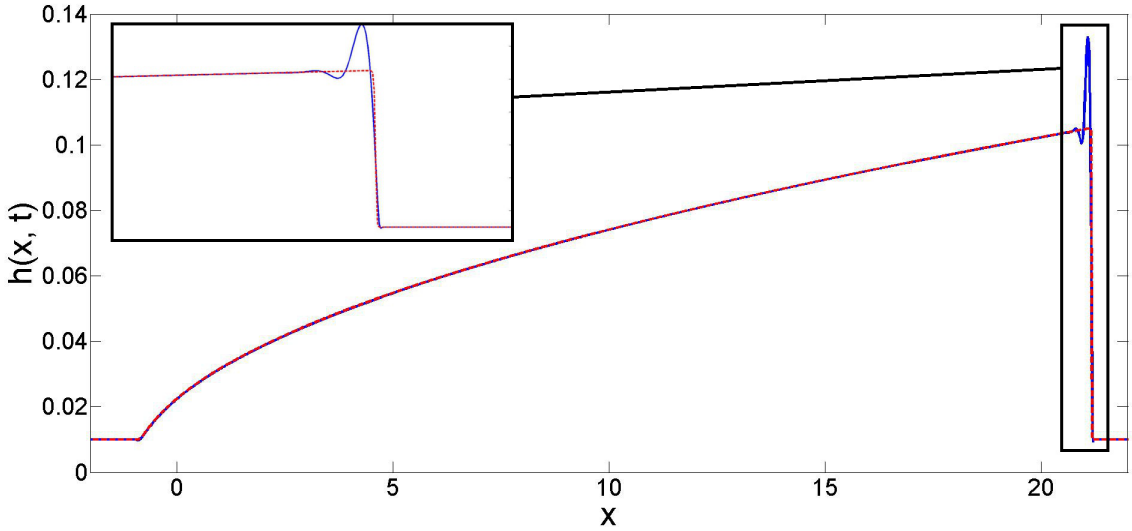

Figure 2.5: Comparing the droplet height h for $t = 2 \times 10^3$. The parameter values are: $b = 20^{-3}$, $\theta = 90^o$ $Ca = 10^{-3}$ (solid line) and $Ca \approx 0$ (dashed line).

2.3 Gravity-driven spreading without capillary effects.

The long time evolution of the droplet, when capillary effects are neglected, can be described using the method of characteristics. Hence, Eq. (2.41), can be written as

$$h_t + \left[\frac{h^3}{3}\right]_x = 0. \tag{2.47}$$

This first-order quasilinear PDE can now be solved using the method of characteristics. Along the characteristic curves $\lambda = \lambda(t)$ we have

$$\frac{dx}{dt} = h^2, \tag{2.48}$$

$$\frac{dh}{dt} = 0. \tag{2.49}$$

Equation (2.49) implies that h is constant along the characteristic curves i.e., $h(x(t), t) = h^0(\xi)$, where $h^0 = h(x, 0)$ and $x(0) = \xi$. Integrating Eq. (2.48) along the characteristics gives

$$x = h^{0^2} t + \xi, \tag{2.50}$$

Figure 2.6 shows the plots of the characteristic curves given by Eq. (2.50) using the initial condition in Eq. (2.43). For this initial condition, there is an intersection of the characteristic curves near the leading edge of the droplet resulting in the formation of a

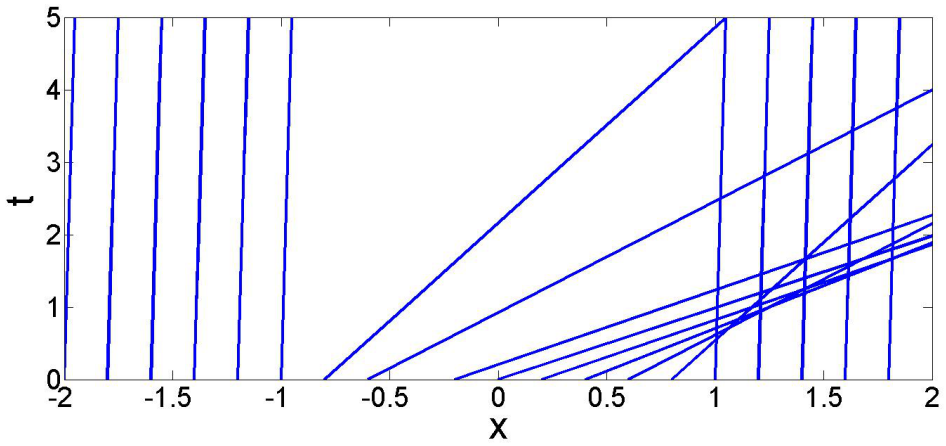

Figure 2.6: The characteristic curves for Eq. 2.47 using the initial condition in Eq. (2.43).

shock like structure. After determining a shock is formed we use Whitham's equal area rule [66] to construct a shock solution (or a weak solution to Eq. (2.47)) as follows. As the flow develops there is a point in time where the solution 'breaks' and becomes multivalued. At this point there exists a weak solution which is discontinuous. Both the multivalued curve and the discontinuous curve must conserve the volume of the drop, hence the discontinuity must 'cut off' lobes of equal area as shown in Fig. 2.7. Consider the conservation equation written in the form

$$h_t + q_x = 0, \tag{2.51}$$

where the flux $q = q(h)$ and $c(h) = q'(h)$. Let $x = s(t)$ be the position of the shock and, $h_1^0 = h^0(\xi_1)$ and $h_2^0 = h^0(\xi_2)$ be the initial values of h at a point ξ_1 and ξ_2 ahead and behind the shock respectively. The equations for the equal area rule can then be

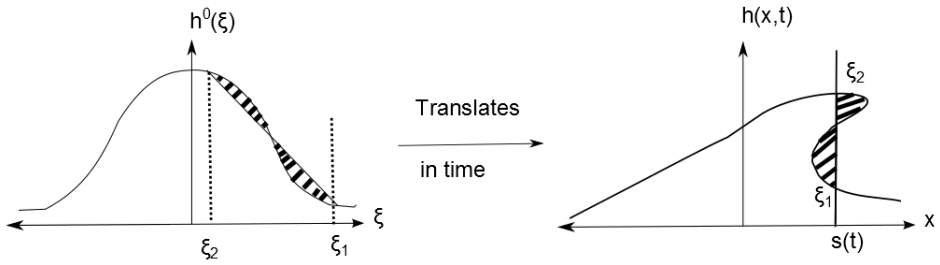

Figure 2.7: Equal area construction showing the transformation to the breaking profile

written as following (Whitham [66])

$$\left[(q_2^0 - q_1^0) - (h_2^0 c_2^0 - h_1^0 c_1^0)\right] \frac{\xi_1 - \xi_2}{c_1^0 - c_2^0} = \int_{\xi_2}^{\xi_1} h^0 d\xi, \tag{2.52}$$

$$s(t) = \xi_1 + c_1^0 t, \tag{2.53}$$

$$s(t) = \xi_2 + c_2^0 t. \tag{2.54}$$

Using $q(h) = \frac{h^3}{3}$ and $c(h) = h^2$, we then solve Eqs. (2.53,2.54) for t to obtain,

$$t = \frac{\xi_1 - \xi_2}{c_2^0 - c_1^0}, \tag{2.55}$$

using which Eq. (2.52) can be written as ,

$$\frac{2}{3}(h_2^{0^3} - h_1^{0^3})t = \int_{\xi_2}^{\xi_1} h^0 d\xi. \tag{2.56}$$

The integral term would take into account the precursor film and we only wish to conserve the volume of the fluid droplet. Hence by subtracting off the contribution

from the precursor film and substituting Eq. (2.55) into the above equation produces,

$$\frac{2t}{3}(h_2^{0^3} - h_1^{0^3}) - bt(h_1^{0^2} - h_2^{0^2}) = \int_{\xi_2}^{\xi_1} h^0 - b \, d\xi. \tag{2.57}$$

As we need the long time solution then we can take limits as time tends towards infinity. As time increases ξ_1 exceeds 1 and then $h_1^0 = b$ and therefore $q_1^0 = \frac{b^3}{3}$ and $c_1^0 = b^2$. Note that as $t \to \infty$ $\xi_2 \to -1$ because the characteristic curve that originates from $x = -1$ is the last to intersect the other characteristic curves (characteristics that originate from $x < -1$ do not intersect). Substitute these values into Eq. (2.57),

$$\frac{2t}{3}(h_2^{0^3} - b^3) - bt(h_2^{0^2} - b^2) = \int_{-1}^{1} h^0 - b \, d\xi = A, \tag{2.58}$$

where A is the volume of the drop. Hence,

$$h_2^{0^3} - \frac{5}{3}b^3 + \frac{3}{2}bh_2^{0^2} - \frac{3A}{2t} = 0. \tag{2.59}$$

As $h_2^0 \gg b$, then Eq. (2.59) gives the relationship for the thinning of the bulk drop as,

$$h_2^0 \approx \left(\frac{3A}{2t}\right)^{1/3}, \tag{2.60}$$

From Eq. (2.54) we can approximate the position of the shock as,

$$s(t) \approx c_2^0 t = h_2^{0^2} t, \tag{2.61}$$

because $\xi \to -1 \ll h_2^{0^2} t$. Substituting the approximation for the height of the leading edge (Eq. (2.60)) into the above equation gives the long time position of the shock,

$$s(t) \approx \left(\frac{9}{4} A^2 t\right)^{1/3}. \tag{2.62}$$

Taking the equation of the charecteristic curves (Eq. (2.50)) and rearranging for $h(x,t)$ we obtain a similarity solution for the height of the bulk drop,

$$h(x,t) = \left(\frac{x-\xi}{t}\right)^{1/2}. \tag{2.63}$$

Rearranging Eq. (2.62) for t and substituting it into the above equation leads to an equation for the evolution of the main bulk drop,

$$h(x,t) \approx h_2^0 \left(\frac{x-\xi}{s(t)}\right)^{1/2}. \tag{2.64}$$

This is the similarity solution calculated from the asymptotic analysis by Huppert [27]. Note the position of the shock ($s(t)$) and the height of the shock (h_2^0) here can be thought of as the position and height of the 'effective' contact line, denoted in the following analysis by x_L and h_L. This analysis conducted here has successfully reproduced the spreading and thinning rates and similarity solution obtained by Huppert [27].

2.4 Description of the late-time self-similar structure.

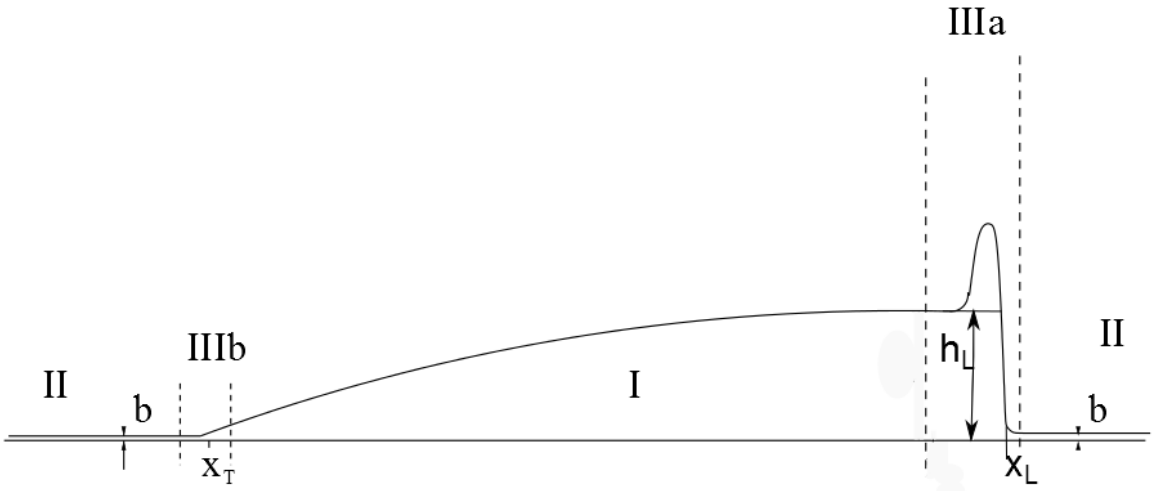

Figure 2.8: Late-time self-similar structure of the spreading fluid droplet.

The numerical solution described in §2.2 shows a multi-region locally self-similar structure for the droplet height, particularly at late-time. As mentioned previously the self-similar structure observed is robust to variation in the parameters which characterise the droplet shape. We describe each region in turn below along with their relevant physics, scalings and approximate solutions. The spreading of the droplet is controlled predominantly by the horizontal component of gravity. Capillary or surface tension effects become important in short transition regions especially in the formation of the capillary ridge at the leading edge of the spreading droplet (see Fig. 2.5 comparing spreading with and without capillary effects). The flow domain of the drop is divided into the following regions (see Fig. 2.8):

- Region I: The bulk droplet region. This long region contains the bulk of the spreading droplet. The dominant flow mechanism in this region is the horizontal component of gravity. It is characterised by the location of its leading edge (the 'effective' contact line ahead of the droplet), $x = x_L(t)$, the height at the leading edge, $h = h_L(t)$, and the location of the trailing edge (the 'effective' contact line behind the droplet), $x = x_T(t)$.

- Region IIIa: The 'effective' contact line region at the leading edge of the droplet. Here surface tension effects are of similar magnitude to the horizontal component of gravity. This region is characterised by the position of the effective contact line $x_L(t)$, the droplet height upstream of the capillary ridge $h_L(t)$ and the precursor film thickness b.

- Region IIIb: The 'effective' contact line region at the trailing edge of the droplet. Here surface tension effects are of a similar to the horizontal forces of gravity. This region is characterised by the position of the capillary wave at the trailing edge of the droplet denoted by $x_T(t)$ and the precursor film height b.

- Region II: The precursor film region. This region is a passive region containing the precursor film ahead and behind the spreading droplet. This region remains undisturbed.

The flow is characterised by 3 variables h_L, x_L and x_T. These variables will be used to describe the solutions of the regions described previously. We will also use these variables to determine the spreading and thinning rates not known *a priori*. We obtain

x_L by locating where the position of the capillary wave downstream of the capillary ridge. h_L is obtained by the global maximum in fluid height in the absence of capillary effects. x_T is the location of the capillary wave at the trailing edge of the droplet. We will now discuss each region in turn, neglecting hereafter the effects vertical component of gravity everywhere except in the capillary ridge region where it appears as a second-order diffusion term smoothing the capillary ridge. We use the numerical solution of the PDE shown in Fig. 2.3 to illustrate the self-similar structure by showing the data collapses when rescaled using the scalings appropriate to each region. We also use this data to validate any assumptions made in the analysis.

2.4.1 Region I: The bulk fluid droplet

This long region between $x_T(t) \leq x \leq x_L(t)$ contains the majority of the spreading droplet. The dominant spreading mechanism is due to the horizontal component of gravity. The numerical solutions shown in Fig. 2.3 suggest a self-similar solution is likely. We now describe this self-similar solution. We set,

$$x = x_T(t) + \xi x_L(t), \quad h(x,t) = h_L(t)H(\xi). \tag{2.65}$$

Figure 2.9 shows that the numerical solution to Eq. (2.41), shown in Fig. 2.3, scale under these scaling's. We now derive an approximate solution for this region. Substi-

tuting the above scaling's into Eq. (2.41) we obtain at leading order in $1/x_L$

$$-\hat{V}(\xi H)_\xi + \left[\frac{H^3}{3}\right]_\xi = 0, \tag{2.66}$$

where $\hat{V} = \dot{x}_L/h_L^2$ is related to the speed of the 'effective' contact line at the leading edge of the droplet. We will continue to use the the dot above a variable (i.e. $\dot{\square}$) to denote the time derivative of a function of time only. In the above equation we assume in the above equation that the fluid volume is conserved (i.e. $(\dot{x_L h_L}) = 0$, confirmed from numerical simulations and will be validated in §2.5) and that the trailing edge of the droplet is pinned (i.e. $\dot{x}_T = 0$). Integrating the above equation with respect to ξ and applying the boundary condition $H = 1$ at $\xi = 1$ also assuming $\hat{V} = 1/3$ at leading order in precursor film (validated in §2.4.2), we obtain

$$H(H^2 - \xi) = 0. \tag{2.67}$$

The solutions of which are $H = 0, \pm\sqrt{\xi}$. As $H = 0$ is a trivial solution and $H = -\sqrt{\xi}$ is an unrealistic one, the solution is,

$$H = \sqrt{\xi}. \tag{2.68}$$

The dashed line in Fig. 2.9 shows this similarity solution. It can be seen that the similarity solution has good agreement with the rescaled numerical solutions. In the

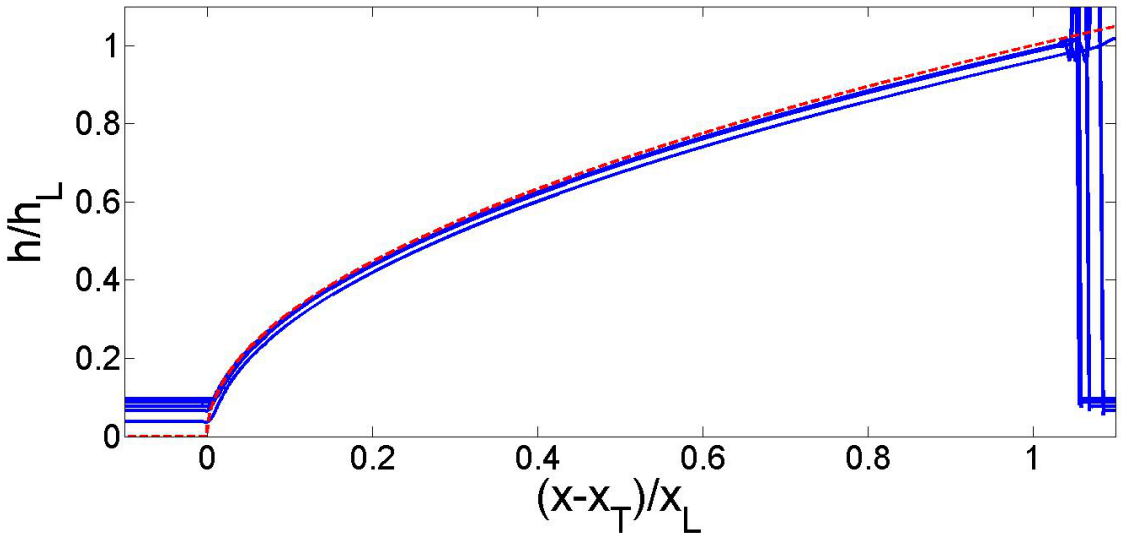

Figure 2.9: Evolution of droplet height h using data from Fig. 2.3 rescaled using Eq. (2.65). The dashed lines show the similarity solution in Eq. (2.68).

original variables this can be written as,

$$h(x,t) = h_L(t)\sqrt{\frac{x - x_T}{x_L(t)}}. \tag{2.69}$$

Hence, $h(x,t) \sim \sqrt{x}$ (where '$\sim$' means 'goes like'), which is consistent with numerics (see Fig. 2.3). This solution was first obtained by Huppert [27] and also Troian *et al.* [63]. We observe from Eq. (2.69) that $h_x,\ h_{xx} \to \infty$ as $x \to x_T$. This implies that the above similarity solution breaks down near $x = x_T$. This means that surface tension and vertical gravity can no longer be neglected in Eq. (2.41) and a transition region including this is required. This is discussed in §2.4.3.

2.4.2 Region IIIa: The 'effective' contact line ahead of the drop.

This region includes the capillary ridge and connects to the precursor film (region II) ahead of it and the bulk drop (region I) behind. The length scale of this region, X (say), is obtained by balancing surface tension with the horizontal component of gravity. Hence,

$$X = (Cah_L)^{\frac{1}{3}}. \tag{2.70}$$

We introduce the following scalings for this region as follows.

$$x = x_L + (Cah_L)^{1/3}\xi, \quad h(x,t) = h_L H(\xi,\tau), \; \tau = \frac{h^{5/3}t}{3Ca^{1/3}}. \tag{2.71}$$

Figure 2.10 show a family of quasi-steady solutions when the numerical solution in

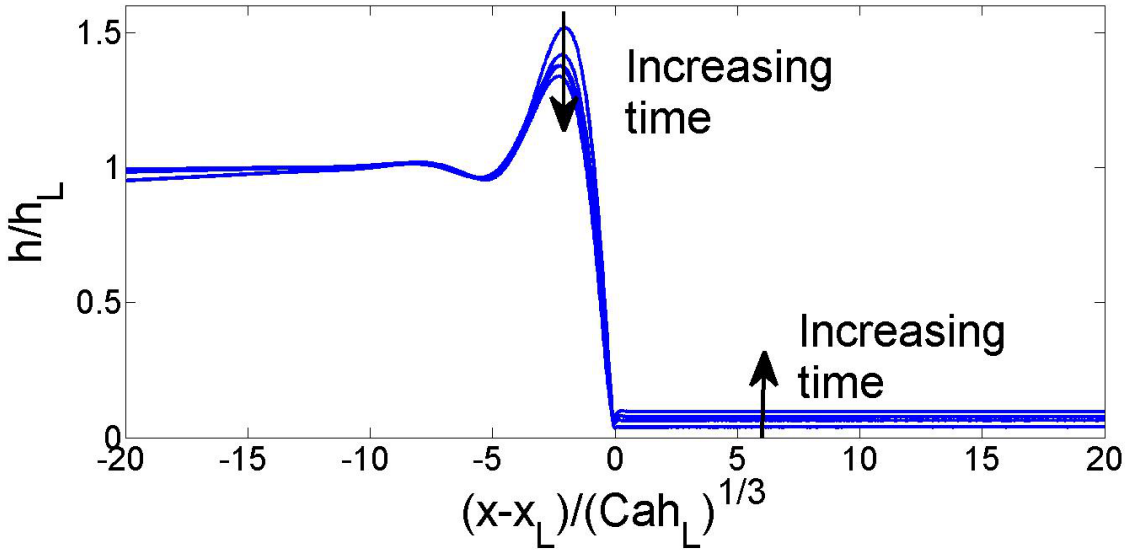

Figure 2.10: Evolution of the droplet height h in region IIIa using data from Fig. 2.3 rescaled using Eq. (2.71).

Fig. 2.3 is scaled using the above scalings. The maximum height of the capillary ridge decreases in time while the film thickness downstream increases. As h_L is decreasing in time (see Fig. 2.3) $s(t) = b/h_L(t)$ is an increasing function of time as the precursor film thickness is fixed. We now derive an approximate solution for this region. Substituting the above scalings into Eq. (2.41) and assuming the solution to be quasi-steady (i.e. assuming $\dot{h}_L \approx 0$), we obtain,

$$-\hat{V}H_\xi + \left[\frac{H^3}{3}H_{\xi\xi\xi} - \hat{D}(\theta)\frac{H^3}{3}H_\xi + \frac{H^3}{3}\right]_\xi = 0, \tag{2.72}$$

where $\hat{V} = \dot{x}_L/h_L^2$ is the dimensionless 'effective' contact line speed and $\hat{D}(\theta) = (\epsilon \cot(\theta) h_L^{2/3})/Ca^{1/3}$. These are supplemented by the boundary (or matching) conditions that,

$$H \to 1 \ \text{ as } \ \xi \to -\infty, \ \ H \to s \ \text{ as } \ \xi \to \infty. \tag{2.73}$$

Equation (2.73) assumes that h is constant far upstream and downstream where is matches onto regions I and II, respectively. This is reasonable considering that h is only weakly ξ dependent under these scalings. While this matching condition is approximate for the main bulk region (region I) it is exact for region II. Then integrating Eq. (2.72) with respect to ξ and using the above boundary conditions gives,

$$\hat{V} = \frac{1}{3}\left(1 + s + s^2\right). \tag{2.74}$$

Using this gives the following ODE,

$$H_{\xi\xi\xi} = -\left[\frac{s^2+s}{H^3}\right] + \left[\frac{1+s+s^2}{H^2}\right] + \hat{D}(\theta)H_\xi - 1,$$
$$H \to 1 \text{ as } \xi \to -\infty,$$
$$H \to s \text{ as } \xi \to \infty. \tag{2.75}$$

Hence complex PDE to a single third order ODE in this region parameterised by $s(t)$. Varying s gives the full family of quasi-steady solutions shown in Fig 2.10. Equation (2.75) was first derived by Troian *et al.*. We solve this ODE numerically using the shooting method as outlined below. We linearise Eq. (2.75) about the upstream boundary condition, i.e., $H \to 1$ as $\xi \to -\infty$. This provides the three initial conditions along with a shooting parameter which we use to integrate Eq. (2.75). The shooting parameter is adjusted so as to satisfy the downstream boundary condition, $H \to s(t)$ as $\xi \to \infty$. Details of the shooting method for these kind of problems can be found in Tuck and Schwartz [64]. Taking,

$$H = 1 + \delta H_1(\xi). \tag{2.76}$$

Substituting into Eq. (2.75) gives at $O(\delta)$,

$$H_{1\xi\xi\xi} = \left(-2 + s + s^2\right) H_1 + \hat{D}(\theta)H_{1\xi}. \tag{2.77}$$

The characteristic equation of the above ODE has three roots, one of which is always negative. This root is discarded since we avoid exponentially growing solution as ξ becomes large and negative. The remaining two roots are always positive (i.e. have positive real part). Depending on the angle of inclination θ, we have 3 cases: complex conjugate, real and equal and real and distinct roots.

Case 1: Complex conjugate roots ($\alpha \pm i\beta$). The solution of Eq. (2.77) can be written as,

$$h_1 \sim 1 + Ae^{\alpha\xi}\cos(\beta(\xi - \xi_0)), \quad \text{as} \quad \xi \to \infty. \tag{2.78}$$

Since the ODE in Eq. (2.75) is translationally invariant, we can fix ξ_0 (large and negative) such that $\cos(\beta(\xi - \xi_0)) = 1$. This gives a one parameter family of solutions and one can shoot by varying the parameter A to satisfy the downstream boundary condition. It can be shown that there is a unique solution in this case.

Case 2: Real and equal (α_1 say). The solution of Eq. (2.77) can be written as,

$$h_1 \sim 1 + e^{\alpha_1\xi}(A + B\xi), \quad \text{as} \quad \xi \to \infty. \tag{2.79}$$

There is a two parameter family of solutions in this case. One can fix a parameter (say A) and shoot with the other parameter to satisfy the downstream boundary condition. There is also a unique solution in this case.

Case 3: Roots are real and distinct (α_1, β_1 say). The solution of Eq. (2.77) can be written

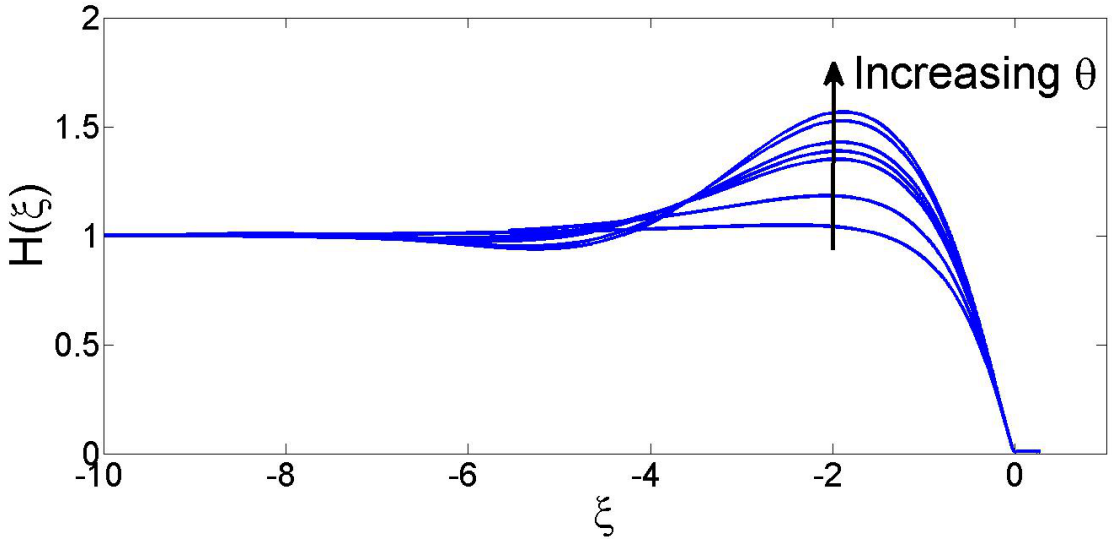

Figure 2.11: The solution to the ODE in Eq. (2.75) for inclination angles $\theta = 90$, 60, 45, 30, 15, 5, 4 and 3 degrees. The parameter $s = 0.01$.

as,

$$h_1 \sim 1 + Ae^{\alpha_1 \xi} + Be^{\beta_1 \xi} \quad \text{as} \quad \xi \to \infty. \tag{2.80}$$

The shooting method is the same as in case 2 and also gives a unique solution.

Figure 2.11 plots the numerical solution to Eq. (2.75) for various angles θ. The parameter $s(t) = 0.01$ is fixed.We observe that behaviour of the numerical solutions in Fig. 2.11 is the same as in Fig. 2.10. We also note that the magnitude of the capillary ridge decreases as θ decreases. The solution to Eq. (2.75) provides a quasi-steady base state for each angle θ whose linear stability to transverse perturbations will be discussed in §3.1.

2.4.3 Region IIIb: The 'effective' contact line region behind the drop.

This short transition region matches the bulk of the drop onto the precursor film at its trailing edge. This region does not actively influence the evolution dynamics. However, for completeness we will discuss the appropriate scalings valid for this region. The dominant mechanism is surface tension and the horizontal component of gravity. This region has very short length scale, X (say), can be obtained by considering where the Region I solution given by Eq. (2.69) breaks down. Here, the neglected surface tension is now of comparable magnitude to the horizontal component of gravity, so $Ca\frac{h^3}{3}h_{xxx}\sim\frac{h^3}{3}$. Using Eq. (2.69), $h\sim h_L\sqrt{\frac{x}{x_L}}$, and comparing the above two effects gives,

$$X\sim Ca^{2/5}\frac{{h^{2/5}}_L}{{x^{1/5}}_L} \text{ and } h\sim\frac{Ca^{1/5}h_L^{6/5}}{x_L^{3/5}}. \tag{2.81}$$

We now introduce the following scalings:

$$x = x_T + Ca^{2/5}\frac{h_L^{2/5}}{x_L^{1/5}}\xi, \quad h(x,t) = \frac{Ca^{1/5}h_L^{6/5}}{x_L^{3/5}}H(\xi). \tag{2.82}$$

Substituting this into Eq. (2.41) and assuming that $\dot{h}_L \approx 0$ gives,

$$-\frac{9}{5}\hat{V}H - \frac{3x_L^{6/5}}{Ca^{2/5}h_L^{12/5}}\dot{x}_T H_\xi + \frac{3}{5}\hat{V}\xi H_\xi + \frac{1}{3}\left[H^3H_{\xi\xi\xi} + H^3 + O\left(\frac{1}{x_L^{2/5}}\right)\right]_\xi = 0, \tag{2.83}$$

where $\hat{V} = \dot{x}_L/h_L^2$. Assuming that the trailing edge of the droplet is pinned and that the vertical component of gravity is small (both of which are true at large inclination angles), or at leading order in $1/x_L^{2/5}$, we obtain

$$H_{\xi\xi\xi\xi} = \frac{3\hat{V}}{5}\left(\frac{3}{H^2} - \xi\frac{H_\xi}{H^3}\right) - \frac{3H_\xi}{H}H_{\xi\xi\xi} - \frac{3}{H}H_\xi,$$
$$H \to \frac{bx_L^{3/5}}{h_L^{6/5}Ca^{1/5}}, H_\xi \to 0 \text{ as } \xi \to -\infty \;\; H \to \xi^{1/2}, H_\xi \to \frac{1}{2}\xi^{-1/2} \text{ as } \xi \to \infty \quad (2.84)$$

Equation (2.84)is similar to that derived by Hocking [25]. Figure 2.12 shows the rescaled solutions to the PDE shown in Fig. 2.3 and the scalings in Eq. (2.82) gives a family of quasi-steady solutions. Equation (2.84) is difficult to solve as it is non-autonomous and has non-constant boundary conditions and will be considered as future work. We note that there would be an additional transition region between this region and region I where surface tension balances both the vertical and horizontal components of gravity this is also not discussed here and will be a topic of future investigation.

2.5 Time evolution of the characteristic variables-spreading and thinning rates

Each of the above described regions are characterised by h_L and x_L. An equation for its time evolution is required to fully describe each region and determine the spreading

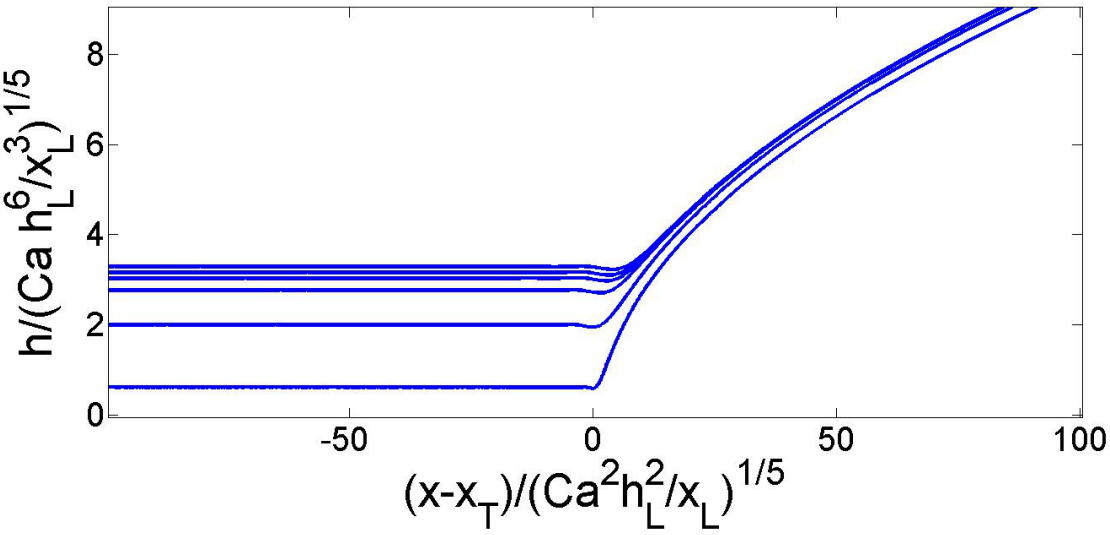

Figure 2.12: Evolution of the droplet height h in region IIIb using data from Fig. 2.3 rescaled using Eq. (2.82).

and thinning rate of the drop, which is not known *a priori*. We derive the evolution equations for h_L and x_L as follows. The volume of the fluid in the drop is conserved. So,

$$A = \int_{-L}^{L} (h - b)dx = \int_{x_T}^{x_L} h_L \sqrt{\frac{x - x_T}{x_L}} dx - b(x_L - x_T), \tag{2.85}$$

where A is the total fluid volume. In the above we neglect the contributions in the two transition regions because they are negligible in comparison to the fluid contained in region I. Assuming $b \ll 1$,

$$A \approx \int_{x_T}^{x_L} h_L \sqrt{\frac{x - x_T}{x_L}} dx = \frac{2}{3} h_L x_L \left(\frac{x_L - x_T}{x_L} \right)^{3/2}. \tag{2.86}$$

Due to the fact that $x_T \ll x_L$, the above equation can be reduced to,

$$h_L = \frac{3}{2x_L} A. \tag{2.87}$$

This provides us with an equation for h_L. Now Eq. (2.74) implies,

$$\dot{x}_L = \frac{1}{3}(h_L^2 + bh_L + b^2) \tag{2.88}$$

Assuming $b \ll 1$ and using Eq. (2.87), and integrating Eq. (2.88) with respect to time gives,

$$x_L = \left(\frac{9}{4}A^2(t - t_0) + x_{L_0}^3\right)^{\frac{1}{3}}, \tag{2.89}$$

where $x_{L_0} = x_L(t = t_0)$, t_0 is some initial time. Using Eq. (2.89) in Eq. (2.87) then gives,

$$h_L = \frac{3A}{2}\left[\frac{1}{\left(\frac{9}{4}A^2(t - t_0) + x_{L_0}^3\right)^{\frac{1}{3}}}\right]. \tag{2.90}$$

This shows that $x_L \sim t^{1/3}$ and $h_L \sim t^{-1/3}$. Figures 2.13(a,b) plot x_L, h_L versus t using Eqs. (2.88, 2.90) (dashed line), with $A = 4/3$ and $t_0 = 10^3$, and compares with the corresponding numerical data (solid lines). The choice of $t = 10^3$ is to allow the self-similar structure to fully develop. The agreement is good and the power-law behaviour for the spreading and thinning rates are as predicted above (see Figs. 2.14 (a,b)). This was first obtained by Huppert [27] except he assumed a power-law time dependence *a priori* and we have managed to extract it naturally from our asymptotic analysis.

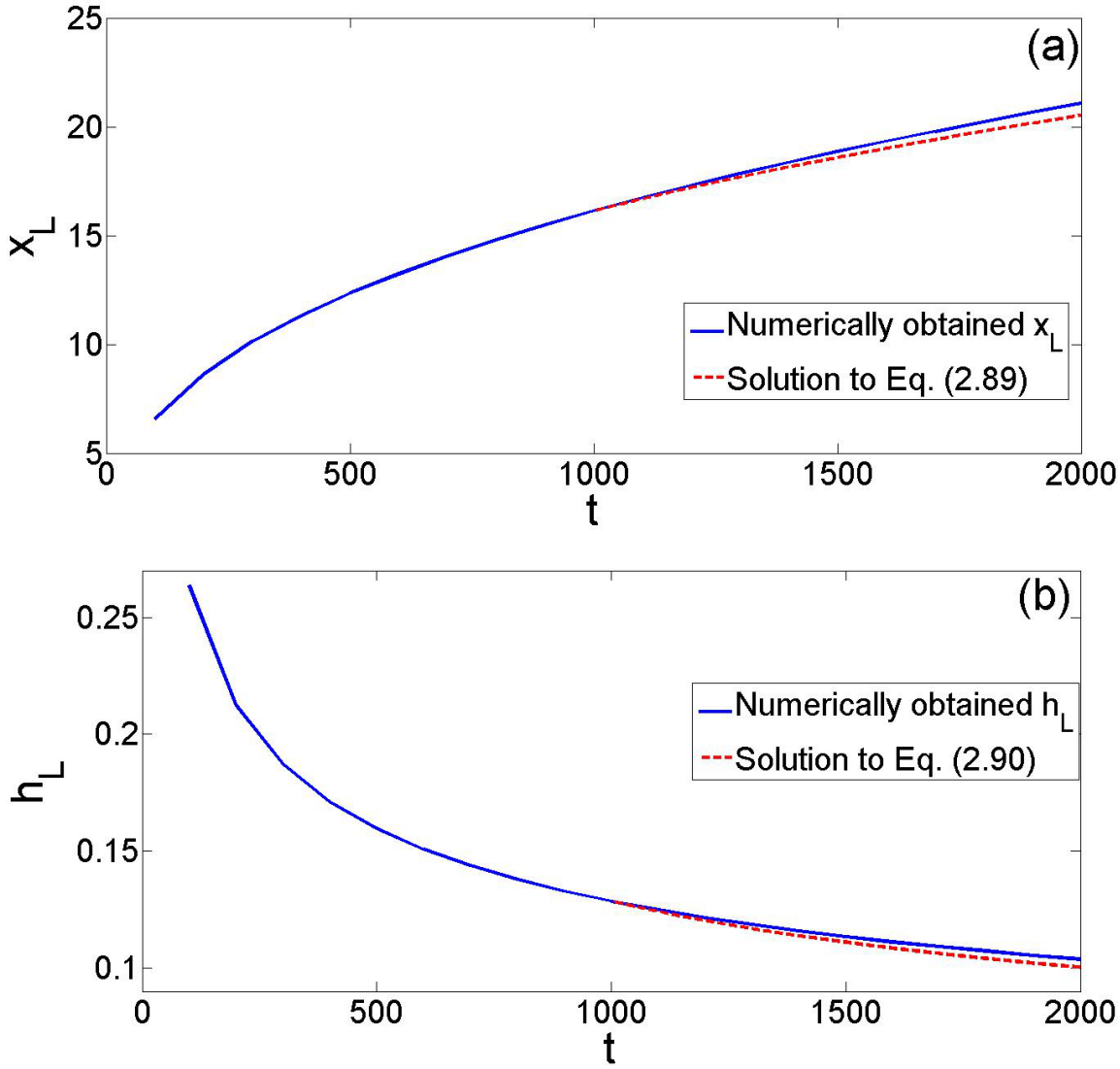

Figure 2.13: Comparing (a) x_L and (b) h_L obtained from the numerical solution of the PDE's (dashed lines) with Eqs. (2.89,2.90)(solid lines).

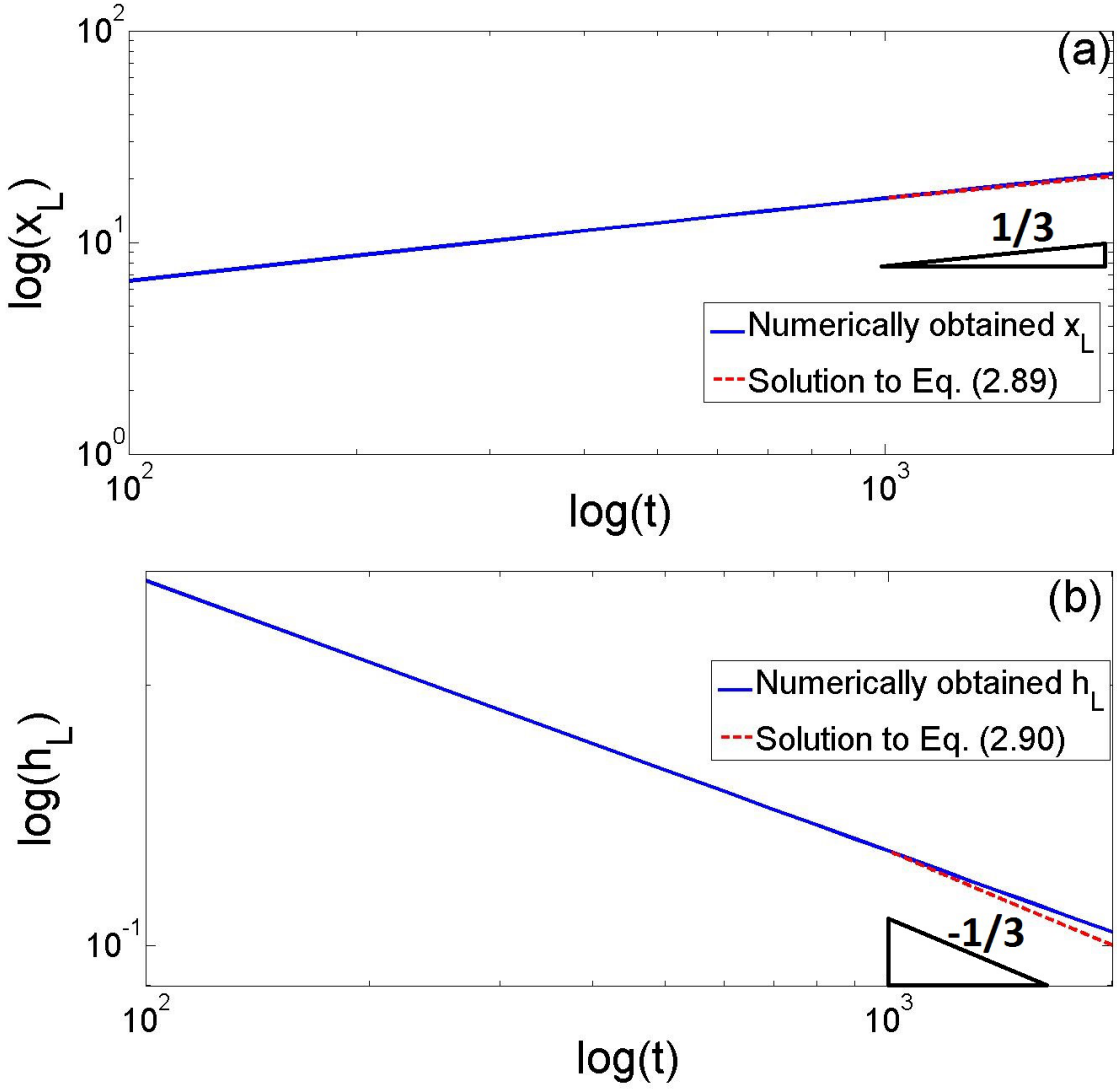

Figure 2.14: Comparing (a) x_L and (b) h_L obtained from the numerical solution of the PDE's (dashed lines) with Eqs. (2.89,2.90)(solid lines)on a log-log plot with the power-law behaviour displayed.

2.6 Concluding remarks

This chapter analyses the spreading of a constant volume thin viscous fluid droplet down a pre-wetted inclined plane using numerical simulations and asymptotic analysis. This problem was first studied by Huppert [27] who identified the similarity solution for the drop height, $h \sim \sqrt{x}$, of the spreading droplet where the horizontal component of gravity is the dominant spreading mechanism. Subsequent studies, particularly, by Troian [63] and Hocking [25] identified short transition region (so called effective' contact line regions) at the leading edge (region IIIa) and trailing edge (region IIIb) of the spreading droplet where surface tension forces are also important. At the leading edge, the quasi-steady evolution is described by the boundary value problem in Eq. (2.75) parametrised by either the 'effective' contact line speed, $\dot{x}_L$, or its upstream height, h_L which decreases as a function of time. It is worth mentioning that this local problem is similar to a model problem of a fluid sheet spreading down an inclined pre-wetted plane from a constant flux source first studied by Bertozzi and Brenner [8]. They showed that a travelling wave solution exists for this problem whose structure is described by the boundary value problem in Eq. (2.75) parameterised by either a constant contact line speed (travelling wave speed) or constant upstream thickness. The quasi-steady BVP at the trailing edge of the droplet (Eq. (2.84)) was first derived and partially analysed by Hocking [25] although he assumes a known time dependence for the spreading and thinning rates in the scalings for this region (as well as other regions).

The methodology followed here is based on Troian's work and does not assume *a priori* the spreading and thinning rates as done by Hocking. The novelty in our approach is being able to fully describe the evolution of each region through two charecteristic variables x_L and h_L. The evolution of x_L and h_L are then obtained by conservation of fluid volume. We have been able to reproduce all the previous results including the late-time droplet spreading rate $t^{1/3}$ and thinning rate $t^{-1/3}$ using this methodology. This concludes our analysis of this problem. The next chapter we will discuss the stability of the 'effective' contact line region to transverse perturbations.

Chapter 3

Viscous fluid droplet spreading down an inclined pre-wetted plane: stability.

As mentioned in the introduction, droplet spreading due to gravity develop 'fingering'-type instabilities. The stability of a spreading droplet of constant volume, discussed in Chapter 2, spreading due gravity will be explored to investigate the conditions that result in fingering instabilities to develop. We will particularly focus on the stability of the droplet's leading edge (region IIIa) where the fingering instabilities are speculated to originate from. We will do this by first performing a linear stability analysis of the 1D base state flow to obtain dispersion relation curves (relationship between growth rate and wavenumber of transverse perturbations) numerically and compare the results to

a small wavenumber analysis (§3.1). The linear stability analysis analyses the stability of a base state to transverse perturbations where we 'freeze' the base state in time and assume that the perturbations grow faster than the base state evolves. To validate these results further we will run two-dimensional simulations (§3.2). Finally, we will discuss the effect of the selected parameters on the fingering behaviour.

3.1 Linear stability analysis of region IIIa

Previously we made the assumption that the free surface was independent of the transverse y direction, this is true initially however as the droplet develops, perturbations in the leading edge grow leading to the fingering behaviour shown in both Hocking[25] and Kondic[34]. As was discussed by Troian [63], Hocking [25] and Bertozzi and Brenner [8] (for constant flux) we believe the onset of the fingering instabilities originated from the 'effective' contact line region, region IIIa. To investigate this we consider the linear stability analysis to transverse perturbations of region IIIa. We first write the two-dimensional equivalent of the governing equation, Eq. (2.72). This can be written as

$$H_\tau - \hat{V}H_\xi + \nabla_{(\xi,\eta)} \cdot \left[Ca\frac{H^3}{3}\nabla_{(\xi,\eta)}\nabla^2_{(\xi,\eta)}H - \hat{D}(\theta)\frac{H^3}{3}\nabla_{(\xi,\eta)}H \right] + \left[\frac{H^3}{3}\right]_\xi = 0, \quad (3.1)$$

where $\eta = \dfrac{y}{(Cah_L)^{1/3}}$ and $\nabla_{(\xi,\eta)} = \left(\dfrac{\partial}{\partial\xi}, \dfrac{\partial}{\partial\eta}\right)$. We use the solution to Eq. (2.75) as the base state and initiate perturbations of this base state in the transverse y direction.

Hence, we impose a small perturbation in the transverse η-direction as

$$H(\xi, \eta, \tau) = H_s(\xi) + \epsilon \hat{H}(\xi) e^{iq\eta + \beta\tau}, \tag{3.2}$$

where H_s is the quasi-steady base state for H obtained by solving Eq. (2.75), $q = (Cah_L)^{1/3} q^*$ is the scaled wavenumber and β is the growth rate, and $\epsilon \ll 1$. We seek a class of perturbations $\hat{H}$ to be such that $\hat{H} \to 0$ as $\xi \to \pm\infty$ and $\hat{H}$ is periodic in η. Substituting this into the Eq. (3.1) at leading order in ϵ gives Eq. (2.78). At $O(\epsilon)$ we obtain the eigenvalue problem:

$$-\beta \hat{H} = L\hat{H}, \tag{3.3}$$

where L is a linear operator defined by

$$\begin{aligned} L = & \frac{H_s^3}{3}\frac{\partial^4}{\partial\xi^4} + \left(\frac{H_s^3}{3}\right)_\xi \frac{\partial^3}{\partial\xi^3} - [\hat{D}(\theta) + 2q^2]\frac{H_s^3}{3}\frac{\partial^2}{\partial\xi^2} + \left[2\hat{V}\right]\frac{\partial}{\partial\xi} \\ & + \left[\frac{(1-3\hat{V})}{H_s} - \left(\frac{H_s^3}{3}\right)_\xi (\hat{D}(\theta) + q^2)\right]\frac{\partial}{\partial\xi} \\ & + \frac{H_s^3}{3} q^2 [\hat{D}(\theta) + q^2] - \frac{(1-3\hat{V})}{H_s^2} H_{s\xi}. \end{aligned} \tag{3.4}$$

One can solve the eigenvalue problem, given by Eq. (3.3), numerically to find the dispersion relation. The numerical solutions of Eq. (3.3) is a non-trivial task due to its stiff nature. An alternative is to solve the corresponding linear PDE: ($\hat{H}_t = -L\hat{H}$), where the linear operator is defined in Eq. (3.4) as an initial value problem (IVP). We use finite differences on a uniform grid to discretise the spatial derivatives the

discretisaton used is the same as that described in §2.2 keeping the time derivatives continuous. The resulting system of ODE's is solved using a stiff ODE solver in MATLAB (ODE15i[56]). We track the evolution from an initial condition $\hat{H} = Ae^{-B\xi^2}$ where $A = 0.1$ and $B = 5$ for a prescribed wavenumber q, inclination angle θ and downstream film thickness s. We seek perturbations such that $\hat{H} \to 0$ as $\xi \to \pm\infty$. Figure 3.1 shows the evolution of $\hat{H}$ (solid lines) for $q = 0.3$ and $\theta = 90^o$ emanating from the base state (dashed line) corresponding to $s = 0.0884$. It is observed under suitable conditions that the disturbances can grow rapidly perturbations are larger immediately after the capillary ridge and behind the 'effective' contact line. At late times the growth of the disturbances is approximately exponential with $\hat{H} \propto \exp(\beta\tau)$. This is repeated varying wavenumber to obtain the dispersion relationship. The computed growth rate β is shown in Fig. 3.2 as a function of wavenumber q for $\theta = 90^o$ and base states evaluated with $s = 0.0523, 0.0656, 0.0884, 0.1106$. The simulations demonstrate convincingly that the most linearly unstable mode has a wavenumber comparable to the width of region IIIa, that as time increases the base state becomes less linearly unstable (as seen in Fig. 3.2 that the maximum growth rate and band of unstable wavenumbers decrease as time increases), and that sufficiently short-wavelength disturbances are linearly stable. Figure 3.3 shows the dispersion relation for varying inclination angles $\theta = 3^o,\ 4^o,\ 5^o,\ 15^o,\ 30^o,\ 60^o,\ 90^o$. It is observed that decreasing the angle of inclination has a stabilising effect with both the maximum growth rate and bandwidth of unstable decreasing. Furthermore, there is a critical inclination angle θ below which the base state is linearly stable for all wavenumbers.

3.1.1 Small-wavenumber analysis

In this section we examine instabilities with large wavelength (or small wavenumber). Numerical dispersion relations (see Fig. 3.2) suggest that the growth rate is quadratic at small wavenumbers, we write $\hat{H} = \hat{H}_0 + q^2\hat{H}_1 + q^4\hat{H}_2 + ...$ and $\beta = \beta_0 + q^2\beta_1 + ...$. At leading order in q we get,

$$\left[\frac{H_s^3}{3}\hat{H}_{0\xi\xi\xi} - \hat{D}(\theta)\frac{H_s^3}{3}\hat{H}_{0\xi} + 2\hat{V}\hat{H}_0 + \frac{(1-3\hat{V})}{H_s}\hat{H}_0\right]_\xi = -\beta_0\hat{H}_0. \tag{3.5}$$

A solution of Eq. (3.5) is

$$\hat{H}_0 = -H_{s\xi}, \quad \beta_0 = 0. \tag{3.6}$$

This is just a translation of the base solution H_s. At $O(q^2)$,

$$\begin{aligned} -\beta_1\hat{H}_0 = \frac{H_s^3}{3}\hat{H}_{1\xi\xi\xi\xi} + \left(\frac{H_s^3}{3}\right)_\xi \hat{H}_{1\xi\xi\xi} - \hat{D}(\theta)\frac{H_s^3}{3}\hat{H}_{1\xi\xi} - 2\frac{H_s^3}{3}\hat{H}_{0\xi\xi} \\ +2\hat{V}\hat{H}_{1\xi} + \frac{1-3\hat{V}}{H_s}\hat{H}_{1\xi} - \left(\frac{H_s^3}{3}\right)_\xi \hat{D}(\theta)\hat{H}_{1\xi} - \left(\frac{H_s^3}{3}\right)_\xi \hat{H}_{0\xi} + \frac{H_s^3}{3}\hat{D}(\theta)\hat{H}_0. \end{aligned} \tag{3.7}$$

Integrating with respect to ξ, using $\hat{H}_0 = -H_{s_\xi}$ and all derivatives of $\hat{H}_0$, $\hat{H}_1 \to 0$ as $\xi \to \pm\infty$ gives,

$$\beta_1 = \frac{1}{3\,(1-s)}\int_{-\infty}^{\infty} (H_s - s)\,(H_s - 1)\,(H_s + 1 + s)\,dx. \tag{3.8}$$

For the base solution to be linearly unstable, $\beta_1 > 0$. Hence a necessary condition for this to happen is that $H_0 > 1$ over some part of the domain. Computing the above

integral for the base solutions shown in Fig. (2.11) shows that the capillary ridge is necessary for the fingering instability to be initiated [63]. As θ decreases, there is a slight bulge above one but is not large enough for β_1 to be positive. Hence, $H_0 > 1$ may not be sufficient for the instability to develop. This is consistent with the dispersion relation shown in Fig. 3.3. Figure 3.4 compares the numerically obtained dispersion relation to that obtained from Eq. (3.8) we see that there is good agreement at small wavenumber however the two lines begin to deviate as the wavenumber exceeds the small wavenumber limit. A correction could theoretically be obtained by calculating the $o(q^4)$ growthrate.

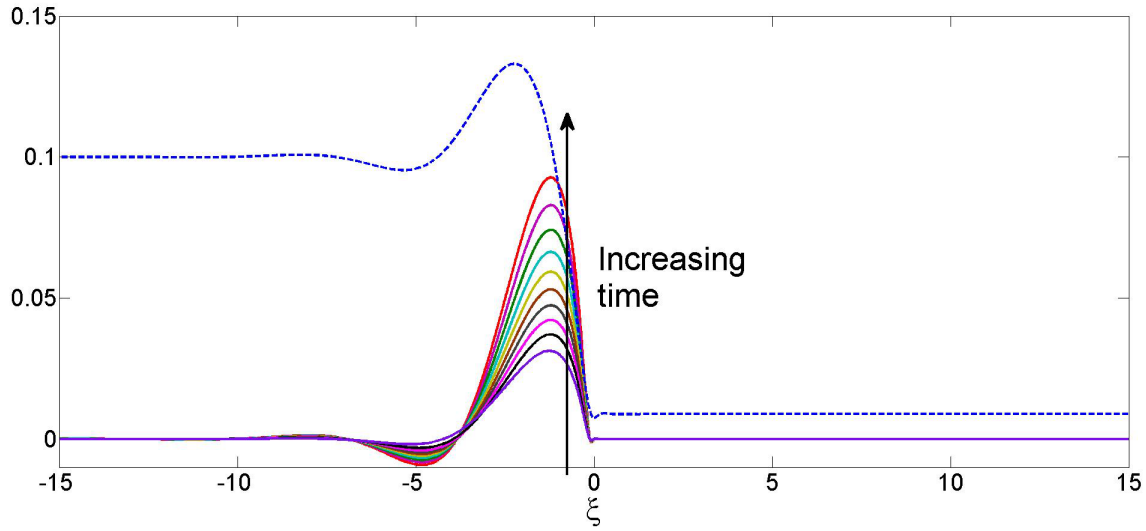

Figure 3.1: Solid lines show solutions of linearised PDE of Eq. (3.3) for $q = 0.3$, $\theta = 90^o$ using a base state H_s (dashed line shows $H_s/10$) corresponding to $s = 0.0884$. Arrows show increasing time between $\tau = 10 - 100$.

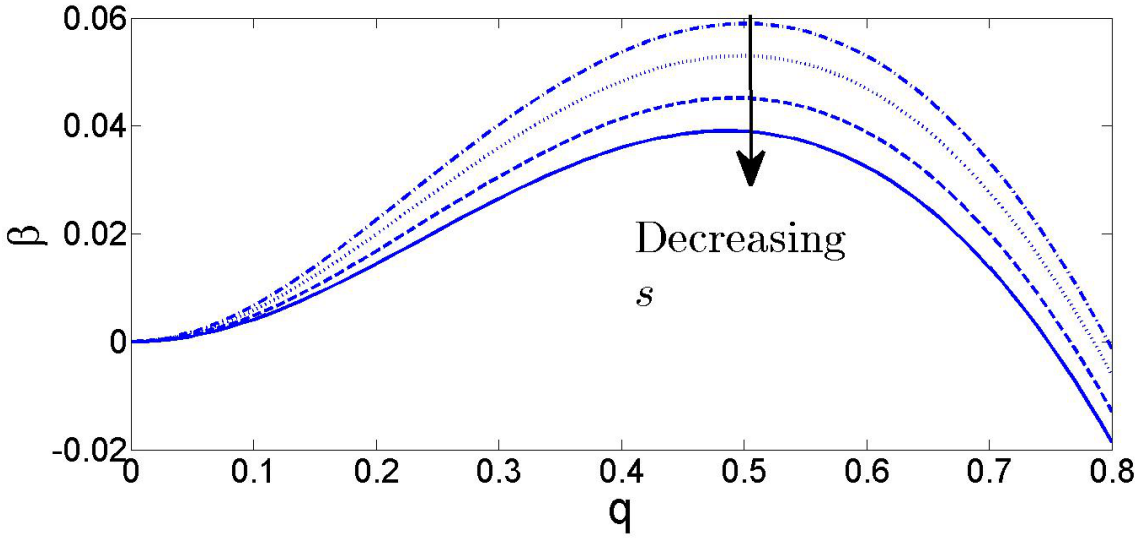

Figure 3.2: Growth rate β versus wavenumber q for $s = 0.0523, 0.0656, 0.0884, 0.1106$ for $\theta = 90^o$.

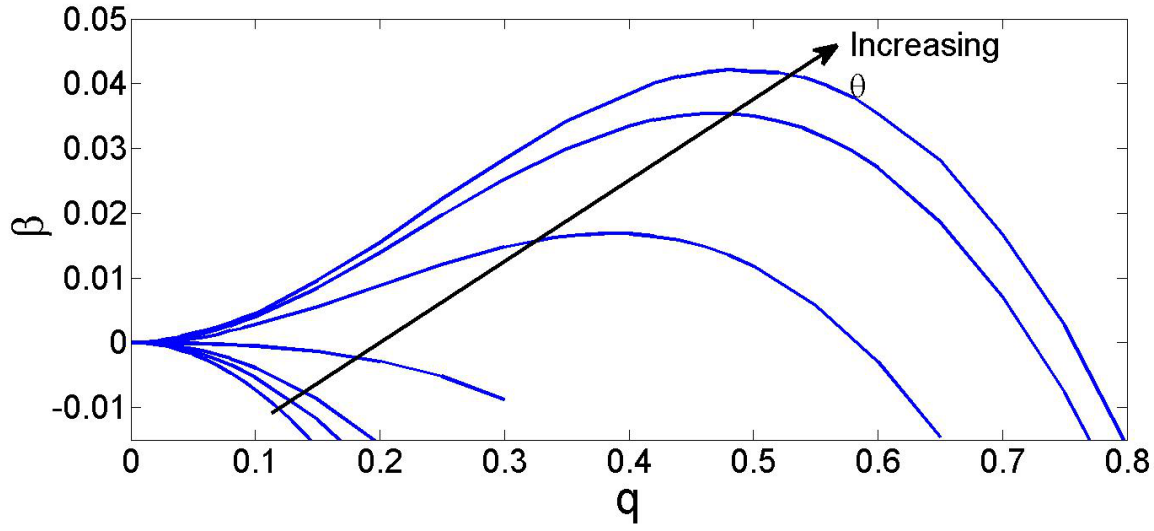

Figure 3.3: Dispersion relation obtained by solving IVP of Eq. (3.3) for $s = 0.01$ for inclination angles of $\theta = 3^o,\ 4^o,\ 5^o,\ 15^o,\ 30^o,\ 60^o,\ 90^o$.

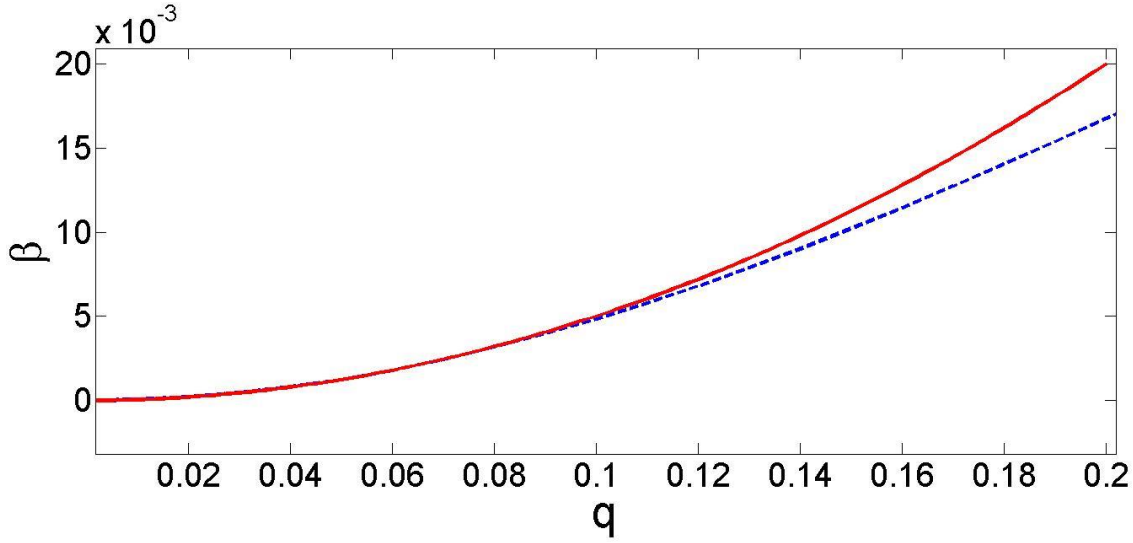

Figure 3.4: Growth rate β versus wavenumber q for $s = 0.0884$ for $\theta = 90^o$. The dotted line shows the numerically obtained dispersion relation and the solid line is that obtained using Eq. (3.8)

In the next section we will validate the linear stability results and explore the stability of the other regions using two-dimensional simulations.

3.2 Two-dimensional numerical simulations and nonlinear stability.

In this section, we examine the nonlinear stability to transverse perturbations of the base state flow discussed in detail in Chapter 2 using two-dimensional numerical simulations. The two-dimensional problem is Eq. (2.40) and can be written as,

$$h_t + \left[Ca\frac{h^3}{3}(h_{xxx} + h_{yyx}) - \hat{D}(\theta)\frac{h^3}{3}h_x \right]_x$$

$$+\left[Ca\frac{h^3}{3}(h_{yyy}+h_{xxy})-\hat{D}(\theta)\frac{h^3}{3}h_y\right]_y+\left[\frac{h^3}{3}\right]_x=0, \tag{3.9}$$

for $-L_1 \leq x \leq L_2$ and $-1/q \leq y \leq 1/q$, where q is the wavenumber of a perturbation in the y direction and L_1, L_2 are arbitrarily chosen lengths. This PDE was derived in §2.1 for the droplet height. This equation is supplemented by four boundary conditions in the x direction which are

$$h = b, \;\; h_x = 0, \quad \text{at} \quad x = L_1, L_2, \tag{3.10}$$

and periodic boundary conditions in the transverse y direction. We start our simulations from two initial conditions: (i) the parabolic droplet shape (Eq. (2.43)) used in the one dimensional simulations (ii) the quasi-steady one dimensional base states at specific times obtained numerically in Chapter 2. We introduce localised periodic transverse perturbations of wavenumber to the initial conditions of the form:

$$h(x,y,0) \;\; = \;\; h_b(x)+\sum_{k=1,l=1}^{P,Q} A_k \cos(q_k \pi y)\exp[-K(x-x_{0l})^2], \tag{3.11}$$

where $h_b(x)$ is the initial condition . P is the number of modes imposed and Q is the number of locations in the x direction across which perturbations are applied denoted by x_{0l}. A_k and q_k denote the amplitude and wavenumber of mode k, respectively, and K controls the width of the localised perturbation. The superposition of perturbations allows the modes to interact and investigate the existence of any dominant mode(s).

We discretise the PDE (Eq. (3.14)) by the finite difference discretisation scheme used in the 1-D simulations. We first define a forward difference and a backward difference in the x direction by,

$$h_{x,i,j} = \frac{h_{i+1,j} - h_{i,j}}{\Delta x}, \;\; h_{\tilde{x},i,j} = \frac{h_{i,j} - h_{i-1,j}}{\Delta x}. \tag{3.12}$$

We also define a forward difference and a backward difference in the y direction by

$$h_{y,i,j} = \frac{h_{i,j+1} - h_{i,j}}{\Delta y}, \;\; h_{\tilde{y},i,j} = \frac{h_{i,j} - h_{i,j-1}}{\Delta y}, \tag{3.13}$$

where i is the index in the x direction and j is the index in the y direction, where $h_{i,j} = h(x_i, y_j, t)$, $i = 0, 1, ..., M$, $j = 0, 1, ...N$. M and N are the number of discretisation points in the x and y directions respectively. Δx and Δy are the grid size in the x and y directions, respectively. Using Eqs. (3.12,3.13) we can discretise Eq. (3.14) as,

$$\begin{aligned} &h_{t,i,j} + \Big[Ca\; a(h_{i+1,j}, h_{i,j})(h_{\tilde{x}x\tilde{x}i,j} + h_{\tilde{y}y\tilde{x}i,j}) - \hat{D}(\theta) a(h_{i+1,j}, h_{i,j}) h_{\tilde{x}i,j}\Big]_x \\ &+ \Big[Ca\; a(h_{i,j+1}, h_{i,j})(h_{\tilde{y}y\tilde{y}i,j} + h_{\tilde{x}x\tilde{y}i,j}) - \hat{D}(\theta) a(h_{i,j+1}, h_{i,j}) h_{y\tilde{i},j}\Big]_y + \left[\frac{h_{i,j}^3}{3}\right]_{\tilde{x}} = 0, \end{aligned} \tag{3.14}$$

where,

$$a(h_{i+1,j}, h_{i,j}) = \frac{h_{i+1,j}^3 + h_{i,j}^3}{6}, \;\; a(h_{i,j+1}, h_{i,j}) = \frac{h_{i,j+1}^3 + h_{i,j}^3}{6} \tag{3.15}$$

This allows us to reduce the bandwidth to a 13 point stencil in comparison to a 21 point

which would be obtained when using a standard centred difference scheme. Leaving the time derivative continuous we obtain a system of ODE's which are solved using the stiff ODE solver DDASPK [10]. The grid size in the x direction was taken to be $\Delta x = 0.01$ and the number of discretisation points in the y direction $Q = 100$ which sufficently resolved the solution structure.

We will begin by exploring the stability to transverse perturbations from an initial parabolic droplet shape.

$$h_b(x) = (1 + b - x^2)[H(1 - x) - H(-1 - x)] + b[H(x - 1) + H(-1 - x)], \qquad (3.16)$$

where $H(x)$ is the Heaviside function. The majority of the following simulations undertaken in this section fix $b = 0.01$, $Ca = 10^{-3}$, $\theta = 90^o$ and $x_{0l} = 0$.

Figure 3.5 shows evolution of h for a single transverse perturbation of amplitude $A = 0.1$ wavenumber $q = 4$ and localisation number $K = 100$. At early time ($t = 0.1$) it can be clearly observed that the initial perturbation in the droplet height still exists. At later time ($t = 5, 10$) the perturbations die out and the evolution is similar to the one dimensional flow. This can be more clearly observed in Fig. 3.6 which shows the contour plots of h for the same parameters and times as used in Fig. 3.5. It can be seen here that at $t = 5$ and $t = 10$ the leading edge of the drop is uniform in the transverse direction. Figure 3.7 shows the surface plots for a single transverse perturbation of amplitude $A = 0.1$ and wavenumber $q = 1$. At early time ($t = 5$) it can be clearly observed that there is a significant in the perturbation of the drop

height in comparison to the initial perturbation. As time progresses, the fluid in that region flows at a quicker speed than where the fluid height is lower thus forming a finger. The finger initially has width similar to the wavelength of the perturbation that was initially prescribed. As time progresses, the finger appears to develop with a preferred width. This can be seen more clearly in the contour plots shown in Fig. 3.8, which shows the early development of a finger at $t = 100$ of width ≈ 0.5 (quarter the wavelength of the initial perturbation). For longer times (not shown here), this finger propagates down the plane with the same width.

We now apply a superposition of perturbations to this base state of amplitude $A_k = 0.1$ and wavenumbers $q_k = 0.5, 1, 5, 10, 15, 25, 30$. We chose these wavenumbers to simulate a real case scenario which may include a wide range of perturbations of varying wavelength. Figure 3.9 shows the 2-D evolution of the fluid interface from this initial perturbation. The surface plots are shown at $t = 0, 10, 100, 1000$. It can be seen that as the flow develops the smaller wavelength perturbations decay and the larger wavelengths begin to grow. However, at later times ($t = 100, 1000$) two fingers develop that are symmetrical about $y = 0$. Figure 3.10 shows the contour plots of the above evolution. The development of the two fingers can be observed more clearly at $t = 100, 1000$. The finger are of the same width and match the width of the fingers shown in Figs. 3.7,3.8 (approximatly 0.5). Based on the results shown here, it appears to indicate that there is a preferred finger width which for this initial flow and parameters chosen is ≈ 0.5.

We will now explore the stability using h_b to be the base state obtained numerically for $b = 0.01$, $Ca = 10^{-3}$ and $\theta = 90^o$ at time $t = 100$ for $b = 0.01$, $\theta = 90^o$ and $Ca = 10^{-3}$. The base state at this time has evolved to a self-similar structure. We now apply a perturbation in the y-direction near the leading edge ($x_{01} = 6.65$) and near the training edge ($x_{02} = -1$) with amplitude $A_k = 0.01$ and $q_k = 0.5, 1, 5, 10, 15, 25, 30$. Figure 3.11 shows the evolution of the droplet from this initial perturbation. Initially some perturbations decay and some grow as seen at $t = 100$ in Fig. 3.11(a). At a much later time ($t = 1100$) shown in Fig. 3.11(b) it can be seen clearly that a perturbation of wavelength $\approx 2/3$ starts dominating at the capillary ridge. For still larger times (not shown here), three fingers of width $\approx 1/3$ develop from this perturbation propagating down the inclined plane with the same width. However, Fig. 3.11(c) show that the perturbations at the trailing edge have not decayed nor grown. This suggests that the trailing edge is linearly stable for all wavenumbers. The corresponding contour plots in Fig. 3.10 clearly shows the above behaviour.

We now investigate the influence of varying the precursor thickness and inclination angle on the stability. Figure 3.14 shows the surface and contour plot for the drop height at $t = 100$ when the precursor thickness $b = 0.1$ corresponding to the initial perturbation used in plotting Figs. 3.7,3.8. We observe that the bulk flow is quicker for a larger precursor film thickness (compare Figs. 3.8(c) and 3.14). Moreover the thinner the precursor film the more unstable the flow is as can be seen by the larger finger length in Fig. 3.8 compared to Fig. 3.14(b). Figure 3.13 shows the influence

of carying the inclination angle θ using an initial perturbation similar to that in Figs. 3.7,3.8. Decreasing the angle of inclination the fingers take longer to develop and are much smaller in length (compare Figs. 3.8 and 3.13). This is again consistent with the linear stability analysis.

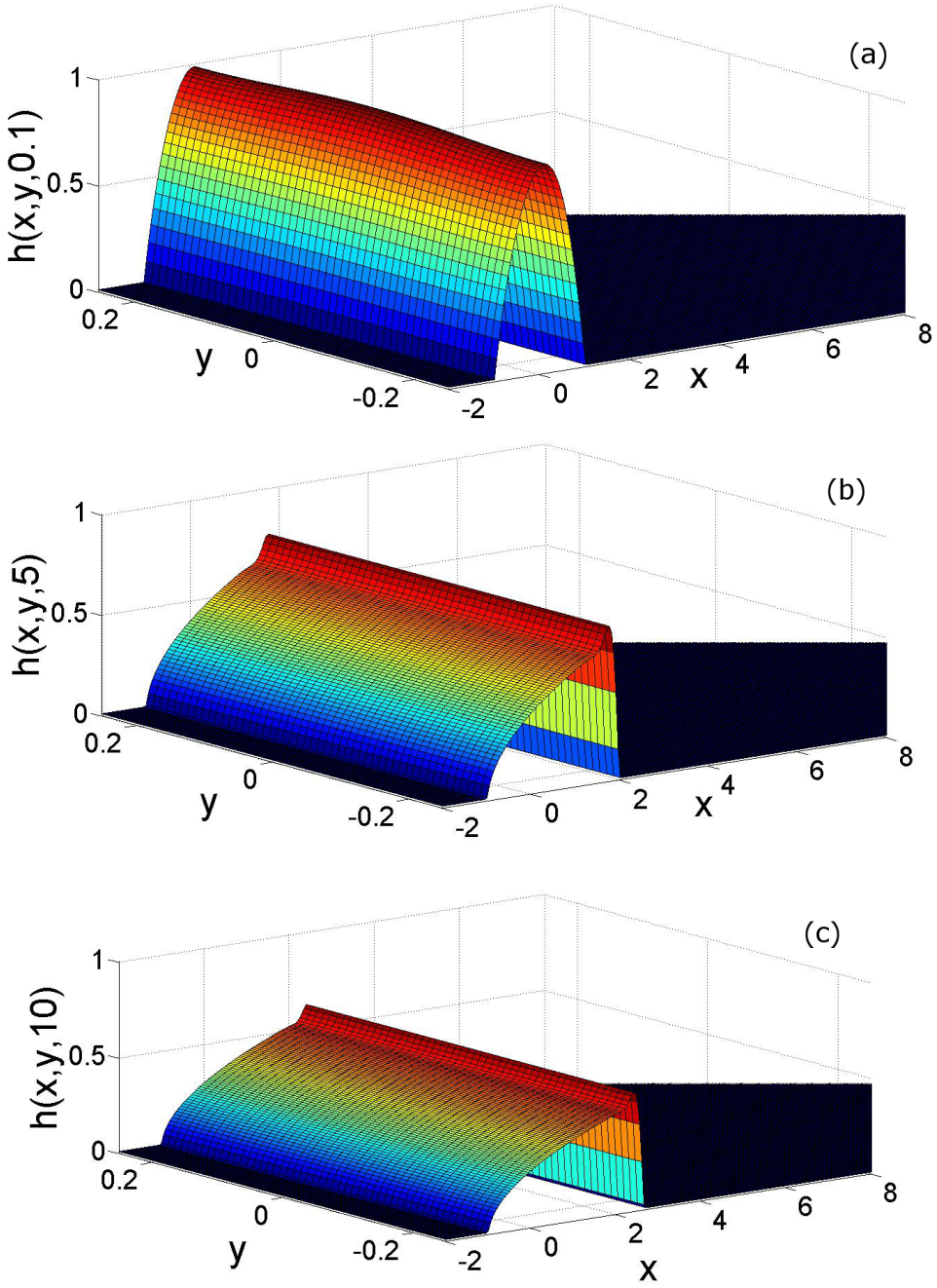

Figure 3.5: Surface plots showing the 2-D evolution of the fluid interface from the initial conditions (Eq. (3.11,3.16)) with a single transverse perturbation of amplitude $A_i = 0.1$ and wavenumber $q_i = 4$. The surface plots are shown at (a)$t = 0.1$, (b) 5, (c) 10.

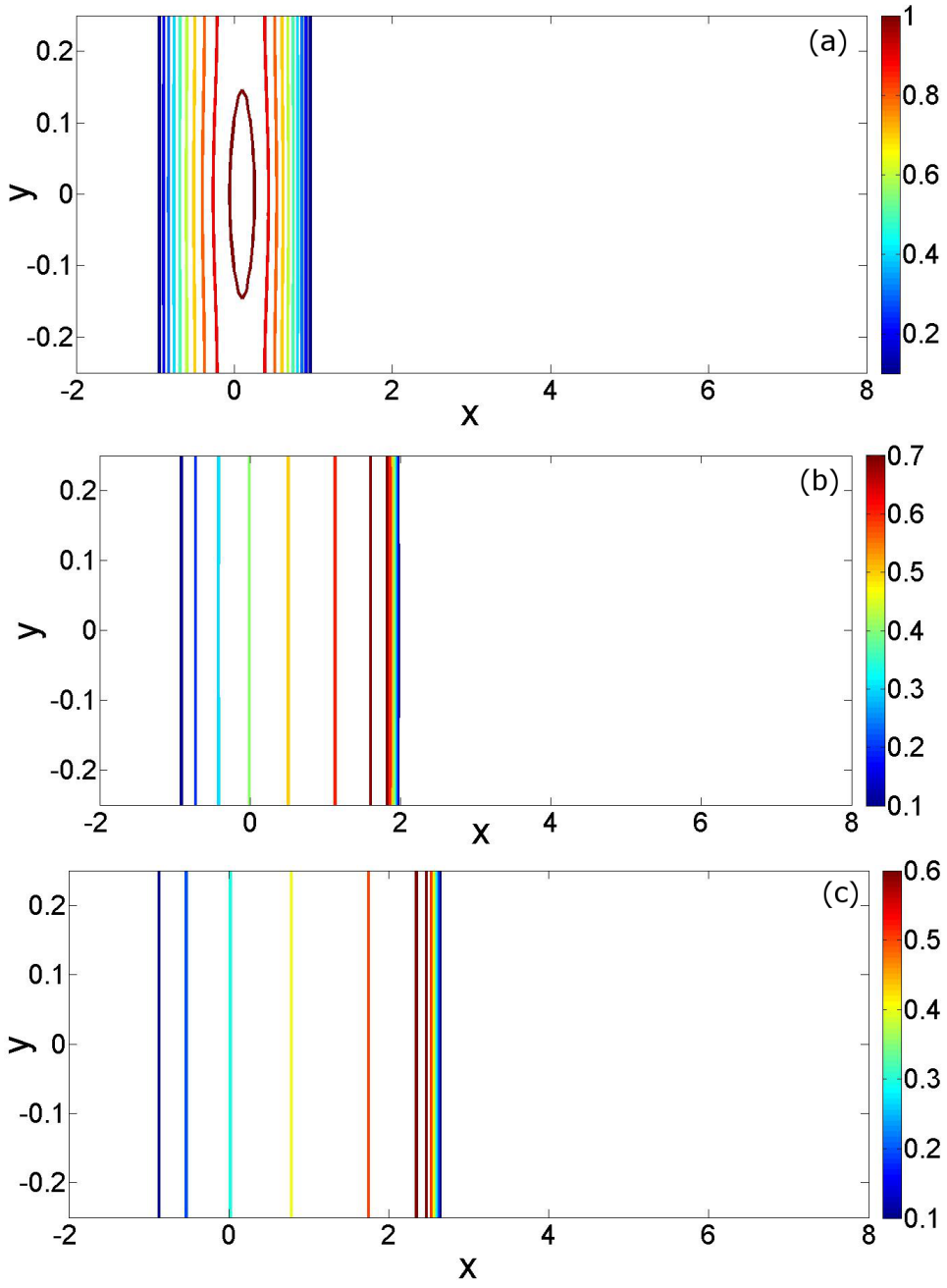

Figure 3.6: Contour plots showing the 2-D evolution of the fluid interface from the initial conditions (Eq. (3.11,3.16)) with a single transverse perturbation of amplitude $A_i = 0.1$ and wavenumber $q_i = 4$. The surface plots are shown at (a)$t = 0.1$, (b) 5, (c) 10.

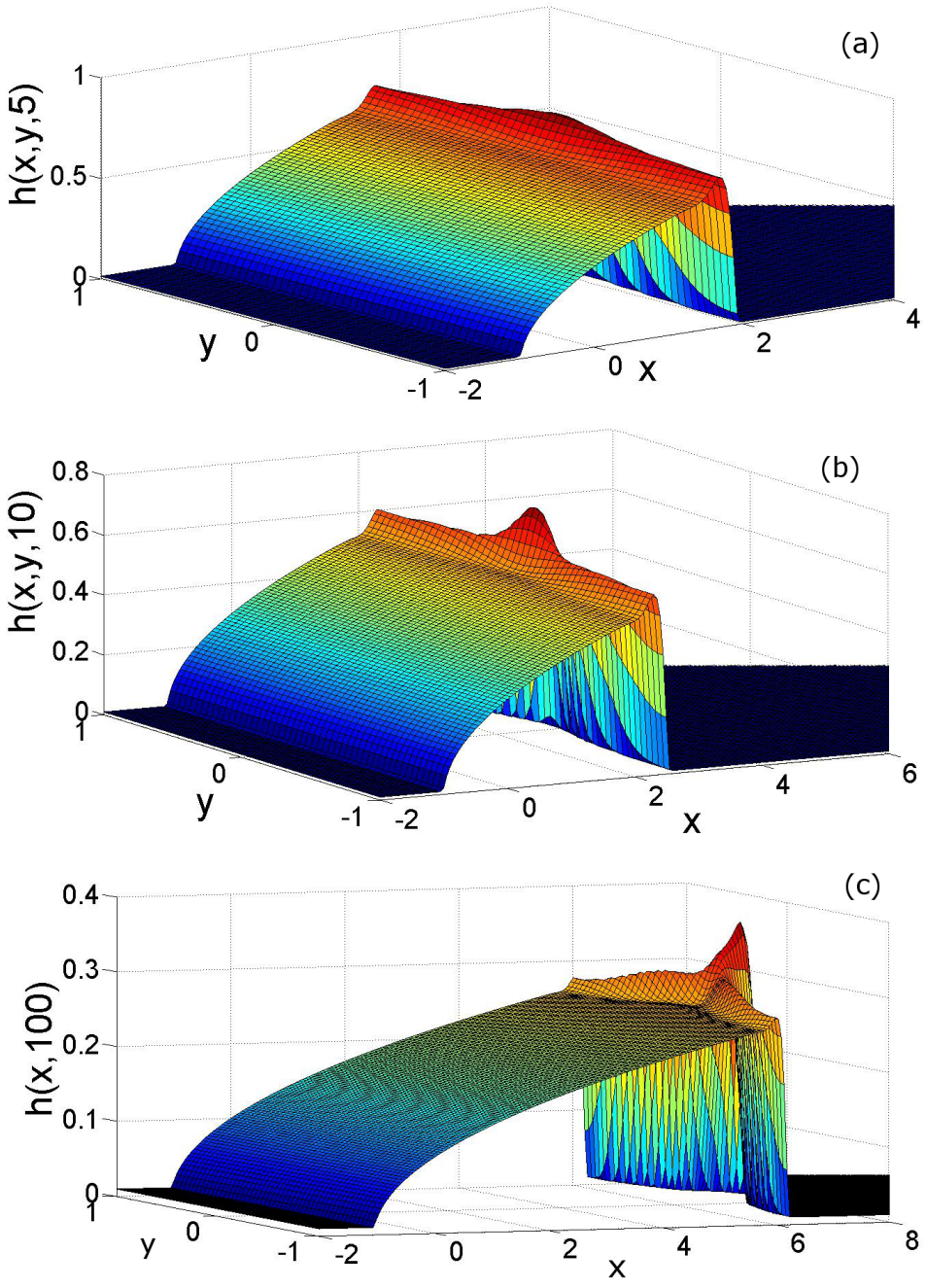

Figure 3.7: Surface plots showing the 2-D evolution of the fluid interface from the initial conditions (Eq. (3.11,3.16)) with a single transverse perturbation of amplitude $A_i = 0.1$ and wavenumber $q_i = 1$. The surface plots are shown at (a)$t = 5$, (b) 10, (c) 100.

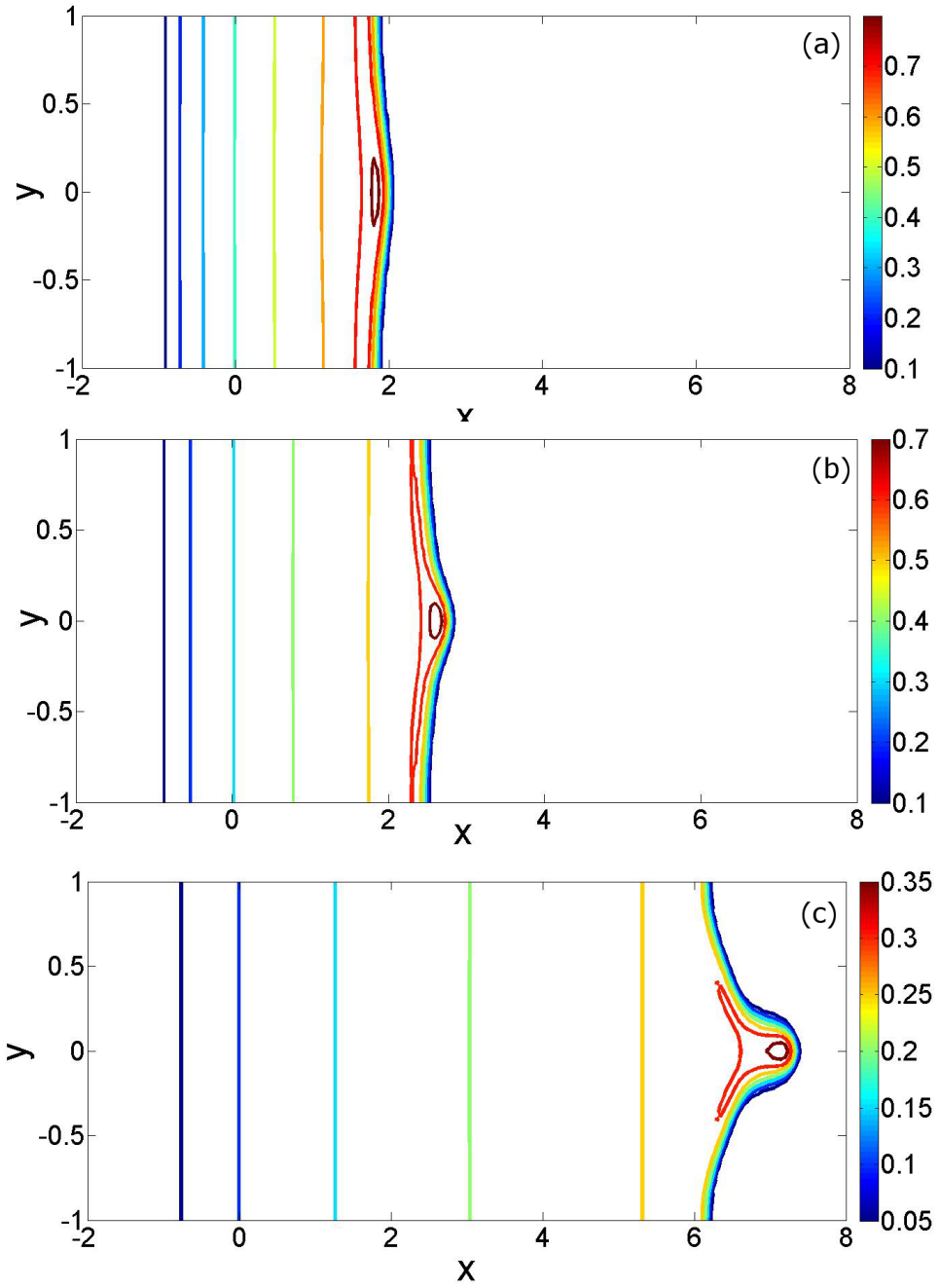

Figure 3.8: Contour plots showing the 2-D evolution of the fluid interface from the initial conditions (Eq. (3.11,3.16)) with a single transverse perturbation of amplitude $A_i = 0.1$ and wavenumber $q_i = 1$. The surface plots are shown at (a)$t = 5$, (b) 10, (c) 100.

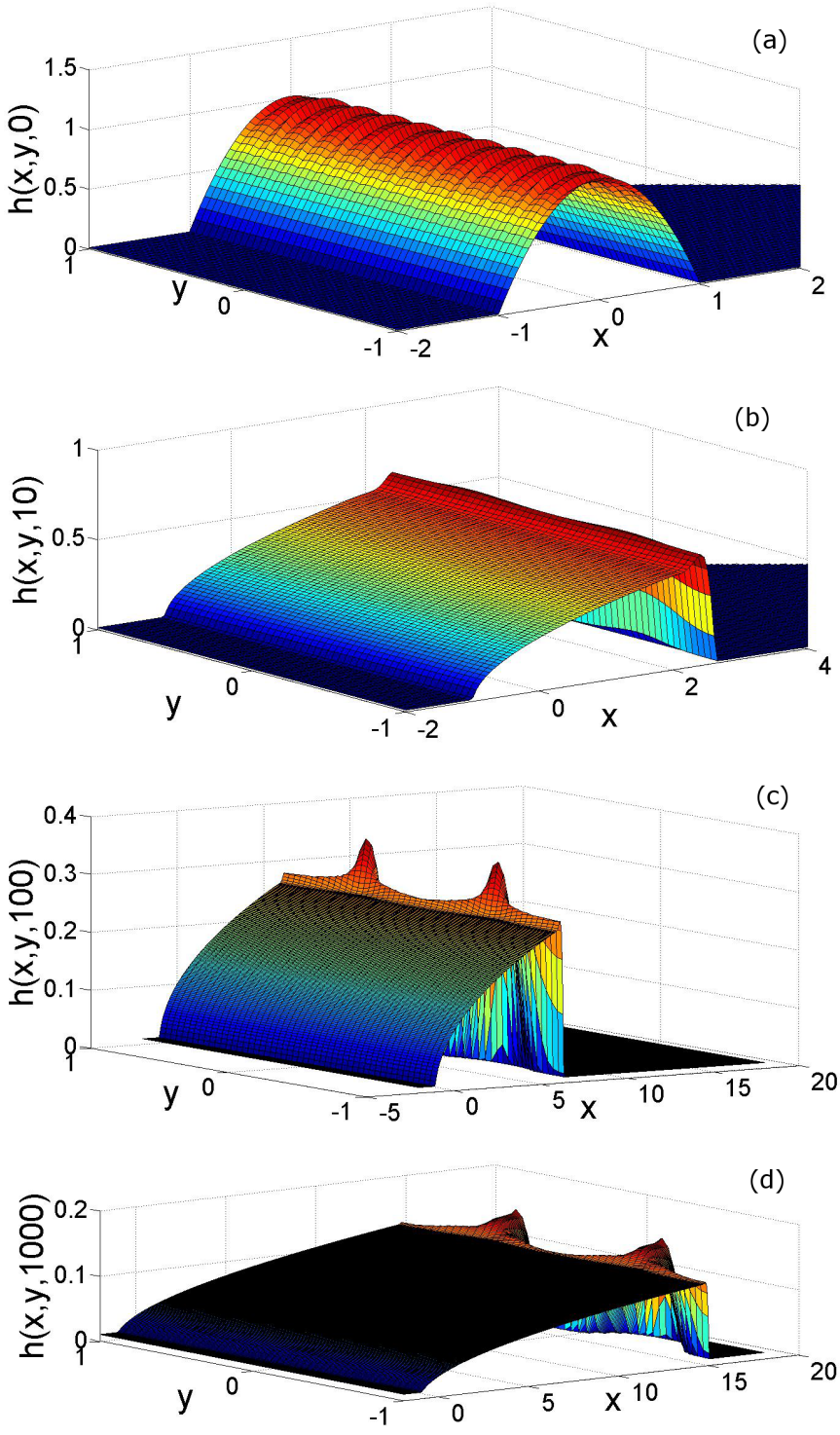

Figure 3.9: Surface plots showing the 2-D evolution of the fluid interface from the initial conditions (Eq. (3.11,3.16)) with multi-mode transverse cosine perturbations of amplitude $A_i = 0.1$ and wavenumber $q_i = 0.5, 1, 5, 10, 15, 25, 30$. The surface plots are shown at (a)$t = 0$, (b) 10, (c) 100, (d) 1000.

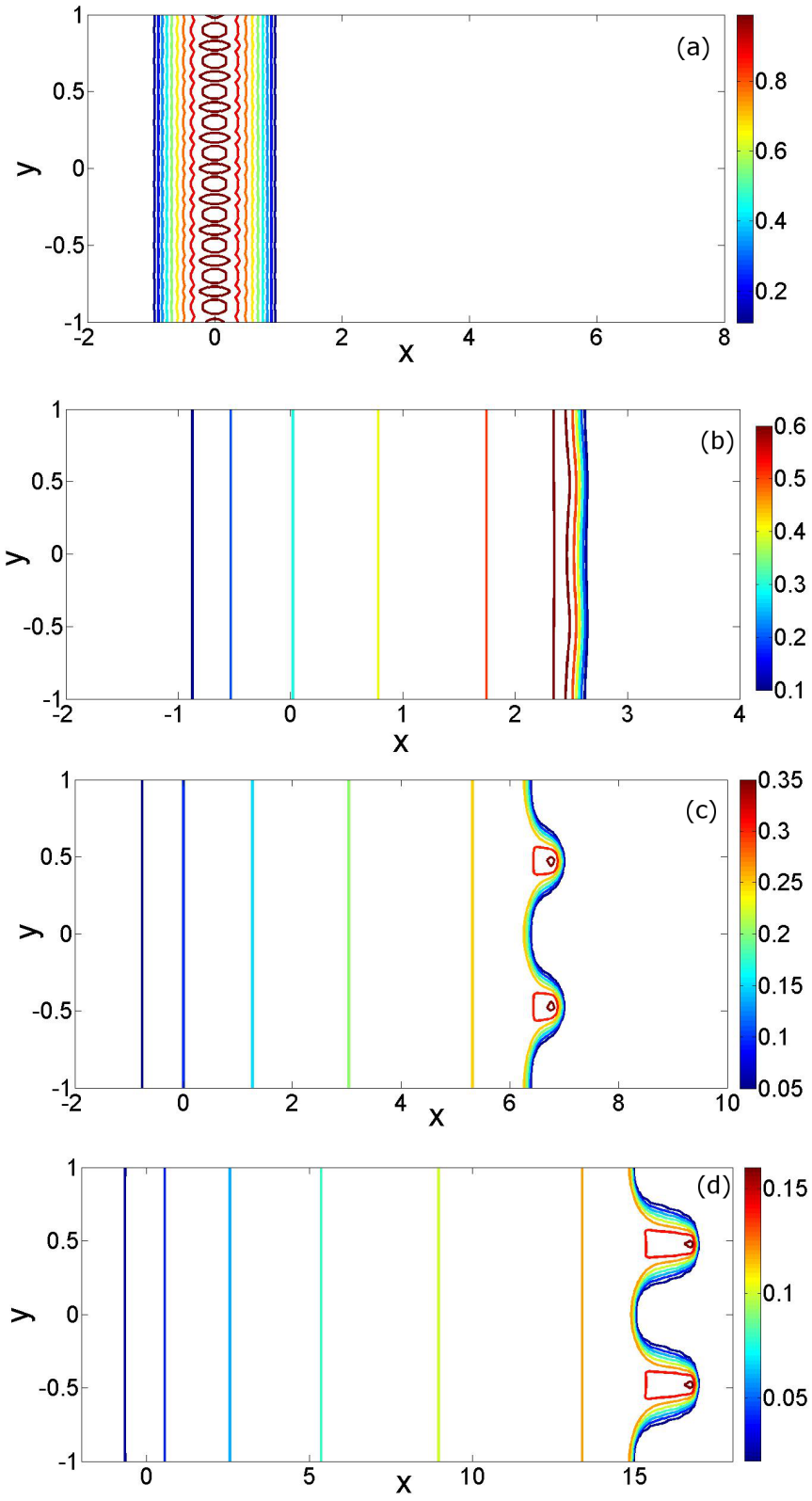

Figure 3.10: Contour plots showing the 2-D evolution of the fluid interface from the initial conditions (Eq. (3.11,3.16)) with multi-mode transverse cosine perturbations of amplitude $A_i = 0.1$ and wavenumber $q_i = 0.5, 1, 5, 10, 15, 25, 30$. The surface plots are shown at (a)$t = 0$, (b) 10, (c) 100, (d) 1000.

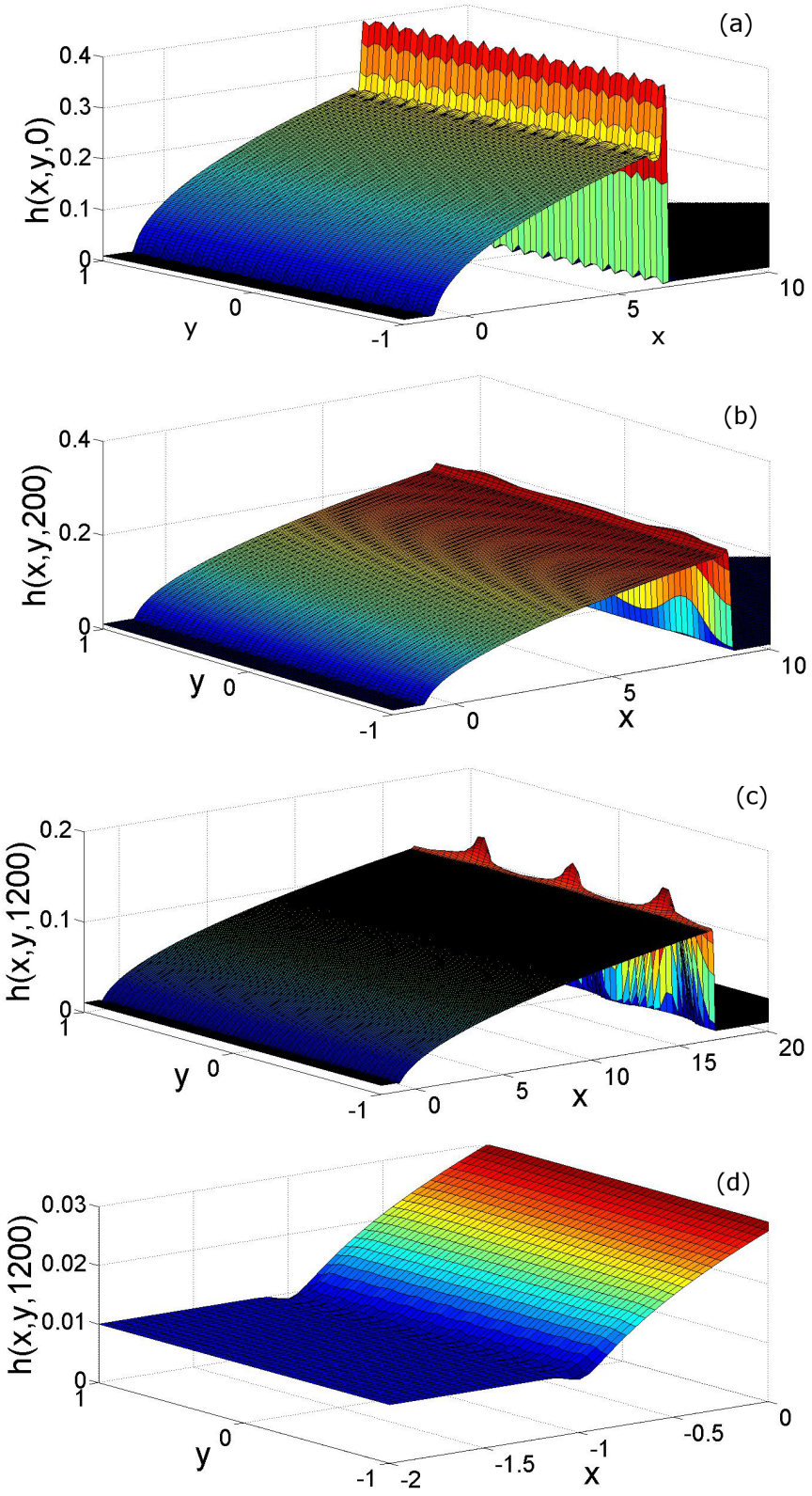

Figure 3.11: Surface plots showing the 2-D evolution of the fluid interface from the base state initial condition at $t = 100$ for $b = 0.01$, $\theta = 90^o$ and $Ca = 10^{-3}$ with a multi-cosine perturbation with $A_i = 0.01$ at $x_0 = 6.65$ with wavenumber $q_i = 0.5, 1, 5, 10, 15, 25, 30$ at time (a) $t = 0$, (b) 200, (c) 1200. (d) shows the trailing edge of the droplet at $t = 1200$.

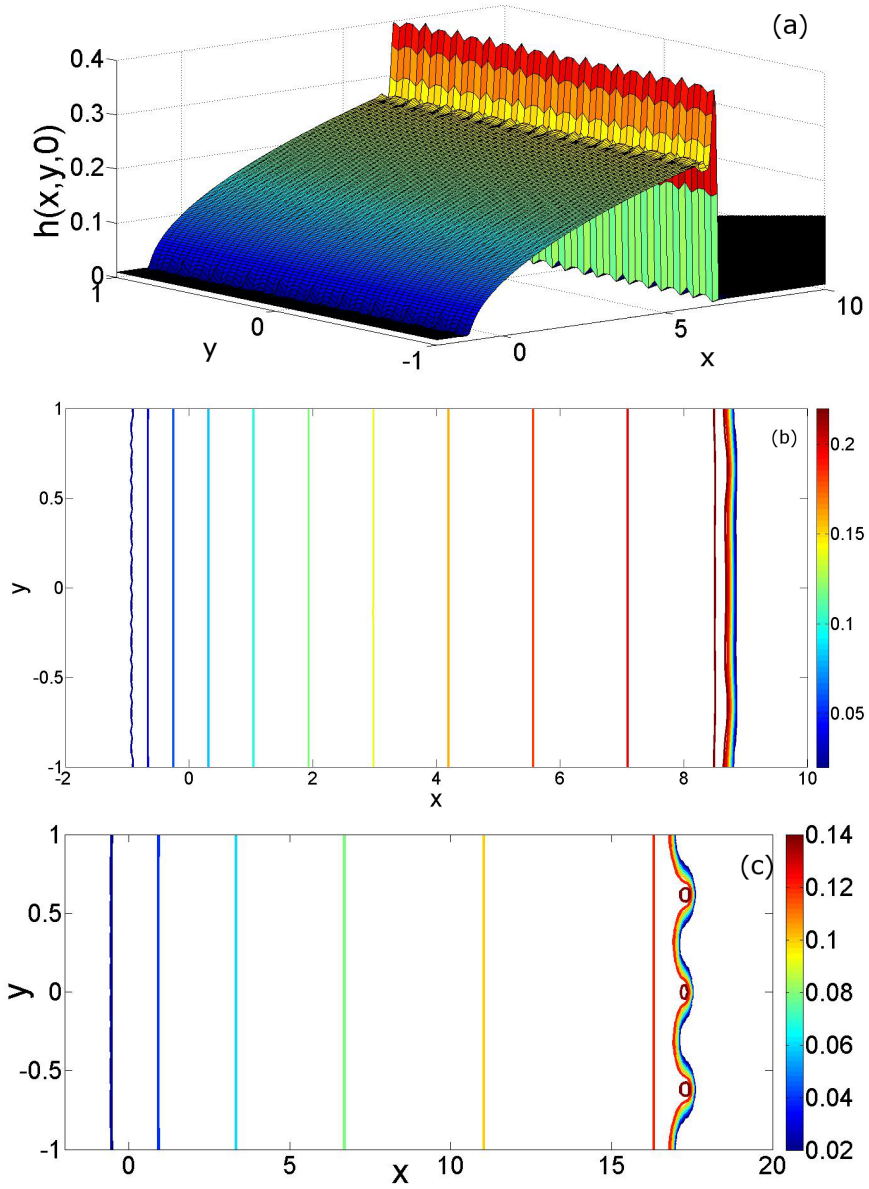

Figure 3.12: Contour plots showing the 2-D evolution of the fluid interface from the base state initial condition shown at $t = 100$ for $b = 0.01$, $\theta = 90^o$ and $Ca = 10^{-3}$ with a multi-cosine perturbation with $A_i = 0.01$ at $x_0 = 6.65$ with wavenumber $q_i = 0.5, 1, 5, 10, 15, 25, 30$ at time (a) $t = 0$, (b) 200, (c) 1200. (d) shows the trailing edge of the droplet at $t = 1200$.

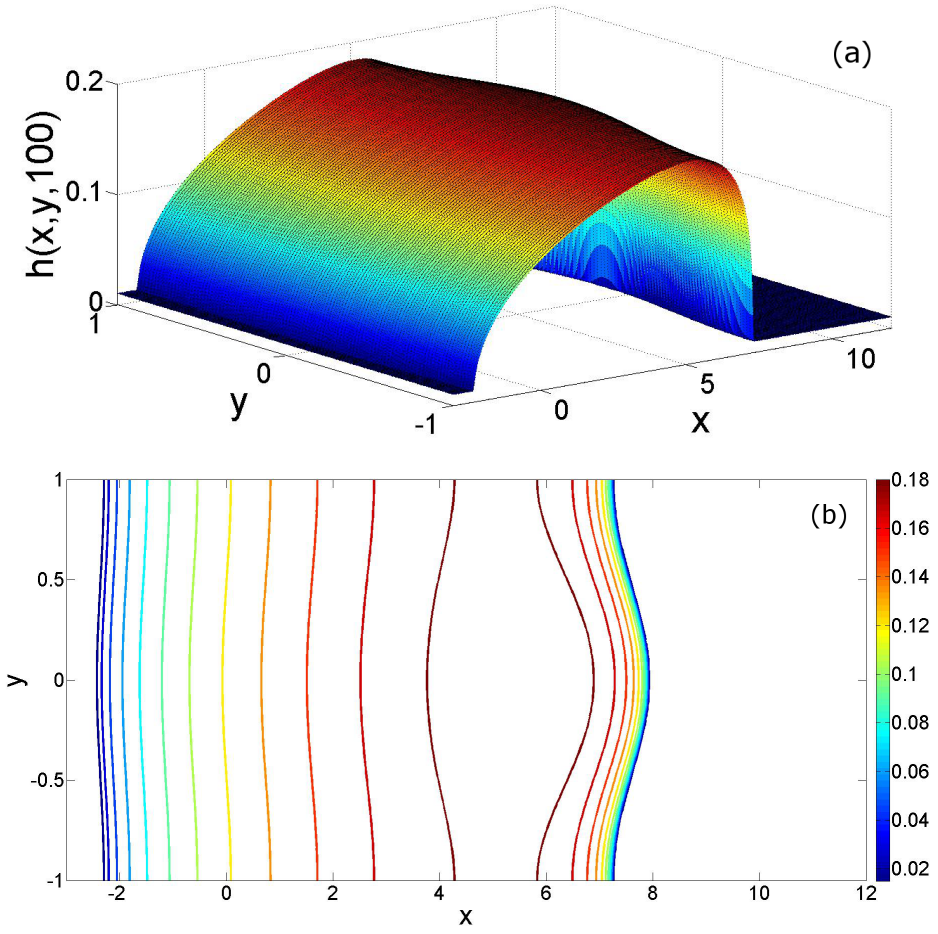

Figure 3.13: (a)Surface plot and (b)contour plot of the fluid interface from the initial conditions (Eq. (3.11,3.16)) with a single transverse perturbation of amplitude $A_i = 0.1$ and wavenumber $q_i = 1$ at $t = 100$

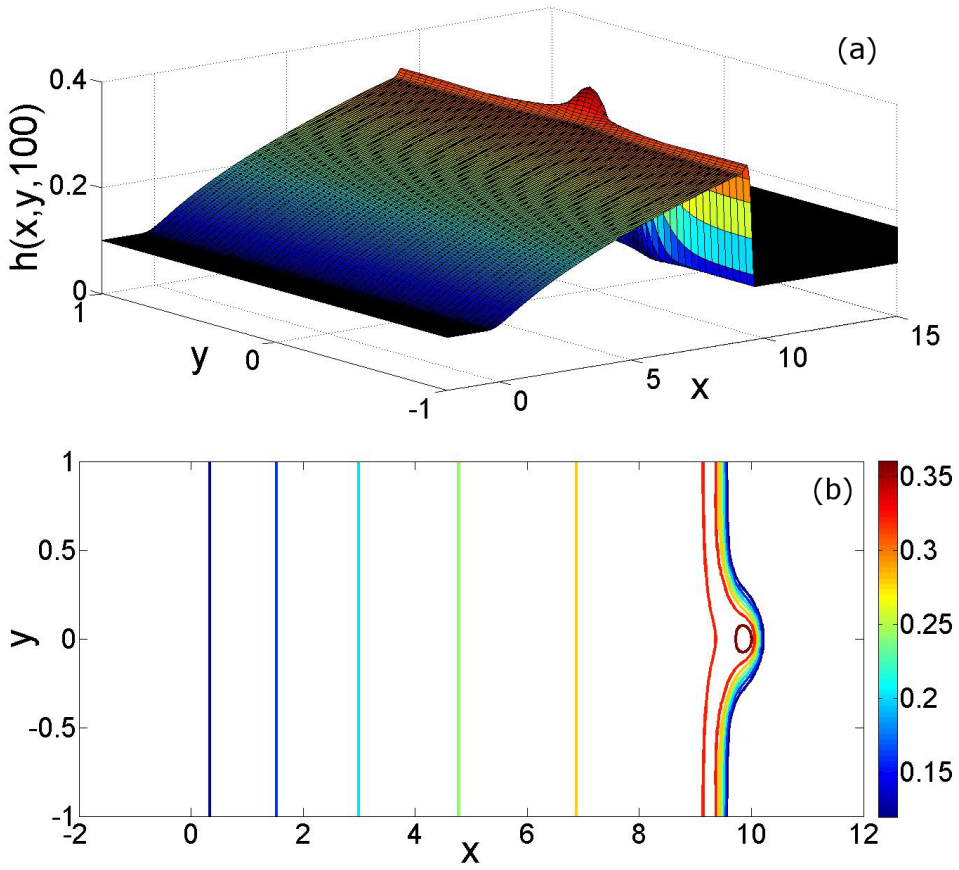

Figure 3.14: Surface and contour plots showing the 2-D evolution of the fluid interface from the initial conditions (Eq. (3.11,3.16)) with a single trasverse cosine perturbation of amplitude $A_i = 0.1$ and wavenumber $q_i = 1$ with a precursor thickness $b = 0.1$. The plots show the surface and contour at time $t = 100$.

3.3 Concluding remarks

This chapter analyses the stability of spreading of a constant volume thin viscous fluid droplet down a pre-wetted inclined plane using linear stability analysis and 2-D numerical simulations. We undertook a linear stability analysis of the effective contact line region which it is speculated that the instabilities originate from. The stability

analysis of the 'effective' contact line region shows this region to be linearly unstable to long-wavelength transverse perturbations. This is consistent with the findings of Troian *et al.* [63] and Bertozzi and Brenner [8]. Surface tension (or capillary effects) which is comparable to gravity here stabilises the shorter wavelengths. The most unstable wavelength is comparable to the length scale of this region, which confirms the speculation that the onset of fingering is initiated here.

We were able to obtain a stability criterion which shows the bulge or capillary ridge at the leading edge to be a necessary condition for the onset of instability. The $o(q^2)$ destabilising term in Eq. (3.8) is $\frac{H_s^3}{3}H_{s\xi\xi\xi}$ which is largest where changes in curvature of the base state H_s are large. As can be observed in Fig. 2.10, the largest change in curvature is in the region immediatly behind the contact line and ahead of the capillary ridge. It is this region that is targeted by the instability resulting in growth of perturbations to the base state here (see Fig. 3.1). As the angle of inclination θ decreases, the change in curvature becomes less severe and the growth of perturbations is considerably reduced. The above destabilising term originates fro the term $q^2\frac{H_s^3}{3}H_{1\xi\xi}$ in Eq. (3.4) which is related to surface-tension-driven flows in the transverse direction due to changes in the base state curvature (commonly referred to as the Rayleigh term). Such forces are generally destabilising resulting in a so-called Rayleigh instability which has been postulated as a possible destabilising mechanism for initiating the fingering instability observed here [59]. We have therefore successfully reproduced the results obtained by Troian *et al.* [63] and Bertozzi and Brenner [8].

The 2-D simulations assuming periodicity of 2 in the transverse y direction confirm the linear stability results. We saw that by increasing the precursor film or decreasing the angle of inclination stabilises the flow. This is consistent with the linear stability analysis done in §3.1, as increasing the precursor film decreases the size of the capillary ridge(the necessary condition for the flow to be linearly unstable). Thinning the precursor film is similar to varying time. The LSA performed showed that by decreasing the precursor film destabilises the flow. The 2-D simulations also indicate a preferred wavelength of perturbation. In the LSA the wavenumber correlating to maximum growth rate appears to be fixed ($q_{max} \approx 0.5 = q^*_{max}(Cah_L)^{1/3}$). We can calculate the wavelength of fingers correlating to $q_{max} \approx 0.5$, taking $h_L = 1$ and $Ca = 10^{-3}$ hence, we obtain $q^*_{max} = 5/\pi \approx 1.6$. This indicates from the initial parabolic drop shape we should see a maximum of two fingers in a period of 2. This is consistent with the two-dimensional simulations. However, with a perturbation of a single wavenumber only a single finger will form as the interaction between modes gives the mechanism for multiple finger to form. In both the superposition and discrete perturbations we observe that from the parabolic droplet shape that fingers of width ≈ 0.5 and hence wavelength of 1 are observed. Fingers become thinner, less unstable and more in number for perturbations to the quasi-steady base state obtained over increasing times. As $q_{max} \approx 0.5$ and is approximatly fixed with time we calculate that for a quasi-steady 1D solution calculated in Chapter 2 that $q^*_{max} \approx 2.4$ for the y domain of length 2. This indicates that we should observe between 2 and 3 fingers. This is consistant with the 2-D simulations. Hence, we speculate that we can predict the width and number

of fingers that develop depending on the initial conditions which is perturbed. It is worth mentioning that for an initial condition from a constant flux source (studdied by Schwartz [54], Eres *et al.* [18] and Kondic [35, 36]) to obtain similar results adjustment to the fluid height at the constant flux source would have to be made. Decreasing the fluid height at the constant flux source would increase the number of fingers and decrease the width and length of the fingers. To the best of our knowledge no work has been undertaken into the effect that varying the initial condition has on the non-linear stability of the flow.

Chapter 4

Spreading of a surfactant-laden viscous droplet down an inclined pre-wetted plane: base state.

In this chapter we will consider the spreading of a thin viscous droplet laden with insoluble surfactant. We will derive the evolution equations for the droplet height and surfactant concentration using lubrication approximation. We use high-resolution numerics to provide an insight into the important physical mechanisms. Asymptotic analysis is used to obtain approximate solutions based on the important mechanisms in each region. The spreading and thinning rates are naturally obtained from our asymptotic analysis and are not assumed to be known *a priori*.

4.1 Mathematical formulation

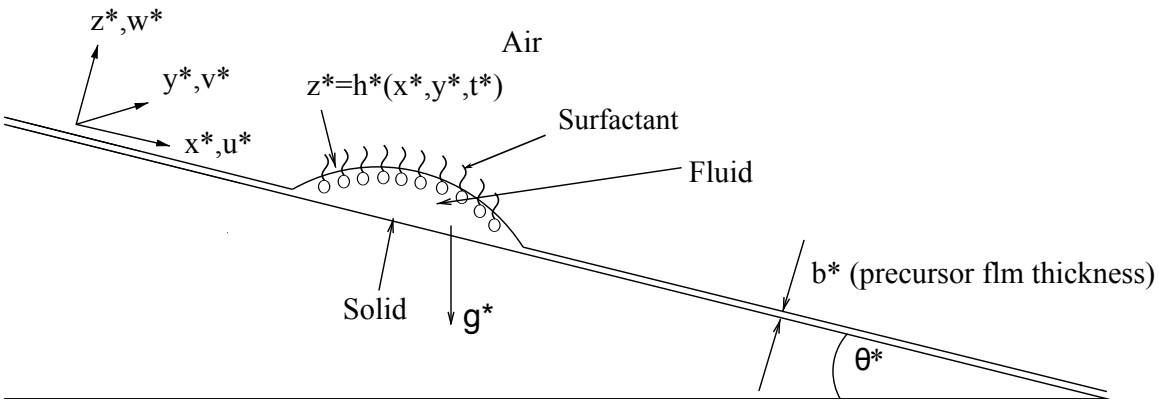

Figure 4.1: Schematic of a surfactant laden spreading droplet on an inclined plane.

Consider the spreading of a thin viscous fluid droplet, of constant volume, loaded with insoluble surfactant down an inclined plane. The surfactant has an initial concentration Γ_m^*. The fluid has viscosity μ^*, density ρ^* and surface tension σ^*. The fluid's surface tension at the initial surfactant concentration is denoted by σ_m^* and the surface tension of a clean, uncontaminated interface is σ_0^*. The plane is pre-wetted with a thin precursor film of thickness b^*. We choose a Cartesian co-ordinate system (x^*, y^*, z^*) with x^* and y^* along the plane, and z^* along the thickness of the drop. θ^* is the angle of inclination. The velocities in the x^*, y^*, z^* directions are given by u^*, v^*, w^*, respectively. The free surface is given by $z^* = h^*(x^*, y^*, t^*)$ and the fluid-solid interface is at $z^* = 0$. All starred variables are dimensional.

4.1.1 Governing equations

The equations of motion of the fluid are given by the Stokes equations

$$0 = -\nabla^* P^* + \rho^* \boldsymbol{g}^* + \mu^* \nabla^{*2} \boldsymbol{u}^*, \tag{4.1}$$

$$0 = \nabla^* \cdot \boldsymbol{u}^*. \tag{4.2}$$

Equations (4.1,4.2) represent conservation of fluid momentum and mass, respectively.

$$\frac{\partial \Gamma^*}{\partial t} + \nabla_s^* \cdot (\Gamma^* \boldsymbol{u}_s^*) + \Gamma^* (\nabla_s^* \cdot \boldsymbol{n}^*)(\boldsymbol{u}^* \cdot \boldsymbol{n}^*) = D_s^* \nabla_s^{*2} \Gamma^* \tag{4.3}$$

Equation (4.3) represents the convective-diffusion equation for surfactant transport. D_s^* is the surfactant diffusion coefficient. ∇^* is the gradient operator and ∇_s^* denotes the surface gradient operator [16].

$$\nabla_s^* = (I - \boldsymbol{n^* n^*}) \cdot \nabla^*, \tag{4.4}$$

with I representing the identity tensor and $\boldsymbol{n}^*$ is the unit outward normal. The fluid in the bulk is assumed to be slow viscous flow, so inertial effects have been neglected in Eq. (4.1). In the analysis which follows surfactant dilation is neglected. In Eq. (4.1), $\mathbf{u}^* = (u^*, v^*, w^*)$ is the fluid velocity and P^* is the fluid pressure relative to atmospheric pressure. Without loss of generality, we take the pressure in the air to be zero. The gravitational acceleration, $\boldsymbol{g}^* = (g^* \sin(\theta), 0, -g^* \cos(\theta))$, where g^* is the magnitude of

gravitational acceleration. We assume that both the fluid viscosity μ^* and its density ρ^* are constant, however surface tension σ^* is not.

4.1.2 Boundary conditions

As before we apply a no slip boundary condition at the fluid-solid interface,

$$u^* = v^* = w^* = 0, \text{ at } z^* = 0. \tag{4.5}$$

At the air-liquid interface, $z^* = h^*(x^*, y^*, t^*)$, we apply [55],

$$-(T_1^* - T^*) \cdot \boldsymbol{n}^* = 2R^*\sigma^*\boldsymbol{n}^* - \nabla_s\sigma^*, \tag{4.6}$$

where $T_1^* = -P_1^*$, is the stress tensor in the air phase, which is assumed to be inviscid. P_1^* is the air pressure. Since pressure is measured relative to atmospheric pressure, without loss of generality, $P_1^* = 0$. $T^* = -P^*I + \boldsymbol{\tau}^*$ is the stress tensor in the fluid phase, where P^* is the liquid pressure, $\boldsymbol{\tau}^* = \mu^*(\nabla\boldsymbol{u}^* + \nabla\boldsymbol{u}^{*T})$ is the viscous component of the stress tensor. σ^* is the surface tension at the air liquid interface. $2R^*$ is the mean curvature of the surface and $\boldsymbol{n}^*$ is the unit outward normal to the surface (pointing out of the liquid). Equation (4.6) is the same as Eq. (2.4) in the gravity derivation except as surfactant alters the surface tension the second term on the RHS has been

included. We assume a linear equation of state which can be written as,

$$\sigma^* = \sigma_0^* - |\frac{d\sigma^*}{d\Gamma^*}|_{(\sigma^*=\sigma_0^*,\Gamma^*=0)}\Gamma^*. \tag{4.7}$$

This equation relates surface tension to surfactant concentration is valid for low concentrations of surfactant. The unit outward normal to the surface $z^* = h^*(x^*, y^*, t^*)$ is

$$\boldsymbol{n}^* = \nabla^*(z^* - h^*(x^*, y^*, t^*)) = \frac{1}{\sqrt{h_{x^*}^{*2} + h_{y^*}^{*2} + 1}}\left(-h_{x^*}^*, -h_{y^*}^*, 1\right). \tag{4.8}$$

The two unit tangents to the free surface, $z^* = h^*(x^*, y^*, z^*)$ are

$$\boldsymbol{t_1^*} = \frac{1}{\sqrt{h_{x^*}^{*2} + 1}}\left(1, 0, h^*{}_{x^*}\right), \tag{4.9}$$

$$\boldsymbol{t_2^*} = \frac{1}{\sqrt{h_{x^*}^{*2} + h_{y^*}^{*2} + 1}\sqrt{h_{x^*}^{*2} + 1}}\left(-h_{x^*}^* h_{y^*}^*, h_{x^*}^{*^2} + 1, h_{y^*}^*\right). \tag{4.10}$$

The normal component of the stress balance at the free surface (Eq. (4.6)) is

$$\begin{aligned} &h_{x^*}^{*2}(P^* - 2\mu^* u_{x^*}^*) - 2\mu^* h_{x^*}^* h_{y^*}^*(v_{x^*}^* + u_{y^*}^*) + 2h_{x^*}^*\mu^*(w_{x^*}^* + u_{z^*}^*) + 2\mu^* h_{y^*}^{*^2}(w_{y^*}^* + v_{z^*}^*) + \\ &h_{y^*}^{*2}(P^* - 2\mu^* v_{y^*}^*) + P^* - 2\mu^* w_{z^*}^* = -\frac{h_{x^*x*}^*(h_{y^*}^{*^2} + 1) + h_{y^*y^*}^*(h_{x^*}^{*^2} + 1) - 2h_{x^*}^* h_{y^*}^* h_{x^*y^*}^*}{(h_{x^*}^{*2} + h_{y^*}^{*2} + 1)^{\frac{1}{2}}}\sigma^*. \end{aligned} \tag{4.11}$$

The two tangential components of Eq. (4.6) are

$$\frac{1}{\sqrt{h_{x^*}^{*2}+h_{y^*}^{*2}+1}}\left[2\mu^* h_{x^*}^*(-u_{x^*}^*+w_{z^*}^*)+\mu^*(1-h_{x^*}^{*^2})(w_{x^*}^*+u_{z^*}^*)-\mu^* h_{y^*}^*(v_{x^*}^*+u_{y^*}^*)\right]$$
$$+\frac{1}{\sqrt{h_{x^*}^{*2}+h_{y^*}^{*2}+1}}\left[-\mu^* h_{x^*}^* h_{y^*}^*(v_{z^*}^*+w_{y^*}^*)\right]=\sigma_{x^*}^*(1-\frac{h_{x^*}^{*^2}}{h_{x^*}^{*2}+h_{y^*}^{*2}+1}), \tag{4.12}$$
$$\frac{1}{\sqrt{h_{x^*}^{*2}+h_{y^*}^{*2}+1}}\left[2\mu^* h_{y^*}^*(h_{x^*}^{*^2}(v_{y^*}^*-u_{x^*}^*)-w_{z^*}^*+v_{y^*}^*)+\mu^* h_{x^*}^*(h_{x^*}^{*^2}+1-h_{y^*}^{*^2})(v_{x^*}^*+u_{y^*}^*)\right]$$
$$+\frac{1}{\sqrt{h_{x^*}^{*2}+h_{y^*}^{*2}+1}}\left[+2\mu^* h_{y^*}^* h_{x^*}^*(w_{x^*}^*+u_{z^*}^*)+\mu^*(h_{y^*}^{*^2}-h_{x^*}^{*^2}-1)(w_{y^*}^*+v_{z^*}^*)\right]$$
$$=h_{x^*}^* h_{y^*}^*\sigma_{x^*}^*(1-\frac{h_{x^*}^{*^2}}{h_{x^*}^{*2}+h_{y^*}^{*2}+1})-(h_{x^*}^{*^2}+1)\sigma_{y^*}^*\left(1-\frac{h_{y^*}^{*^2}}{h_{x^*}^{*2}+h_{y^*}^{*2}+1}\right). \tag{4.13}$$

The final boundary condition used is the kinematic boundary condition,

$$h_{t^*}^*=-u_s^* h_{x^*}^*-v_s^* h_{y^*}^*+w_s^*. \tag{4.14}$$

4.1.3 Nondimensionalisation

We nondimensionalise the equations based on length scales H^* and L^* , a characteristic drop thickness (e.g. the initial drop height) and length (e.g. the initial drop length), respectively, a characteristic speed $U^*=(\rho^* g^* \sin(\theta)H^{*2})/\mu^*$ (balancing viscous forces with the horizontal component of gravity), a characteristic pressure $P^*=(\mu^* U^* L^*)/H^{*2}$ (balancing the pressure gradient with viscous forces)and a characteristic time $T^*=L^*/U^*$. We nondimensionalise the surface tension σ^* with σ_0^* and the surfactant concentration with Γ_m^*. Table 4.1 shows the typical values of the

dimensional quantities. Hence we nondimensionalise the variables as

$$(x, y) = \frac{(x^*, y^*)}{L^*}, (z, h) = \frac{(z^*, h^*)}{H^*}, (u, v) = \frac{(u^*, v^*)}{U^*},$$
$$w = \frac{w^*}{\epsilon U^*}, P = \frac{\epsilon H^* P^*}{\mu U^*}, t = \frac{t^* U^*}{L^*}, \epsilon = \frac{H^*}{L^*}, \Gamma = \frac{\Gamma^*}{\Gamma_m^*}, \sigma = \frac{\sigma^*}{\sigma_0^*}. \tag{4.15}$$

Here, ϵ is the aspect ratio, which is typically much less than one for these problems. It

Physical quantities	Typical value
Viscosity, μ^* (for silicon oil)	0.051 kg/ms[68]
Surface tension, σ^* (for silicon oil DM5-10)	0.021 N/m
Density, ρ^* (for silicon oil DM5-10)	950 kg/m^3
Characteristic Height, H^*	0.001m
Characteristic Length, L^*	0.01m
Characteristic speed, $U^* = \frac{\rho^* g^* \sin(\theta) H^{*2}}{\mu^*}$	0.0186 m/s
Characteristic pressure, $P^* = \frac{\mu^* U^* L^*}{H^{*2}}$	9.6 kg/(m s^2)
Characteristic time, $T^* = \frac{L^*}{U^*}$	0.5376 s

Table 4.1: Typical values of the dimensional quantities Characteristic speed, pressure and time are calculated using viscosity, surface tension and density displayed here.

is worth mentioning that a scalings based on balancing viscous and Marangoni forces is also commonly used (see [15, 12, 13, 46]). We prefer to use the scalings above as we are interested in understanding how surfactant effects can influence the gravity-driven spreading process.

Substituting the above dimensionless variables into the fluid bulk equations and boundary conditions produces a set of dimensionless equations. In the fluid bulk we obtain

$$u_x + v_y + w_z = 0, \tag{4.16}$$

$$-P_x + \epsilon^2 u_{xx} + \epsilon^2 u_{yy} + u_{zz} + 1 = 0, \tag{4.17}$$

$$-P_y + \epsilon^2 v_{xx} + \epsilon^2 v_{yy} + v_{zz} = 0, \tag{4.18}$$

$$-P_z + \epsilon^4 w_{xx} + \epsilon^4 w_{yy} + \epsilon^2 w_{zz} - \epsilon \cot(\theta) = 0. \tag{4.19}$$

On the free surface, $z = h(x, y, t)$, the nondimensionalised normal stress balance is

$$\frac{1}{\epsilon^2 h_x^2 + \epsilon^2 h_y^2 + 1}[P(\epsilon^2 h_x^2 + \epsilon^2 h_y^2 + 1) - \epsilon^4 h_x^2 u_x - 2\epsilon^4 h_x h_y (v_x - u_y) + 2\epsilon^2 h_x(\epsilon^2 w_x + u_z)$$
$$+2\epsilon^3(\epsilon^2 w_y + v_z) - 2\epsilon^3 h_y^2 v_y + 2\epsilon^2 w_x] = -Ca \frac{h_{xx}(1 + \epsilon^2 h_y^2) + h_{yy}(1 + \epsilon^2 h_x^2) - 2\epsilon^2 h_y h_x h_{xy}}{(\epsilon^2 h_x^2 + \epsilon^2 h_y^2 + 1)^{\frac{3}{2}}}$$
. (4.20)

Where Ca= $(\epsilon^3 \sigma)/(\mu U)$, is the capillary number and is assumed $O(1)$. The nondimensional tangential interfacial stress boundary conditions are

$$2\epsilon^2 h_x(-u_x + w_z) + (1 - \epsilon^2 h_x^2)(\epsilon^2 w_x + u_z) - \epsilon^2 h_y(v_x + u_y) - \epsilon^2 h_x h_y(v_z + \epsilon^2 w_y)$$
$$= \sqrt{\epsilon^2 h_x^2 + \epsilon^2 h_y^2 + 1} \left(1 - \frac{\epsilon^2 h_x^2}{\epsilon^2 h_x^2 + \epsilon^2 h_y^2 + 1}\right) \frac{\sigma_0^*}{\mu^* U^*} \sigma_x, \tag{4.21}$$
$$2\epsilon^2 h_y(\epsilon^2 h_x^2(-v_y + u_x) + w_z - v_y) - \epsilon^2 h_x(\epsilon^2 h_x^2 - \epsilon^2 h_y^2 - 1)(v_x + u_y) - 2\epsilon^2 h_y h_x(\epsilon^2 w_x + u_z)$$
$$+(-\epsilon^2 h_y^2 + \epsilon^2 h_x^2 + 1)(\epsilon^2 w_y + v_z) =$$
$$\sqrt{\epsilon^2 h_x^2 + \epsilon^2 h_y^2 + 1} \left[\epsilon^2 h_x h_y \left(1 - \frac{\epsilon^2 h_x^2}{\epsilon^2 h_x^2 + \epsilon^2 h_y^2 + 1}\right) \frac{\sigma_0^*}{\mu^* U^*} \sigma_x\right]$$
$$-\sqrt{\epsilon^2 h_x^2 + \epsilon^2 h_y^2 + 1} \left[(\epsilon^2 h_x^2 + 1) \left(1 - \frac{\epsilon^2 h_x^2}{\epsilon^2 h_x^2 + \epsilon^2 h_y^2 + 1}\right) \frac{\sigma_0^*}{\mu^* U^*} \sigma_y\right]. \tag{4.22}$$

The nondimensional kinematic condition is,

$$h_t + h_x u|_{z=h(x,y,t)} + h_y v|_{z=h(x,y,t)} - w|_{z=h(x,y,t)} = 0. \tag{4.23}$$

The no slip boundary condition on $z = 0$ in dimensionless form is

$$u = v = w = 0. \tag{4.24}$$

We finally nondimensionalise the equation of state to obtain,

$$\sigma = 1 - \hat{M}\Gamma \tag{4.25}$$

where $\hat{M} = \frac{\frac{d\sigma^*}{d\Gamma^*}|_{(\sigma^*=\sigma_0^*,\Gamma^*=0)}}{\sigma_0^*}\Gamma_M^* = (\sigma_0^* - \sigma_m^*)/\sigma_0^*$ is the Marangoni number describing the strength of the surfactant in comparison to surface tension gradients.

4.1.4 Lubrication theory

The nondimensional equations obtained can be simplified using the fact that the aspect ratio $\epsilon \ll 1$. We seek solutions of the form

$$(u, v, w, P, h, \Gamma) = (u_0, v_0, w_0, P_0, h_0, \Gamma_0) + \epsilon^2(u_1, v_1, w_1, P_1, h_1, \Gamma_1) + ...$$

Substituting this into Eqs. (4.16-4.25) at leading order in ϵ, the mass and momentum conservation equations,

$$u_{0x} + v_{0y} + w_{0z} = 0, \tag{4.26}$$

$$-P_{0x} + u_{0zz} + 1 = 0, \tag{4.27}$$

$$-P_{0y} + v_{0zz} = 0, \tag{4.28}$$

$$-P_{0z} - D(\theta) = 0, \tag{4.29}$$

where, $D(\theta) = \epsilon \cot(\theta)$ and is assumed $O(1)$. We include this effect at leading order to allow us to investigate a range of angles $0 \leq \theta \leq \pi/2$. At leading order in ϵ, the surfactant transport equation becomes

$$\Gamma_t + \nabla \cdot (\boldsymbol{u}_s \Gamma) = \frac{\nabla^2 \Gamma}{Pe}, \tag{4.30}$$

where $Pe = \frac{U^* L^*}{D_s^*}$ is a Pećlet number. We assume that surface dilation can be neglected. At $z = h_0(x, y, t)$, using Eq. (4.25), we have at leading order in ϵ,

$$h_{0t} + h_{0x} u_0 + h_{0y} v_0 - w_0 = 0, \tag{4.31}$$

$$-Ca(h_{0xx} + h_{0yy}) = P_0, \tag{4.32}$$

$$u_{0z} = M\Gamma_{0x}, \tag{4.33}$$

$$v_{0z} = M\Gamma_{0y}, \tag{4.34}$$

where $M = (\sigma_0^* \hat{M})/(\mu^* U^*)$ is the Marangoni number and $Ca = (\epsilon^3 \sigma^*)/(\mu^* U^*)$, is the Capillary number and is assumed $O(1)$. We have also used Eq. (4.25) to obtain Eqs. (4.33,4.34) At $z = 0$, we have at leading order in ϵ,

$$u = v = w = 0 \tag{4.35}$$

Integrating Eq. (4.29) with respect to z and applying Eq. (4.32) we obtain,

$$P_0 = D(\theta)(h_0 - z) - Ca(h_{0xx} + h_{0yy}). \tag{4.36}$$

Differentiating the above equation with respect to x and substituting it into Eq. (4.27)

$$u_{0zz} = -1 + D(\theta)h_{0x} - Ca(h_{0xxx} + h_{0yyx}). \tag{4.37}$$

Integrating with respect to z twice and applying the two boundary conditions for u_0 in Eqs. (4.33, 4.35) gives

$$u_0 = [Ca(h_{0xxx} + h_{0yyx}) - D(\theta)h_{0x} + 1]\left[h_0 z - \frac{z^2}{2}\right] - Mz\Gamma_{0x}. \tag{4.38}$$

To obtain the equation for v_0, we differentiate Eq. (4.36) with respect to y then substitute it into Eq. (4.28). Integrating the resulting equation with respect to z twice and applying the boundary conditions for v_0 in Eqs. (4.34, 4.35) gives,

$$v_0 = [Ca(h_{0xxy} + h_{0yyy}) - D(\theta)h_{0y}]\left[h_0 z - \frac{z^2}{2}\right] - Mz\Gamma_{0y}. \tag{4.39}$$

Differentiating Eqs. (4.38, 4.39) with respect to x and y, respectively, and substituting it into Eq. (4.26) gives on integration with respect to z, gives an equation for w_0. Finally substituting the expressions for the velocities into the kinematic condition produces an equation for the evolution of the free surface. This can be written in compact

form as,

$$h_{0_t} + \nabla \cdot \left(Ca \frac{h_0^3}{3} \nabla \nabla^2 h_0 - D(\theta) \frac{h_0^3}{3} \nabla h_0 - M \frac{h_0^2}{2} \nabla \Gamma_0 \right) + \left(\frac{h_0^3}{3} \right)_x = 0 \tag{4.40}$$

Evaluating velocities at the surface we obtain,

$$\boldsymbol{u}_s = \frac{h_0^2}{2} \left(Ca \nabla \nabla^2 h + 1 - D(\theta) \nabla h \right) - M h \nabla \Gamma. \tag{4.41}$$

Substituting this into the surfactant transport equation (Eq. (4.30)) we obtain,

$$\Gamma_{0_t} + \nabla \cdot \left(Ca \frac{h_0^2}{2} \Gamma_0 \nabla \nabla^2 h_0 - D(\theta) \frac{h_0^2}{2} \Gamma_0 \nabla h_0 - M h_0 \Gamma_0 \nabla \Gamma_0 \right) + \left(\frac{h_0^2}{2} \Gamma_0 \right)_x - \frac{\nabla^2 \Gamma_0}{Pe} = 0. \tag{4.42}$$

The terms in brackets in Eqs. (4.40,4.42) represent the fluid and surfactant flux driven by surface tension or capillary forces (second term), vertical gravity (third term), Marangoni forces (fourth term) and horizontal gravity (fifth term). For a given surfac-

Parameter	Definition	Range/Typical value
Aspect ratio	$\epsilon = \frac{H^*}{L^*}$	$0 - 0.1$
Precursor film thickness	b	$0 - 1$
Capillary number	$Ca = \frac{\epsilon^3 \sigma^*}{\mu^* U^*}$	0.0221
Gravity balance	$D(\theta) = \epsilon \cot(\theta)$	$0 - \infty$
Marangoni number	$M = (\sigma_0^* - \sigma_m^*)/(\mu^* U)$	$0 - 10$
Pećlet number	$Pe = \frac{U^* L^*}{D_s^*}$	$100 - 10^5$

Table 4.2: Typical values of the nondimensional quantities calculated using values in Table 4.1.

tant system M can be scaled out by rescaling Γ to Γ/M including the initial surfactant concentration Γ_M^*. Varying M enables us to compare relative strengths of different sur-

factant systems in generating surface tension gradients starting from the same initial surfactant concentration Γ_M^*. Hence we keep the Marangoni number in the governing equations. In what follows, we drop the subscript '0' in Eqs. (4.40, 4.42) for ease. Table 4.2 shows the nondimensional parameters and the typical range of values using values in Table 4.1. In the next section we seek 1D solutions of Eqs. (4.40,4.42) by assuming that h and Γ only vary in the x-direction with no dependence in y.

4.2 1D drop spreading : numerical results

We first consider the spreading of the droplet assuming no variation in the y-direction. The 1D version of Eqs. (4.40,4.42) are then given by

$$h_t + Q_x = 0;\ Q = \left[Ca\frac{h^3}{3}h_{xxx} - D(\theta)\frac{h^3}{3}h_x - M\frac{h^2}{2}\Gamma_x + \frac{h^3}{3}\right], \tag{4.43}$$

$$\Gamma_t + q_x = 0;\ q = \left[Ca\frac{h^2}{2}\Gamma h_{xxx} - D(\theta)\frac{h^2}{2}\Gamma h_x - Mh\Gamma\Gamma_x + \frac{h^2}{2}\Gamma\right] - \frac{\Gamma_x}{Pe}. \tag{4.44}$$

These coupled pair of partial differential equations are supplemented by six boundary conditions, which are,

$$h = b,\ \ \Gamma = 0,\ \ h_x = 0, \quad \text{at} \quad x = \pm L, \tag{4.45}$$

where b is the precursor thickness, and L is an arbitrary length. This characterises a flat precursor film and zero surfactant concentration far upstream and downstream

from the spreading droplet. The initial conditions are chosen as: (shown in Fig. 4.2)

$$\begin{aligned} h(x,0) &= (1+b-x^2)[H(1-x)-H(-1-x)]+b[H(x-1)] \\ &\quad +b[H(-1-x)], \end{aligned} \tag{4.46}$$

$$\Gamma(x,0) = H(1-x)-H(-1-x). \tag{4.47}$$

where $H(x)$ is the Heaviside function. The initial condition for the fluid droplet assumes a parabolic shape connecting to a precursor film ahead and behind it. The initial condition for the surfactant concentration is such that there is a uniform surfactant concentration over the initial droplet and zero surfactant concentration outside of the droplet. This leads to large surfactant concentration gradients to be present initially at the two 'effective' contact lines of the droplet. We seek the time evolution of the

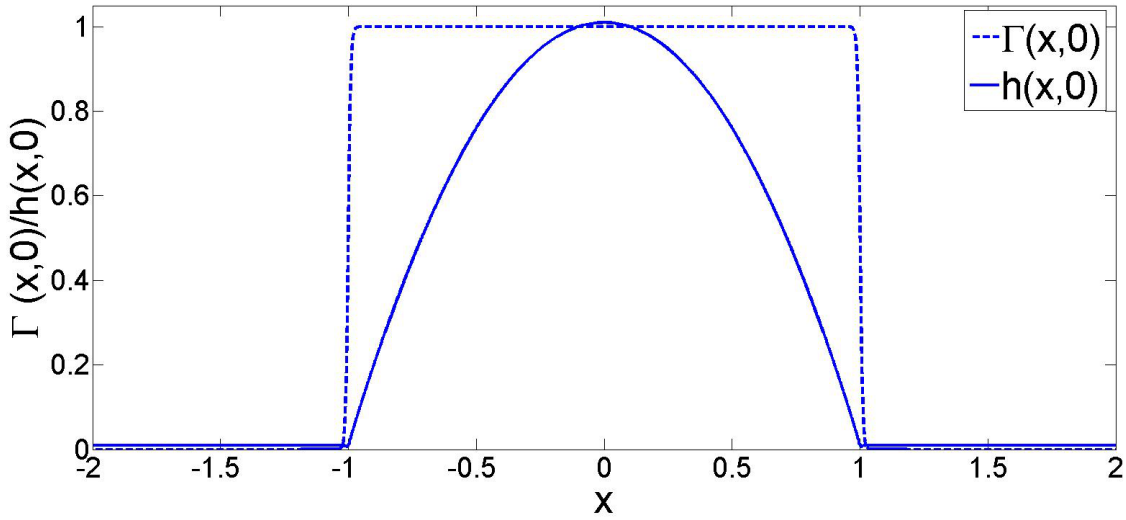

Figure 4.2: The initial drop shape and distribution of surfactant.

free surface of the drop and concentration of surfactant for various inclination angles θ

keeping the precursor thickness, capillary number, Peclet number and Marangoni number fixed. However, we will compute numerical simulations varying these parameters to understand the influence they have on the spreading of the droplet. Our focus is on the late-time evolution once the initial transient behaviour has died out allowing theoretical investigation of self similar spreading dynamics. We first discretise the spatial derivatives in Eqs. (4.43 , 4.44) using finite differences keeping the time derivative continuous. We define a forward difference and backward difference by,

$$h_{x,i} = \frac{h_{i+1} - h_i}{\Delta x}, \;\; h_{\tilde{x},i} = \frac{h_i - h_{i-1}}{\Delta x}, \tag{4.48}$$

respectively, where $h_i = h(x_i, t)$, $i = 0, 1, ..., N$. N is the number of discretisation points and Δx is the grid size. Using these forward and backward differences we can discretise Eqs. (4.43,4.44) such that,

$$h_{t,i} + [Ca\ a(h_{i+1}, h_i)h_{\tilde{x}x\tilde{x},i} - D(\theta)a(h_{i+1}, h_i)h_{\tilde{x},i} - Mc(h_{i+1}, h_i)\Gamma_{\tilde{x},i}]_x + \left[\frac{h_i^3}{3}\right]_{\tilde{x}} = 0, \tag{4.49}$$

$$\Gamma_{t,i} + [Ca\ d(h_{i+1}\Gamma_{i+1}, h_i\Gamma_i)h_{\tilde{x}x\tilde{x},i} - D(\theta)d(h_{i+1}\Gamma_{i+1}, h_i\Gamma_{i,j})h_{\tilde{x},i} - Me(h_{i+1}\Gamma_{i+1}, h_i\Gamma_i)\Gamma_{\tilde{x},i}]_x + \left[\frac{h_i^2\Gamma_i}{2}\right]_{\tilde{x}} + \frac{\Gamma_{\tilde{x}xi}}{Pe} = 0, \tag{4.50}$$

where,

$$a(h_{i+1}, h_i) = \frac{h_{i+1}^3 + h_i^3}{6}, \;\; c(h_{i+1}, h_i) = \frac{h_{i+1}^2 + h_i^2}{4},$$
$$d(h_{i+1}\Gamma_{i+1}, h_i\Gamma_i) = \frac{h_{i+1}^2\Gamma_{i+1} + h_i^2\Gamma_i}{4},$$

$$e(h_{i+1}\Gamma_{i+1}, h_i\Gamma_i) = \frac{h_{i+1}\Gamma_{i+1} + h_i\Gamma_i}{2}, \tag{4.51}$$

so that these are second order approximations hence Eqs. (4.49,4.50) are second order accurate. The finite difference scheme used in the above discretisation uses a 5-point stencil. This has the advantage of a smaller bandwidth (in comparison a 7-point stencil using the standard centred-difference scheme) while still maintaining second order accuracy. This scheme is commonly used in thin film problems (see [34, 38]). Our numerical scheme employed a fixed but spatially non-uniform grid, with grid points clustered in regions where we anticipated a rapid spatial variation. We used implicit time-stepping and validated convergence using grid refinement. For the simulations shown, the grid spacing varied from 10^{-4} where the film was extremely thin (particularly at the trailing edge of the droplet) to 10^{-3} elsewhere. The resulting differential equations are solved using the ODE solver DASSL [9]. The overall features of the flow are as reported by Edmonstone *et al.* [15, 12, 13], our finer computational grid allowed us to resolve some important features not described previously. Moreover, we compute solutions to much longer times than reported previously which allows us to describe theoretically their asymptotic structure.

Figures 4.3(a,b) shows the late time evolution ($t = 10^3 - 10^6$) of the drop height h and surfactant concentration Γ, respectively, for $\theta = 90^o$, $M = 1$, $Ca = 10^{-3}$, $Pe = 10^5$ and $b = 10^{-3}$. Inspection of these figures reveals there are several main features of the evolution of the droplet. The first is the main bulk droplet spreading under the

influence of horizontal gravity with surfactant concentration almost constant. Region I flows in the same manner as the main bulk droplet in the gravity-driven problem (see §2.4.1). Figure 4.4 compares the fluid profile spreading under gravity (dashed line) to the fluid profile spreading under gravity and surfactant related effects (solid line) the surfactant profile is shown be the dotted line. It clearly shows that the flow under gravity and surfactant related effects matches the flow under gravity only where the surfactant concentration is approximately uniform. As the surfactant concentration increases rapidly it can be seen that the surfactant and gravity-driven fluid profile deviates from the gravity-driven profile into a fluid 'hump'. Towards the leading edge of region I there is an abrupt jump in surfactant concentration gradient and fluid height due to competition between horizontal gravity and Marangoni forces. This dramatic increase in surfactant concentration gradient slows down the spreading rate of the droplet resulting in a jump in the fluid height. Towards the leading edge of the so-called fluid 'hump' there is a short region in which gravity balances Marangoni and capillary forces. This region contains a so-called capillary ridge where there is an abrupt jump in fluid height as the main bulk droplet connects onto the precursor film ahead. Between the capillary ridge and the precursor film is a fluid front driven by Marangoni forces. The surfactant concentration is linear across this fluid front. Ahead of the fluid front the precursor film remains undisturbed. At the trailing edge of the spreading droplet is an ultra thin film which matches onto a similar fluid front at its trailing edge. The fluid fronts form almost instantly due to the large surfactant concentration gradients present in the initial condition (see Fig. 4.2). The large surfactant concentration gradients

'suck' fluid from the precursor film creating these fluid fronts. The fluid front at the leading edge of the droplet remains self similar during the times investigated. Initially the fluid front region at the trailing edge of the drop flows in a similar manner to the other fluid front region. It is solely Marangoni driven flow as gravity has little effect. But as time progresses the strength of the Marangoni forces decreases and become of similar size and then become dominated by the horizontal component of gravity. This is similar to what was discussed by Grotberg and Jensen [30]. It can be seen from Fig. 4.5 that at $t = 5000$ the fluid front is well defined and is approximately $2b$ in height however as time progresses it can be seen that the front breaks down and become smoothened. Due to this fact it would be impossible to obtain a similarity solution for this region that holds for several orders of time. Mavromoustaki *et al.* have discussed the dynamics of this region and explored its stability using linear stability analysis [47] [48]. They were able to obtain a power law behaviour for the spreading of this region however as my results show as the strength of the Marangoni forces start to become dominated by the horizontal component of gravity the power law behaviour of this region should break down. As the fluid begins to flow back down the inclined plane we speculate that it will eventually result in a structure resembling the capillary ridge at the leading edge of the droplet. Figure 4.5 shows the trailing edge fluid front and ultra thin films for $M = 1$, $Ca = 10^{-3}$, $Pe = 10^5$ and $\theta = 90^o$ for $t = (1, 5) \times 10^3, (4, 5) \times 10^6$. We mentioned previously that at early times the front was well defined. As time progresses the height of the fluid front decreases and begins to change the direction of the flow. We clearly observe that at late-late time ($t = 4, 5 \times 10^6$) a satellite capillary

ridge has formed (see Fig. 4.5 inset).

Figure 4.6 compares the (a) droplet height h (b) surfactant concentration Γ for $t = 5 \times 10^5$. The parameter values are: $Ca = 10^{-3}$, $M = 1$, $b = 10^{-3}$, $Pe = 10^5$, $\theta = 90^\circ$ (dashed line), $\theta = 60^\circ$ (dotted line) and $\theta = 3^\circ$ (solid line). We can see that the overall droplet height and surfactant concentration remains unchanged, except for the amplitude of the capillary ridge which decreases as the angle of inclination θ (see inset Fig. 4.6 (a)).

Figure 4.7 compares the (a) droplet height h and (b) surfactant concentration Γ for $M = 1$ and 0.1 at $t = 10^4$. The parameter values are: $Ca = 10^{-3}$, $b = 10^{-3}$, $\theta = 90^\circ$, $Pe = 10^5$. The solid lines depict $M = 1$ and the dashed lines $M = 0.1$. We therefore see that by lowering the Marangoni number slows the speed of the spreading droplet. Moreover the fluid 'hump' develops at an earlier time with lower Marangoni number. The surfactant is swept to the leading edge of the spreading droplet more readily causing large surfactant concentration gradients at earlier time which slows the fluid there. We also note that the satellite capillary ridge at the trailing edge forms at earlier times with a smaller Marangoni number.

Figure 4.8 the (a)droplet height h (b) surfactant concentration Γ at $t = 5 \times 10^5$, with $M = 1$, $\theta = 90^o$ and $Pe = 10^5$. The solid line shows the fluid where $Ca = 10^{-3}$ and dashed line $Ca = 0$. We can see that the overall droplet height and surfactant concentration remains unchanged, except within short regions such as the capillary ridge, leading edge of the fluid fronts and the ultra thin film (all shown in insets in Fig.

4.8(a)). We also note that there is a shift in the maximum surfactant concentration (see inset Fig. 4.8(b)). We see that the maximum surfactant concentration, for $Ca = 0$, is not aligned with the minimum just ahead of the capillary ridge and is shifted to the left slightly. We also note for future reference the steep drop in surfactant concentration observed immediately after the maximum surfactant concentration (see inset Fig. 4.8(b)). Therefore the solutions obtained, downstream of the trailing edge of the droplet are robust for a variety of parameters and persist at late-late times. Taking $Ca = 0$ is valid here due to the diffusive effects of the Marangoni and surfactant diffusion terms.

As might be anticipated from Figs 4.3(a,b), much of the late time spreading is locally self similar. The upstream structures resemble closely to those observed when a surfactant-laden droplet spreads on a horizontal plane whose self-similar structure is discussed in detail in Jensen and Naire [32], hence we do not include their description here. Moreover, numerical simulations show almost negligible fluid or surfactant flux across the trailing edge of the droplet, which enables us to de-couple the spreading dynamics of the bulk droplet and the downstream structures from the upstream ones. Our main focus here is in describing the spreading dynamics of the bulk droplet and the downstream structures whose self-similar structure we examine in more detail next.

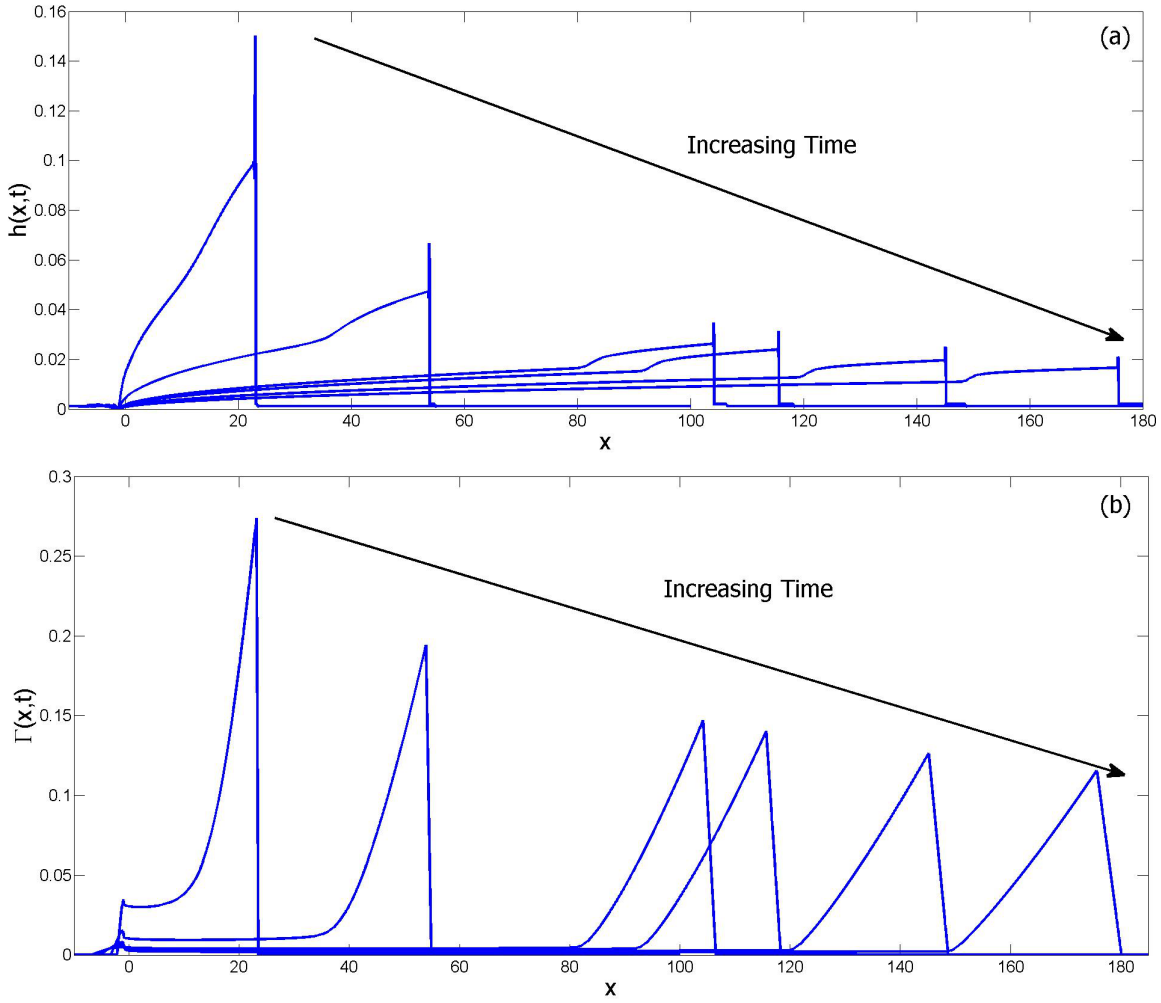

Figure 4.3: Late time evolution of (a) droplet height h and (b) surfactant concentration Γ for $t = (0.001, 0.01, 0.1, 0.2, 0.5, 1) \times 10^6$. The parameter values are: $Ca = 10^{-3}$, $M = 1$, $b = 10^{-3}$, $\theta = 90°$, $Pe = 10^5$.

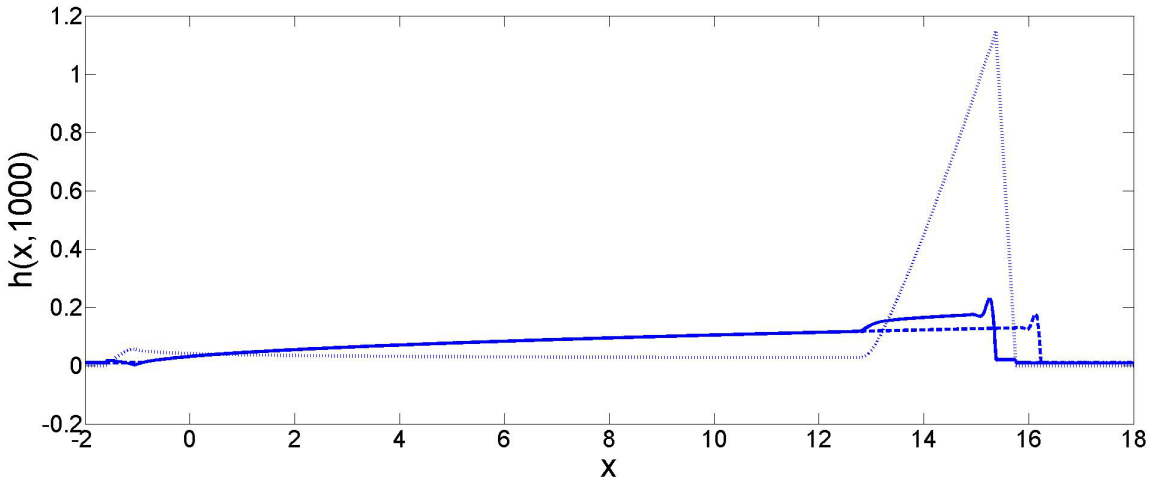

Figure 4.4: Comparing the fluid profile at $t = 1000$ for flow with and without surfactant The parameter values are: $Ca = 10^{-3}$, $M = 1$, $b = 10^{-3}$, $\theta = 90°$, $Pe = 10^5$. The solid line depicts flow with surfactant and the dashed line depicts the flow without surfactant.

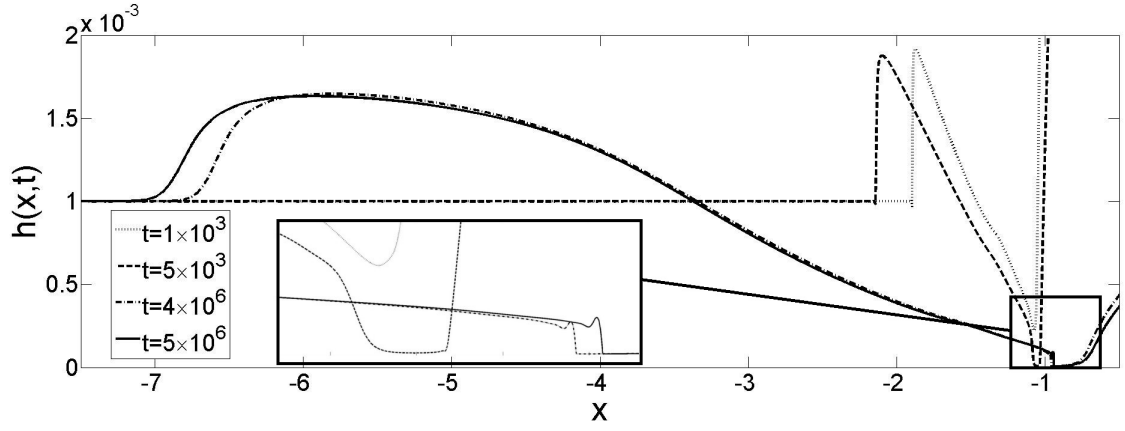

Figure 4.5: The evolution of the trailing edge of the droplet for $M = 1$, $Ca = 10^{-3}$, $Pe = 10^5$ and $\theta = 90^o$ for $t = (1, 5) \times 10^3, (4, 5) \times 10^6$.

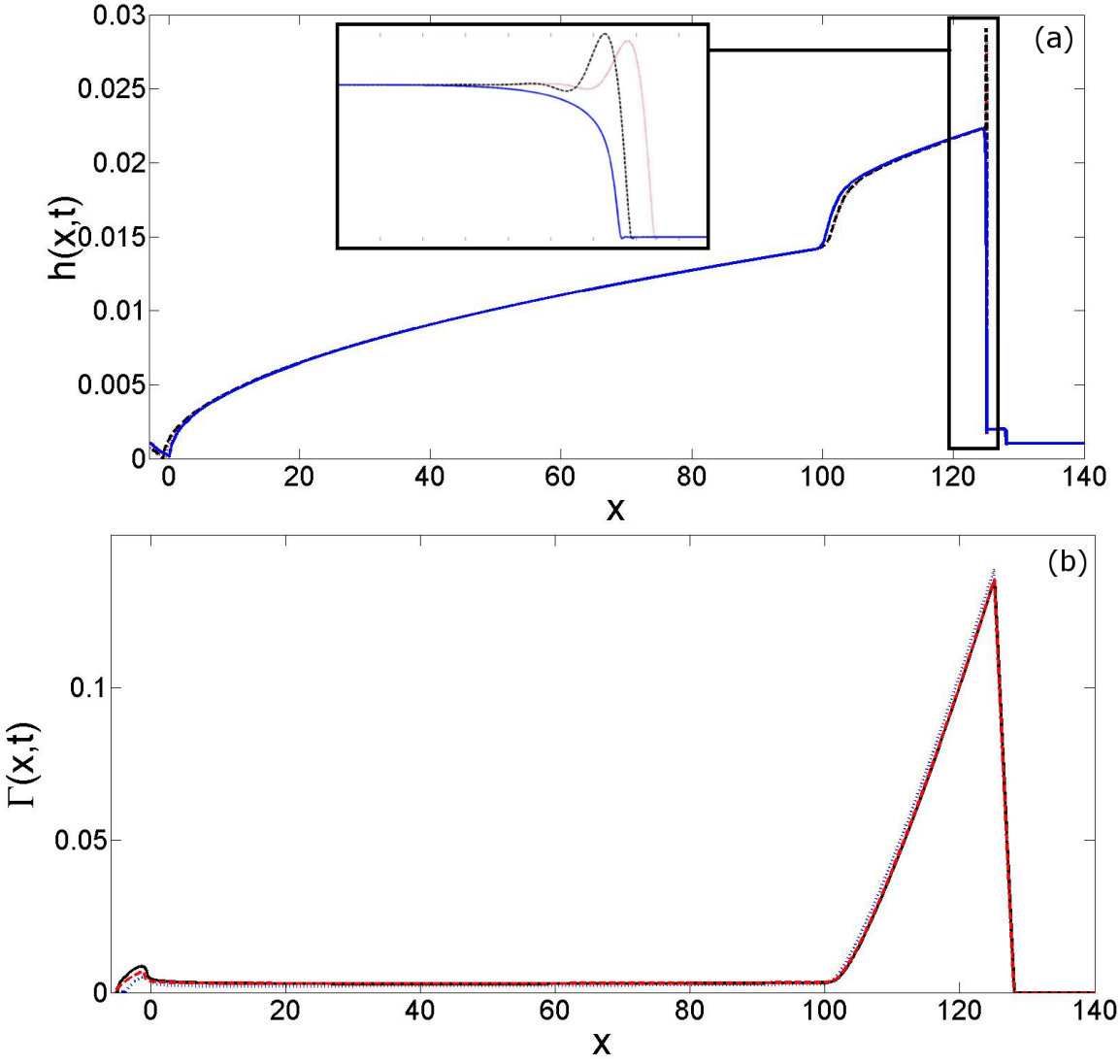

Figure 4.6: Comparing the (a) droplet height h and (b) surfactant concentration Γ for $t = 5 \times 10^5$. The parameter values are: $Ca = 10^{-3}$, $M = 1$, $b = 10^{-3}$, $Pe = 10^5$, $\theta = 90^\circ$ (dashed line), $\theta = 60^\circ$ (dotted line) and $\theta = 3^\circ$ (solid line).

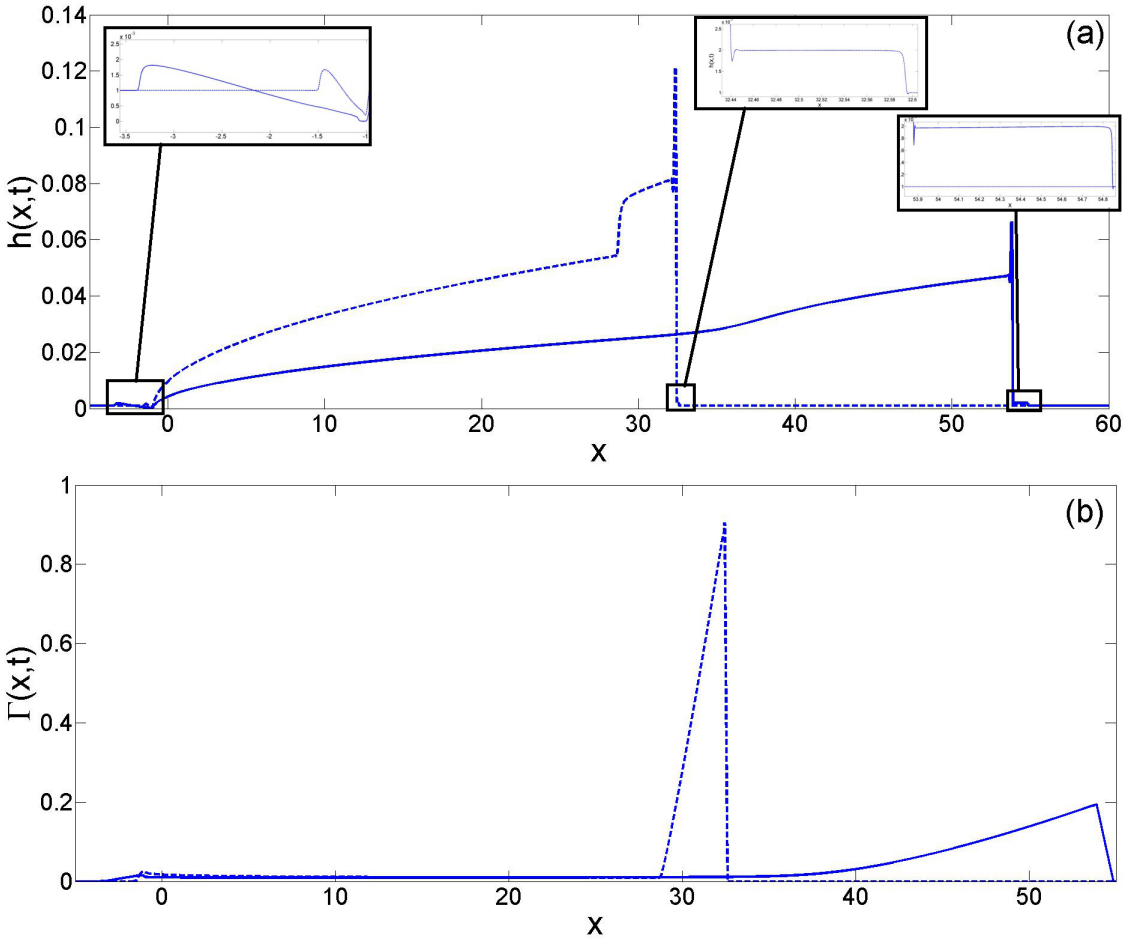

Figure 4.7: Comparing the (a) droplet height h and (b) surfactant concentration Γ for $M = 1$ and 0.1 at $t = 10^4$. The parameter values are: $Ca = 10^{-3}$, $b = 10^{-3}$, $\theta = 90°$, $Pe = 10^5$. The solid lines depict $M = 1$ and the dashed lines $M = 0.1$.

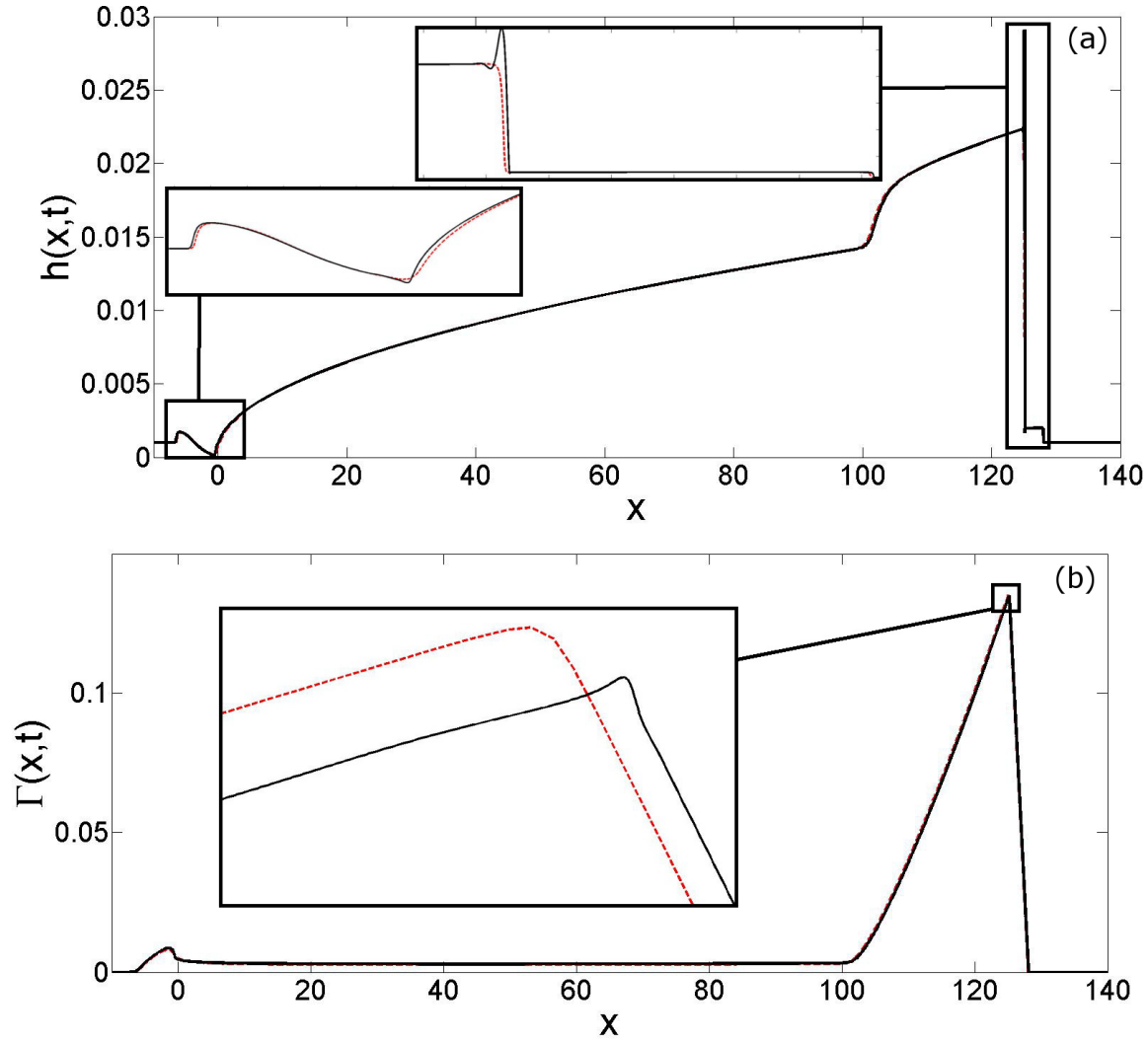

Figure 4.8: Comparing the (a)droplet height h (b) surfactant concentration Γ at $t = 5 \times 10^5$, with $M = 1$, $\theta = 90^o$, $b = 10^{-3}$ and $Pe = 10^5$. The solid line shows the fluid where $Ca = 10^{-3}$ and dashed line $Ca = 0$. The insets show the comparison of the fluid fronts at the leading and trailing edge with and without capillary effects and the maximum surfactant concentration.

4.3 Description of the late-time self-similar structure

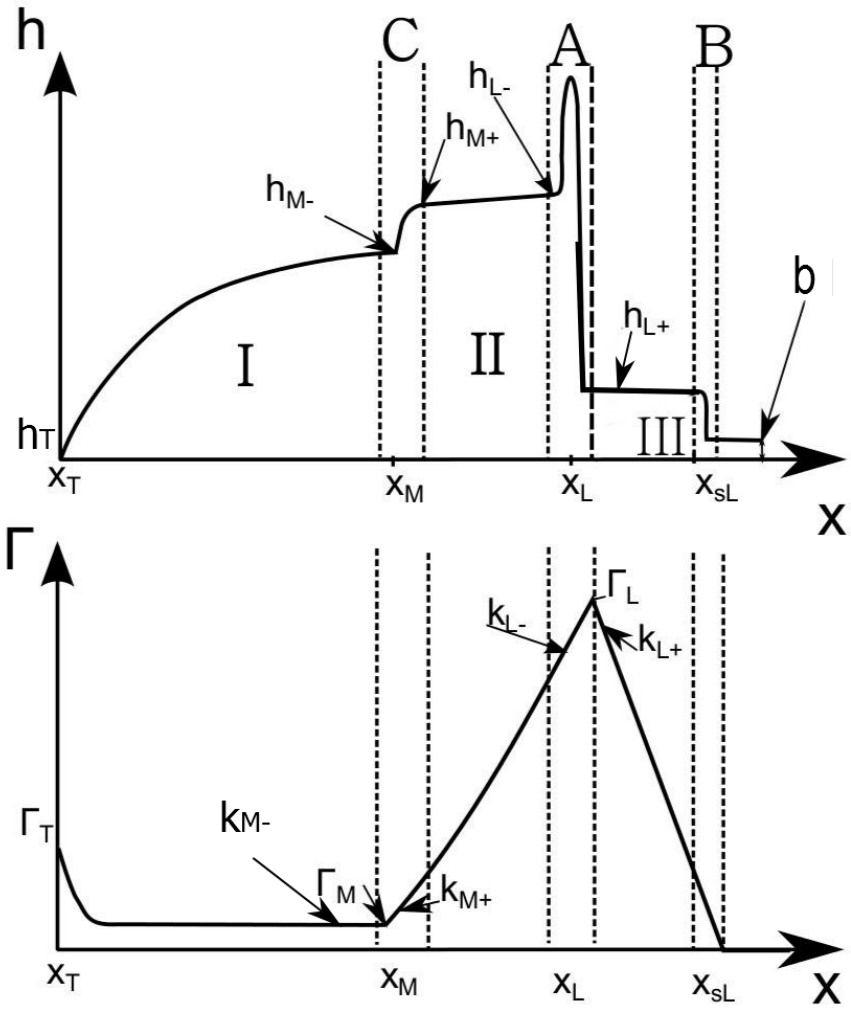

Figure 4.9: Schematic of the self-similar structure of the spreading drop and surfactant concentration.

We postulate that the numerical solution described in the previous section shows a multi-region self-similar structure for both the surfactant concentration and the droplet height, particularly, at late time. As mentioned previously the self-similar structure

observed is robust to variation in the parameters which characterise the droplet shape. We describe each region in turn below along with their relevant physics, scalings and approximate solutions. The spreading of the droplet is controlled by the delicate interplay between Marangoni forces and the horizontal component of gravity. Capillary or surface tension effects become important in short transition regions especially in the formation of the capillary ridge at the leading edge of the spreading droplet (see Fig 4.8 comparing spreading with and without capillary effects). The flow domain of the drop is divided into the following regions (see Fig. 4.9):

- Region I: The main bulk droplet region. This long region contains the bulk of the spreading droplet. The surfactant concentration in this region remains relatively constant, $\Gamma = \Gamma_M(t)$. The dominant fluid flow and surfactant transport mechanism in this region is due to the horizontal component of gravity. The leading edge of this region is at $x = x_M(t)$ while the trailing edge is at $x = x_T(t)$. The height of the drop is characterised by $h(x_M) = h_{M^-}(t)$.

- Region II: The fluid 'hump' region. This region within the main bulk droplet contains a 'hump' in the droplet height. The dominant flow and surfactant transport mechanism in this region is due to the horizontal component of gravity competing with Marangoni forces. This region has its trailing edge at $x = x_M(t)$ and the leading edge is at $x = x_L(t)$. The height of fluid in this region is characterised by $h(x_M) = h_{M^+}(t)$ at its trailing edge and $h(x_L) = h_{L^-}(t)$ at its leading edge. The surfactant concentration increases monotonically from $\Gamma = \Gamma_M(t)$ to the

maximum surfactant concentration $\Gamma = \Gamma_L(t)$.

- Region III: The fluid front region. The dominant flow and surfactant transport mechanism is due to Marangoni forces. The leading edge of the front is at $x = x_{SL}(t)$ and it's trailing edge at $x = x_L(t)$. The height of this region is characterised by the height of the front just after the capillary ridge $h(x_L) = h_{L^+}(t)$. The surfactant trailng edge concentration decreases monotonically in this region from $\Gamma = \Gamma_L(t)$ at the to $\Gamma = 0$ at the leading edge.

- Region IV: The precursor film region. This region is a passive region containing the precursor film ahead of the spreading droplet. The film remains undisturbed.

- Region A: The 'effective' contact line region. Here, the surface tension forces are of similar magnitude to that due to the horizontal component of gravity and Marangoni forces. This region is characterised by the position of the 'effective' contact line $x_L(t)$, the drop height upstream of the capillary ridge $h_{L^-}(t)$ and the film thickness at it's downstream end $h = h_{L^+}(t)$. The surfactant concentration in this region is characterised by the maximum surfactant concentration $\Gamma_L(t)$ as well as the surfactant concentration gradients $\Gamma_x(x_{L^-}) = k_{L^-}$ and $\Gamma_x(x_{L^+}) = k_{L^+}$, respectively.

- Region B: The leading edge of the fluid front, region III. The structure of this region has been described in detail previously (see Jensen and Grotberg [30], Jensen and Halpern [31], Jensen [29]).

- Region C: The region near $x = x_M$ joining the main bulk of the droplet (region I) to the fluid hump region (region II). There is an abrupt jump in the fluid height from h_{M^-} to h_{M^+}. The surfactant concentration is continuous but there is a jump in surfactant concentration gradient from $\Gamma_x(x_{M^-}) = k_{M^-}$ to $\Gamma_x(x_{M^+}) = k_{M^+}$.

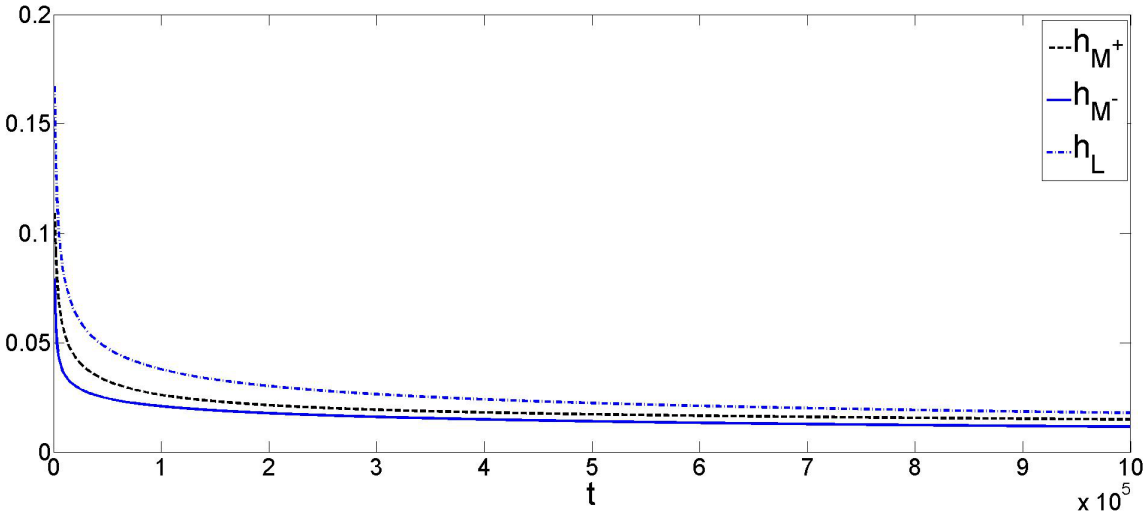

Figure 4.10: Time evolution of h_{L^-}, h_{M^+} and h_{M^-} from $t = 10^3 - 10^6$.

The flow is of the droplet is charecterised by 15 variables, h_{L^-}, h_{L^+}, h_{M^-}, h_{M^+}, h_T, Γ_L, Γ_M, Γ_T, k_{M^+}, k_{M^-}, k_{L^+}, k_{L^-}, x_{SL}, x_L and x_M. These variables will be used to describe the solutions of the regions described previously. We will also use these variables to determine the spreading and thinning rates not known *a priori*. We obtain x_M by locating where the fluid height first changes curvature from concave down to concave up for $x < 0$ and the fluid height at this position is denoted by h_{M^-}. The minimum surfactant concentration in region I is used to determine Γ_M. h_{M^+} is calculated by determining the drop height where the drop changes curvature from concave up to concave down immediately after x_M and the surfactant concentration gradient at this

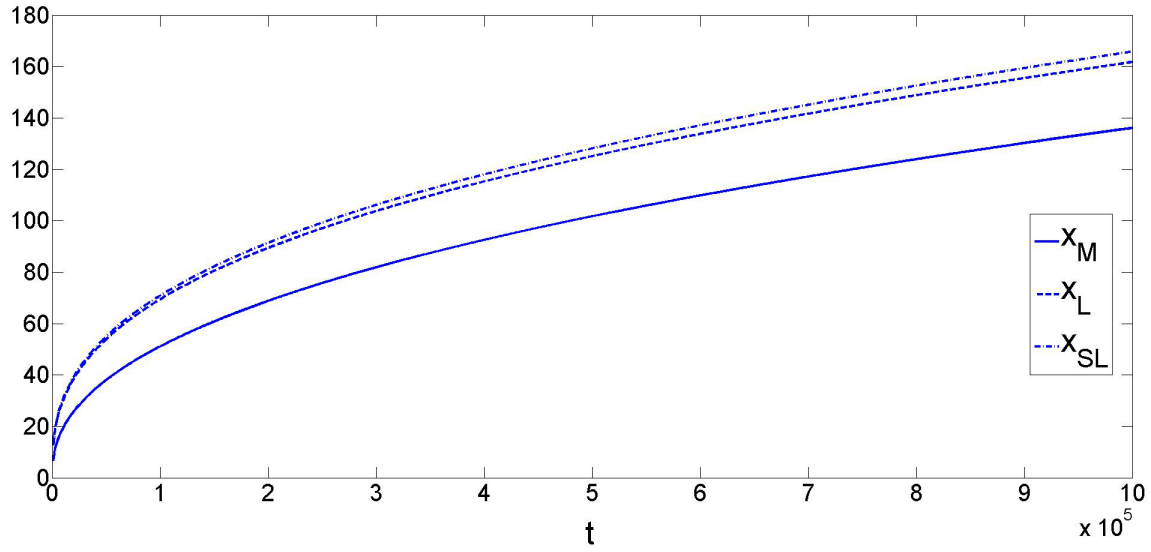

Figure 4.11: Time evolution of x_L, x_M and x_{SL} from $t = 10^3 - 10^6$.

position is k_{M^+}. The position of the 'effective' contact line is determined at the position of the global maximum surfactant concentration Γ_L and is denoted by x_L. The droplet height at the leading edge, h_{L^-}, is determined by the maximum droplet height in the absence of capillary effects. k_{L^-} is obtained by calculating the surfactant concentration gradient where $h = h_{L^-}$. The surfactant concentration gradient ahead of Γ_L is calculated by finding where the surfactant concentration gradient remains constant ahead of Γ_L and is denoted by k_{L^+}. The location of the leading edge of the downstream fluid front is obtained by satisfying $\Gamma(x_{SL}) = 10^{-5}$. Hence x_{SL} is calculated by finding where $\Gamma < 10^{-5}$ ahead of $\Gamma = \Gamma_L$. x_T is the location of the global minimum of fluid height. The fluid height at this position is denoted by h_T. The local maximum surfactant concentration at $x = x_T$ is denoted by Γ_T. Figures 4.10-4.15 show the evolution of all the variables obtained from $t = 10^3 - 10^6$. All variables, except x_L and Γ_L, obtained have been done so using numerical simulations without capillary effects this allows for

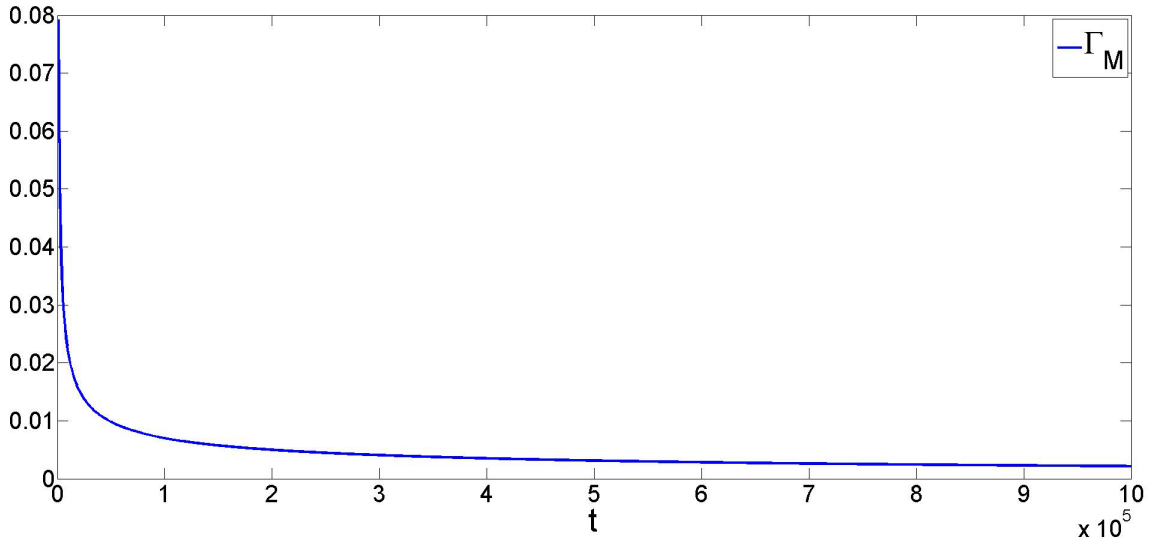

Figure 4.12: Time evolution of Γ_M from $t = 10^3 - 10^6$.

easier calculation of these variables. Figures 4.10-4.15 show the time evolution of the charecteristic variables.

We will now discuss each region in turn, neglecting hereafter the effects of surfactant diffusion. The vertical component of gravity is also neglected everywhere except in the capillary ridge region where it appears as a second-order diffusion term smoothing the capillary ridge. Surface tension effects are negligible everywhere except regions A and B. Where possible we obtain the scalings for each region based upon the competing physical mechanisms. We use the numerical solution of the PDE's shown in Fig 4.3 to illustrate the locally self-similar structure by showing that the data collapses when rescaled using scalings appropriate to each region. We also use this data to validate any assumptions made in the analysis. From these solutions we will derive an approximate DAE (Differential-Algerbraic Equation) model describing the evolution of the system.

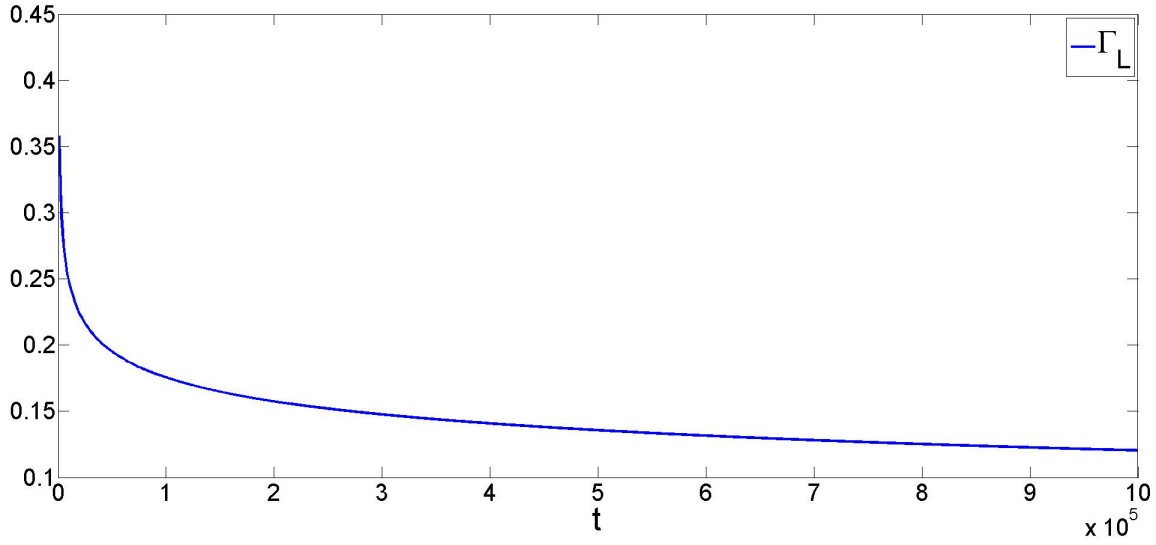

Figure 4.13: Time evolution of Γ_L from $t = 10^3 - 10^6$.

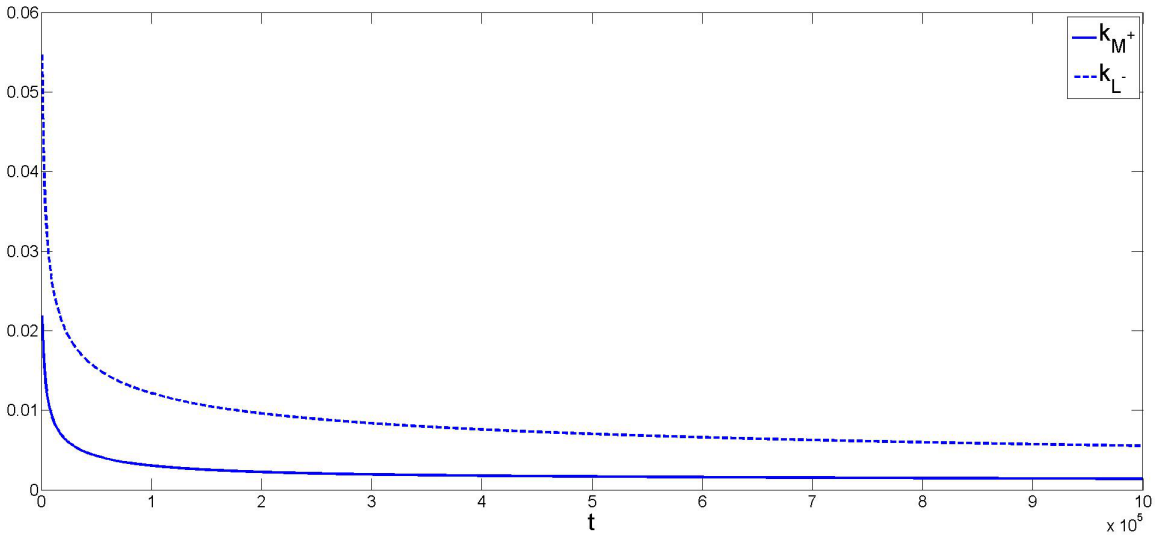

Figure 4.14: Time evolution of k_{L^-} and k_{M^+} from $t = 10^3 - 10^6$.

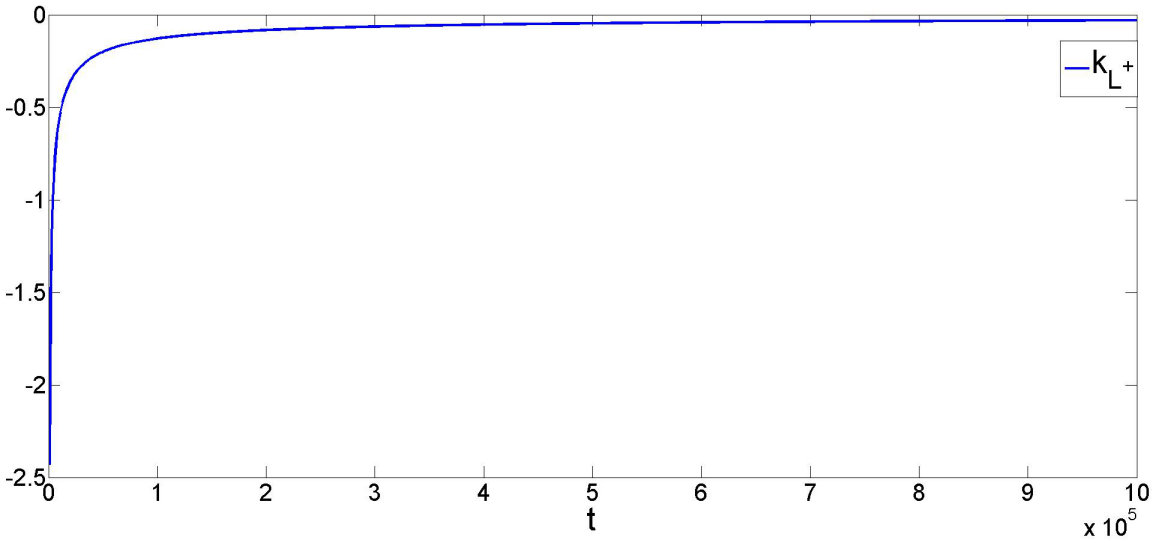

Figure 4.15: Time evolution of k_{L^+} from $t = 10^3 - 10^6$.

4.3.1 Region I: The main bulk fluid droplet

This long region between $x_T(t) \leq x \leq x_M(t)$ contains the majority of the spreading droplet. The surfactant concentration is relatively constant. The dominant spreading mechanism is due to the horizontal component of gravity. There is little contribution from the Marangoni terms except near the near $x = x_T(t)$ and $x = x_M(t)$. We neglect capillary and the vertical component of gravity to approximate the PDE's as,

$$h_t + \frac{1}{3}(h^3)_x - M\frac{1}{2}(h^2\Gamma_x)_x = 0, \tag{4.52}$$

$$\Gamma_t + \frac{1}{2}(\Gamma h^2)_x - M(h\Gamma\Gamma_x)_x = 0. \tag{4.53}$$

Writing $\Gamma(x,t) = \Gamma_M(t) + \hat{\Gamma}(x,t)$, $|\hat{\Gamma}| \ll \Gamma_M$; gives at leading order in $\hat{\Gamma}/\Gamma_M$,

$$h_t + \left[\frac{h^3}{3} - \frac{1}{2}Mh^2\hat{\Gamma}_x\right]_x = 0 \tag{4.54}$$

$$\frac{\dot{\Gamma}_M}{\Gamma_M} + \left[\frac{1}{2}h^2 - Mh\hat{\Gamma}_x\right]_x = 0. \tag{4.55}$$

Integrating Eq. (4.55) and applying the boundary conditions $h = h_T$, $\hat{\Gamma}_x = 0$ at $x = x_T$, gives the surfactant flux,

$$\frac{1}{2}h^2\Gamma_M - Mh\Gamma_M\hat{\Gamma}_x = -\dot{\Gamma}_M(x - x_T) + \frac{1}{2}h_T^2\Gamma_M. \tag{4.56}$$

Re-arranging Eq. (4.56) and substitute into Eq. (4.54) gives the evolution equation of the drop height,

$$h_t + \frac{1}{12}(h^3)_x + \left[-\frac{1}{2}\frac{\dot{\Gamma}_M}{\Gamma_M}(x - x_T)h + \frac{1}{4}h_T^2 h \right]_x = 0. \tag{4.57}$$

Equation (4.57) has a solution,

$$h(x,t) = \frac{h_{M^-}}{\sqrt{x_M}}\sqrt{x - x_T + \frac{x_M h_T^2}{h_{M^-}^2}}, \tag{4.58}$$

if the following compatibility conditions are satisfied (as well as assuming $\dot{x}_T \approx 0$ i.e., pinning the droplet's trailing edge which is confirmed by numerical results):

$$V_1 = \frac{\dot{x}_M}{h_{M^-}^2} = \frac{1}{3}, \tag{4.59}$$

$$V_2 = -\frac{\dot{\Gamma}_M x_M}{\Gamma_M h_{M^-}^2} = \frac{1}{2} \tag{4.60}$$

$$V_3 = -\frac{\dot{h}_T}{h_T}\frac{x_M}{\dot{x}_M} = \frac{3}{2} \tag{4.61}$$

Figure 4.16 shows that the above conditions are approximately satisfied at late times. The solution obtained (assuming $x_T, h_T \approx 0$) is the same as that derived by Huppert [27]; Troian *et al.* [63] for gravity-driven spreading of a droplet. Substituting Eq. (4.58) into Eq. (4.56) and then applying Eqs. (4.59-4.61), we obtain $\hat{\Gamma}_x = 0$, implying that $\Gamma(x,t) = \Gamma_M(t)$ in this region. Figure 4.17(a,b) show the numerical solutions shown in Fig. 4.3 to collapse in this region when rescaling h by h_{M^-}, Γ by Γ_M and x by

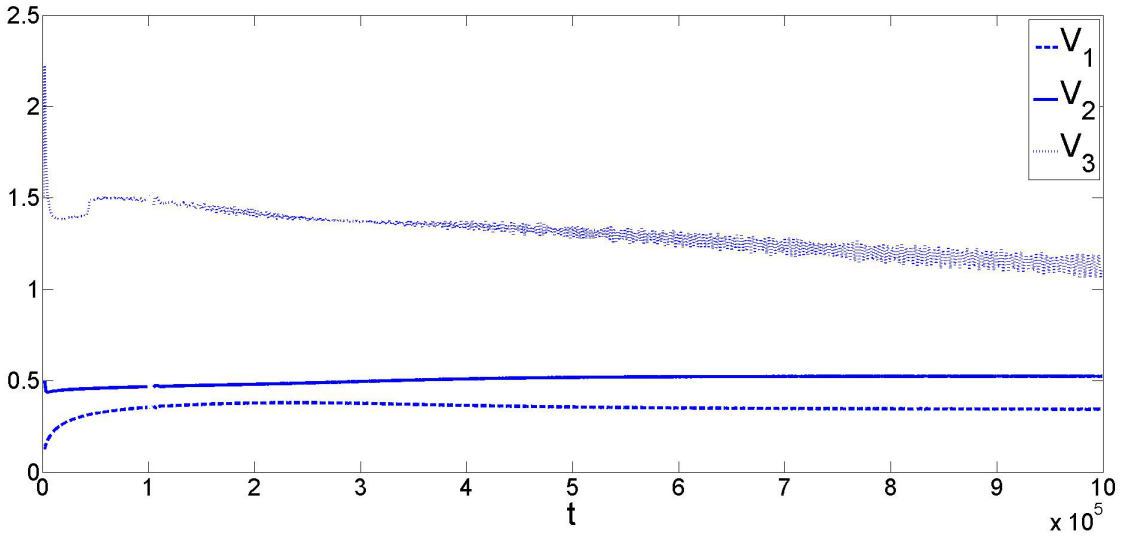

Figure 4.16: $V_1 = \dot{x}_M/h_{M^-}^2$, $V_2 = -(\dot{\Gamma}_M x_M)/(\Gamma_M h_{M^-}^2)$, $V_3 = -\frac{\dot{h}_T}{h_T}\frac{x_M}{\dot{x}_M}$ versus time.

x_M. The similarity solution for h (dashed line) given by Eq. (4.58) and $\Gamma = \Gamma_M$ have good agreement with the rescaled numerical solutions. Figure 4.17(b) shows that the rescaled numerical solutions lie close to Γ_M except that Γ is non-uniform especially at $x = x_T$ (where Γ decreases as x increases) and at $x = x_M$ (where Γ increases as x decreases). We will now describe the behaviour of the solution near the trailing edge of the bulk droplet ($x = x_T$). The above linearised analysis is not valid here since the change in Γ from Γ_M are appreciable (see Fig. 4.17(b)) and does not allow any meaningful approximation to be made. However, a qualitative understanding can be obtained as follows. Integrating Eq. (4.53) and applying the boundary conditions $h = h_T$, $\Gamma = \Gamma_T > \Gamma_M$, $\Gamma_x = 0$ at $x = x_T$ gives the Marangoni surfactant flux

$$-Mh\Gamma\Gamma_x = -\int_{x_T}^{x} \Gamma_t dx + \frac{1}{2}(h_T^2\Gamma_T - h^2\Gamma). \tag{4.62}$$

The contribution from the unsteady term is positive since $\Gamma_t < 0$ for all x and this dominates the horizontal component of gravity near $x = x_T$ resulting in positive Marangoni surfactant flux. For this to occur $\Gamma_x < 0$ of Γ decreases. As x gets larger, the negative contribution from the horizontal gravity increases (due to h increasing) offsetting the positive contribution from the unsteady term resulting in the Marangoni surfactant flux to become zero there and $\Gamma = \Gamma_M$, as described by the linearised analysis above. We also note that the derivatives of h become large as $x \to x_T$, therefore capillary terms need to be included to regularise the solution. This suggests the existence of an inner region where capillary and Marangoni forces compete. This region is not discussed in this thesis. Next, we analyse region C to describe the evolution h and Γ near $x = x_M$.

4.3.2 Region C

This is a short region near $x = x_M$ that connects the main bulk drop to the fluid 'hump' region. There is an abrupt jump in drop height, from h_{M^-} to h_{M^+}, and surfactant concentration gradient, from k_{M^-} to k_{M^+} (see Fig. 4.3(a,b)). This is due the Marangoni forces opposing the horizontal component of gravity, impeding the flow downward but not reversing it resulting in an accumulation of fluid and the formation of a shock like structure. We will now derive the conditions ensuring continuity of fluid and surfactant flux in this region assuming Γ is continuous across this region and $k_{M^-} \approx 0$. We consider a moving frame of reference about $x = x_M$ travelling with speed $\dot{x}_M$. We denote $h|_{x=x_{M^-}} = h_{M^-}$, $h|_{x=x_{M^+}} = h_{M^+}$, $\Gamma_x|_{x=x_{M^-}} = k_{M^-} \approx 0$ and $\Gamma_x|_{x=x_{M^+}} = k_{M^+} > 0$.

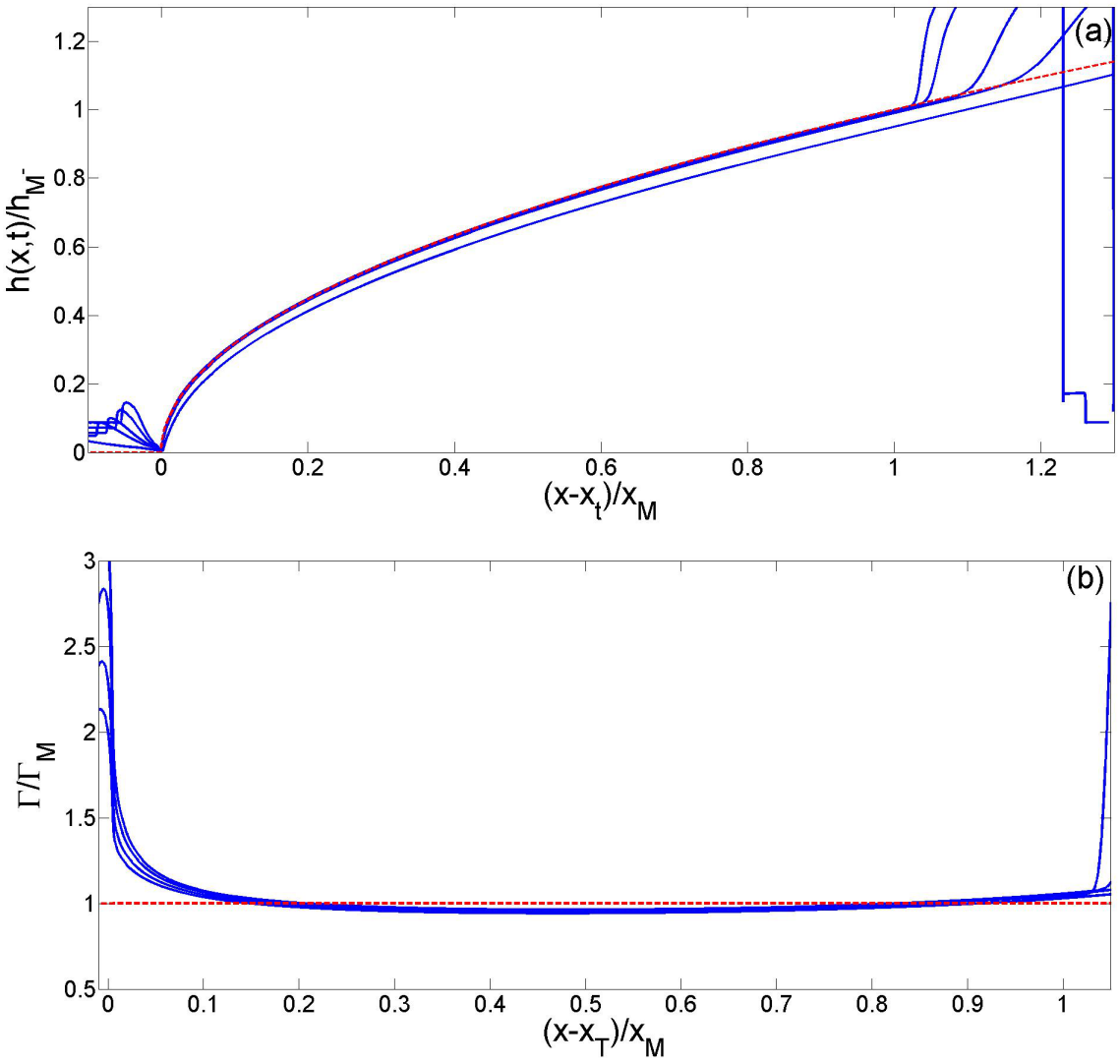

Figure 4.17: The evolution of (a) h and (b) Γ in region I using the data shown in Fig. 4.3. The dashed lines show the similarity solutions for h given by Eq. (4.58) and $\Gamma(x,t) = \Gamma_M(t)$.

We neglect the horizontal component of gravity and capillary terms in the following analysis as the lengthscale of this region is long enough for these effects to be negligible at leading order. Equations (4.43,4.44) can be written as,

$$h_t - \dot{x}_M h_x + \left[\frac{h^3}{3} - M\frac{h^2}{2}\Gamma_x\right]_x = 0, \tag{4.63}$$

$$\Gamma_t - \dot{x}_M \Gamma_x + \left[\frac{\Gamma h^2}{2} - Mh\Gamma\Gamma_x\right]_x = 0. \tag{4.64}$$

Integrating Eq. (4.63) with respect to x across $x = x_M$ gives,

$$-\dot{x}_M [h]_-^+ + \left[\frac{h^3}{3} - M\frac{h^2}{2}\Gamma_x\right]_-^+ = 0, \text{ which implies,}$$

$$\dot{x}_M = \frac{1}{3}(h_{M^+}^2 + h_{M^+}h_{M^-} + h_{M^-}^2) - M\frac{h_{M^+}^2 k_{M^+}}{2(h_{M^+} - h_{M^-})}, \tag{4.65}$$

which ensures continuity of fluid flux across $x = x_M$. Similarly integrating Eq. (4.64) across $x = x_M$ gives,

$$\left[\frac{\Gamma h^2}{2} - Mh\Gamma\Gamma_x\right]_-^+ = 0, \text{ which implies,}$$

$$k_{M^+} = \frac{h_{M^+}^2 - h_{M^-}^2}{2Mh_{M^+}}, \tag{4.66}$$

which ensures continuity of surfactant flux across $x = x_M$. We have assumed $k_{M^-} \approx 0$ above. Figures (4.18,4.19) test the validity of Eqs. (4.65,4.66) using numerical values; the agreement is good at late times.

To describe the approximate solution in this region, we assume $\Gamma_t \approx \dot{\Gamma}_M$. Substituting

this into Eq. (4.44) and integrating (neglecting capillary and vertical gravity) using $h = h_{M^-}$, $\Gamma = \Gamma_M$ and $\Gamma_x = k_{M^-} \approx 0$ at $x = x_M$ gives

$$\frac{1}{2}h^2\Gamma - Mh\Gamma\Gamma_x = -\dot{\Gamma}_M(x - x_M) + \frac{1}{2}h_{M^-}^2\Gamma_M. \tag{4.67}$$

Rearranging and substituting this into Eq. (4.43) (neglecting capillary and vertical gravity) gives

$$h_t + \frac{1}{12}(h^3)_x + \left[-\frac{1}{2}\frac{\dot{\Gamma}_M}{\Gamma}(x - x_M)h + \frac{1}{4}\frac{h_{M^-}^2\Gamma_M}{\Gamma}h\right]_x = 0. \tag{4.68}$$

In Fig. 4.20 we test the assumption $\Gamma_t \approx \dot{\Gamma}_M$ the surfactant flux $\frac{1}{2}h^2\Gamma - Mh\Gamma\Gamma_x$, obtained using numerical solutions (solid lines) to that from Eq. (4.67) (dashed lines) at times (a) $t = 10^5$, (b) $t = 5\times10^5$ and (c) $t = 10^6$. We observe that the approximation is reasonably accurate around $x = x_M$ (considering x_M is defined numerically quite arbitrarily) but breaks down further away from $x = x_M$. We were unable to obtain an analytical solution for Eqs. (4.67,4.68). However Eq. (4.67) can be considered as a quadratic equation for h in terms of Γ and can be solved to obtain,

$$h(x,t) = M\Gamma_x + \sqrt{(M\Gamma_x)^2 - \left[2\frac{\dot{\Gamma}_M}{\Gamma}(x - x_M) - \frac{\Gamma_M h_{M^-}^2}{\Gamma}\right]}. \tag{4.69}$$

Upstream of this region where $\Gamma_x \approx 0$ (or $\Gamma \approx \Gamma_M$) we obtain (using Eq. (4.60))

$$h(x,t) = \sqrt{-\frac{\dot{\Gamma}_M}{\Gamma_M}(x - x_M) + h_{M^-}^2} = \frac{h_{M^-}}{\sqrt{x_M}}\sqrt{x}, \tag{4.70}$$

which matches the solution in Region I.

Figure 4.21 shows a comparison between the numerical results for h (solid lines) and Eq. (4.70) (dashed lines) in this region for times (a) $t = 10^5$, (b) $t = 5 \times 10^5$ and (c) $t = 10^6$. We use the numerical solutions for Γ, Γ_x while computing the approximation for h in Eq. (4.69). We observe that Eq. (4.70) is a very good approximation for h around $x = x_M$. Further away from $x = x_M$ the approximation although over estimating h, captures the gross behaviour, particularly the jump in h, even though Eq. (4.67) breaks down here. This suggests that although the flow and surfactant transport in this region are unsteady, it is the positive jump in Γ_x that causes the positive jump in h. Since Γ_t can no longer be approximated by $\dot{\Gamma}_M$ further away from $x = x_M$ this necessitates the introduction of another region (region II) even though the essential physics in both regions are the same. We will consider this region next.

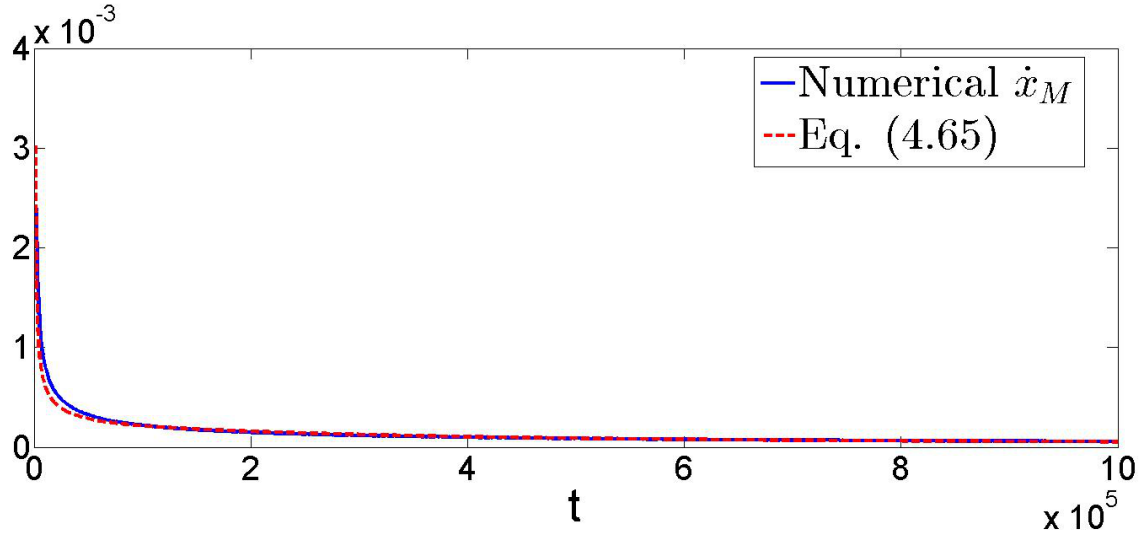

Figure 4.18: Testing the validity of ($\dot{x}_M$) obtained numerically (solid line) with that obtained from Eq. (4.65) (dashed line).

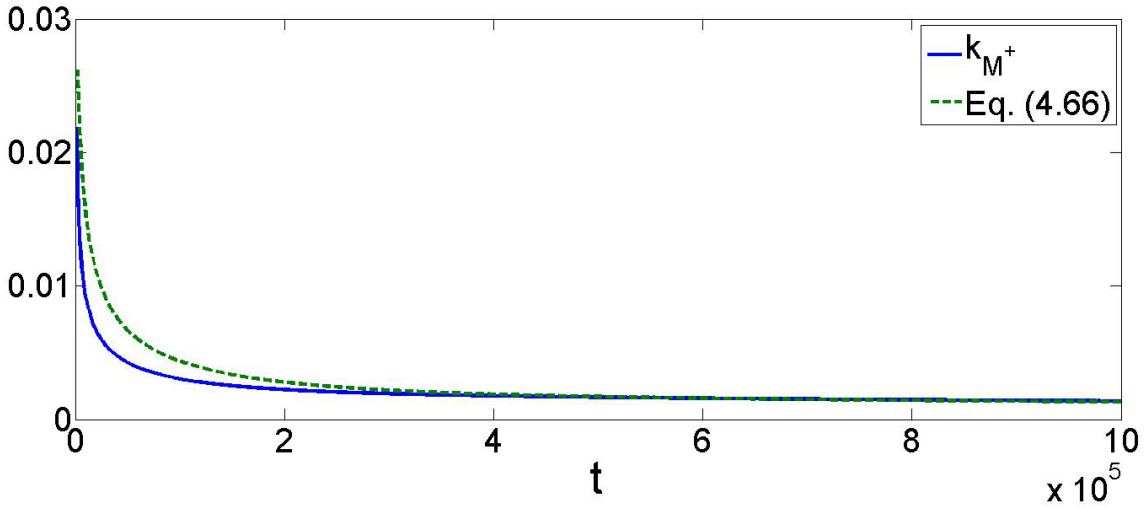

Figure 4.19: Testing the validity of k_{M^+} obtained numerically (solid line) with that obtained from Eq. (4.66) (dashed line).

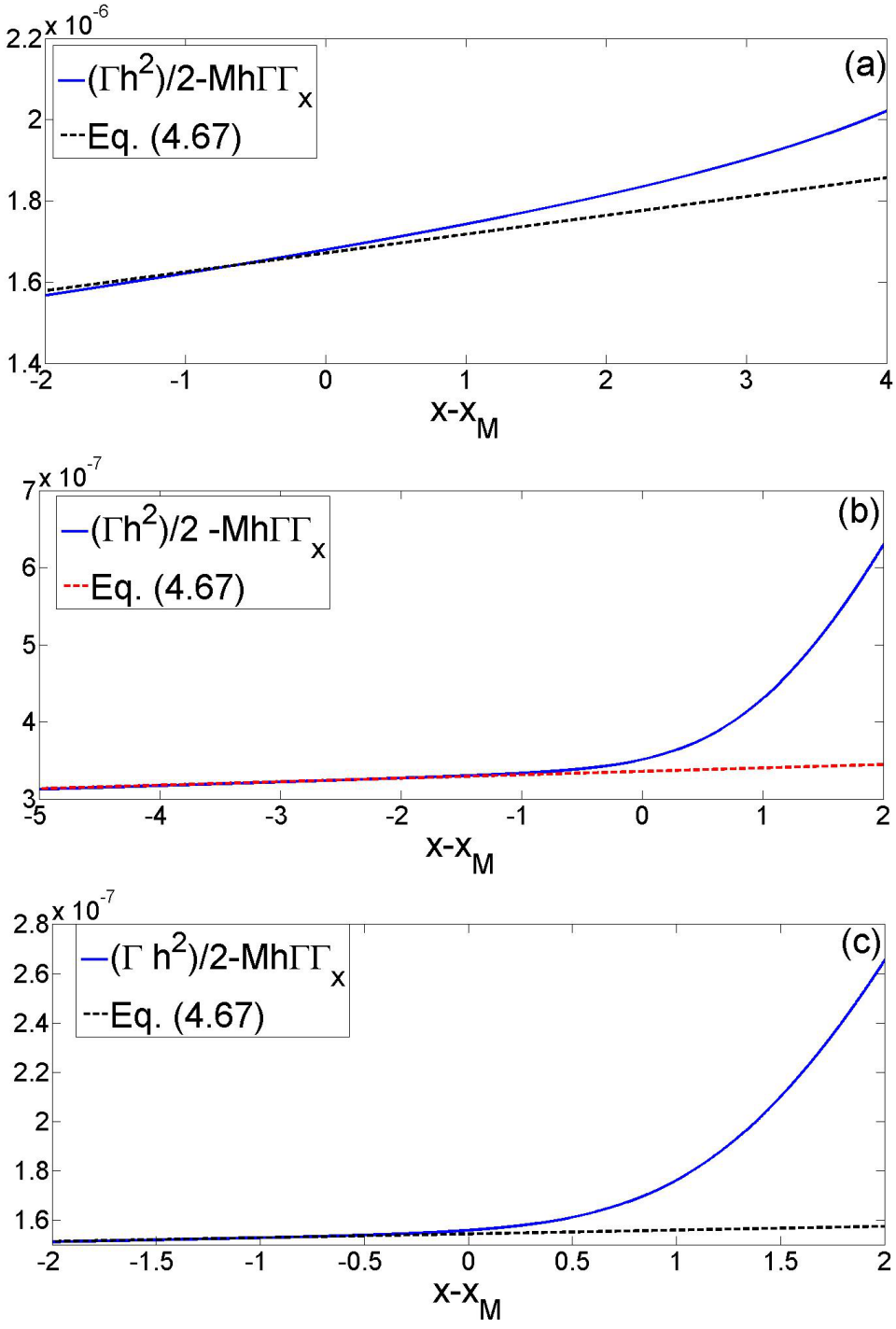

Figure 4.20: Testing the validity of the assumption that $\Gamma_t \approx \dot{\Gamma}_M$ in region C by comparing the surfactant flux obtained numerically (solid lines) to that obtained from Eq. (4.67) (dashed line) at times (a) $t = 10^5$, (b) $t = 5 \times 10^5$ and (c) $t = 10^6$.

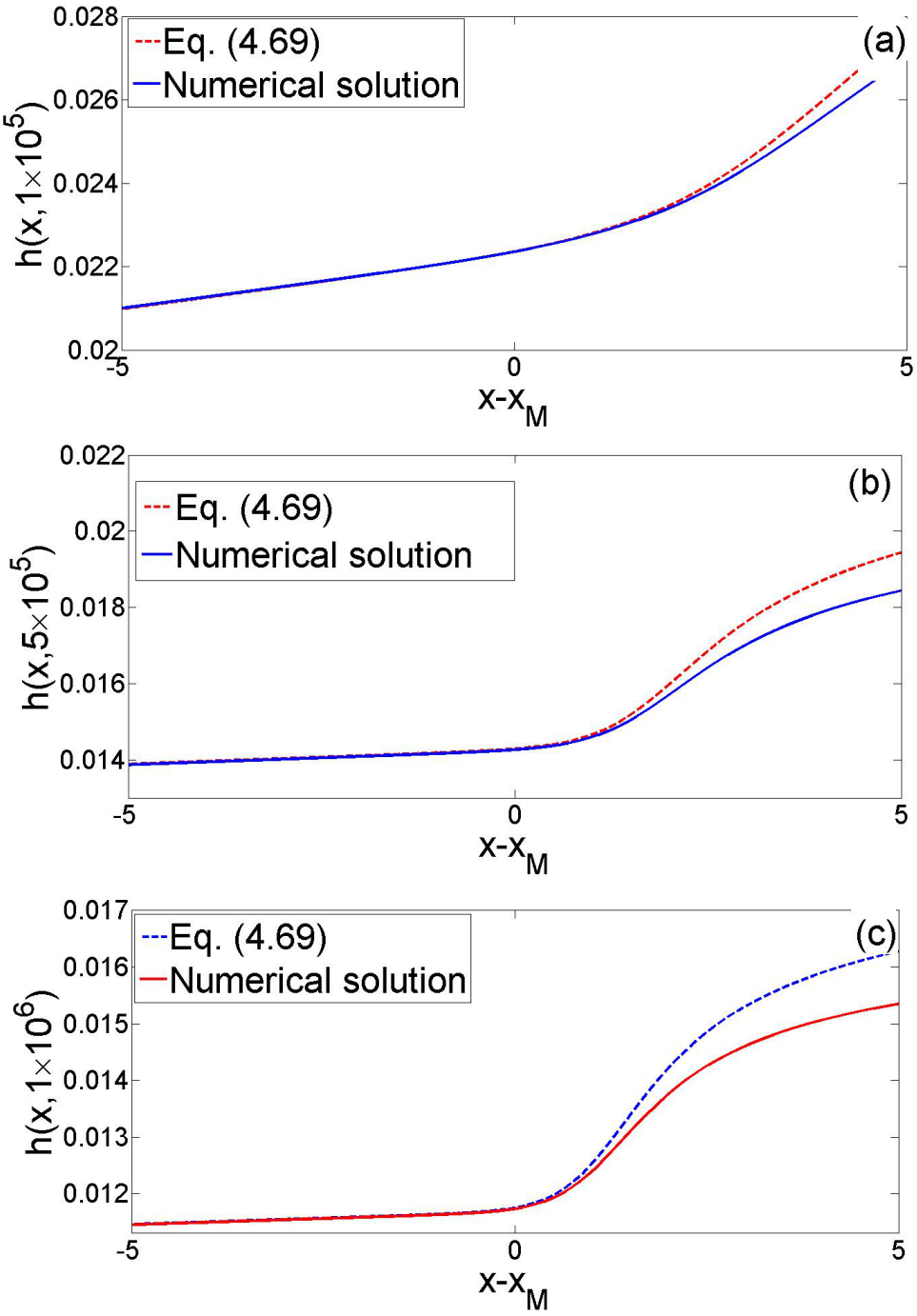

Figure 4.21: Comparing the numerical solution for h in region C (solid lines) with the approximation in Eq. (4.70) (dashed lines) at times (a) $t = 10^5$, (b) $t = 5 \times 10^5$ and (c) $t = 10^6$.

4.3.3 Region II: The fluid 'hump' region.

This region is part of the bulk droplet in $x_{M^+}(t) \leq x \leq x_L(t)$ where the fluid upwells due to competeing reverse Marangoni and horizontal gravity fluxes resulting in fluid accumulation and hump-like region is formed. There is a rapid increase in the surfactant concentration (from Γ_M to Γ_L), h varies between h_{M^+} to h_{L^-} and Γ_x varies between k_{M^+} and k_{L^-}. Taking Eq. (4.53) and integrating (neglecting capillary and vertical gravity) applying the conditions that $h = h_{M^+}$, $\Gamma = \Gamma_M$ and $\Gamma_x = k_{M^+}$ at $x = x_{M^+}$ we obtain,

$$\frac{h^2}{2}\Gamma - Mh\Gamma\Gamma_x = -\int_{x_{M^+}}^{x} \Gamma_t dx + \frac{\Gamma_M h_{M^-}^2}{2} - Mh_{M^-}\Gamma_M k_{M^+}. \tag{4.71}$$

Rearranging and substituting into Eq. (4.52) gives,

$$h_t + \frac{1}{12}(h^3)_x + \left[\frac{h}{2\Gamma}\left(-\int_{x_{M^+}}^{x} \Gamma_t dx + \frac{\Gamma_M h_{M^-}^2}{2} - Mh_{M^-}\Gamma_M k_{M^+}\right)\right]_x = 0 \tag{4.72}$$

Equations (4.71,4.72) prove difficult to solve analytically. However Eq. (4.71) is a quadratic equation for h, solving which we obtain,

$$h = M\Gamma_x + \sqrt{(M\Gamma_x)^2 + \frac{2}{\Gamma}\left(\int_{x_M}^{x} \Gamma_t dx + \frac{\Gamma_M h_{M^-}^2}{2} - Mh_{M^-}\Gamma_M k_{M^+}\right)}. \tag{4.73}$$

Equation (4.71) is the surfactant flux over this region. As we saw previously the surfactant flux to the left of this region was derived in Eq. (4.67), which had good agreement up to a point then the numerical solution deviates from the analytical solution obtained.

We therefore have to modify this equation. The integral in Eq. (4.73) is evaluated using a linear approximations of Γ_t by taking $\Gamma_t|_{x=x_{M^+}} = \dot{\Gamma}_M$ and $\Gamma_t|_{x=x_L} = \dot{\Gamma}_L$. We take

$$\Gamma_t \approx \left[\frac{\dot{\Gamma}_L - \dot{\Gamma}_M}{x_L - x_M}\right](x - x_M) + \dot{\Gamma}_M. \tag{4.74}$$

Substituting Eq. (4.74) into Eqs. (4.71,4.73) gives

$$\begin{aligned}\frac{h^2}{2}\Gamma - Mh\Gamma\Gamma_x = \quad & -\frac{1}{2}\left[\frac{\dot{\Gamma}_L - \dot{\Gamma}_M}{x_L - x_M}\right](x - x_M)^2 - \dot{\Gamma}_M(x - x_M) \\ & + \frac{1}{2}h_{M^-}^2\Gamma_M,\end{aligned} \tag{4.75}$$

which we can solve as a quadratic equation for h to obtain

$$\begin{aligned}h(x,t) \;=\; & \sqrt{(M\Gamma_x)^2 - \frac{1}{\Gamma}\left[\left(\frac{\dot{\Gamma}_L - \dot{\Gamma}_M}{x_L - x_M}\right)(x - x_M)^2 - h_{M^-}^2\left(\frac{x - x_M}{x_M} + 1\right)\Gamma_M\right]} \\ & + M\Gamma_x.\end{aligned} \tag{4.76}$$

Figures 4.22(a,b,c) show the numerically obtained surfactant flux in this region with the approximate surfactant flux obtained from Eq. 4.75) at (a) $t = 1 \times 10^5$, (b) $t = 5 \times 10^5$ and (c) $t = 1 \times 10^6$. We can see that there is deviation from the numerically obtained surfactant flux. This indicates that there is a need for a better approximation to the integral in Eq. (4.72). We cannot obtain a better approximation currently as to obtain a quadratic approximation, for Γ_t, we would have to have the evolution of another

characteristic variable of Γ in this region. However we use the linear approximation for the time derivative and the numerical solution for Γ and Γ_x in Eq. (4.73) to determine the approximate drop height h in this region. Figure 4.23 shows that, despite the weak approximation of Γ_t, Eq.(4.73) has good agreement with the numerical solution at late time. The solution becomes a better match as time increases. We believe that a more refined approximation of the integral involving Γ_t in Eq. (4.76) would make the agreement much better. Region C and II indicate that the approximation to Γ_t has only a corrective effect on the shape of the fluid profile. The Γ_x terms are the major contributors to the fluid profile.

Evaluating Eq. (4.76) at $x = x_L$ we obtain,

$$h_{L^-} = Mk_{L^-} + \sqrt{(Mk_{L^-})^2 - \frac{1}{\Gamma_L}\left((\dot{\Gamma}_L - \dot{\Gamma}_M)(x_L - x_M) - \frac{h_{M^-}^2 x_L \Gamma_M}{x_M}\right)}. \quad (4.77)$$

Figure 4.24 shows the numerically obtained h_{L^-} to that obtained from Eq. (4.77). It can be seen that there is reasonable agreement between the two especially at late time. We will now explore the 'effective' contact line region at the leading edge of the droplet which contains the capillary ridge.

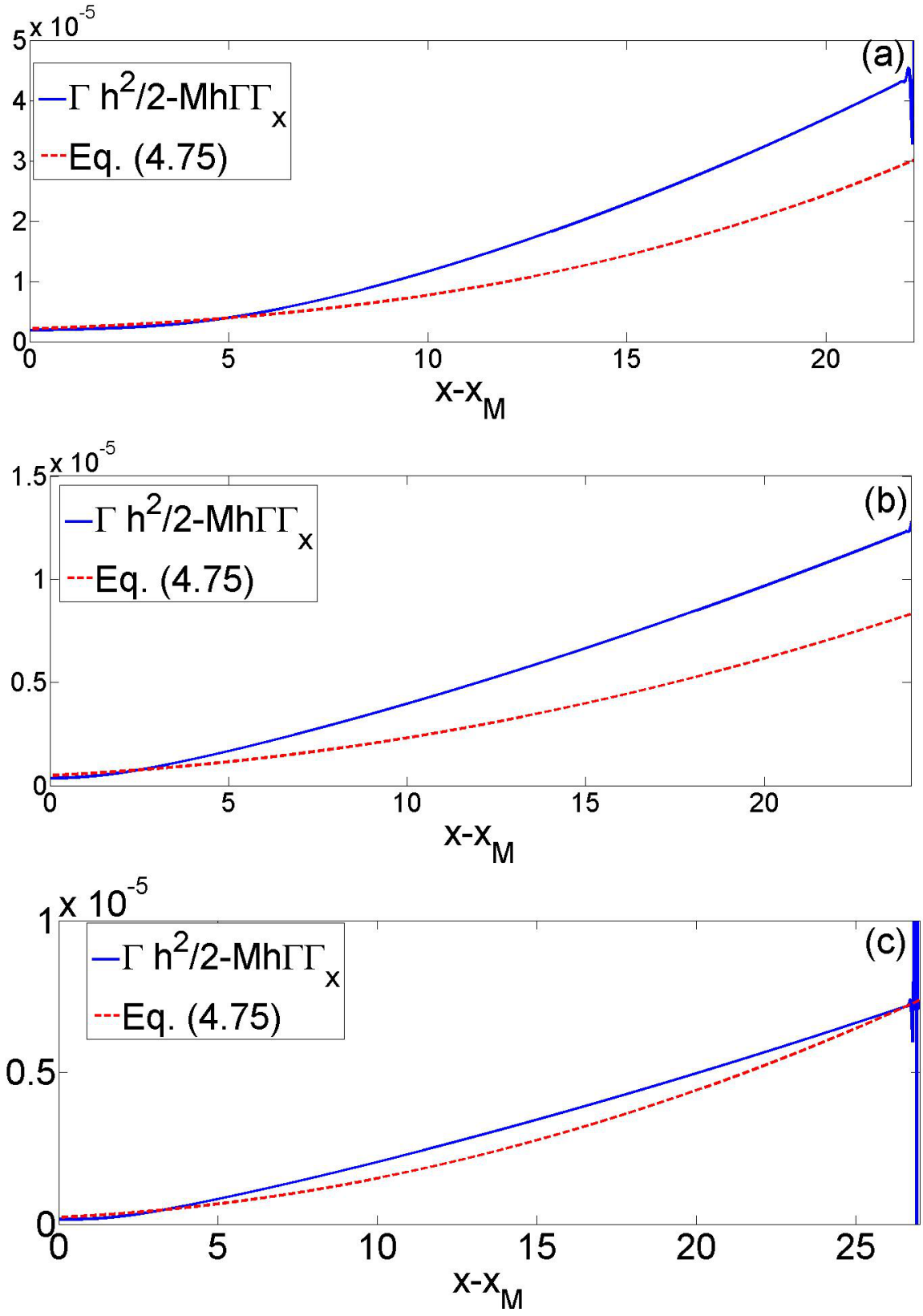

Figure 4.22: Comparing the numerically obtained surfactant flux in this region to Eq. (4.72) and approximating $\dot{\Gamma}$ with a linear approximation with $\Gamma_t|_{x=x_{M^+}} = \dot{\Gamma}_M$ and $\Gamma_t|_{x=x_L} = \dot{\Gamma}_L$ at (a) $t = 1 \times 10^5$, (b) $t = 5 \times 10^5$ and (c) $t = 1 \times 10^6$.

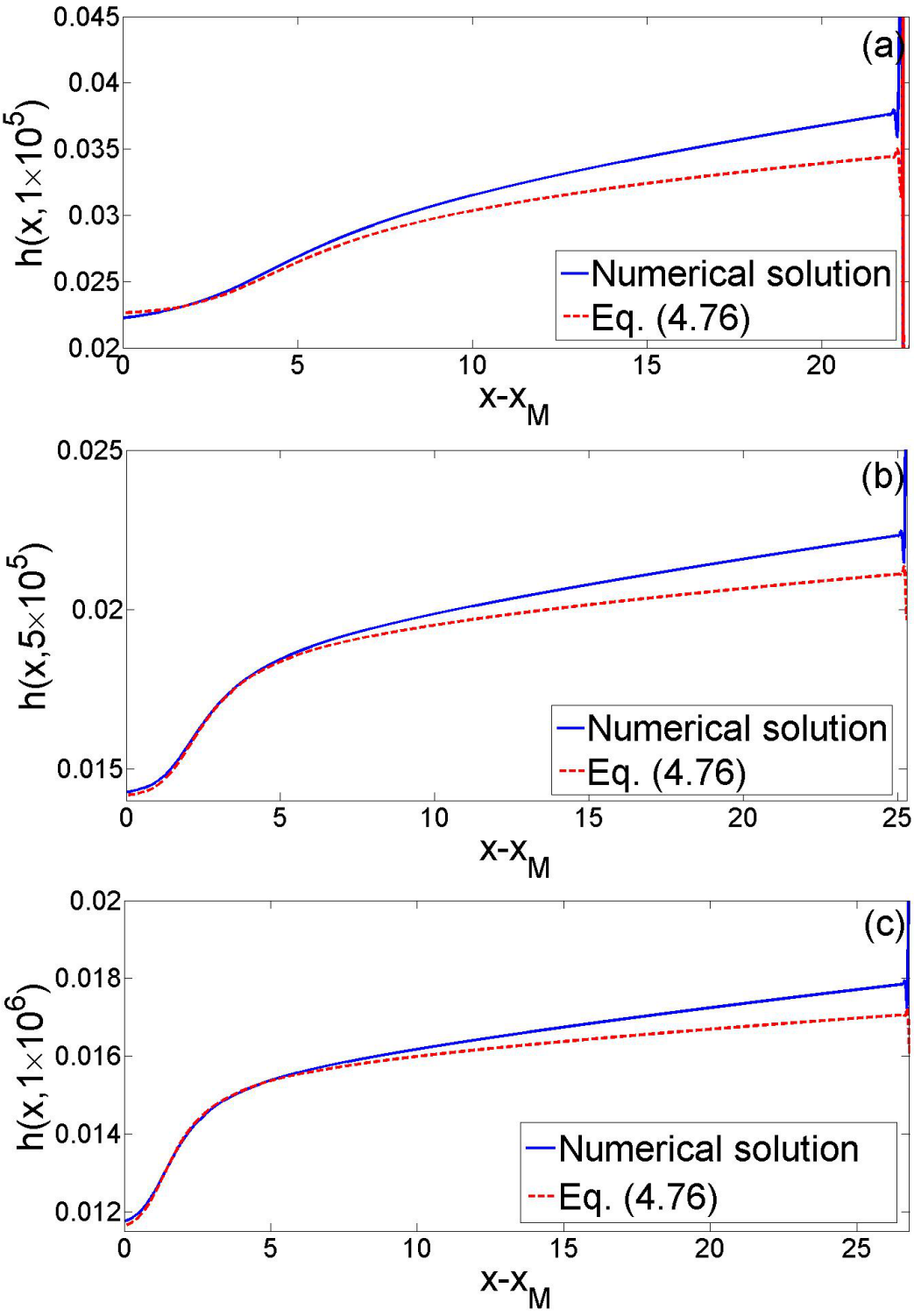

Figure 4.23: Comparing the numerically obtained fluid profile in this region to Eq. (4.73) using numerically obtained Γ and Γ_x and$\Gamma_t|_{x=x_{M^+}} = \dot{\Gamma}_M$ and $\Gamma_t|_{x=x_L} = \dot{\Gamma}_L$ at (a) $t = 1 \times 10^5$, (b) $t = 5 \times 10^5$ and (c) $t = 1 \times 10^6$.

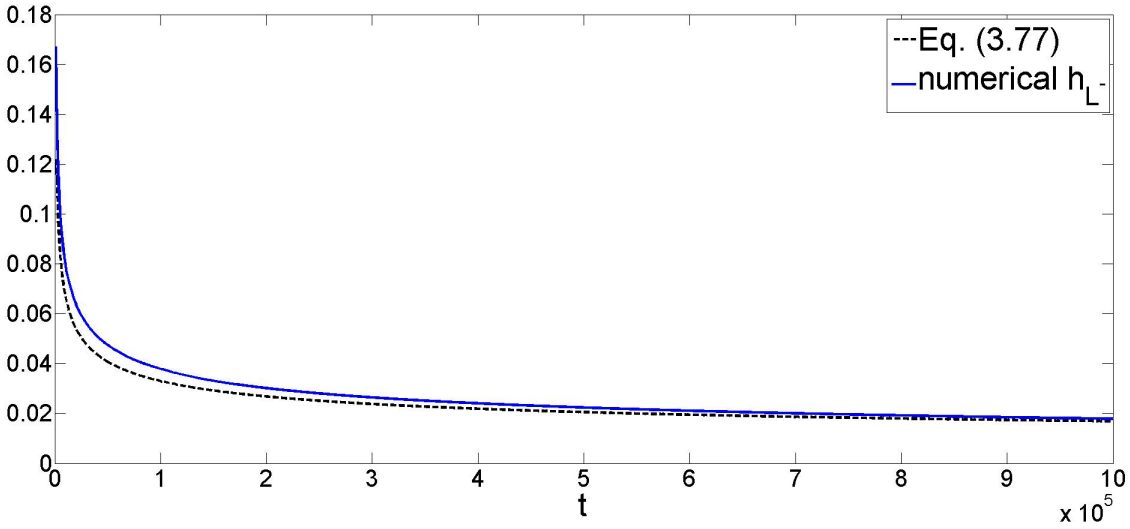

Figure 4.24: Comparing the numerically obtained h_{L^-} (solid line) to that obtained in Eq. (4.77) (dashed line).

4.3.4 Region A: The 'effective" contact line region ahead of the main droplet

This region includes the capillary ridge and connects to the fluid front (region III) ahead of it and connects to the fluid 'hump' region (region II). The length scale of this region, X (say), is obtained by balancing capillary effects with the horizontal component of gravity. Hence,

$$X = (Cah_{L^-})^{1/3}. \tag{4.78}$$

Balancing the horizontal component of gravity with the Marangoni term we obtain $\Gamma_x \sim h_{L^-}/M$, so $\Gamma \sim Ca^{1/3} {h_{L^-}}^{4/3}/M \ll \Gamma_L$. We then set

$$h(x,t) = h_{L^-} H(\xi), \quad x = x_L + (Cah_{L^-})^{1/3}\xi, \quad \Gamma = \Gamma_L + \frac{Ca^{1/3} {h_{L^-}}^{4/3}}{M} G(\xi). \tag{4.79}$$

Figures 4.25(a,b) show a family of quasi-steady solution when the numerical solution in Figs. 4.3(a,b) is scaled using these variables. We now derive an approximate solution for this region. Substituting the above scalings into Eqs. (4.43,4.44) and assuming the solution to be quasi-steady (i.e. assuming $\dot{h_{L^-}} \approx 0$), we obtain,

$$-\hat{V} H_\xi = \left[-\frac{H^3}{3} H_{\xi\xi\xi} + \frac{H^2}{2} G_\xi - \frac{H^3}{3} + \hat{D}(\theta) \frac{H^3}{3} H_\xi \right]_\xi, \tag{4.80}$$

$$0 = \left[-\frac{H^2}{2} H_{\xi\xi\xi} + H G_\xi - \frac{H^2}{2} + \hat{D}(\theta) \frac{H^2}{2} H_\xi \right]_\xi, \tag{4.81}$$

subject to the boundary (or matching) conditions that,

$$H \to 1,\ H_\xi, H_{\xi\xi\xi} \to 0,\ \ G_\xi \to k^- \ \text{ as } \ \xi \to -\infty, \tag{4.82}$$

$$H \to \frac{h_{L^+}}{h_{L^-}} = s(t),\ \ H_\xi, H_{\xi\xi\xi} \to 0,\ \ G_\xi \to k^+ \text{as } \ \xi \to \infty \tag{4.83}$$

where $\hat{V} = \dfrac{\dot{x}_L}{h_{L^-}^2}$ is a dimensionless contact line speed, $\hat{D}(\theta) = (\epsilon \cot(\theta) h_{L^-}^{2/3})/(Ca^{1/3})$, $k^- = Mk_{L^-}/h_{L^-}$ and $k^+ = Mk_{L^+}/h_{L^-}$. Equations (4.82,4.83) assumes that h is constant far upstream and downstream where it matches onto regions II and III, respectively. This is reasonable considering that h in both these regions is only very weakly linear (see Figs 4.23(a,b,c), 4.27(a)). Γ is linear matching onto regions II and III with slope $k_{L^-}(> 0)$ and $k_{L^+}(< 0)$, respectively. While this matching condition is approximate for the fluid 'hump' region, it is exact when matching onto the fluid front since Γ is linear there (see region III description). After integrating Eq. (4.81) and applying the boundary conditions in Eq. (4.82) one obtains,

$$HG_\xi = \left(k^- - \frac{1}{2}\right) + \frac{H^2}{2} H_{\xi\xi\xi} + \frac{H^2}{2} - \hat{D}(\theta)\frac{H^2}{2} H_\xi. \tag{4.84}$$

After integrating Eq. (4.80) and applying both Eq. (4.84) and the boundary conditions in Eq. (4.83) one obtains,

$$\frac{H^3}{12}\left[H_{\xi\xi\xi} + 1 - \hat{D}(\theta) H_\xi\right] = \frac{1}{2}\left(k^- - \frac{1}{2}\right)[H - s(t)] + \hat{V}[H - s(t)] + \frac{s(t)^3}{12}. \tag{4.85}$$

Applying the boundary conditions in Eq. (4.82) to Eq. (4.85), we obtain

$$\hat{V} = \frac{1}{12}(1 + s + s^2) - \frac{1}{2}(k^- - \frac{1}{2}). \tag{4.86}$$

This ensures continuity of fluid flux across this region. Substitution of the above equation into Eq. (4.85) and rearranging for $H_{\xi\xi\xi}$ one obtains,

$$H_{\xi\xi\xi} = -\left[\frac{s^2 + s}{H^3}\right] + \left[\frac{1 + s + s^2}{H^2}\right] + \hat{D}(\theta)H_\xi - 1. \tag{4.87}$$

Substitution of Eq. (4.87) into Eq. (4.84) gives,

$$G_\xi = \frac{1}{H}\left(k^- - \frac{1}{2}\right) - \frac{1}{2H^2}(s^2 + s) + \frac{1}{2H}(s^2 + s + 1). \tag{4.88}$$

Applying the boundary conditions in Eq. (4.83) to Eq. (4.88), we obtain a relationship between k^+ and k^-,

$$k^- - sk^+ = \frac{1}{2}(1 - s^2). \tag{4.89}$$

This ensures continuity of surfactant flux across this region. Hence, we have simplified in this region the complex set of PDE's to a single third order ODE for H (Eq. (4.87)) and a first order ODE for G (Eq. (4.88)). Equation (4.87) is the same as the equation for the leading edge region for the gravity-driven problem (Eq. (2.75)) and can be solved numerically in the same way. Equation (4.88) can be numerically integrated after substituting the numerical solution for H. The constant arising from this integration is

chosen such that $G(0) = 0$ (since by definition $\xi = 0$ is where G has a maximum). The dashed lines in Fig. 4.25(a,b) show the numerical Eqs. (4.87,4.88), for $s = 0.1$, $k^- = 0.3153$, $k^+ = -1.797$ and $\hat{V} = 0.18485$. The choice of the value of these parameters equates to 'fixing' time, so to obtain the full family of solutions we can vary these parameters accordingly. It can be seen that they have good agreement with the family of quasi-steady solutions shown. We note that the location where Γ is maximum (i.e. $\Gamma = \Gamma_L$) is slightly offset to the right of the capillary ridge (see Figs. 4.25(a,b)). Equation (4.86) can be rewritten using Eq. (4.89) as,

$$\hat{V} = \frac{1}{3}(1 + s + s^2) - \frac{1}{1-s}\left(\frac{1}{2}k^- - \frac{1}{2}s^2 k^+\right). \tag{4.90}$$

We can write Eq. (4.90) in original variables as,

$$\dot{x}_L = \frac{h_{L^-}^2}{3}\left(1 + \frac{h_{L^+}}{h_{L^-}} + \frac{h_{L^+}^2}{h_{L^-}^2}\right) + \frac{M}{h_{L^-} - h_{L^+}}\left(-\frac{1}{2}h_{L^-}^2 k_{L^-} + \frac{1}{2}h_{L^+}^2 k_{L^+}\right). \tag{4.91}$$

We can also write Eq. (4.89) in its original variables as,

$$M\left[h_{L^-}k_{L^-} - h_{L^+}k_{L^+}\right] = \frac{1}{2}(h_{L^-}^2 - h_{L^+}^2) \tag{4.92}$$

Equation (4.91) shows how competing effects of the horizontal component of gravity (first bracket) and Marangoni fluxes ahead and behind the contact line (second bracket) alter the speed of the contact line. The forward Marangoni flux term is trying to increase the speed of the contact line where as the reverse Marangoni flux is trying to

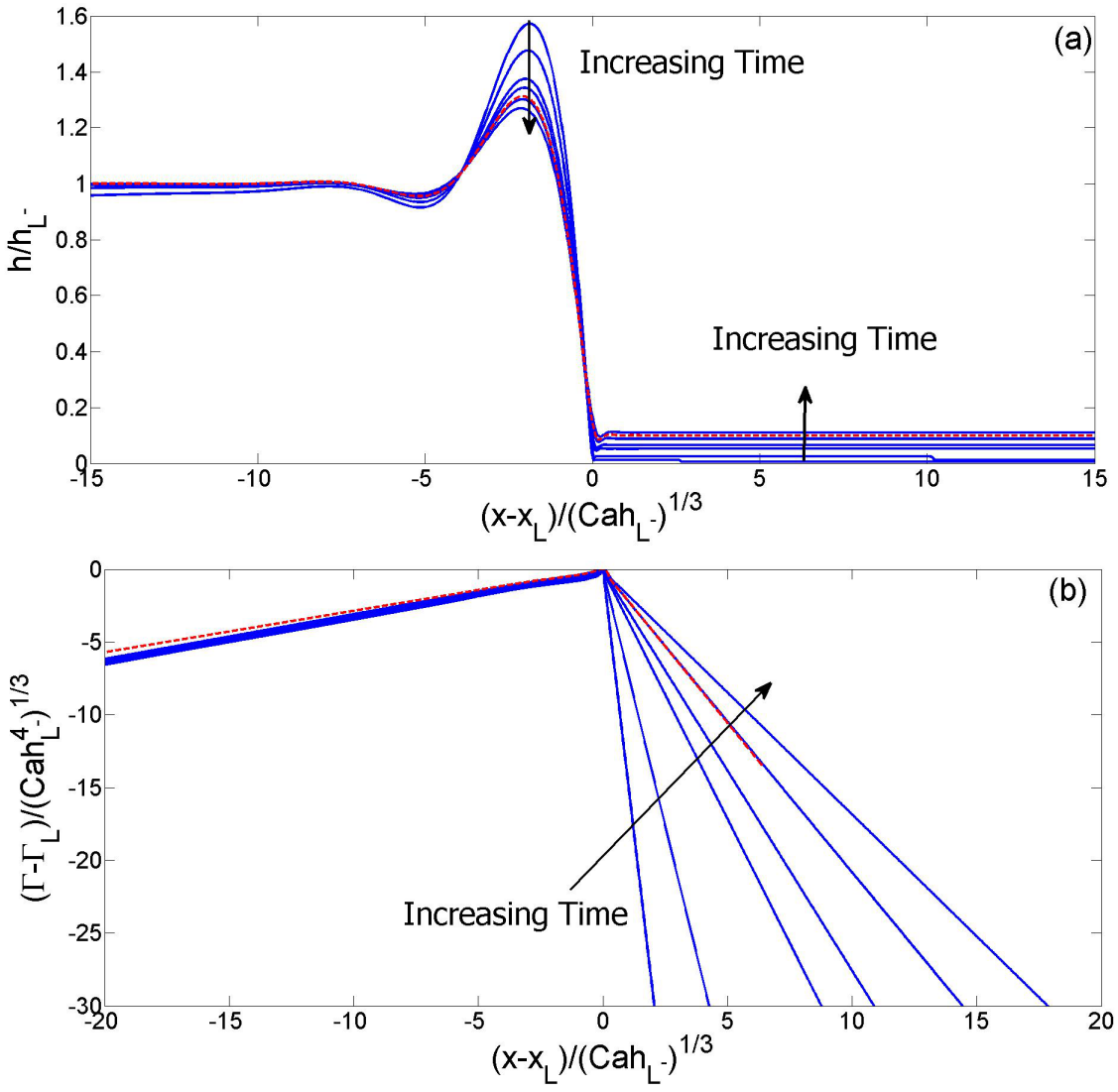

Figure 4.25: Evolution of (a) h and (b) Γ in region A using data from Fig. 4.3 rescaled using Eq. (4.79). The dashed lines show the solution to Eqs. (4.87,4.88) for or $s = 0.1$, $k^- = 0.3153$, $k^+ = -1.797$ and $\hat{V} = 0.18485$.

slow the flow by drawing fluid out of the 'effective' contact line. The reverse Marangoni is the dominant term and hence the speed of the 'effective' contact line is impeded with the inclusion of surfactant when compared to gravity-driven flow alone. Figure 4.26 shows the comparison between the numerically computed $\dot{x}_L$ and that obtained from Eq. (4.91) which are indistinguishable.

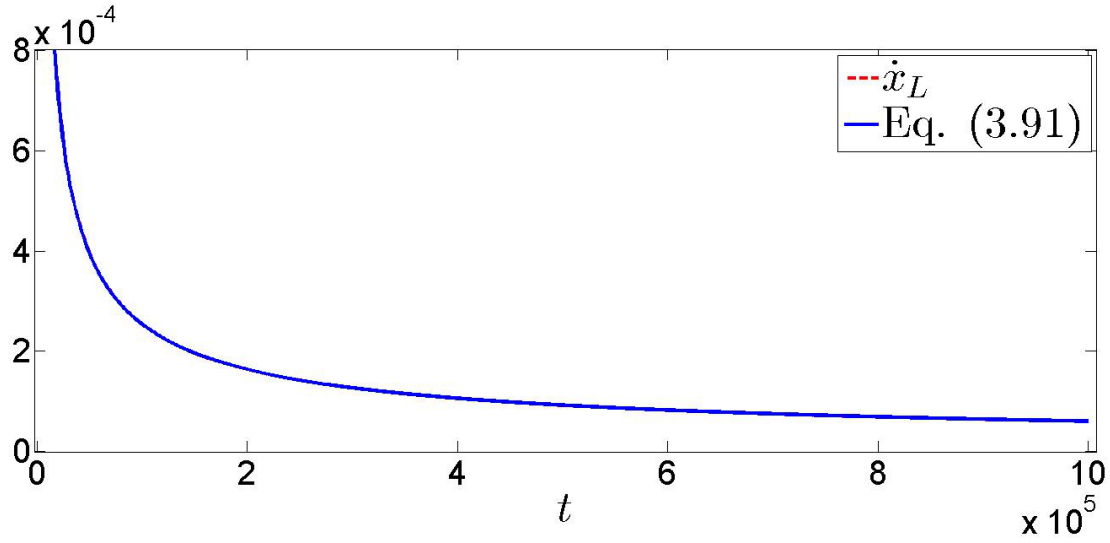

Figure 4.26: Testing the validity of $\dot{x}_L$ obtained numerically (solid line) with that obtained from Eq. (4.91)(dashed line). The two curves are indistinguishable.

4.3.5 Region III: Fluid front region.

This region includes the spreading fluid front in $x_L(t) \leq x \leq x_{SL}(t)$. The lengthscale of this region is $x_{SL} - x_L$. The flow in this region is predominantly controlled by Marangoni forces. The height of the fluid front is $o(b)$, hence forces due to gravity are of magnitude $o(b^3)$ and are small in comparison to Marangoni forces. Balancing convective and Marangoni forces $\dot{x}_{SL} h_x \sim M(h^2\Gamma_x)_x$ implies $\Gamma_x \sim \frac{\dot{x}_{SL}}{Mb}$. Hence, $\Gamma \sim \frac{\dot{x}_{SL}(x_{SL}-x_L)}{Mb}$ across this region. Note $x_{SL} > x_L$ for all t. We then set,

$$x = x_{SL} + (x_{SL} - x_L)\xi, \quad h(x,t) = bH(\xi), \quad \Gamma = \frac{\dot{x}_{SL}(x_{SL} - x_L)}{Mb} G(\xi). \tag{4.93}$$

Figure 4.27(a,b) show the numerical solution for thes region to collapse under these

scalings. Substitution into Eqs. (4.43,4.44), we obtain at leading order

$$H_\xi \left[-\xi(1-\gamma)-\gamma\right] + \left[-\frac{1}{2}H^2 G_\xi\right]_\xi = 0, \tag{4.94}$$

$$G\left[\alpha\alpha_1 + 1 - \gamma\right] + G_\xi\left[-\xi(1-\gamma)-\gamma\right] + \left[-HGG_\xi\right]_\xi = 0, \tag{4.95}$$

where $\gamma = \frac{\dot{x}_L}{\dot{x}_{SL}}$, $\alpha = \frac{x_{SL}\ddot{x}_{SL}}{\dot{x}_{SL}^2}$, $\alpha_1 = 1 - \frac{x_L}{x_{SL}}$. Assuming,

$$\gamma = \frac{\alpha\alpha_1}{2} + 1, \tag{4.96}$$

reduces Eq. (4.95) to,

$$\frac{\alpha\alpha_1}{2}G + G_\xi\left[\frac{\alpha\alpha_1}{2}\xi - (\frac{\alpha\alpha_1}{2}+1)\right] - \left[HGG_\xi\right]_\xi = 0. \tag{4.97}$$

Figure 4.28 compares γ obtained numerically to that in Eq. (4.96). There is good agreement with the noise in data attributed to approximations to the derivatives involved in the relevant variables. Integrating Eq. (4.97) then applying the boundary conditions $G = 0$, $H = 2$ at $\xi = 1$ we obtain

$$\alpha\alpha_1\xi G - (\alpha\alpha_1 + 2)G - 2HGG_\xi = 0. \tag{4.98}$$

We then rearrange Eq. (4.98) for HG_ξ to obtain,

$$HG_\xi = \frac{\alpha\alpha_1}{2}\xi - \frac{\alpha\alpha_1 + 2}{2} \tag{4.99}$$

Substituting the above into Eq. (4.94) to obtain,

$$\frac{\alpha\alpha_1}{4}(\xi H_\xi) - \left[\frac{\alpha\alpha_1 + 2}{4}\right] H_\xi - \frac{\alpha\alpha_1}{4} H = 0. \Rightarrow \tag{4.100}$$

$$\alpha\alpha_1(\xi H_\xi) - (\alpha\alpha_1 + 2)H_\xi - \alpha\alpha_1 H = 0. \tag{4.101}$$

Integrating Eq. (4.101) and using the boundary condition $H = 2$ at $\xi = 1$ we obtain

$$H(\xi) = 2\left[\frac{\xi - A}{1 - A}\right], \tag{4.102}$$

where $A = 1 + 2/(\alpha\alpha_1)$. Numerical results (in Fig. 4.29) shows that A is large and negative with $A \approx -50$(the noise in the data is attributed to the numerical approximation in computing the derivatives involved). We then substitute Eq. (4.102) into Eq. (4.99) to obtain

$$G_\xi = -\frac{1}{2}. \tag{4.103}$$

Integrating and applying the boundary condition $G = 0$ at $\xi = 1$ we obtain,

$$G(\xi) = -\frac{1}{2}(\xi - 1). \tag{4.104}$$

Figure 4.27(a,b) show the above similarity solutions for H and G, depicted by dashed lines, overlaid on the numerical solutions rescaled using the scalings in Eq. (4.93). It can be seen that there is good agreement with the rescaled numerical simulations. We note that since A is large and negative so the slope of h is small and positive, hence

$h \approx 2b$ in this region which makes it appear to look like a 'step'.

Then, to leading order, as $x \to x_L^+$ we obtain

$$\Gamma_L = \frac{\dot{x}_{SL}(x_{SL} - x_L)}{2Mb}, \tag{4.105}$$

$$k_{L^+} = -\frac{\dot{x}_{SL}}{2Mb}. \tag{4.106}$$

$$h_{L^+} = 2b \tag{4.107}$$

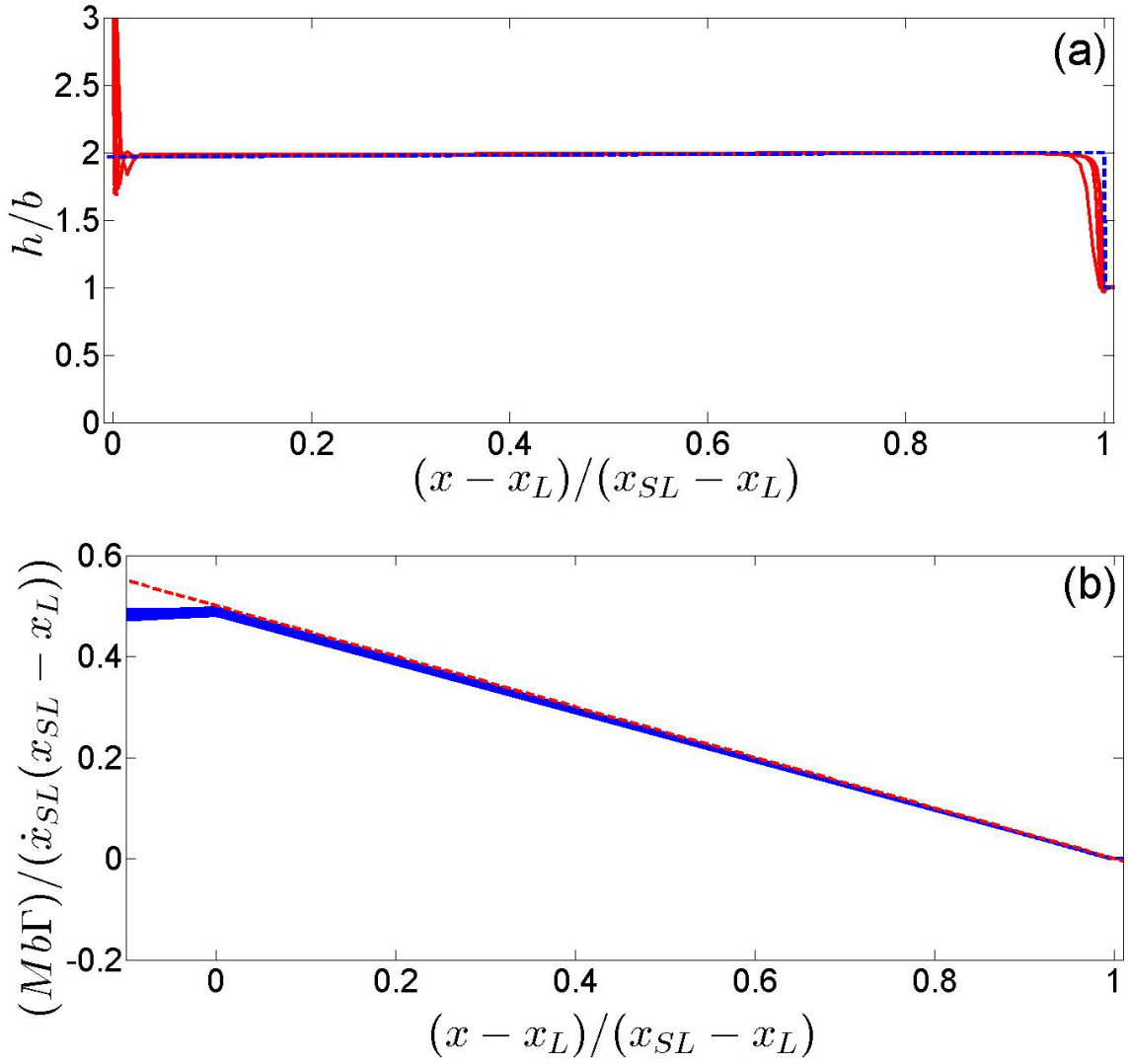

Figure 4.27: Evolution of (a)h and (b)Γ region III using data from Fig. 4.3 and scalings from Eq. (4.93). The dashed line is the similarity solution for H using Eq. (4.102) and G using Eq. (4.104).

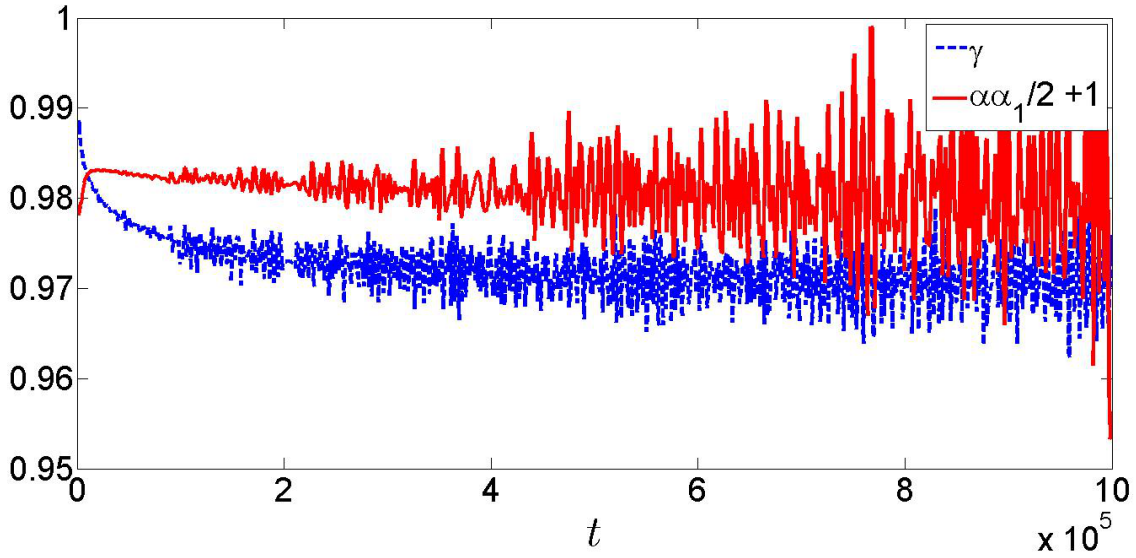

Figure 4.28: Comparison between γ obtained from the numerical solution to that assumed in Eq. 4.96.

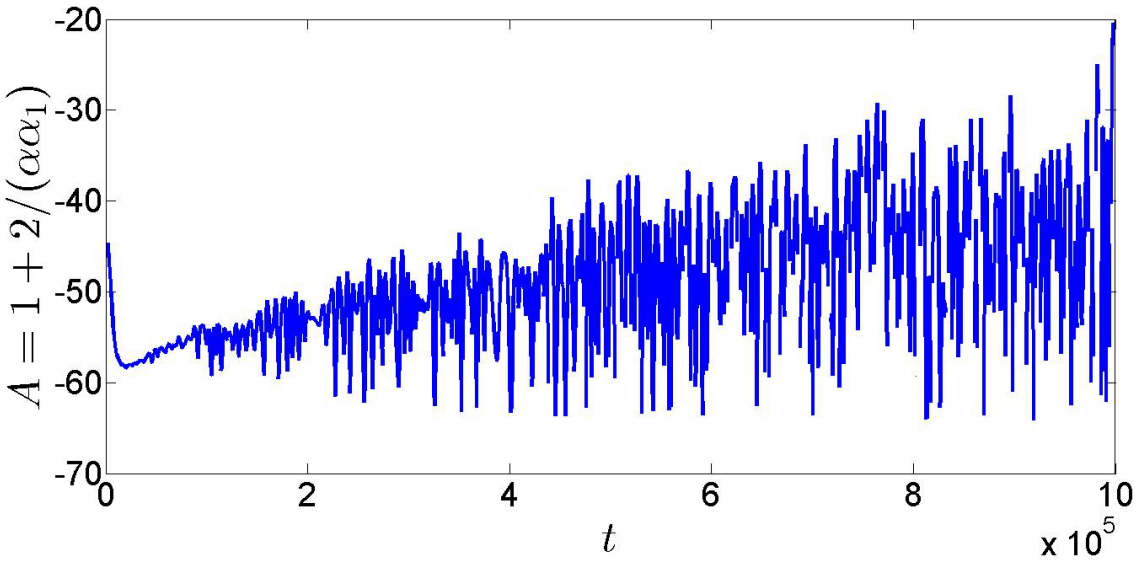

Figure 4.29: Evolution of $A = 1 + 2/(\alpha\alpha_1)$ with time.

4.3.6 Region B: Kinematic shock region

A kinematic shock-like structure at the leading edge of region III which is 'smoothened' in comparison to the analytical solution (see Fig. (4.27)). The structure of this kinematic shock near $x = x_{SL}$ has been described in detail by (Jensen and Grotberg [30]; Jensen and Halpern [31]; Jensen [29]) and is not discussed here. In the parameter regime relevant here, the discontinuity in the film thickness is smoothed by capillary effects and the jump in the surfactant gradient is smoothed by surface diffusion, but the region remains dynamically passive.

4.3.7 Region IV: Precursor film region

This is the precursor film region. This region remains undisturbed far upstream of the spreading droplet and is dynamically passive.

We will now derrive a differential-algebraic equation (DAE) model to obtain the time dependence of the characteristic variables.

4.4 Differential-Algebraic equation (DAE) model of the evolution of the characteristic variables: spreading and thinning rates

We now derive an approximate DAE model to determine the time evolution of the characteristic variables. Using which we dervive the spreading and thinning rates which are not known *a priori*. Each of the previously described regions are characterised by 13 quantities: h_{L^-}, h_{L^+}, h_{M^-}, h_{M^+}, Γ_L, Γ_M, k_{M^+}, k_{M^-}, k_{L^+}, k_{L^-}, x_{SL}, x_L and x_M. We have derived previously equations for ten variables Γ_M, k_{M^-}, x_M, k_{M^+}, h_{L^-}, k_{L^-}, x_L, Γ_L, k_{L^+} and h_{L^+} which are:

$$\dot{\Gamma}_M = \frac{\Gamma_M h_{M^-}^2}{2x_M}, \tag{4.108}$$

$$k_{M^-} = 0, \tag{4.109}$$

$$\dot{x}_M = \frac{1}{3}(h_{M^+}^2 + h_{M^+}h_{M^-} + h_{M^-}^2) - M\frac{h_{M^+}^2 k_{M^+}}{2(h_{M^+} - h_{M^-})}, \tag{4.110}$$

$$k_{M^+} = \frac{h_{M^+}^2 - h_{M^-}^2}{2Mh_{M^+}}, \tag{4.111}$$

$$h_{L^-} = Mk_{L^-} + \sqrt{(Mk_{L^-})^2 - \frac{1}{\Gamma_L}\left((\dot{\Gamma}_L - \dot{\Gamma}_M)(x_L - x_M) - \frac{h_{M^-}^2 x_L \Gamma_M}{x_M}\right)}, \tag{4.112}$$

$$k_{L^-} = \frac{h_{L^+}k_{L^+}}{h_{L^-}} + \frac{1}{2Mh_{L^-}}(h_{L^-}^2 - h_{L^+}^2), \tag{4.113}$$

$$\dot{x}_L = \frac{h_{L^-}^2}{3}\left(1 + \frac{h_{L^+}}{h_{L^-}} + \frac{h_{L^+}^2}{h_{L^-}^2}\right) + \frac{M(-\frac{1}{2}h_{L^-}^2 k_{L^-} + \frac{1}{2}h_{L^+}^2 k_{L^+})}{h_{L^-} - h_{L^+}}, \tag{4.114}$$

$$\Gamma_L = \frac{\dot{x}_{SL}(x_{SL} - x_L)}{2Mb}, \tag{4.115}$$

$$k_{L^+} = -\frac{\dot{x}_{SL}}{2Mb}, \tag{4.116}$$

$$h_{L^+} = 2b. \tag{4.117}$$

Equations for two of the three remaining variables are derived using the conservation of fluid volume and surfactant mass in the region $x_T \leq x < \infty$:

$$\begin{aligned} A &= \int_{x_T}^{\infty}(h-b)dx = \int_{x_T}^{x_M}(h-b)dx + \int_{x_M}^{x_L}(h-b)dx \\ &\quad + \int_{x_L}^{x_{SL}}(h-b)dx, \end{aligned} \tag{4.118}$$

$$B = \int_{x_T}^{\infty}\Gamma dx = \int_{x_T}^{x_M}\Gamma dx + \int_{x_M}^{x_L}\Gamma dx + \int_{x_L}^{x_{SL}}\Gamma dx, \tag{4.119}$$

where A and B are the total fluid volume and surfactant mass, respectively. Since we do not analytical solutions for h and Γ in region II we approximate this region as a trapezium with height h_{M^+} and surfactant concentration Γ_M at $x = x_M$ and height h_{L^-} and surfactant concentration Γ_L at $x = x_L$. Using this, Eq. (4.118)can be approximated as

$$\begin{aligned} A &\approx \int_{x_T}^{x_M}\left(\frac{h_{M^-}}{\sqrt{x-x_T}}\sqrt{x_M} - b\right)dx + \left(\frac{h_{M^+}+h_{M^-}}{2} - b\right)(x_L - x_M) \\ &\quad + \int_{x_L}^{x_{SL}}(2b-b)dx. \end{aligned} \tag{4.120}$$

We assume that here that $h_T \ll h_{M^-}$ is negligible. Upon integration we obtain,

$$A \approx \frac{2}{3}\frac{(x_M - x_T)^{3/2}h_{M^-}}{\sqrt{x_M}} + \frac{1}{2}(h_{L^-} + h_{M^+})(x_L - x_M) + b(x_{SL} - 2x_L + x_T). \tag{4.121}$$

Upon rearrangement for h_{M^+} we obtain

$$h_{M^+} \approx \frac{2A - \frac{4}{3}x_M h_{M^-} - 2b(x_{SL} - 2x_L)}{x_L - x_M} - h_{L^-} \tag{4.122}$$

We have neglected x_T here since $x_T \ll x_M$ at late times. Equation (4.119) can be approximated as

$$B \approx \int_{x_T}^{x_M} \Gamma_M dx + \frac{(\Gamma_M + \Gamma_L)}{2}(x_L - x_M) + \frac{\Gamma_L}{2}(x_{SL} - x_L) \tag{4.123}$$

Upon integration we obtain,

$$B \approx \Gamma_M x_M + \frac{(\Gamma_M + \Gamma_L)}{2}(x_L - x_M) + \frac{\Gamma_L}{2}(x_{SL} - x_L). \tag{4.124}$$

Upon substitution of Eq. (4.115) and rearrangement for $\dot{x}_{SL}$ we obtain,

$$\dot{x}_{SL} \approx \frac{4Mb\left[B - \frac{\Gamma_M}{2}(x_M + x_L)\right]}{(x_{SL} - x_L)(x_{SL} - x_M)} \tag{4.125}$$

The equation for the remaining variable h_{M^-} is derived as follows. As discussed in Section 4.3.1 region I behaves similarly to region I in the gravity-driven problem. Hence, using similarity, we can write

$$\frac{h_{M^-}}{\hat{h}_L,} = \sqrt{\frac{x_M}{\hat{x}_L}} \tag{4.126}$$

where $\hat{x}_L$ and $\hat{h}_L$ denote the position and height, respectively, of the leading edge of the droplet flowing under the influence of gravity only. Using Eqs. (2.89,2.90) for $\hat{x}_L$

and $\hat{h}_L$, we obtain,

$$h_{M^-} = \frac{3A}{2} \frac{\sqrt{x_M}}{\left[\frac{9}{4}A^2(t-t_0)\hat{x}_{L0}^3\right]^{1/2}}, \tag{4.127}$$

where $\hat{x}_{L0} = \hat{x}_L(t = t_0)$. We now have a closed system of thirteen differential-algebraic equations (DAE) parametrised by A, B, M and b. We solve these equations numerically and compare with the corresponding numerical data. The numerical simulations used $A = 4/3$, $B = 2$, $M = 1$ and $b = 10^{-3}$. Initial values for the differential equations are fitted from the numerical solution at $t_0 = 10^5$. These are used to determnine consistent initial conditions for the algebraic equations. The DAEs are solved numerically and their solution provides good approximation for the behaviour in $t > 10^5$ (solid line in Figs. 4.30-4.33) when compared to the those obtained from the numerical simulations of the PDE. We note from Fig. (4.32)(a) that the evolution of k_{M^+} and k_{L^-} is not that accurate compared to numerical data owing to the arbitrariness of which both these variables are computed numerically.

Figures 4.30-4.33 suggest a power-law behaviour at late times for the spreading and thinning rates. We extract this behaviour by plotting the evolution of the characteristic variables on a log-log plot. Figures 4.34-4.37 show that $(x_M, x_L, x_{SL}) \propto t^{1/3}$ and $(h_{L^-}, h_{M^-}) \propto t^{-1/3}$. We now attempt to derive analytically the spreading and thinning rates shown. From Eq. (4.125) that $\dot{x}_{SL} \propto \frac{1}{x_{SL}^2}$ which implies that $x_{SL} \propto t^{1/3}$. h_{M^-} and x_M are similar to the gravity-driven spreading hence are proportional to $t^{-1/3}$ and $t^{1/3}$ respectively. Equation (4.124) indicates that $\Gamma_L(x_{SL} - x_M) \propto B$, as Γ_M is relatively small and constant, which implies that $\Gamma_L \propto t^{-1/3}$. Equation (4.116) indicates that

$k_{L^+} \propto \dot{x}_{SL} \propto t^{-2/3}$. By balancing the second and third terms in Eq. (4.113) we obtain $h_{L^-} \propto k_{L^+}^{1/2} = t^{-1/3}$ then by balancing the first and third terms we obtain $k_{L^-} \propto h_{L^-} = t^{-1/3}$. Taking Eq. (4.114) and using k_{L^+}, k_{L^-} and assuming $b \ll 1$ we obtain

$$\dot{x}_L = \frac{h_{L^-}^2}{12} + \frac{\dot{x}_{SL}}{2}. \tag{4.128}$$

Therefore $\dot{x}_L \propto t^{-2/3}$ which implies $x_L \propto t^{1/3}$. Equation (4.111) indicates, by balancing terms, that $h_{M^+} \propto h_{M^-} \propto t^{-1/3}$ and also $k_{M^+} \propto h_M^+ \propto t^{-1/3}$. We cannot analytically obtain a power law behaviour for Γ_m by solving Eq. (4.108). These time dependence's match the numerically extrapolated spreading and thinning rates (see Figs. 4.34-4.37). Hence we have successfully derived the thinning and spreading rates of the spreading droplet based on volume conservation arguments for fluid and surfactant.

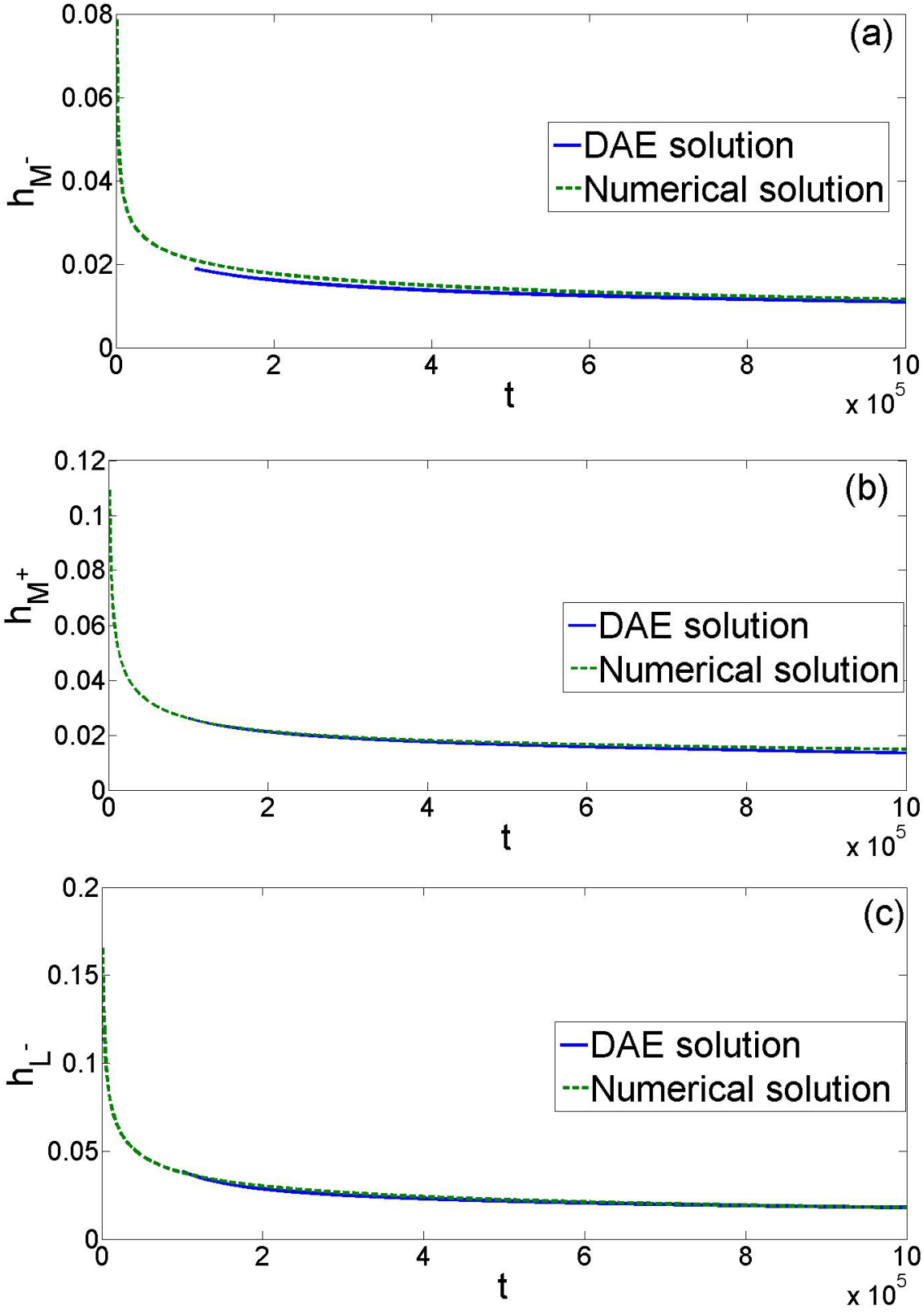

Figure 4.30: Comparing the numerically obtained fluid profile to that obtained by solving the system of DAE's for (a) h_{M^-}, (b) h_{M^+} and (c) h_{L^-} from time $t = 1 \times 10^5$.

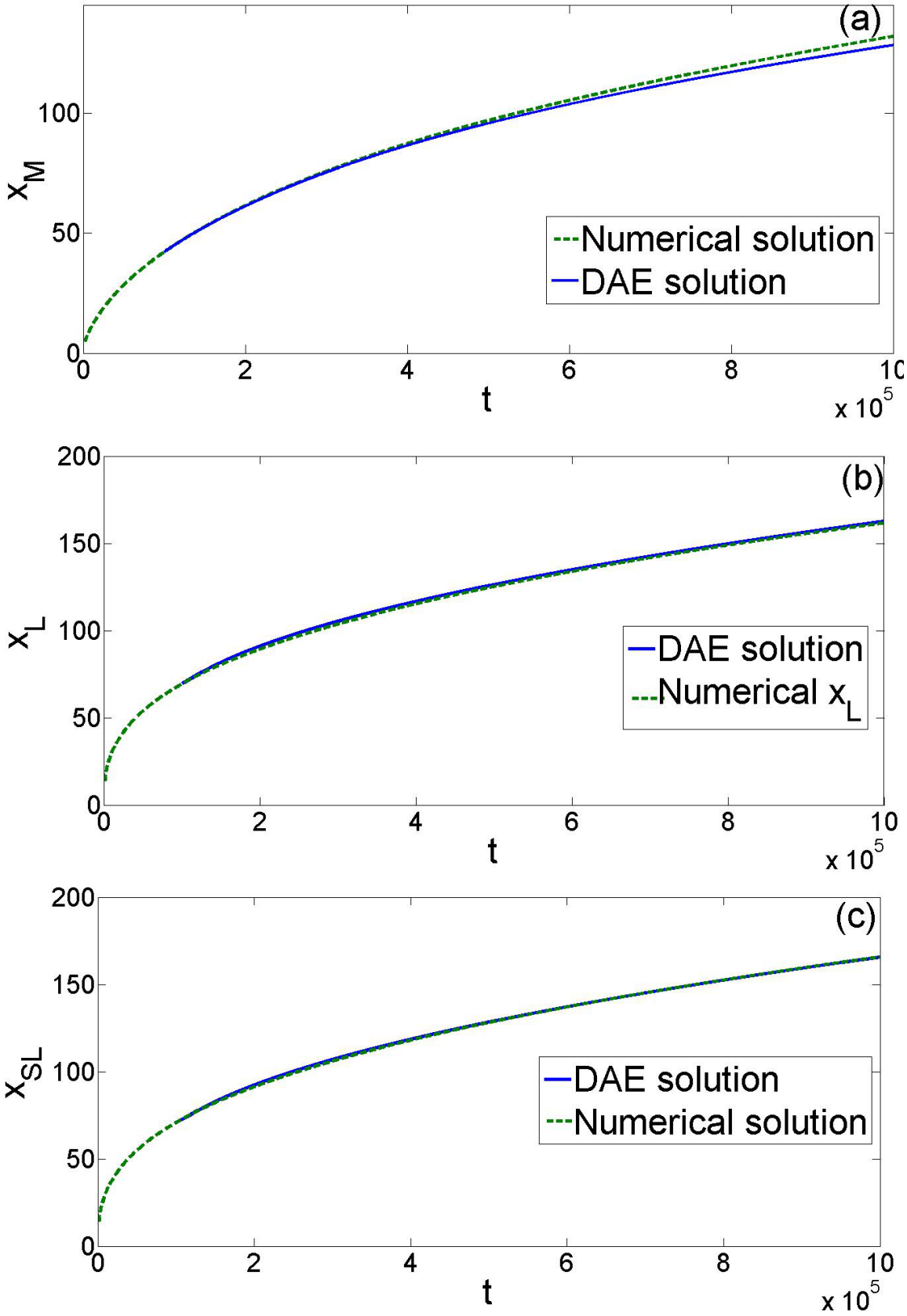

Figure 4.31: Comparing the numerically obtained fluid profile to that obtained by solving the system of DAE's for (a) x_M, (b) x_L and (c) x_{SL} from time $t = 1 \times 10^5$.

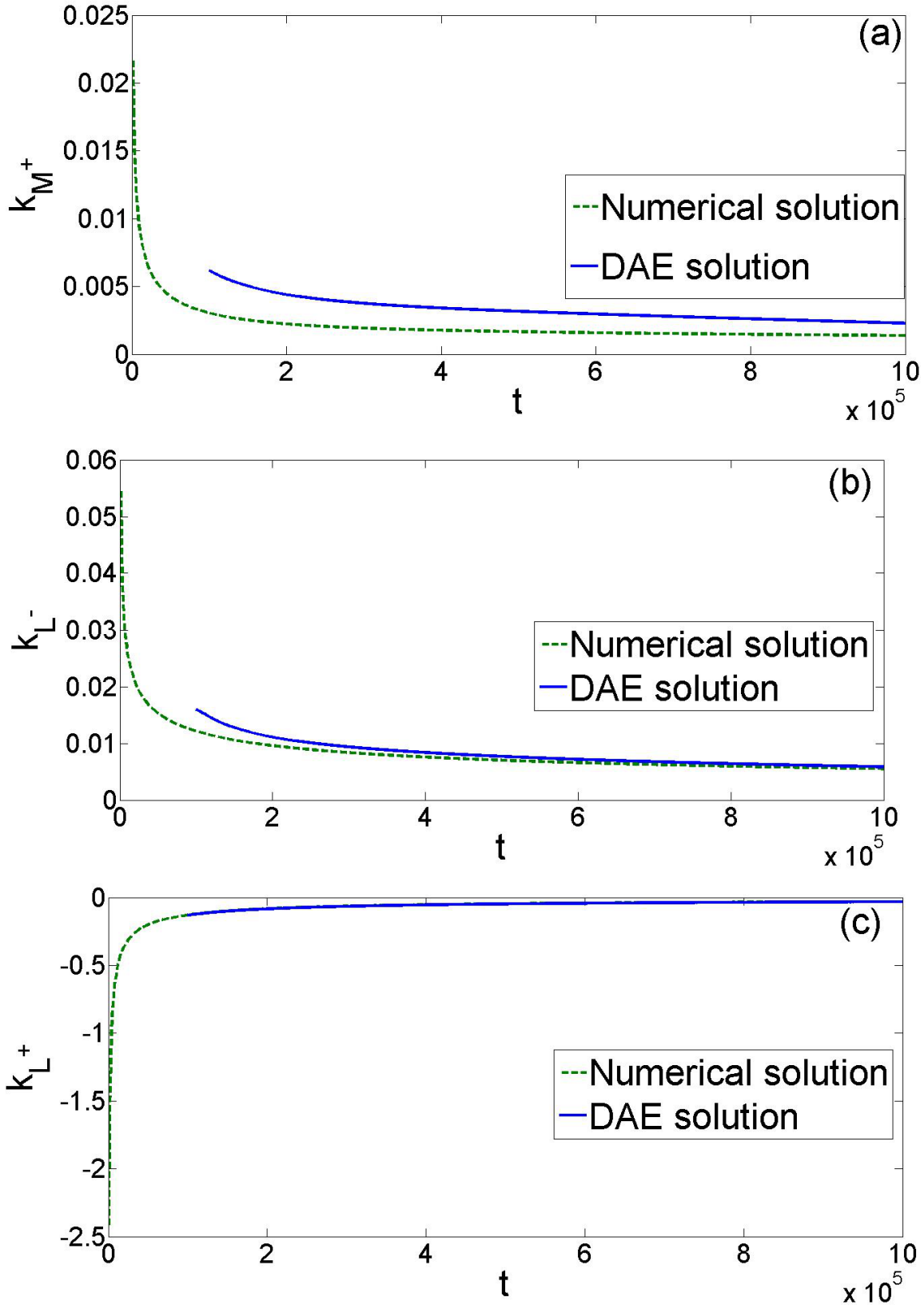

Figure 4.32: Comparing the numerically obtained fluid profile to that obtained by solving the system of DAE's for (a) k_{M^+} (b) k_{L^-} and (c) k_{L^+} from time $t = 1 \times 10^5$.

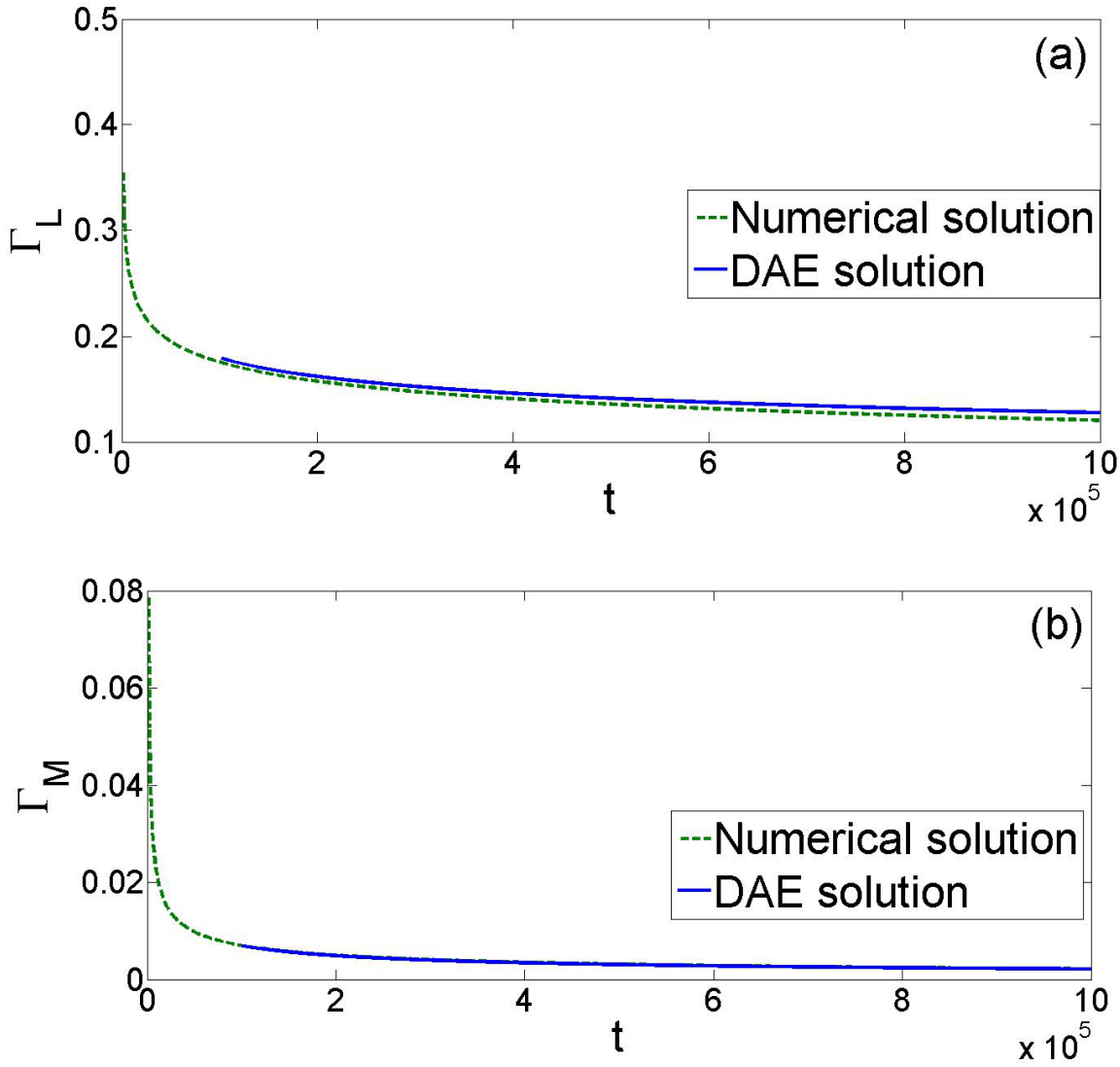

Figure 4.33: Comparing the numerically obtained fluid profile to that obtained by solving the system of DAE's for (a) Γ_L and (b) Γ_M from time $t = 1 \times 10^5$.

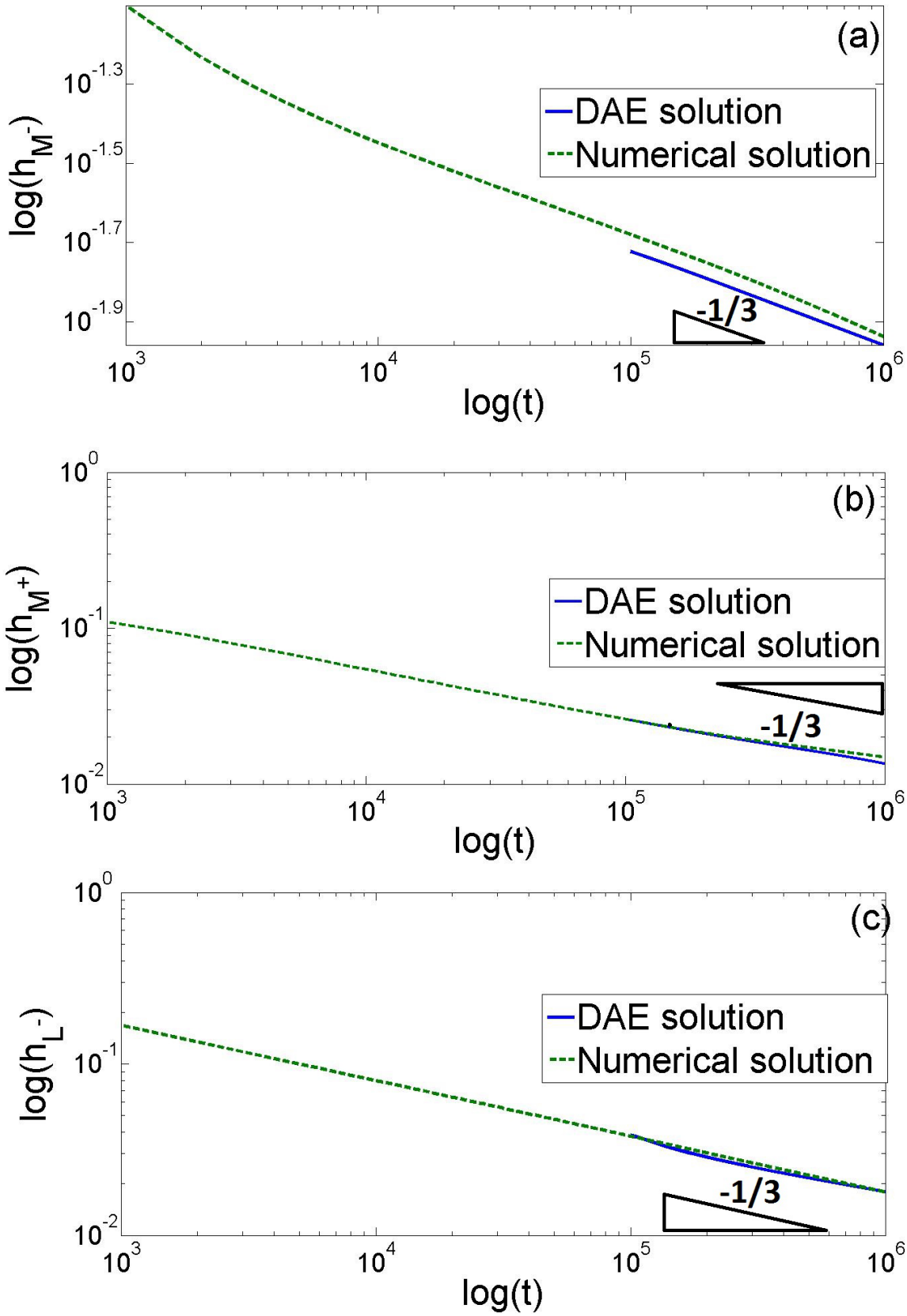

Figure 4.34: Comparing (a) h_{M^-}, (b) h_{M^+} and (c) h_{L^-} obtained from the numerical solution of the PDE's (dashed lines) with the DAE model (solid lines) for $t > 10^5$.

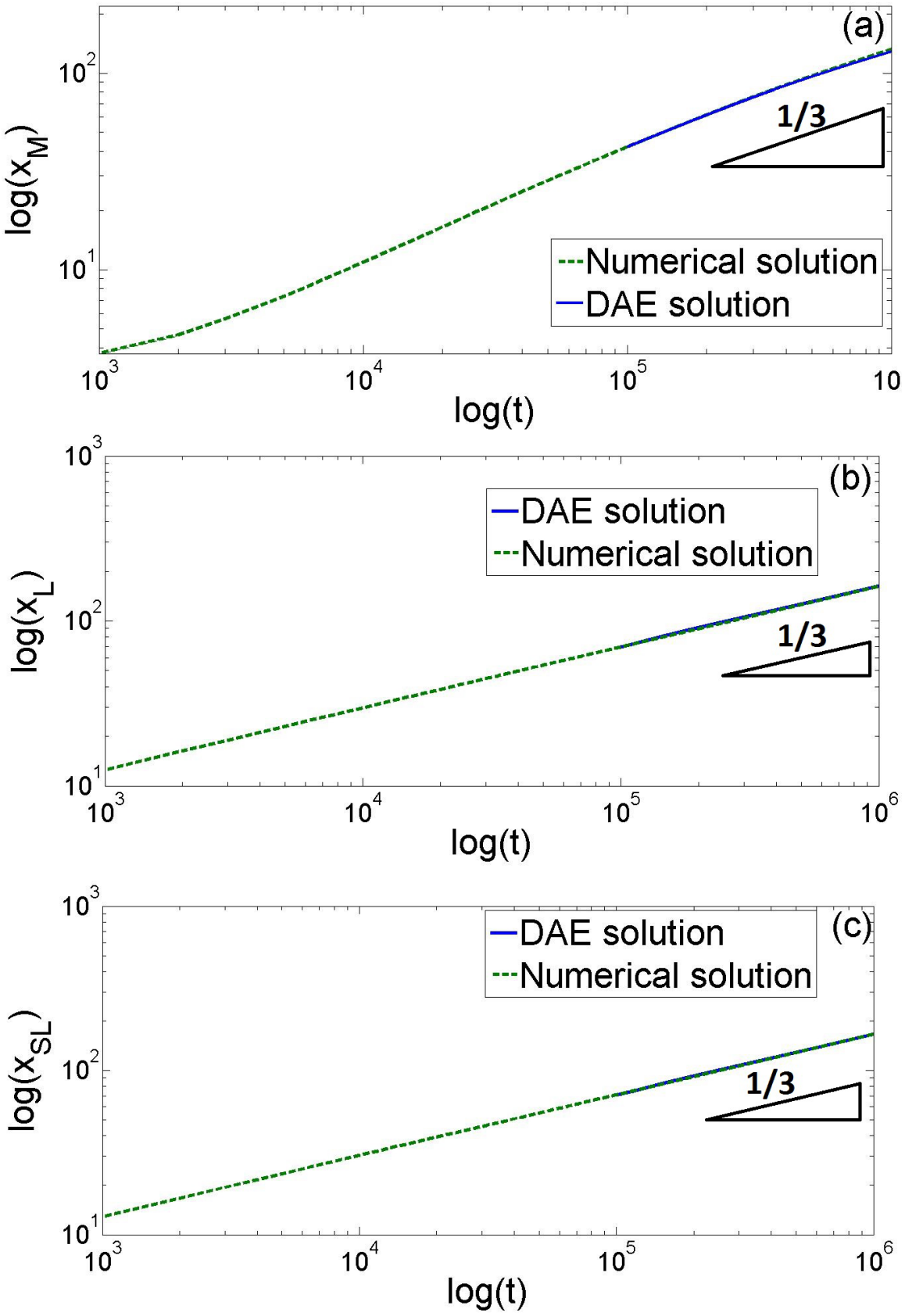

Figure 4.35: Comparing (a) x_M, (b) x_L and (c) x_{SL} obtained from the numerical solution of the PDE's (dashed lines) with the DAE model (solid lines) for $t > 10^5$.

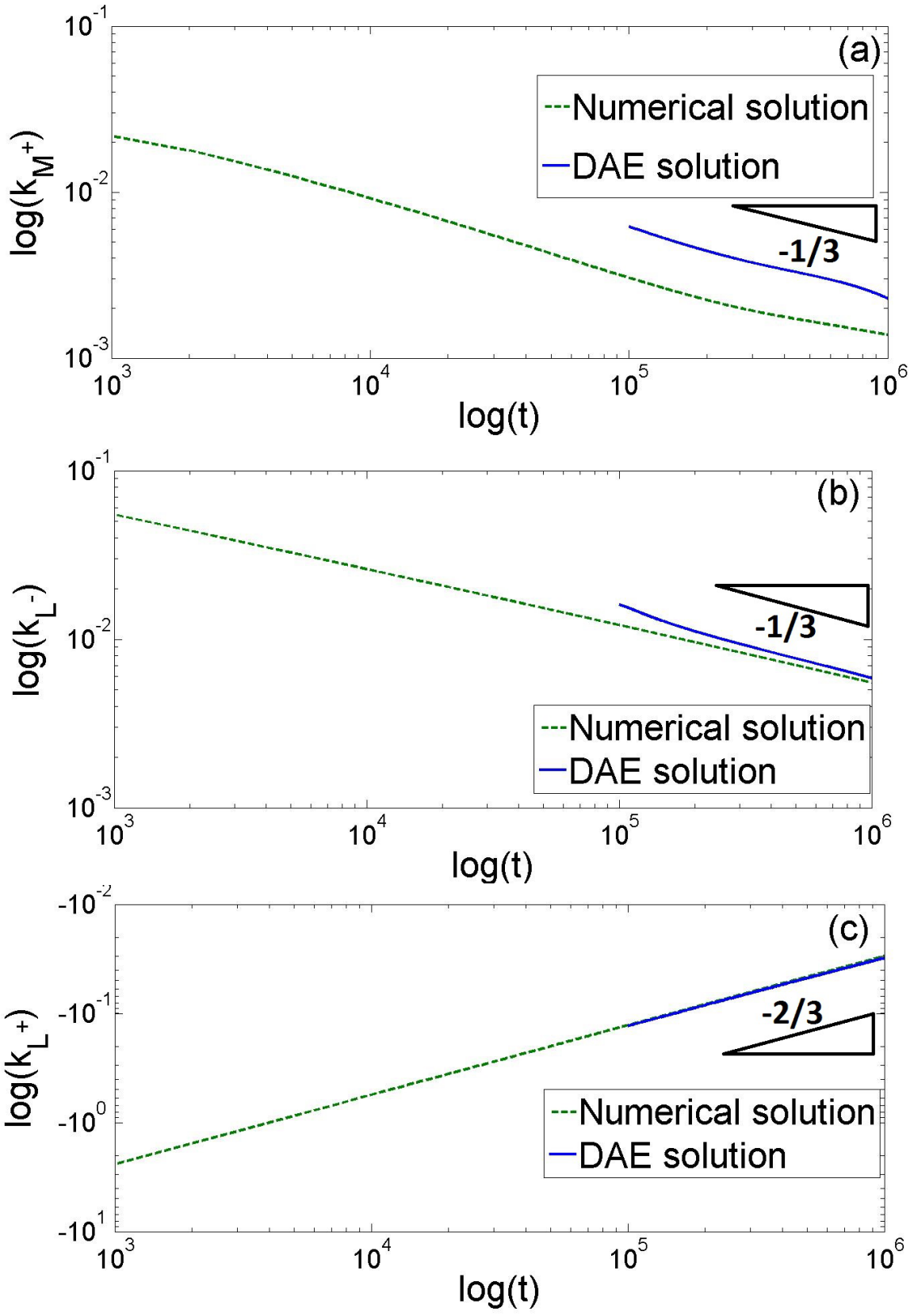

Figure 4.36: Comparing the numerically obtained fluid profile to that obtained by solving the system of DAE's for (a) k_{M^+} and k_{L^-}, (b) k_{L^+} and (c) Γ_L from time $t = 1 \times 10^5$ plotted log-log plot with the power law behaviour displayed.

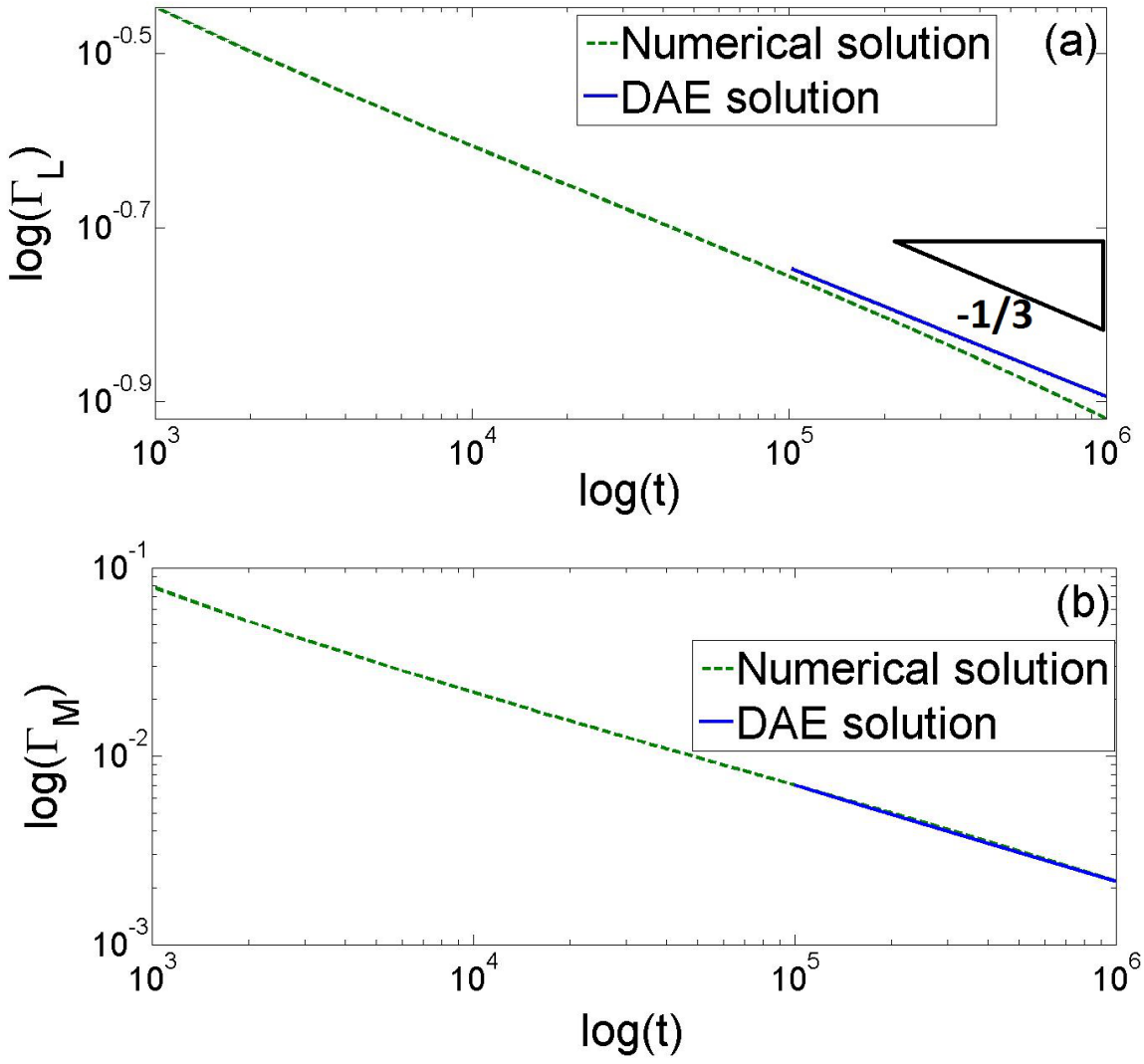

Figure 4.37: Comparing the numerically obtained fluid profile to that obtained by solving the system of DAE's for (a) Γ_L and (b) Γ_M from time $t = 1 \times 10^5$ plotted log-log plot with the power law behaviour displayed.

4.5 Concluding remarks

This chapter analyses the late-time spreading of a thin liquid droplet laden with insoluble surfactant down a pre-wetted inclined plane using simulations and asymptotic analysis. Our results provide insights into some important physical mechanisms that were not accessible from previous computational studies [15, 12, 13]. Our analysis shows the existence of a multi-region locally self-similar structure that is robust for a range of parameters and initial conditions. We have focused on the spreading of the spreading of the bulk droplet and the fluid front ahead of it and elucidated the important physical mechanisms relevant in these regions. The horizontal component of gravity dominates the bulk spreading of the drop where the surfactant concentration equilibrates rapidly and is constant (region I). As we move towards the front of this region Marangoni forces become important as the surfactant is swept downstream by gravity. They now compete with gravity and impede the flow resulting in the fluid to accumulate here in the form of a hump (region II). At leading edge of the droplet there is a short transition region were Marangoni, gravity and surface tension forces compete (region A). Marangoni forces compete with the horizontal gravity to slow down the 'effective' contact line speed compared to gravity-driven spreading alone. Surface tension is responsible for the formation of a so-called capillary ridge similar to gravity-driven spreading. Ahead of the spreading droplet a fluid front is formed due to dominant Marangoni forces.

A similarity solution describing the spreading of the main bulk droplet (region I) is

obtained. This solution shows that $h(x,t) \sim \sqrt{x}$ and $\Gamma(x,t) = \Gamma_M(t)$. This solution for the droplet height is the same as that obtained by Huppert [27] and Troian *et al.* [63] for gravity-driven spreading. We have derived a novel differential equation for Γ_M which shows how the almost uniform concentration in this region decreases with time.

In the fluid hump region (regions C and II), the unsteady nature of the problem and the large change in surfactant concentration here proved difficult to obtain analytical solutions. However, we have obtained a new semi-analytical approximate solution which captures the gross evolution of this region, particularly the jump in droplet height. A similar region has also been observed for the flow down an inclined plane from a constant flux source [15]. A travelling wave solution is used to derive a semi-analytic solution which is more straight forward that the one here [38, 39].

We were able to show that by balancing Marangoni forces the horizontal component of gravity and capillary effects that region A (containing the capillary ridge) rescales to give a family of quasi-steady solutions. To leading order, the evolution of the drop height is shown to be independent of the surfactant concentration and is the same as that of the gravity driven flow. The effects of surfactant are shown to influence the Contact line speed. Equation (4.91) shows that the slowing down of the contact line speed is due to the Marangoni effect competing against gravity.

We have derived a similarity solution for the fluid front at the leading edge of the spreading droplet which matches well with the rescaled numerical results. This region is similar to that discussed by Jensen and Grotberg [30], Jensen and Halpern [31] and

Jensen [29] except that is appears to be like a 'step' over the relatively short region between the leading edge and that of the spreading droplet. A proper step with height equal to twice the precursor thickness is observed for flow down an inclined plane from a constant-flux source [15] and analysed using a travelling wave solution [38, 39].

We observed that the structures upstream of the trailing edge of the droplet showed a a variety of behaviours over the time scales considered. At early times, a fluid front (similar to that at the droplets leading edge) travelling up the incline is observed conecting to the trailing edge of the droplet via an ultra thin film. This is similar to a surfactant-laden droplet spreading on a horizontal plane studdied by Warner *et al.* [65] and Jensen and Naire [32]. At late times, the Marangoni forces driving this front upstream decrease causing it to slow down and thin. Eventually, gravity changes the course of the flow to go down the incline and we observe the formation of a satellite droplet. The spreading flow is reminiscent of that from a constant-flux source (in this case coming from the precursor film behind) and includes a satellite capillary ridge. Such structures have not been observed previously. Such late-time spreading structures have not been reported in previous works.

The spreading and thinning rates are naturally obtained from our asymptotic analysis and are not assumed to be known *a priori*. Our analysis shows that the drop spreads at a rate $t^{1/3}$ and thins at a rate $t^{-1/3}$ which are obtained both numerically and analytically via a reduced DAE model. Notwithstanding the approximations made in deriving the DAE mode, it is a very good fit to the numerical solution at late times. Although the

spreading and thinning rates are the same in the gravity driven spreading, this is the first time they have been obtained for surfactant and gravity-driven spreading.

Having described the one-dimensional flow and corresponding structures to a reasonable accuracy, we will consider their stability particularly the stability of region A, to transverse perturbations. This is done in Chapter 5.

Chapter 5

Spreading of a surfactant-laden viscous droplet down an inclined pre-wetted plane: stability.

In this chapter, we will explore the stability to transverse perturbations of a viscous droplet of constant volume laden with insoluble surfactant spreading down an inclined pre-wetted plane due to gravity and surfactant-related effects. In §5.1, we will undertake a linear stability analysis of the 'effective' contact line at the leading edge of the spreading droplet, region A (see Fig. 4.9), where it is speculated that the instabilities originate from. We obtain a dispersion relation curves (relationship between growth rate and wavenumber of transverse perturbations) and compare the results to a small wavenumber analysis. To validate these results further we will run 2-D simulations,

§5.2. Finally, we will discuss the effect of selected parameters on the fingering behavior.

5.1 Linear Stability analysis of Region A

Having captured, to a reasonable level of accuracy, the structure and dynamics of the spatially one dimensional flow, we now investigate it's stability to small amplitude disturbances with wavenumber q^*. In the same way as the gravity-driven case, we believe that the instability originates from the 'effective' contact line region. This is validated by Edmonstone *et al.* [15, 12],

[13] and Mavromoustaki *et al* [48, 46], who use transient growth analysis and linear stability analysis respectively, to show that the growth of perturbations localised in this region. We will therefore perform, as we did previously, a linear stability analysis using the solutions for H and G in Eqs. (4.87,4.88) as the base state. We first take the two dimensional versions of Eqs. (4.43) and (4.44) and applying the following scalings, $y = (Ca/h_L^-)^{1/3}\eta$ and $t = \left(Cah_L^{-5}\right)^{1/3}\tau$ along with the scalings in Eq. (4.79), reduces the problem in this region to,

$$H_\tau - \hat{V}H_\xi = \hat{\nabla}\cdot\left(-\frac{H^3}{3}\hat{\nabla}\hat{\nabla}^2 H + \frac{H^2}{2}\hat{\nabla}G + \hat{D}(\theta)\frac{H^3}{3}\hat{\nabla}H\right) - \left(\frac{H^3}{3}\right)_\xi \quad (5.1)$$

$$0 = \hat{\nabla}\cdot\left(-\frac{H^2}{2}\hat{\nabla}\hat{\nabla}^2 H + H\hat{\nabla}G + \hat{D}(\theta)\frac{H^2}{2}\hat{\nabla}H\right) - \left(\frac{H^2}{2}\right)_\xi, \quad (5.2)$$

where $\hat{\nabla} = (\partial/\partial\xi, \partial/\partial\eta)$. We perform a normal mode analysis by setting

$(H(\xi,\eta,\tau), G(\xi,\eta,\tau)) = (H_s(\xi), G_s(\xi)) + \epsilon(\hat{H}(\xi), \hat{G}(\xi))e^{iq\eta+\beta\tau}$, where $(H_s(\xi), G_s(\xi))$

denote the quasi-steady base state for H and G respectively which are obtained by solving Eqs. (4.87,4.88), $q = (Cah_{L^-})^{1/3}q^*$ is the scaled wavenumber and β is the growth rate, and $\epsilon \ll 1$. At leading order in ϵ, we recover the the quasi-steady equations (4.80,4.81). At $O(\epsilon)$ the linearised unsteady disturbance satisfies,

$$\begin{aligned}
\beta\hat{H} - \hat{V}\hat{H}_\xi &= \left[\frac{H_s^2}{2}\hat{G}_\xi + H_s\hat{H}G_{s\xi} - \frac{H_s^3}{3}\left(\frac{\partial^2}{\partial\xi^2} - q^2\right)\hat{H}_\xi - H_s^2\hat{H}H_{s\xi\xi\xi} + \hat{D}(\theta)\frac{H_s^3}{3}\hat{H}_\xi\right]_\xi + \\
&\quad \left[\hat{D}(\theta)H_s^2\hat{H}_1 H_{s\xi}\right]_\xi - q^2\frac{H_s^2}{2}\hat{G} + q^2\frac{H_s^3}{3}\left(\frac{\partial^2}{\partial\xi^2} - q^2\right)\hat{H} \\
&\quad -(H_s^2\hat{H})_\xi - q^2\hat{D}(\theta)\frac{H_s^3}{3}\hat{H} \qquad (5.3) \\
0 &= \left[H_s\hat{G}_\xi + \hat{H}G_{s\xi} - \frac{H_s^2}{2}\left(\frac{\partial^2}{\partial\xi^2} - q^2\right)\hat{H}_\xi - H_s\hat{H}H_{s\xi\xi\xi} + \hat{D}(\theta)\frac{H_s^2}{2}\hat{H}_\xi\right]_\xi + \\
&\quad \left[\hat{D}(\theta)H_s\hat{H}H_{s\xi}\right]_\xi - q^2H_s\hat{G} + q^2\frac{H_s^2}{2}\left(\frac{\partial^2}{\partial\xi^2} - q^2\right)\hat{H} - (H_s\hat{H})_\xi \\
&\quad -q^2\hat{D}(\theta)\frac{H_s}{2}\hat{H} \qquad (5.4)
\end{aligned}$$

The above two equations are the eigenvalue problem for this region. One can solve the eigenvalue problem numerically to find the dispersion relation, i.e., relationship between β and q. This is a non trivial task to undertake: we can however replace $\beta\hat{H}$ by $\hat{H}_\tau$ and solve it numerically as an initial value problem (IVP). An alternative approach may also be used [7]. We use finite difference on a uniform grid to discretise the spatial derivatives, as we did in §4.2 keeping the time derivative continuous. The resulting PDE's are solved using a stiff ODE solver in Matlab[56]. We track the evolution of localised disturbances from a prescribed initial disturbance (normal distribution perturbation centred about 0 on the base state). We look for perturbations that decay to

zero at the boundaries. Substituting the base state into the discretised equations then solving the IVP until a steady growth rate β is obtained without the perturbations growing to the boundary. The evolution depends on the wavenumber q, the contact line speed $\hat{V}$, s, k^- and k^+. Using the relations in Eqs. (4.86, 4.89), we need only to prescribe values for two parameters which we chose to be s and k^+. Varying the base state equates to varying time as s, k^+ and $\hat{V}$ all vary with time. For small q, growing disturbances in G ultimately reach the boundaries of the domain, which prevented us from computing reliable results for $q < 0.1$. Figure 5.1(a),(b) show the evolution of $\hat{H}$ and $\hat{G}$ (solid lines), respectively for $q = 0.3$ at an inclination angle $\theta = 90^o$ emanating from a base state evaluated at $t = 2 \times 10^5$ (dashed line) (corresponding to $s = 0.0884$ and $k^+ = -2$). It is observed that under suitable conditions disturbances can grow rapidly: perturbations to $\hat{H}$ are larger immediately ahead of the capillary ridge and behind the fluid front, while perturbations to $\hat{G}$ are larger where the base state surfactant concentration has a maximum, features identified previously by Edmonstone *et al.* [13]. It is also noted that $\hat{G}$ is minimum where $\hat{H}$ is maximum and vice versa. At late times ($\tau > 50$) the growth of the disturbances is approximately exponential. Comparing Figs 3.1,5.1 we see that the disturbances grow much quicker with the inclusion of surfactant. At late times the growth of the disturbances is exponential. Figure 5.2 shows β against q for an inclination angle of 90^o at times $t = 10^4$, 10^5, 2×10^5, 5×10^5 and 10^6. The shape of the dispersion relation resembles that obtained by [13] using transient growth analysis. The dispersion relation demonstrates convincingly that the most unstable mode has a wavenumber comparable to the width of region A. This

indicates that this region is linearly unstable to perturbations of these wavelengths. At higher wavenumbers, the growth rate is negative implying that the region is linearly stable to perturbations at these wavenumbers. It is also observed that the maximum growth rate and bandwidth of unstable wavenumbers decrease as time increases. Figure 5.3 shows the dispersion relation for $s = 0.0884$ and $k^+ = -2$ for inclination angles $\theta = 3^o$, 60^o and 90^o. It can be seen that decreasing the inclination angle decreases the maximum growth rate and the bandwidth of unstable wavenumbers. This result is in agreement with the transient growth analysis conducted by Edmonstone *et al.* [13]. Finally, in Fig. 5.4 we compare the dispersion relation between surfactant and gravity-driven spreading (solid line) and gravity-driven spreading alone(dashed line) using a base state, H_s, corresponding to $s = 0.0884$ and $k^+ = -2$. We observe that the growth rate and band of unstable wavenumbers are significantly smaller for the gravity-driven case indicating the additional destabilising contribution due to surfactant. Moreover, at small wavenumbers the dispersion relation behaves differently with quadratic behaviour for gravity-driven spreading and linear for surfactant and gravity-driven spreading. Furthermore, for gravity-driven spreading alone there is a critical inclination angle θ below which the base state is linearly stable for all wavenumbers (see Fig. 3.3). In contrast, it is speculated that the surfactant and gravity-driven spreading is linearly unstable for all angles of inclination [13]. These are analysed in more detail in the next section by performing a small-wavenumber analysis about the base state, which forms part of the discrete spectrum of the linear operator in Eqs. (5.3,5.4).

5.1.1 Small-wavenumber analysis

In this section we examine the wavelengths intermediate between the width of region A, II and III. Since the numerical results suggest that at leading order the growth rate is linear in wavenumber, we write $[\hat{H},\hat{G},\beta] = [\hat{H},\hat{G},\beta]_0 + q[\hat{H},\hat{G},\beta]_1 + q^2[\hat{H},\hat{G},\beta]_2 + \mathrm{O}(q^3)$. Then substituting this into Eqs. (5.3,5.4), we obtain at leading order in q $(\hat{H}_0,\hat{G}_0) = (-H_{s\xi},-G_{s\xi})$ and $\beta_0 = 0$. This represents a simple translation of the base state. At $O(q)$ we get

$$\begin{aligned} -\beta_1 H_{s\xi} - \hat{V}\hat{H}_{1\xi} &= \left[\frac{H_s^2}{2}\hat{G}_{1\xi} + H_s G_{s\xi}\hat{H}_1 - \frac{H_s^3}{3}\hat{H}_{1\xi\xi\xi} - H_s^2 H_{s\xi\xi\xi}\hat{H}_1 + \hat{D}(\theta)\frac{H_s^3}{3}\hat{H}_{1\xi}\right]_\xi \\ &\quad + \left[\hat{D}(\theta)H_s^2 H_{s\xi}\hat{H}_1 - H_s^2\hat{H}_1\right]_\xi, \qquad (5.5) \\ 0 &= \left[H_s\hat{G}_{1\xi} + \hat{H}_1 G_{s\xi} - \frac{H_s^2}{2}\hat{H}_{1\xi\xi\xi}\hat{H}_1 + \hat{D}(\theta)\frac{H_s^2}{2}\hat{H}_{1\xi} + \hat{D}(\theta)H_s H_{s\xi}\hat{H}_1\right]_\xi \\ &\quad + \left[-H_s\hat{H}_1\right]_\xi. \qquad (5.6) \end{aligned}$$

Integrating the Eqs. (5.5,5.6) from $\xi = -\infty$ to $\xi = \infty$ and applying the boundary conditions,

$$\begin{aligned} &H_s \to s,\ \ G_{s\xi} \to k^+,\ \ (H_{s\xi},\ \ H_{s\xi\xi\xi},\ \ \hat{H}_1,\hat{H}_{1\xi},\hat{H}_{1\xi\xi\xi}) \to 0,\ \ \hat{G}_{1\xi} \to A(\text{constant}) \\ &\text{as}\ \ \xi \to +\infty, \qquad (5.7) \\ &H_s \to 1,\ \ G_{s\xi} \to k^-,\ \ (H_{s\xi},\ \ H_{s\xi\xi\xi},\ \ \hat{H}_1,\hat{H}_{1\xi},\hat{H}_{1\xi\xi\xi}) \to 0,\ \ G_{1\xi} \to B \\ &\text{as}\ \ \xi \to -\infty. \qquad (5.8) \end{aligned}$$

The conditions for $G_{1\xi}$ are required to balance the unsteady and Marangoni terms (first and third terms) in Eq. (5.5) and are also motivated, in part, by the fact the leading order solution G_0 tends to constant values $-k^-$ and $-k^+$ as $\xi \to -\infty, \quad \infty$, respectively. We therefore obtain,

$$\beta_1 = \left[\frac{\frac{1}{2}As^2 - \frac{B}{2}}{1-s} \right], \tag{5.9}$$

$$B = As \tag{5.10}$$

which implies,

$$\beta_1 = -B/2 = -As/2 \tag{5.11}$$

To determine the growth rate β_1, we need to determine either A or B. We assume that for $q \ll 1$, the eigenfunctions have a 3 region structure: an inner region where $\xi = O(1)$ and $\hat{H} = -H_{s\xi}$, $\hat{G} = -G_{s\xi}$, and two outer regions of $O(1/q)$. We now show how perturbations to G affect the surfactant gradient ahead and behind the effective contact line. To describe the outer region we rescale $\xi = z/q$, $\hat{G} = \tilde{G}/q$, $\beta = q\tilde{\beta}$, $\hat{H} = \tilde{H}$. Substituting the rescalings into Eqs. (5.3) and (5.4) and after dividing by q we obtain,

$$\begin{aligned} \tilde{\beta}\tilde{H} - \hat{V}\tilde{H}_z \;=\; & \left[\frac{H_s^2}{2}\tilde{G}_z + H_s G_{s\xi}\tilde{H} - q^3 \frac{H_s^3}{3}\left(\frac{\partial^2}{\partial z^2} - 1 \right)\tilde{H}_z \right]_z \\ & + \left[-H_s^2 H_{s\xi\xi\xi}\tilde{H} + q\hat{D}(\theta)\frac{H_s^3}{3}\tilde{H}_z + \hat{D}(\theta)H_s^2 H_{s\xi}\tilde{H} \right]_z \\ & - \frac{H_s^2}{2}\tilde{G} + q^3\frac{H_s^3}{3}\left(\frac{\partial^2}{\partial z^2} - 1 \right)\tilde{H} - (H_s^2\tilde{H})_z - q\hat{D}(\theta)\frac{H_s^3}{3}\tilde{H}, \end{aligned} \tag{5.12}$$

$$
\begin{aligned}
0 &= \left[H_s\tilde{G}_z + \tilde{H}G_{s\xi} - q^3\frac{H_s^2}{2}\left(\frac{\partial^2}{\partial z^2} - 1\right)\right]_z - H_sH_{s\xi\xi\xi}\tilde{H} + q\hat{D}(\theta)\frac{H_s^2}{2}\tilde{H}_z \\
&\quad + \left[\hat{D}(\theta)H_sH_{s\xi}\tilde{H}\right]_z - H_s\tilde{G} + q^3\frac{H_s^2}{2}\left(\frac{\partial^2}{\partial z^2} - 1\right)\tilde{H} - (H_s\tilde{H})_z \\
&\quad - q\hat{D}(\theta)\frac{H_s^2}{2}\tilde{H}. \qquad (5.13)
\end{aligned}
$$

At leading order in q, using the fact that $H_s \to s$, $G_{s\xi} \to k^+$, $H_{s\xi}, H_{s\xi\xi\xi} \to 0$ as $\xi \to \infty$, we obtain,

$$
\begin{aligned}
\tilde{\beta}\tilde{H} - \hat{V}\tilde{H}_z &= \left[\frac{s^2}{2}\tilde{G}_z + sk^+\tilde{H}\right]_z - \frac{s^2}{2}\tilde{G} - s^2\tilde{H}_z, \qquad (5.14) \\
0 &= \left[s\tilde{G}_z + k^+\tilde{H}\right]_z - s\tilde{G} - s\tilde{H}_z. \qquad (5.15)
\end{aligned}
$$

Rearranging Eq. (5.15) we obtain,

$$
\tilde{G}_{zz} - \tilde{G} = \left(1 - \frac{k^+}{s}\right)\tilde{H}_z. \qquad (5.16)
$$

Substituting the above equation into the Eq. (5.14) we obtain,

$$
\tilde{H}_z - \frac{\tilde{\beta}}{\alpha}\tilde{H} = 0, \qquad (5.17)
$$

where $\alpha = \left[\frac{s^2}{2} + \frac{sk^+}{2} - s^2 + \hat{V}\right]$. The solution to the above equation is $\tilde{H} = \tilde{H}_0 e^{\tilde{\beta}z/\alpha}$. For $\tilde{H}$ to be bounded and $\tilde{\beta} > 0$, $\tilde{H}_0 = 0$, as $\alpha > 0$ for some values of s. Hence Eq. (5.16) becomes

$$
\tilde{G}_{zz} - \tilde{G} = 0. \qquad (5.18)
$$

The solution of Eq. (5.18) is $\tilde{G} = C_1 e^z + C_2 e^{-z}$ as $z \to \infty$. As we require a decaying solution, implies $C_1 = 0$. Hence, the solution in the outer region ahead of the contact line is,

$$\hat{G} = \frac{C_2}{q} e^{-q\xi} = \frac{C_2}{q}(1 - q\xi + q^2\xi^+ o(\xi^3)). \tag{5.19}$$

Expanding $e^{-q\xi}$ in a power series in ξ and matching to the inner region, we obtain $C_2 = -qk^+$. Hence,

$$\hat{G} = -k^+ + qk^+\xi - \frac{q^2}{2}k^+\xi^2 + o(\xi^3), \quad \text{as } \xi \to 0^+. \tag{5.20}$$

By taking the limit as $\xi \to \infty$ we obtain $A = k^+$ and hence,

$$\beta_1 = -\frac{k^+ s}{2}. \tag{5.21}$$

Equations (5.12) and (5.13) at leading order in q and now applying $H_s \to 1, \quad G_{s\xi} \to k^-, \quad H_{s\xi}, H_{s\xi\xi\xi} \to 0, \quad \text{as } \xi \to -\infty$, we obtain,

$$\tilde{\beta}\tilde{H} - \hat{V}\tilde{H}_z = \left[\frac{1}{2}\tilde{G}_z + k^-\tilde{H}\right]_z - \frac{1}{2}\tilde{G} - s\tilde{H}_z \tag{5.22}$$

$$0 = \left[\tilde{G}_z + k^-\tilde{H}\right]_z - \tilde{G} - \tilde{H}_z. \tag{5.23}$$

Rearranging Eq. (5.23) we obtain,

$$\tilde{G}_{zz} - \tilde{G} = \left(1 - k^-\right)\tilde{H}_z. \tag{5.24}$$

Substituting the above equation into Eq. (5.22) we obtain,

$$\tilde{H}_z - \frac{\tilde{\beta}}{\alpha}\tilde{H} = 0, \tag{5.25}$$

where $\alpha = \left[\frac{1}{2} + \frac{k^-}{2} - 1 + \hat{V}\right]$. The solution to the above equation is $\tilde{H} = \tilde{H}_0 e^{\tilde{\beta}z/\alpha}$. For $\tilde{H}$ to be bounded and $\tilde{\beta} > 0$, then $\tilde{H}_0 = 0$. Hence Eq. (5.24) becomes,

$$\tilde{G}_{zz} - \tilde{G} = 0. \tag{5.26}$$

The solution of which is $\tilde{G} = C_1 e^z + C_2 e^{-z}$ as $z \to -\infty$. As we want a decaying solution as $z \to -\infty$, implies $C_2 = 0$. Hence, the solution in the outer region behind the contact line is,

$$G = \frac{C_1}{q} e^{q\xi}. \tag{5.27}$$

Expanding $e^{q\xi}$ in a power series in ξ then matching to the inner region we obtain $C_1 = -qk^-$. Hence,

$$\hat{G} = -k^- - qk^-\xi - \frac{q^2}{2}k^{-^2} - \xi + o(\xi^2) \tag{5.28}$$

So, $B = -k^-$. Using Eq. (5.31) we obtain the $O(q)$ growthrate,

$$\beta_1 = \left[\frac{\frac{1}{2}k^+ s^2 + \frac{1}{2}k^-}{1 - s}\right]. \tag{5.29}$$

Noting that $k^- > 0$, $k^+ < 0$ and $s < 1$, the growthrate $\beta_1 > 0$ if $k^-/2 > -k^+ s^2/2$, i.e. the $O(q)$ Marangoni flux behind the contact line dominates that ahead of the

contact line. If this condition is satisfied, a mechanism for the flow to become linearly unstable at $O(q)$ is due to the forward Marangoni flux behind the contact line drawing more fluid into the contact line region than the forward Marangoni flux ahead of the contact line region dragging fluid out. This results in growth of the perturbations in h consequently destabilising the flow and the constant line (consistent with Fig. 5.1 where $\hat{H}$ is positive and growing immediately behind the contact line (and ahead of the capillary ridge) coinciding with $\hat{G}_\xi$ which is negative there). We now verify whether the above condition is satisfied. Using $A = sk^+$, $B = -k^-$ in Eq. (5.10) gives,

$$-k^- = sk^+. \tag{5.30}$$

Figure 5.5(a) shows that Eq. (5.30) is approximately satisfied. Using which the above condition can be re-written as $k^-(1 - s^2) > 0$ which is always satisfied. Rearranging Eq. (4.89) then the above relationship gives $k^- = (1 - s^2)/4$ and $k^+ = -(1 - s^2)/(4s)$ (Fig. 5.5(b,c) shows that these relationships are approximately satisfied). Equation (5.29) can now be re-written as,

$$\beta_1 = \frac{1 - s^2}{8} \approx \frac{1}{8} \ \text{(since } s \ll 1\text{)}. \tag{5.31}$$

Equation (5.31) shows that the $O(q)$ growthrate is always positive and independent of the angle of inclination. Hence the flow is linearly unstable for all angles of inclination confirming the speculation by Edmonstone *et al.* [13]. We also note from numerics

that s increases gradually with time so β_1 decreases confirming the observation in Fig. 5.2 that as time increases the base state becomes less linearly unstable. The analysis also shows the Marangoni effect to be dominant at this order with gravity having no influence. Figures 5.6 (a,b) show the $O(q)$ approximation, $\beta \approx q/8$ (dashed lines) along with numerical dispersion curves (solid lines) for inclination angles $\theta = 90^o, 3^o$ respectively. We see that at higher inclination angles the $O(q)$ approximation slightly underestimates the numerical dispersion relation and at small inclination angles it overestimates. Hence an $O(q^2)$ correction is needed to better approximate the dispersion curve. We now determine the $O(q^2)$ growth rate. At $O(q^2)$ we obtain,

$$\begin{aligned}
\beta_1 H_1 - \beta_2 H_{s\xi} - \hat{V} H_{2\xi} &= \left[\frac{H_s^2}{2} G_{2\xi} + H_s G_{s\xi} H_2 - \frac{H_s^3}{3} H_{2\xi\xi\xi} - \frac{H_s^3}{3} H_{s\xi\xi} - H_s^2 H_{s\xi\xi\xi} H_2\right]_\xi \\
&\quad + \left[\hat{D}(\theta)\frac{H_s^3}{3} H_{2\xi} + \hat{D}(\theta) H_s^2 H_{s\xi} H_2\right]_\xi + \frac{H_s^2}{2} G_{s\xi} - \frac{H_s^3}{3} H_{s\xi\xi\xi} \\
&\quad - (H_s^2 H_2)_\xi + \hat{D}(\theta)\frac{H^3}{3} H_{s\xi} \qquad (5.32) \\
0 &= \left[H_s G_{s\xi} + G_{s\xi} H_2 - \frac{H_s^2}{2} H_{2\xi\xi\xi} - \frac{H_s^2}{2} H_{s\xi\xi} - H_s H_{s\xi\xi\xi} H_2\right]_\xi \\
&\quad + \left[\hat{D}(\theta)\frac{H_s^2}{2} H_{2\xi} + \hat{D}(\theta) H_s H_{s\xi} H_2\right]_\xi + H_s G_{s\xi} - \frac{H_S^2}{2} H_{s\xi\xi\xi} \\
&\quad - (H_s H_2)_\xi + \hat{D}(\theta)\frac{H_s^2}{2} H_{s\xi} \qquad (5.33)
\end{aligned}$$

Integrating the above equations from $\xi = -\infty$ to $\xi = +\infty$, using the boundary conditions,

$$(H_1, H_2, H_{2\xi}, H_{2\xi\xi\xi}) \to 0, \quad \text{as} \quad \xi \to \pm\infty. \qquad (5.34)$$

Also, $G_{2\xi} \to -k^- \xi$ (using Eq. (5.20)) as $\xi \to -\infty$ and $G_{2\xi} \to -k^+ \xi$ as $\xi \to +\infty$ (using

Eq. (5.28)). Also using the boundary conditions for the base state (Eqs. (5.7,5.8)) we obtain,

$$(1-s)\beta_2 = \frac{-s^2}{2}k^+\xi\Big|_{\xi\to\infty} + \frac{k^-}{2}\xi\Big|_{\xi\to-\infty} + \int_{-\infty}^{\infty}\frac{H_s^2}{2}G_{s_\xi}d\xi - \int_{-\infty}^{\infty}\frac{H_s^3}{3}H_{s_{\xi\xi\xi}}d\xi + \int_{-\infty}^{\infty}\hat{D}(\theta)\frac{H_s^3}{3}H_{s\xi}d\xi \tag{5.35}$$

Equation (5.35) shows that the $O(q^2)$ growthrate β_2 is controlled by competing Marangoni, capillary and vertical gravity fluxes. The first two terms on the right hand side of Eq. (5.35) cancel the divergent contribution of the Marangoni flux (the third term on the RHS) far ahead and behind the contact line, respectively. For spreading without surfactant this reduces to the stability criterion Eq. (3.8) derived by Bertozzi and Brenner [8]. Using Eqs. (4.86-4.89) and rearranging determines $O(q^2)$ growth rate β_2:

$$\beta_2 = \frac{1}{1-s}\left[\frac{1}{2}\int_{-\infty}^{\infty}\frac{1}{2}H_s^2G_{s\xi}d\xi - \frac{1}{2}s^2k^+\xi\Big|_{\xi\to\infty} + \frac{1}{s}k^-\xi\Big|_{\xi\to\infty}\right] + \frac{1}{1-s}\left[\frac{1}{3}\int_{-\infty}^{\infty}(H_s-1)(H_s-s)(H_s+s+1)d\xi\right]. \tag{5.36}$$

The first set of square brackets are the contribution from the Marangoni flux and the second from the capillary flux. The contribution from the capillary flux remains a positive contribution if $H_s > 1$ for a considerable part of the domain. Hence a large capillary ridge is necessary for this to happen. We numerically approximate the integrals involved to compute the growth rate β_2. For large inclination angles, the second integral in Eq. (5.36) is positive and dominates the first which is negative due to

the steep drop in surfactant concentration observed immediately ahead of the maximum surfactant concentration (see Fig. 4.7). This results in a net downward flow out of the contact line region which has a stabilising influence on the growth of the perturbations at this order. As the inclination angle decreases, the positive contribution from the second integral gradually decreases becoming negative below some threshold angle θ and the contribution from the second integral decreases in magnitude while still being negative. Hence below this threshold angle β_2 is always negative. Figures 5.6(a,b) show that the $O(q^2)$ approximation, $\beta \approx \beta_1 q + \beta_2 q^2$, (dot-dashed lines) along with the numerical dispersion relation (solid lines) for inclination angles $\theta = 90^o, 3^o$, respectively, with $\beta_2 = 0.0207$ for $\theta = 90^o$ and $\beta_2 = -0.0847$ for $\theta = 3^o$. We observe that the $O(q^2)$ correction provides a much better approximation of the dispersion relation at small wavenumbers.

In the next section we undertake 2D simulations by which we can validate the LSA undertaken here.

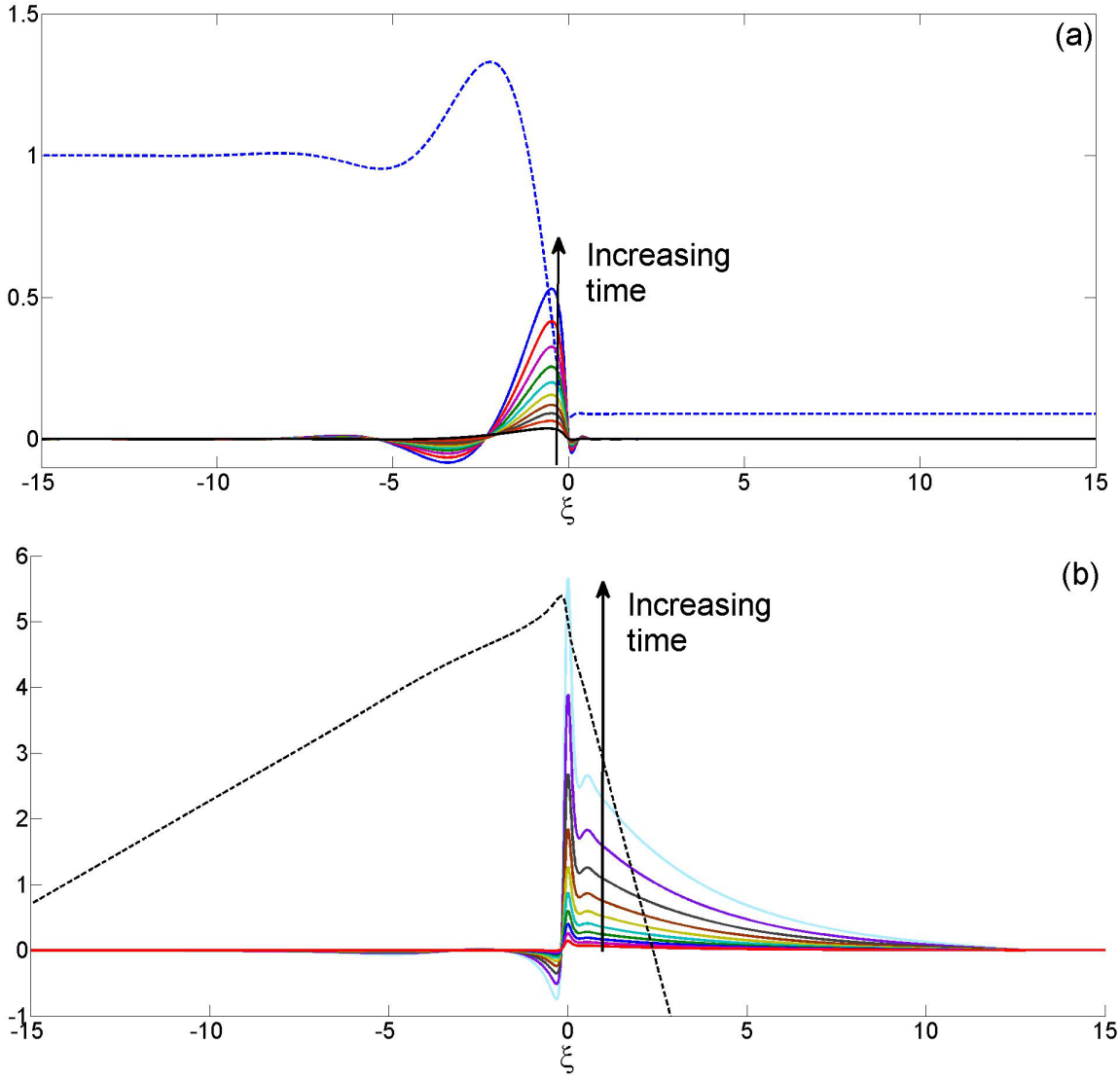

Figure 5.1: Solid lines show solutions of Eqs. (5.3,5.4) for $q = 0.3$, $\theta = 90^o$ using a base state (dashed lines) evaluated at $t = 2 \times 10^5$ ($s = 0.0884$ and $k^+ = -2$). Arrows show increasing time between $10 - 100$.

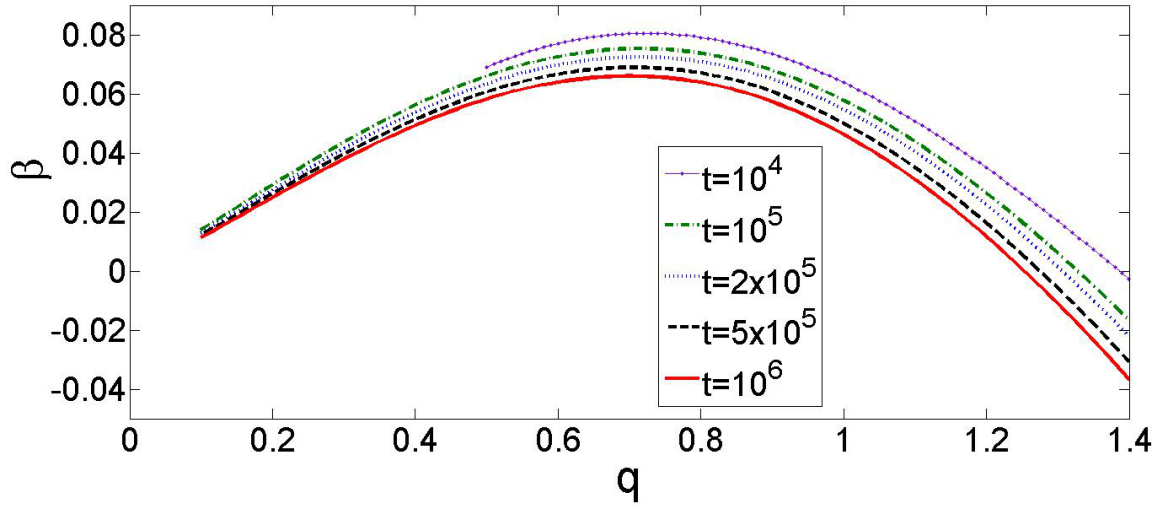

Figure 5.2: Large-time growthrate β versus wavenumber q for $t = 10^4$, 10^5, 2x10^5, 5x10^5 and 10^6 for inclination angle of 90^o for surfactant and gravity driven instability.

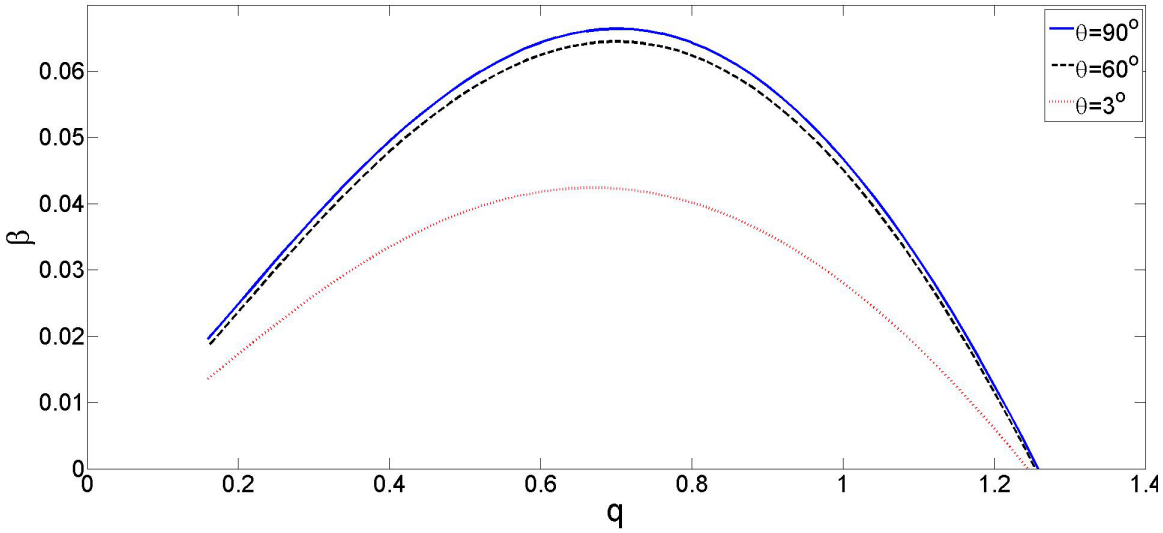

Figure 5.3: Large-time growthrate β versus wavenumber q for $s = 0.0884$ and $k^+ = -2$ for inclination angles of 90^o, 60^o and 3^o.

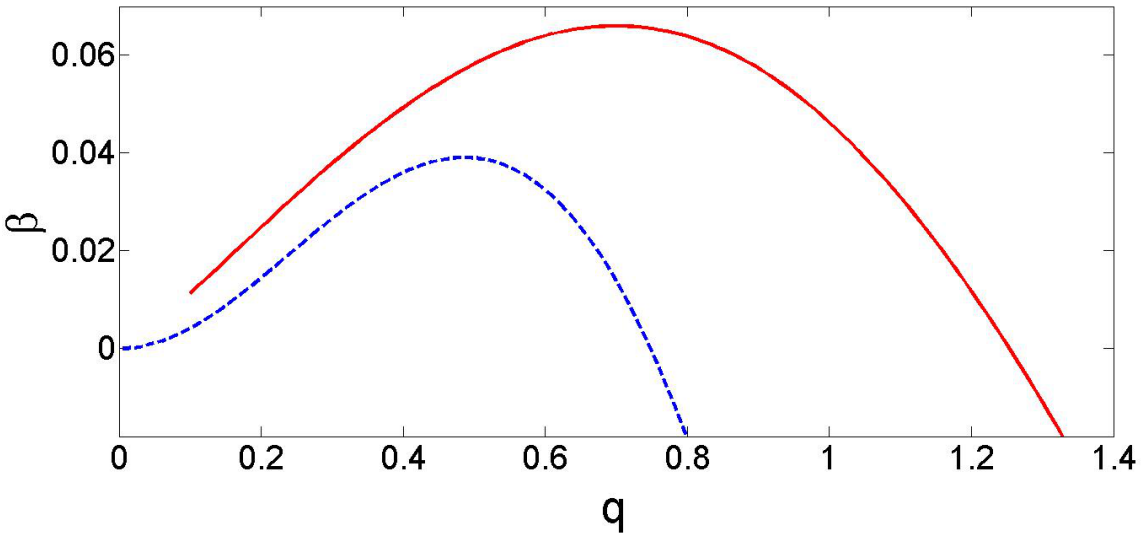

Figure 5.4: Large-time growthrate β versus wavenumber q for the base-state with $s = 0.0884$ for inclination angle of 90^o for gravity-driven flow and $k^+ = -2$ for the surfactant and gravity-driven flow.

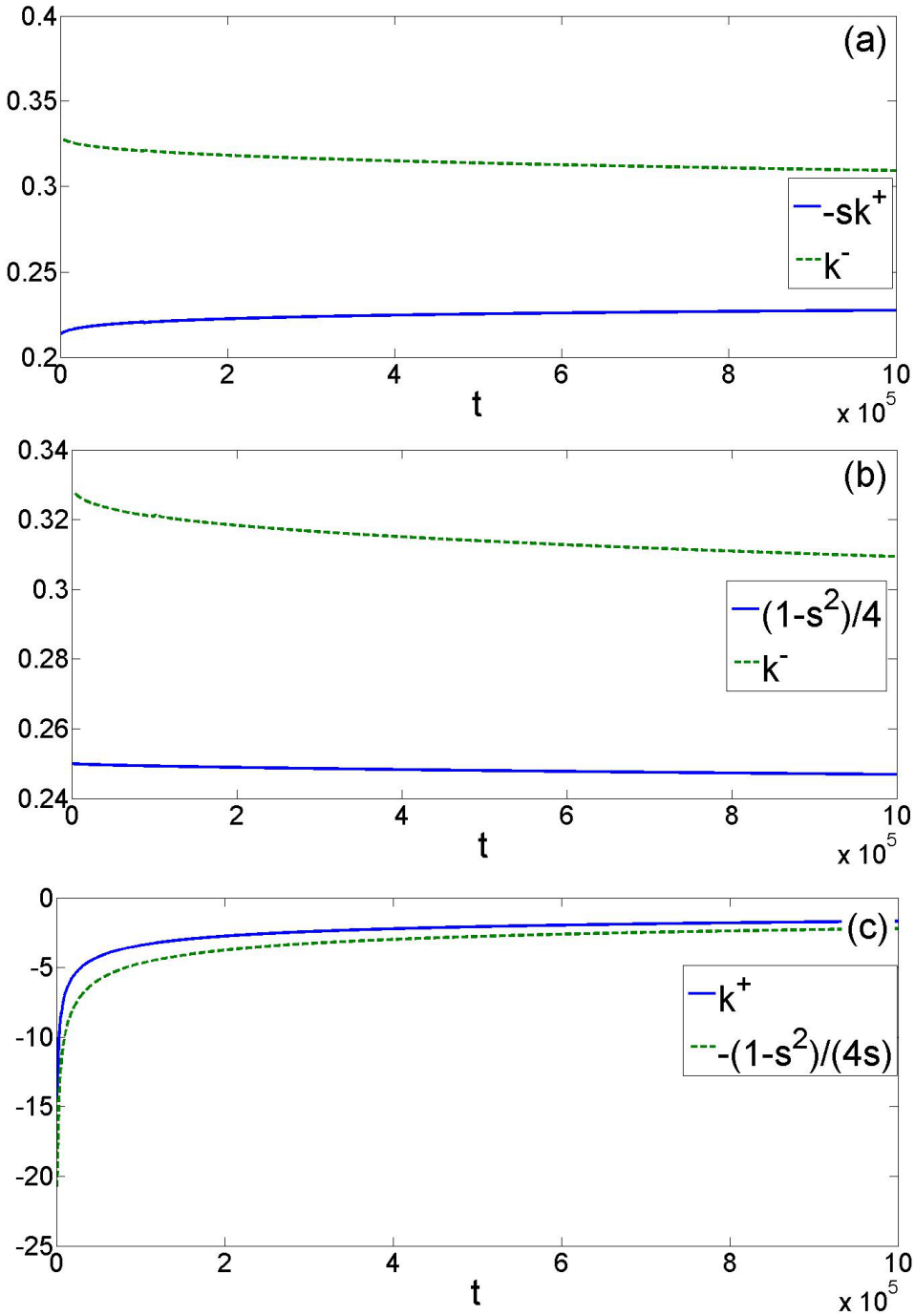

Figure 5.5: Testing the validity of (a) Eq.(5.30), (b) $k^- = (1-s^2)/4$ and (c) $k^+ = -(1-s^2)/(4s)$.

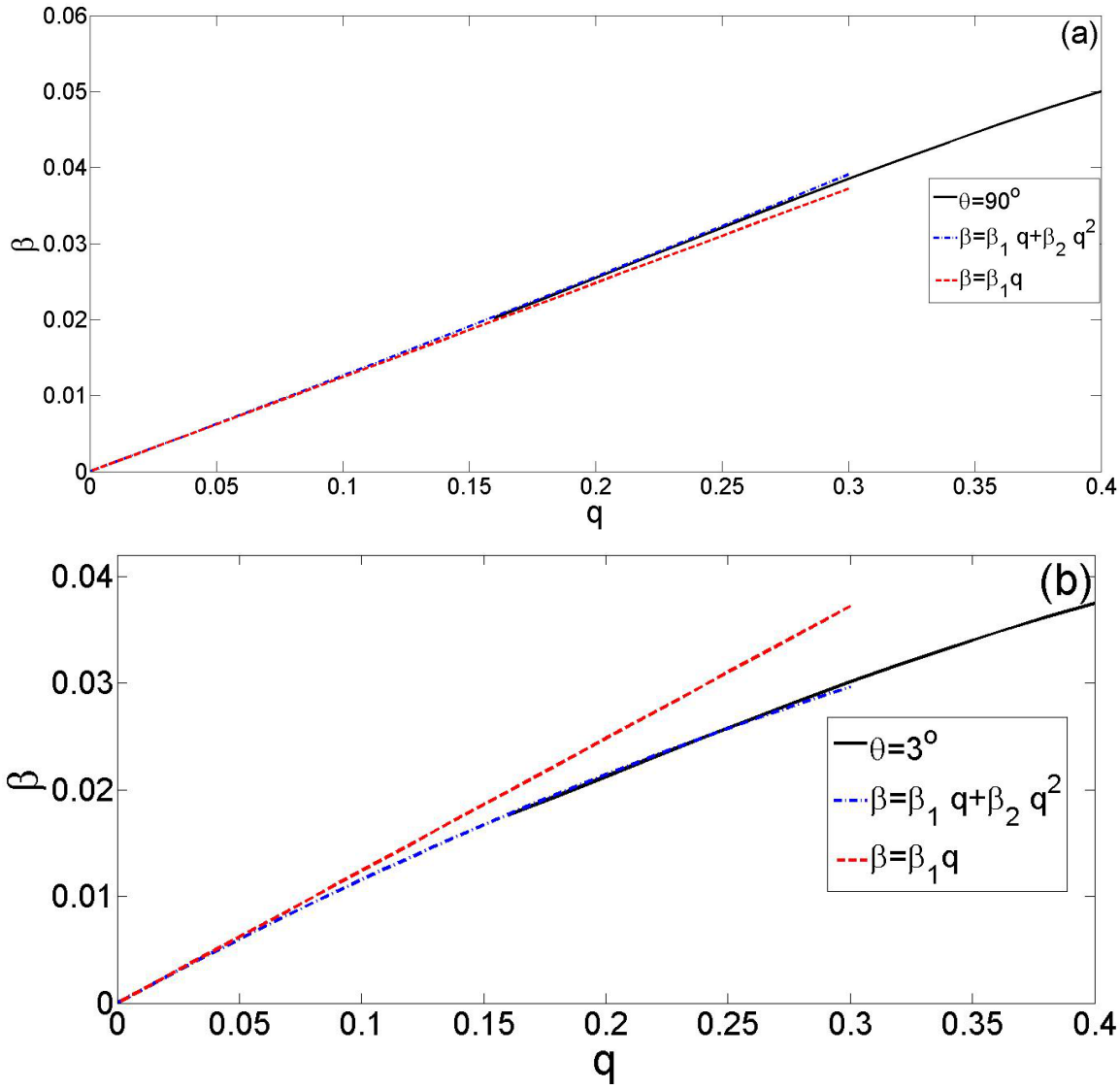

Figure 5.6: Comparing large-time numerical dispersion relation (solid lines) to the small wavenumber approximation, $\beta \approx \beta_1 q$ (dashed lines) and $\beta \approx \beta_1 q + \beta_2 q^2$ (dot-dashed lines) for $s = 0.0844$, $k^- = -2$ for an inclination angle of (a)$\theta = 90^o$ and (b) $\theta = 3^o$.

5.2 Two-dimensional numerical simulations and nonlinear stability.

In this section, we examine the nonlinear stability to transverse perturbations of the base state flow discussed in detail in Chapter 4. The two-dimensional problem is given by Eqs. (4.40,4.42) and can be written as,

$$h_t + \left[Ca\frac{h^3}{3}(h_{xxx} + h_{yyx}) - \hat{D}(\theta)\frac{h^3}{3}h_x - M\frac{h^2}{2}\Gamma_x \right]_x + \left[Ca\frac{h^3}{3}(h_{yyy} + h_{xxy}) - \hat{D}(\theta)\frac{h^3}{3}h_y - M\frac{h^2}{2}\Gamma_y \right]_y + \left[\frac{h^3}{3} \right]_x = 0, \tag{5.37}$$

$$\Gamma_t + \left[Ca\frac{h^2\Gamma}{2}(h_{xxx} + h_{yyx}) - \hat{D}(\theta)\frac{h^2\Gamma}{2}h_x - Mh\Gamma\Gamma_x \right]_x + \left[Ca\frac{h^2\Gamma}{2}(h_{yyy} + h_{xxy}) - \hat{D}(\theta)\frac{h^2\Gamma}{2}h_y - Mh\Gamma\Gamma_y \right]_y + \left[\frac{h^2\Gamma}{2} \right]_x - \frac{\Gamma_{xx}}{Pe} = 0. \tag{5.38}$$

for $-L_1 \leq x \leq L_2$ and $-1/q \leq y \leq 1/q$, where q is the wavenumber of a perturbation in the y direction and L_1, L_2 are arbitrarily chosen lengths. These equations are supplemented by six boundary conditions in the x direction which are,

$$h = b, \quad h_x = 0, \quad \Gamma = 0, \quad \text{at} \quad x = -L_1, L_2, \tag{5.39}$$

and periodic boundary conditions in the transverse y direction. These boundary conditions characterise a flat precursor film and zero surfactant concentration far ahead and behind of the spreading droplet. We also define periodic boundary conditions in

the transverse direction. We follow the same procedure as in §3.2 to introduce localised periodic transverse perturbations of varying amplitude and wavenumber of the form in Eq. (3.11). These perturbations are only superimposed on the base state for droplet height, h, and not in surfactant concentration Γ. The base state is taken to be either the initial parabolic droplet shape and surfactant concentration (Eqs. (4.46,4.47)) used for the 1D simulations or quasi-steady 1D solutions for h and Γ at specific times obtained numerically in Chapter 4.

We first define a forward difference and a backward difference in the x direction by,

$$(h,\Gamma)_{x,i,j} = \frac{(h,\Gamma)_{i+1,j} - (h,\Gamma)_{i,j}}{\Delta x}, \quad (h,\Gamma)_{\tilde{x},i,j} = \frac{(h,\Gamma)_{i,j} - (h,\Gamma)_{i-1,j}}{\Delta x}. \tag{5.40}$$

We also define a forward difference and a backward difference in the y direction by

$$(h,\Gamma)_{y,i,j} = \frac{(h,\Gamma)_{i,j+1} - (h,\Gamma)_{i,j}}{\Delta y}, \quad (h,\Gamma)_{\tilde{y},i,j} = \frac{(h,\Gamma)_{i,j} - (h,\Gamma)_{i,j-1}}{\Delta y}, \tag{5.41}$$

where i is the index in the x direction and j is the index in the y direction. Where $(h,\Gamma)_{i,j} = (h,\Gamma)(x_i, y_j, t)$, $i = 0, 1, ..., N$, $j = 0, 1, ...M$. N and M are the number of discretisation points and Δx and Δy are the grid sizes in the x and y directions respectively. Using Eqs. (5.40,5.41) we can discretise Eqs. (5.37,5.38) such that,

$$\begin{aligned} h_{t,i,j} \quad & + \Big[Ca\ a(h_{i+1,j}, h_{i,j})(h_{\tilde{x}x\tilde{x}i,j} + h_{\tilde{y}y\tilde{x}i,j}) - \hat{D}(\theta)a(h_{i+1,j}, h_{i,j})h_{\tilde{x}i,j}\Big]_x \\ & + \left[-Mc(h_{i+1,j}, h_{i,j})\Gamma_{\tilde{x}i,j}\right]_x + \left[Ca\ a(h_{i,j+1}, h_{i,j})(h_{\tilde{y}y\tilde{y}i,j} + h_{\tilde{x}x\tilde{y}i,j})\right]_y \end{aligned}$$

$$+\left[-\hat{D}(\theta)a(h_{i,j+1},h_{i,j})h_{\tilde{y}i,j}-Mc(h_{i+1,j}\Gamma_{i+1,j},h_{i,j}\Gamma_{i,j})\Gamma_{\tilde{y}i,j}\right]_y+\left(\frac{h_{i,j}^3}{3}\right)_{\tilde{x}}=0, \quad (5.42)$$

$$\Gamma_{t,i,j} \quad +\left[Ca\ d(h_{i+1,j}\Gamma_{i+1,j},h_{i,j}\Gamma_{i,j})(h_{\tilde{x}x\tilde{x}i,j}+h_{\tilde{y}y\tilde{x}i,j})-\hat{D}(\theta)d(h_{i+1,j}\Gamma_{i+1,j},h_{i,j}\Gamma_{i,j})h_{\tilde{x}i,j}\right]_x$$

$$+\left[-Me(h_{i+1,j}\Gamma_{i+1,j},h_{i,j}\Gamma_{i,j})\Gamma_{\tilde{x}i,j}\right]_x+\left[Ca\ d(h_{i,j+1}\Gamma_{i,j+1},h_{i,j}\Gamma_{i,j})(h_{\tilde{y}y\tilde{y}i,j}+h_{\tilde{x}x\tilde{y}i,j})\right]_y$$

$$+\left[-\hat{D}(\theta)d(h_{i,j+1}\Gamma_{i,j+1},h_{i,j}\Gamma_{i,j})h_{\tilde{y}i,j}-Me(h_{i,j+1}\Gamma_{i,j+1},h_{i,j}\Gamma_{i,j})\Gamma_{\tilde{y}i,j}\right]_y$$

$$+\left(\frac{h_{i,j}^2\Gamma_{i,j}}{2}\right)_{\tilde{x}}=0 \quad (5.43)$$

where,

$$a(h_{i+1,j},h_{i,j})=\frac{h_{i+1,j}^3+h_{i,j}^3}{6},\quad a(h_{i,j+1},h_{i,j})=\frac{h_{i,j+1}^3+h_{i,j}^3}{6},$$
$$c(h_{i+1,j},h_{i,j})=\frac{h_{i+1,j}^2+h_{i,j}^2}{4},\quad c(h_{i,j+1},h_{i,j})=\frac{h_{i,j+1}^2+h_{i,j}^2}{4},$$
$$d(h_{i+1,j}\Gamma_{i+1,j},h_{i,j}\Gamma_{i,j})=\frac{h_{i+1,j}^2\Gamma_{i+1,j}+h_{i,j}^2\Gamma_{i,j}}{4},$$
$$d(h_{i,j+1}\Gamma_{i,j+1},h_{i,j}\Gamma_{i,j})=\frac{h_{i,j+1}^2\Gamma_{i,j+1}+h_{i,j}^2\Gamma_{i,j+1}}{4},$$
$$e(h_{i+1,j}\Gamma_{i+1,j},h_{i,j}\Gamma_{i,j})=\frac{h_{i+1,j}\Gamma_{i+1,j}+h_{i,j}\Gamma_{i,j}}{2},$$
$$e(h_{i,j+1}\Gamma_{i,j+1},h_{i,j}\Gamma_{i,j})=\frac{h_{i,j+1}\Gamma_{i,j+1}+h_{i,j}\Gamma_{i,j+1}}{2}.$$

Leaving the time derivative continuous we obtain a system of ODE's which is solved using the Fortran ODE solver DDASPK [10]. The grid size in the x direction was taken to be $\Delta x = 0.01$ and the number of discretisation points in the y direction $Q = 100$ which sufficiently resolved the solution structure. We will begin by exploring the stability a superposition of transverse perturbations on initial conditions prescribed for the 1D solution in Section 4.2, Eqs. (4.46,4.47). The localised perturbation is imposed

at the origin, so $x_{0l} = 0$. The base parameter values for the numerical simulations are: $b = 0.1$, $Ca = 10^{-3}$, $M = 0.1$, $Pe = 10^5$ and $\theta = 90^o$. Figure 5.7 shows the evolution of the fluid surface and surfactant concentration, for a perturbation of wavelength $q_k = 1$ and amplitude $A_k = 0.1$ at time $t = 20$. As time progresses, the fluid in the perturbed region flows at a quicker speed than where the fluid height is lower thus forming a finger. The surfactant gets 'swept' to the outside of the finger causing surfactant contrition gradient to form which draw more fluid into the finger promoting growth. The finger initially has width similar to the wavelength of the perturbation that was initially prescribed. The finger also flows over the fluid front ahead of the leading edge as the surfactant concentration gradients die out this is consistent with Edmonstone *et al.* and Mavromoustaki. Figure 5.9 shows the two dimensional evolution of the fluid surface and surfactant concentration, for a perturbation of wavelength $q_k = 2$ and amplitude $A_k = 0.1$ at time $t = 20$. We can see that by varying the wavelength of the perturbations we can vary the wavelength and growth rate of the protrusions. We observe that initially the perturbations grow with the same wavenumber that was initially prescribed. As the flow develops the fingers go to a preferred wavelength (measured as finger width). This wavelength is width is smaller than that observed of the gravity-driven flow (see Fig. 3.14). By comparing the dispersion curves for gravity and gravity and surfactant-driven flow, we see that the wavenumber corresponding to the maximum growth rate is larger for the gravity and surfactant-driven flow thus the wavelength of the observed finger should be smaller. It can be seen that from these figures at early time the fluid advects the surfactant along so that the maximum

surfactant concentration is at the same location as the maximum droplet height. The contour plots (Figs. 5.8,5.10) show that at early time behind the maximum surfactant concentration is a 'well' in the surfactant concentration behind it. As time progresses, the surfactant gets swept to either side of the domain (see Fig. 5.10(b)). Thus resulting transverse surfactant concentration gradients generate surface tension gradient-driven flows pulling fluid into the finger. This further destabilises the flow and promotes finger development. This is consistent with the results of Mavromoustaki *et al.* [48, 46].

We now examine the stability for h and Γ of the flow using a base state (h_b) obtained numerically at for $b = 0.01$, $Ca = 10^{-3}$, $\theta = 90^o$ and $M = 0.1$ at $t = 100$. We introduce transverse perturbations to the base state at the capillary ridge. We add the perturbations with $q_k = 0.5, 1, 5, 10, 15, 25, 30$, amplitude $A_k = 0.1$, at the capillary ridge $K = 100$. Figure 5.11 shows the leading edge of the droplet is linearly unstable initially some perturbations decay and others grow. At late times ($t = 100$) four fingers form of the same wavelength (measured as finger width). This can be seen more clearly in Fig. 5.12 that the fingers have width≈ 0.2. For larger times (not shown here) four fingers of width ≈ 0.2 develop and propogate down the inclined plane. The surfactant concentration is greater outside of the fingers this promotes finger growth as discussed earlier.

Figures 5.13(a,b), 5.14(a,b) shows the fluid interface and contour plots, respectively, for the flow from the initial condition with $M = 1$, $q_k = 1$, $b = 0.1$ and $x_{0l} = 0$. It can be seen from Fig. 5.14(a,b) that the length of the finger is longer with smaller

Marangoni number. This is because the surface tension gradients which promote the development of the fingering behaviour form at an earlier time. We also not the the surfactant is not swept to either side of the domain. Hence this is in agreement with Mavroumoustaki *et al.* who stated that it was the surfactant concentration gradient being larger outside the base of the finger which aids the growth of the finger.

Figure 5.15 show the comparison between the length of the fingers when the precursor film is thinned for $M = 0.1$, $q_k = 1$ $x_{0l} = 0$ for the precursor films $b = 0.1$, and 0.001. The length of the finger vary from 1.5-1.8.

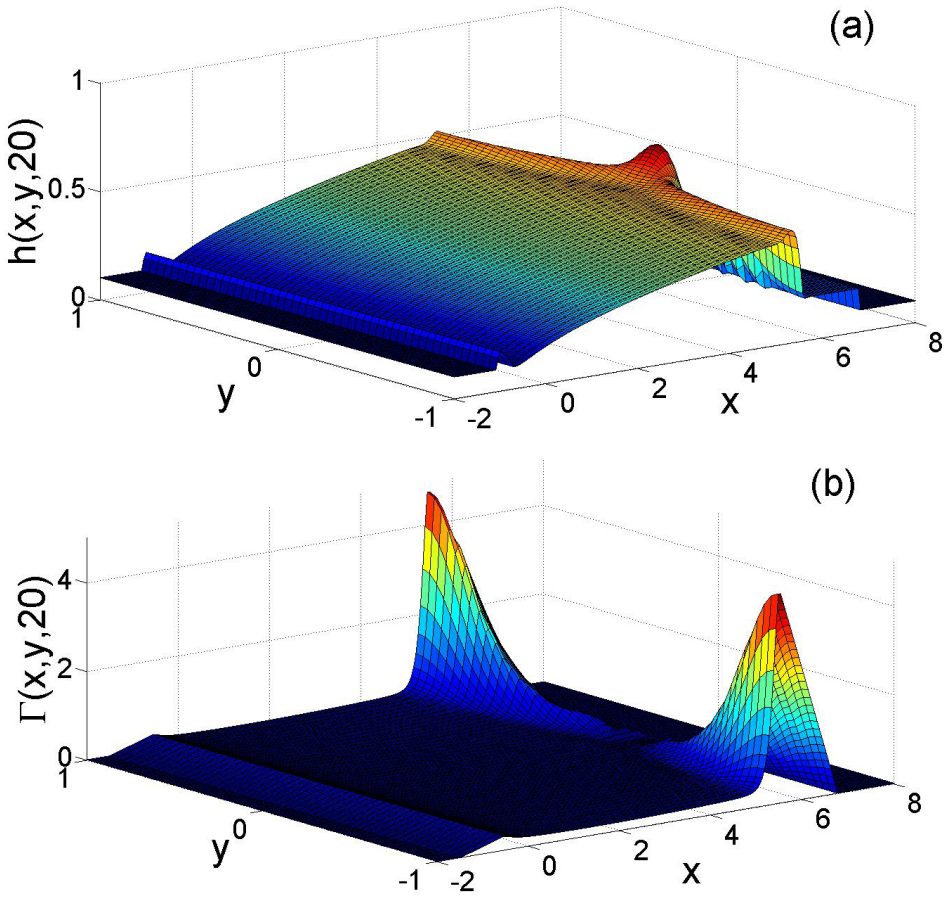

Figure 5.7: Surface plots for (a) the fluid interface h (b) the surfactant concentration Γ at time $t = 20$, $M = 0.1$, $b = 0.1$, $\theta = 90^o$ and $Pe = 10^5$. From the initial conditions in with perturbations in the transverse direction of amplitude $A_i = 0.1$, wavenumber $q_i = 1$.

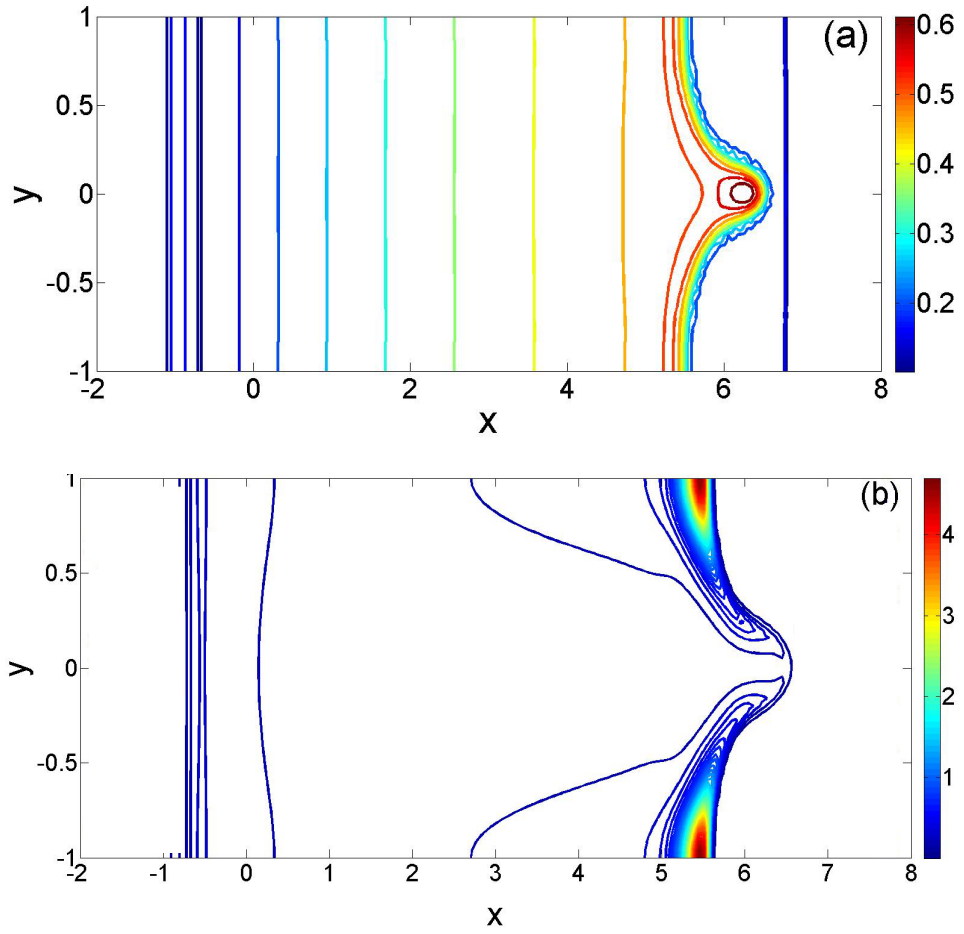

Figure 5.8: Contour plots for (a) the fluid interface h (b) the surfactant concentration Γ at time $t = 20$, $M = 0.1$, $b = 0.1$, $\theta = 90^o$ and $Pe = 10^5$. From the initial conditions in with perturbations in the transverse direction of amplitude $A_i = 0.1$, wavenumber $q_i = 1$.

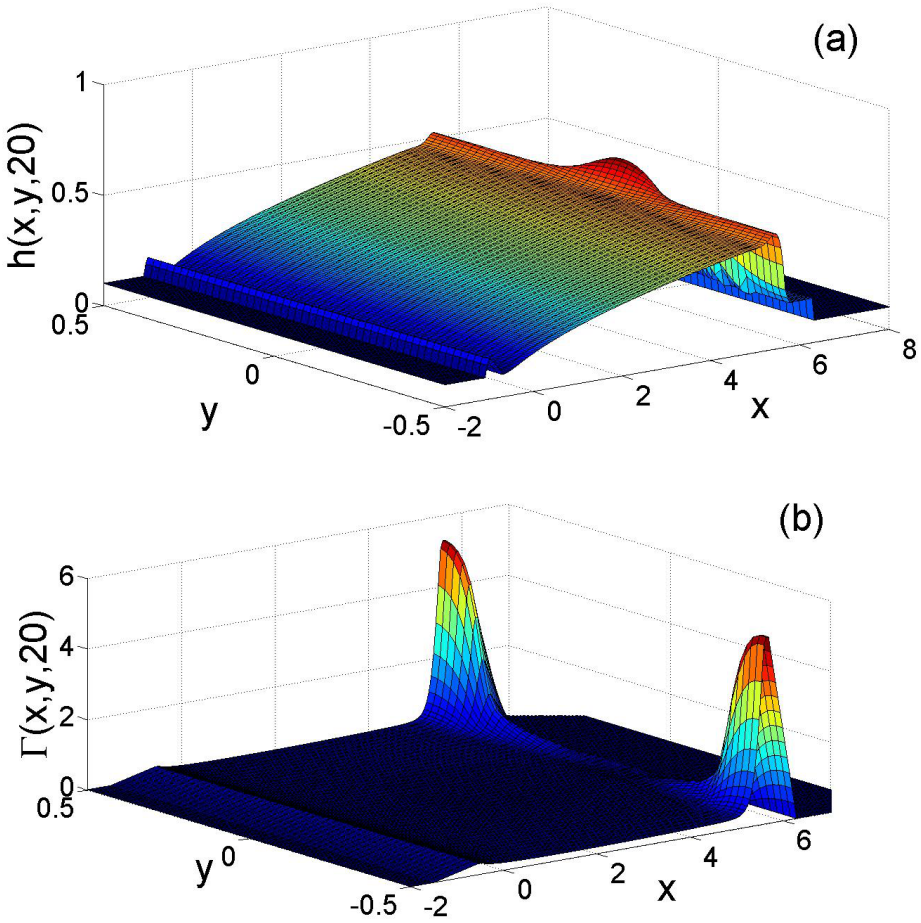

Figure 5.9: Surface plots for (a) the fluid interface h (b) the surfactant concentration Γ at time $t = 20$, $M = 0.1$, $b = 0.1$, $\theta = 90^o$ and $Pe = 10^5$. From the initial conditions in with perturbations in the transverse direction of amplitude $A_i = 0.1$, wavenumber $q_i = 2$.

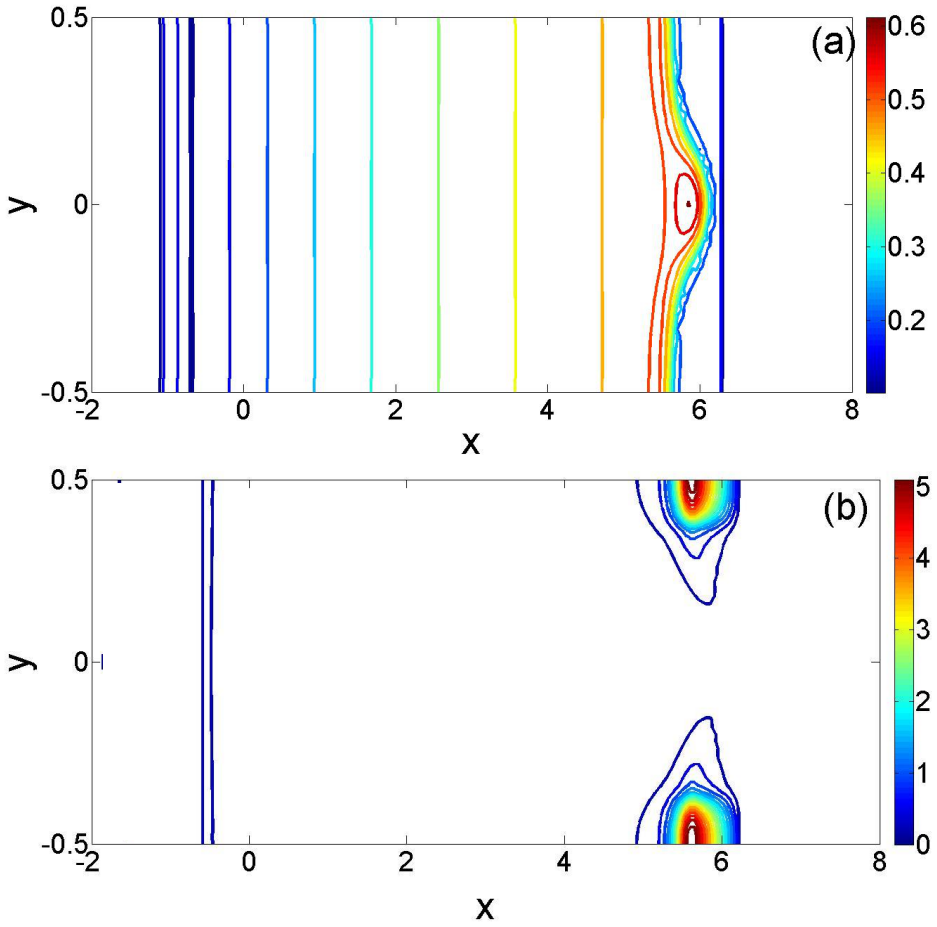

Figure 5.10: Contour plots for (a) the fluid interface h (b) the surfactant concentration Γ at time $t = 20$, $M = 0.1$, $b = 0.1$, $\theta = 90^o$ and $Pe = 10^5$. From the initial conditions with perturbations in the transverse direction of amplitude $A_i = 0.1$, wavenumber $q_i = 2$.

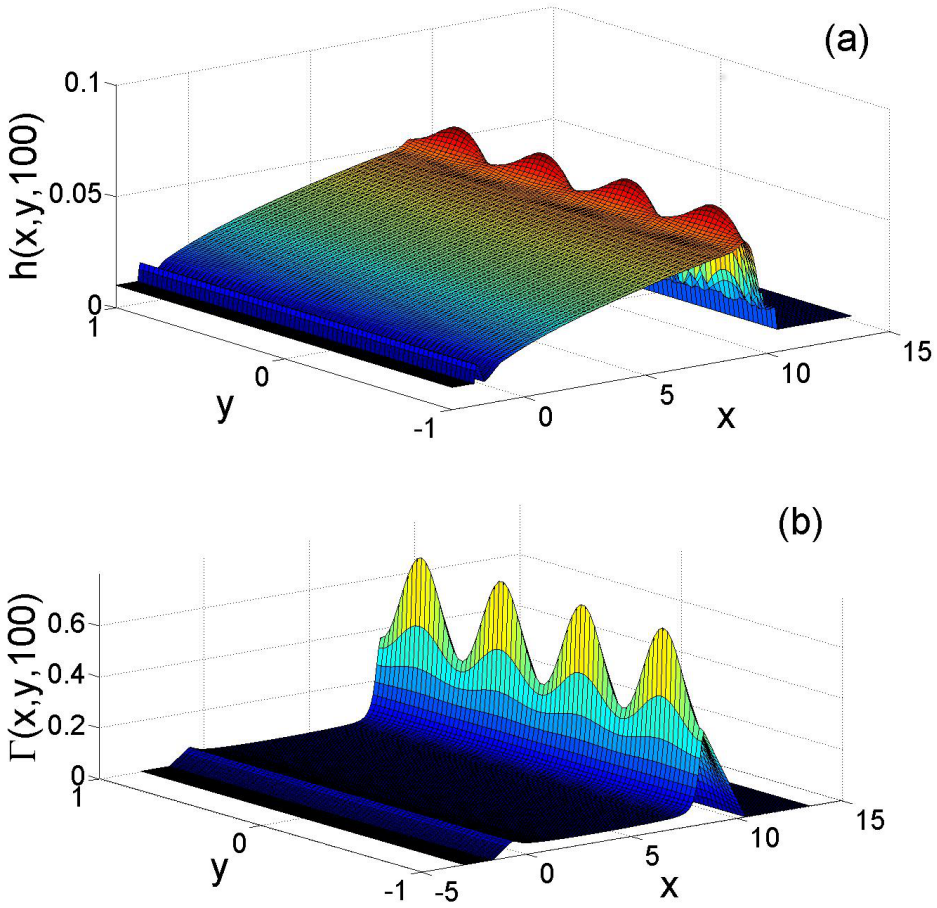

Figure 5.11: Surface plots showing the 2-D evolution of the (a) fluid interface h (b) surfactant concentration Γ at time $t = 100$, $M = 0.1$, $b = 0.01$, $\theta = 90^o$ and $Pe = 10^5$. From the initial conditions with perturbations in the transverse direction of amplitude $A_i = 0.1$, wavenumber $q_i = 0.5, 1, 5, 10, 15, 25, 30$.

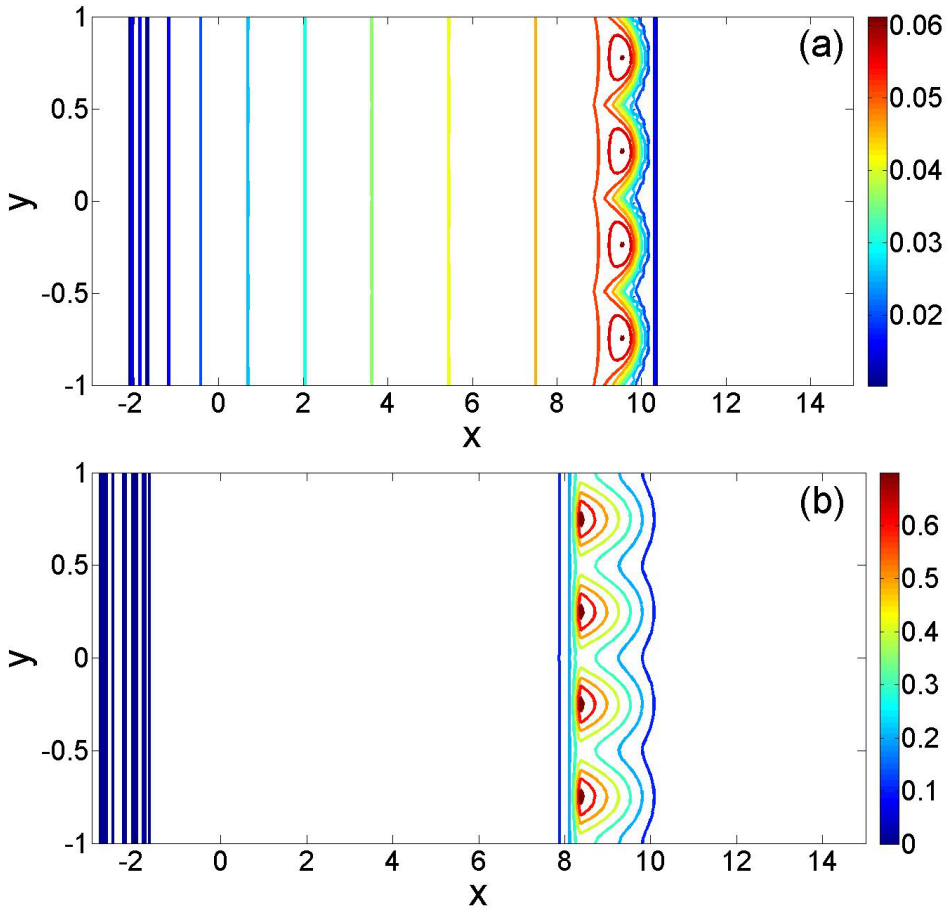

Figure 5.12: Contour plots showing the 2-D evolution of the (a) fluid interface h (b) surfactant concentration Γ at time $t = 100$, $M = 0.1$, $b = 0.01$, $\theta = 90^o$ and $Pe = 10^5$. From the initial conditions with perturbations in the transverse direction of amplitude $A_i = 0.1$, wavenumber $q_i = 0.5, 1, 5, 10, 15, 25, 30$.

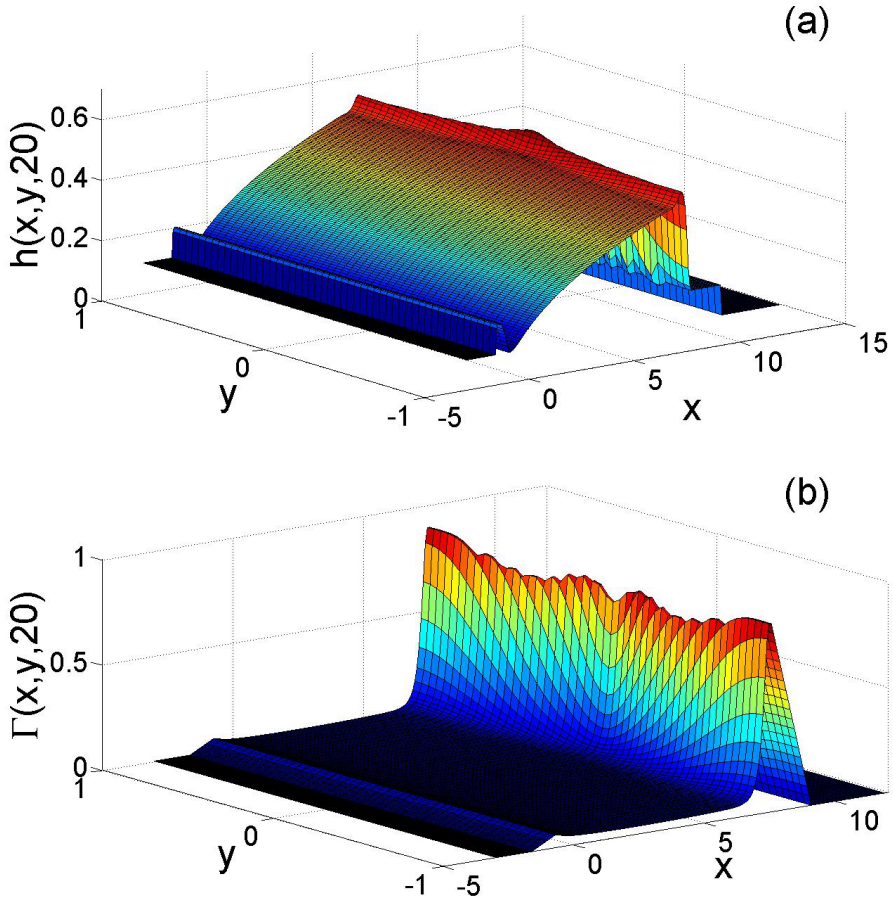

Figure 5.13: Surface plot for the (a)droplet height (b) surfactant concentration for $A_i = 0.1$, $q_i = 1$ and $M = 1$ at time $t = 10$.

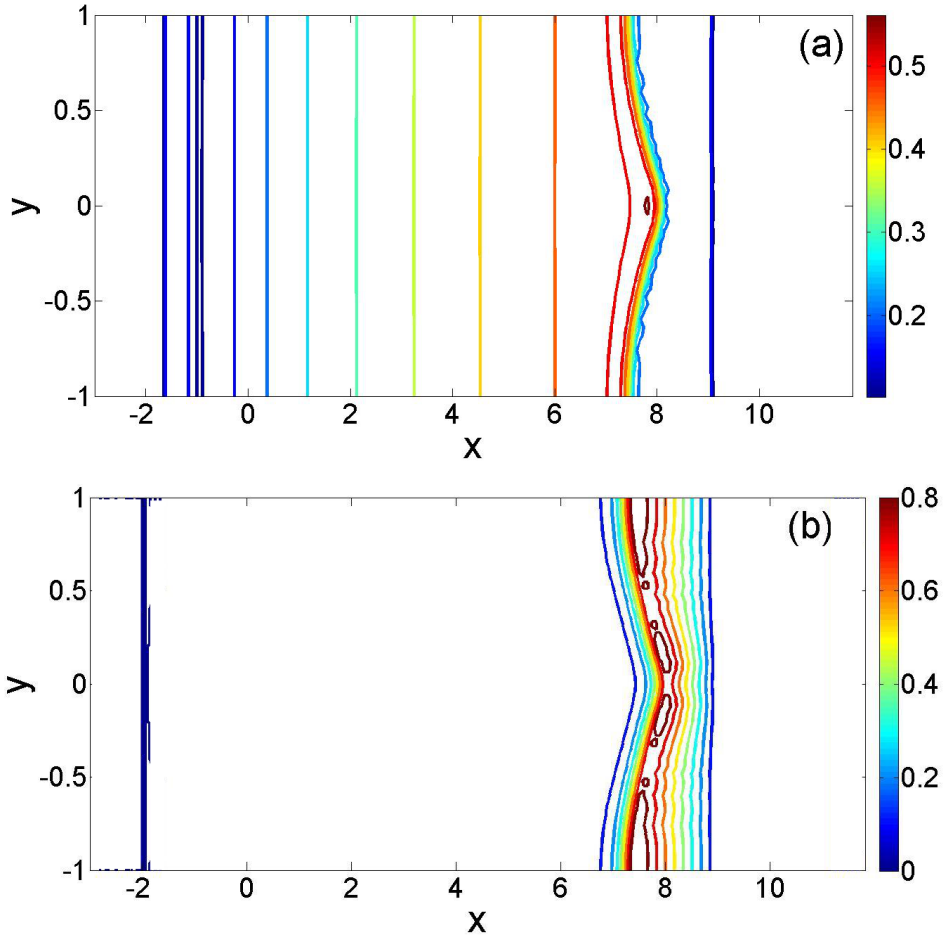

Figure 5.14: Contour for the (a)droplet height (b) surfactant concentration for $A_i = 0.1$, $q_i = 1$ and $M = 1$ at time $t = 10$.

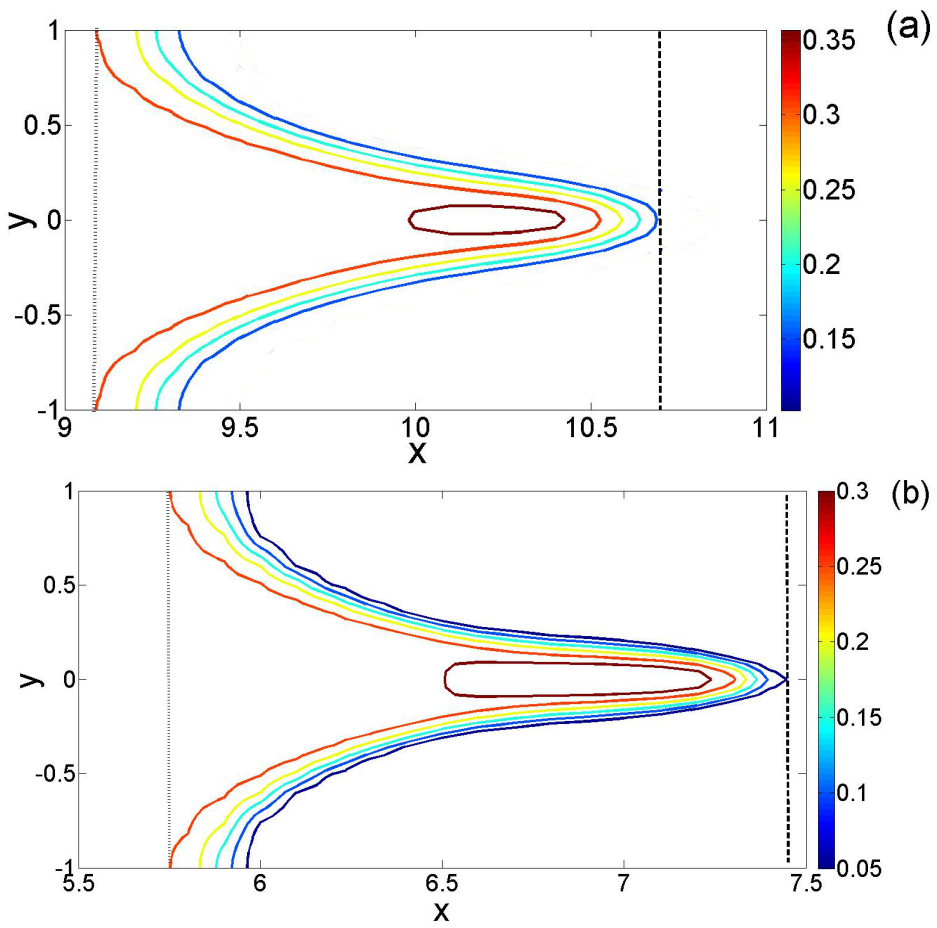

Figure 5.15: Contour plot of the finger formed for $A_i = 0.1$, $q_i = 1$ and $M = 0.1$ at time $t = 100$ for precursor film thickness $b =$(a)0.1, (b)0.001.

5.3 Concluding remarks

This chapter analyses the stability of a thin viscous surfactant laden fluid droplet, of constant volume, flowing down an inclined pre-wetted plane using linear stability analysis and 2-D simulations. We undertook a linear stability analysis of the 'effective' contact line region which we believe that the onset of the fingering instability originate from. We undertook a linear stability analysis of the 'effective' contact line region at the leading edge of the droplet (region A). We showed that this region to be linearly unstable to long-wavelength transverse perturbations by solving Eqs. (5.3,5.4) numerically as an IVP. The wavelength of the most unstable wavenumber are comparable to the length scale of this region, which confirms the speculation that the onset of fingering is initiated here. This is in agreement with the transient growth analysis performed by of Edmonstone *et al* [15, 12, 13], as well as the LSA undertook by Mavromoustaki *et al.* [46, 48] furter more we showing that the addition of surfactant had a destabilising effect is in agreement with the TGA undertaken by other researchers. We demonstrated that this region become less linearly unstable as time progressed and as the angle of inclination was decreased. Comparing the linear stability of this region to the leading edge region of the gravity-driven flow we see that the addition of insoluble surfactant has an additional destabilising effect. Furthermore we demonstrated that the leading order behaviour for the surfactant and gravity-driven case was markedly different than the solely gravity-driven case. This motivated us to undertake a small wavenumber analysis expanding in powers of wavenumber and were able to obtain a

stability criterion. This stability criterion supports the results that as time increases this region becomes less linearly unstable, as $s = 2b/h_{L^-}$ increases with time. Equation (5.31) also indicates that the thinner the precursor film the more linearly unstable the flow is. Moreover it concludes that this region is linearly unstable for all inclination angles θ. This is due to the fact for all angles of inclination the stability criterion is met. The Marangoni effect is shown to be the dominant driving mechanism behind this instability at small inclination angles. This stability criterion shows that even at small inclination angles, where a solely gravity-driven flow is linearly stable, surfactant related effects destabilise the front. Equation (5.29) compares the relative surfactant flux ahead and behind the 'effective' contact line. A mechanism for the flow to become linearly unstable at $O(q)$ is due to the forward Marangoni flux behind the contact line drawing more fluid into the contact line region than the forward Marangoni flux ahead of the contact line region dragging fluid out. This results in growth of the perturbations in h consequently destabilising the flow and the constant line (consistent with Fig. 5.1 where $\hat{H}$ is positive and growing immediately behind the contact line (and ahead of the capillary ridge) coinciding with $\hat{G}_\xi$ which is negative there). If we consider the speed of the front, $\dot{x}_L = \hat{V} h_{L^-}^2$, where $\hat{V} = (1 + s + s^2)/12 - (k^- - 1/2)/2$, now consider transverse perturbations in H and G noting that where there is a positive perturbation in H there is a negative one in G. The negative perturbation in G means that where there is the positive perturbation in H there is high surface tension and where there is a negative perturbation in H there is low surface tension. Therefore fluid is drawn into the region increasing the magnitude of the positive perturbation and therefore h_{L^-} and

therefore it will flow quicker than the one with the negative perturbation.

We also obtained the $o(q^2)$ growth rate and showed that out small wavenumber approximation is a very good match for the numerical dispersion relation. At $o(q^2)$ the capillary term, which is the same as that derived by Troian *et al* [63], competes with the Marangoni term. We observe from the calculation of Eq. (5.36) that the capillary is of a similar magnitude to the Marangoni term, however the capillary term is slightly more than the Marangoni term for 90^o hence the $o(q^2)$ is a small positive correction to the o(q) small wavenumber approximation. This is due to the large contribution from the capillary ridge. The large negative contribution to the Marangoni term is due to the large surfactant concentration gradient just upstream of the maximum surfactant concentration, Γ_L. As the inclination angle decreases so does the contribution capillary ridge and therefore the capillary term. The effects of the Marangoni term becomes less negative however at a lesser rate than the capillary term. Hence at small inclination angles the $o(q^2)$ correction is negative. The small wavenumber approximations matched well with the numerically obtained dispersion curves giving weight to our claim that the leading order behaviour is linear with wavenumber.

The two-dimensional simulations supports the claim from the linear stability analysis that the surfactant concentration gradient is important for the flow to become linearly unstable. We were also able to show that, as in the 2-D simulations for the gravity-driven flow, there is a preferred wavenumber which is the most unstable wavelength and is consistent with the LSA undertaken. Also note that the LSA undertaken show that

the surfactant concentration gradients behind the effective contact line are important for the instability to grow. Finally we observe that wherever a positive perturbation to h occurs a negative perturbation to Γ develops. We also see that the fingers are more developed here in comparison to the gravity-driven spreading (see Fig. 3.14). Therefore we clearly see that the addition of the surfactant destabilises the flow supporting the claims made by the LSA. In the LSA the wavenumber correlating to maximum growth rate appears to be fixed ($q_{max} \approx 0.8 = q^*_{max}(Cah_L)^{1/3}$). We can calculate the wavelength of fingers correlating to $q_{max} \approx 0.8$, taking $h_L = 1$ and $Ca = 10^{-3}$ hence, we obtain $q^*_{max} = 8/\pi \approx 2.5$. This indicates from the initial parabolic drop shape we should observe that fingers of width ≈ 0.4. Fingers become thinner, less unstable and more in number for perturbations to the quasi-steady base state obtained over increasing times. As $q_{max} \approx 0.8$ and is approximately fixed with time we calculate that for a quasi-steady 1D solution calculated in Chapter 4. Hence, we speculate that we can predict the width and number of fingers that develop depending on the initial conditions which is perturbed. However for multiple fingers to be observed we need interaction between wavenumbers where some are decaying and others growing. Also note that the LSA undertaken show that the surfactant concentration gradients behind the effective contact line are important for the instability to grow. Finally we observe that wherever a positive perturbation to h occurs a negative perturbation to Γ develops. We also see that the fingers are more developed here in comparison to the gravity-driven spreading (see Fig. 3.14). Therefore we clearly see that the addition of the surfactant destabilises the flow supporting the claims made by the LSA. The flow

becomes more unstable by thinning the precursor film.

As with the gravity-driven stability by varying the initial condition we can vary the preferred wavelength of fingers. In the LSA the wavenumber correlating to maximum growth rate appears to be fixed ($q_{max} \approx 0.8 = q^*_{max}(Cah_L)^{1/3}$). We can calculate the wavelength of fingers correlating to $q_{max} \approx 0.8$, taking $h_L = 0.3$ and $Ca = 10^{-3}$ hence, we obtain $q^*_{max} = 5/\pi \approx 4.3$. This means we should observe a maximum of 4 fingers of equal width.

We also showed that by increasing the Marangoni number stabilised the flow as the fluid was not swept to the outside of the domain as readily the transverse Marangoni fluxes are not drawing fluid into the finger and therefore do not promote destabilise the flow as much as smaller marangoni number. By thinning the precursor film the flow destabilised. Although the length of the fingers were of a similar magnitude we can explain this as follows. At this prescribed wavenumber there may not by a large difference between the growth rates (see approximately small wavenumber Fig. 5.2) and therefore the length of the finger, although slightly different in length, are similar in magnitude. This is in agreement with the LSA and similar to that discussed in Section 5.1.

This concludes our stability analysis of the spreading of a viscous fluid droplet, with and without insoluble surfactant, down an inclined pre-wetted plane.

Chapter 6

Conclusions and future work

In this thesis we have theoretically modelled a viscous droplet spreading down an inclined pre-wetted plane due to gravity alone as well including surfactant-related effects using high-resolution numerics and asymptotic analysis. The evolution of a droplet, of constant volume spreading due to gravity alone has been well studied. However, our results for the spreading of a surfactant laden droplet of constant volume provide insights into some important physical mechanisms that were not accessible from previous computational studies. Particularly, the existence of the fluid 'hump' region and the late-time structures observed upstream of the trailing edge of the spreading droplet. We obtained novel approximate solutions for the regions downstream of the trailing edge based on the competing physical mechanisms. A key finding of this study was found when investigating the stability of the 'effective' contact line region (region A). We showed convincingly that the fingering instabilities originate from this region.

Moreover, the flow is shown to be linearly unstable for all angles of inclination. A small wavenumber analysis demonstrated that at long wavelength the growth rate is a linear function of wavenumber. A stability criterion in this limit was derived and the Marangoni effect was shown to be responsible for the instability in the small wavenumber limit. Jensen and Naire [32], while investigating the spreading of a viscous fluid droplet laden with surfactant on a horizontal plane. have also shown the growth rate to vary linearly with wavenumber in the small wavenumber limit. This suggests that maybe there is a smooth transition in the stability behaviour between the spreading on an inclined plane with that on a horizontal plane as the angle of inclination is decreased. This requires further investigation and is planned for future work.

This study, shows that the addition of surfactant has an added destabilising effect. Our results show that the fingers observed when surfactant is present are smaller in width when compared to the fingers observed when spreading occurs due to gravity alone. We therefore predict that more fingers should be observed when surfactant is present. In light of this we note that the addition of surfactant results in a larger number of undesirable dry spots when compared to gravity-driven spreading alone. We recommend that the addition of surfactant would not be beneficial to applications that require a uniform coating of a substrate. Where the addition of surfactant is necessary to the application, such as in surfactant replacement therapy, it would be preferable to choose a surfactant with a large Marangoni number. We observe that for larger Marangoni numbers the surfactant is not swept from the base of the finger

as readily and therefore does not promote growth of the instability in comparison to smaller Marangoni numbers.

There are limitations to this study. Our scalings are based on the horizontal component of gravity and as the angle of inclination is reduced towards the horizontal the scalings break down. If we wished to study the small inclination angle limit we would have to use the scalings based on the Marangoni number. This would allow comparisons to be with surfactant-laden drop spreading on a horizontal plane. Lubrication approximation is not valid where there are steep changes in fluid height. We see that at the leading edge of the spreading droplet there are large gradients. Therefore, to test the validity of our results full numerical simulations of the Navier-Stokes equations and boundary conditions would need to be undertaken using, for example, boundary element methods. With respect to the 2-D results obtained for the nonlinear stability of the flow, we have only examined periodic perturbations to the base state. The perturbations may not be periodic in a real case scenario, hence the fingers observed experimentally may not match precisely to those predicted from this study.

The two-dimensional simulations for the gravity-driven flow indicated that the trailing edge of the bulk droplet appearred marginally stable. As part of future work we will analyse the linear stability of this region using the as a base state the solution of the boundary value problem for the trailing edge of the droplet derived in §2.4.3. Another extension to this work is to explore the effect of soluble surfactants. We do not believe that the overall flow would be dramatically affected with the inclusion of a soluble

surfactant and therefore the structure obtained here should still be observed. Another future direction is to consider the stability of the spreading of a fluid film down a prewetted inclined plane from a constant flux source. The 'effective' contact line region for thus problem can be described by the same boundary value problem given by Eqs. (4.87, 4.88) in Chapter 4. The linear stability of this base state should then follow along similar lines as done here. Finally, we wish to obtain some experimental results to verify what has been obtained theoretically in this work. To the best of our knowledge there has been no experimental results published for a surfactant laden drop spreading down an inclined plane. We hope that our results, once published would provide motivation for doing this.

Bibliography

[1] D. Acheson, *Elementary Fluid dynamics*, Oxford University Press, 1998.

[2] A. Afsar-Siddiqui, P. Luckham, and O. Matar, *The spreading of surfactant solutions on thin liquid films*, Adv. Colloid Interface Sci., 106 (2003), pp. 183–236.

[3] ——, *Unstable spreading if aqueous anionic surfactant solutions on liquid film. 2. highly soluble surfactant*, Langmuir, 19 (2003), pp. 703–708.

[4] ——, *Unstable spreading if aqueous anionic surfactant solutions on liquid film. 2. sparingly soluble surfactant*, Langmuir, 19 (2003), pp. 696–702.

[5] ——, *Dewetting behavior of aqueous cationic surfactant solutions on liquid films*, Langmuir, 20 (2004), pp. 7575–7582.

[6] C. Ancey, *Plasticity and geophysical flows: a review*, J. Non-Newt Fluid Mech., 142 (2007), pp. 4–35.

[7] A. Bernoff, A. Bertozzi, and T. Witelski, *Axisymmetric surface diffusion: Dynamics and stability of self-similar pinch-off*, Notices Amer. Math. Soc., 45 (1998).

[8] A. Bertozzi and M. Brenner, *Linear stability and transient growth in driven contact lines*, Phys. Fluids, 9 (1997), pp. 530–539.

[9] K. Brennan, S. Campbell, and L. Petzold, *Numerical solution of initial-value problems in differentialalgebraic equations*, Philadelphia, 1996.

[10] P. Brown, A. Hindmarsh, and L. Petzold, *Using krylov methods in the solution of large-scale differential- algebraic systems*, SIAM J. Sci. Comput., 15 (1994), pp. 1467–1488.

[11] E. Dussan and S. Davis, *On the mothion of a fluid-fluid interface along a solid surface*, J. Fluid Mech, 65 (1974), pp. 71–95.

[12] B. Edmonstone, O. Matar, and R. Craster, *Coating of an inclined plane in the presence of insoluble surfactant*, J. Colloid Interface Science, 287 (2005), pp. 261–272.

[13] ——, *Surfactant-induced fingering phenomena in thin film flow down an inclined plane*, Physica D, 209 (2005), pp. 62–79.

[14] B. Edmonstone, O. Matar, and R. Craster, *A note on the coating of an inclined plane in the presence of soluble surfactant.*, J. Colloid Sci., 293 (2006), pp. 222–229.

[15] B. Edmonstone, O. Matar, and C. R., *Flow of surfactant-laden thin films down an inclined plane*, J. Engrg. Maths, 50 (2004), pp. 141–156.

[16] D. Edwards, H. Brenner, and D. Wasan, *Interfacial Transport Processes and Rheology*, Butterworth-Heinemann, 1991.

[17] C. D. Eggleton, *Insoluble surfactants on a drop in an extensional flow: a generalization of the stagnated surface limit to deforming interfaces*, J. Fluid Mech, 385 (1999), pp. 79–99.

[18] M. Eres, L. Schwartz, and R. Roy, *Fingering phenomena for driven coating films.*, Phys. Fluids, 12 (2000), pp. 1278–1295.

[19] F. Fowler, H. Fowler, and D. Thompson, *The Oxford Pocket Dictionary of Current English*, Oxford Univ. Pr., 8 ed., 2000.

[20] A. Frumkin, *Electrocapillary curve of higher aliphatic acids and the state equation of the surface layer*, Z. Phys. Chem., 116 (1925).

[21] H. Greenspan, *On the motion of a small viscous droplet that wets a surface*, J. Fluid Mech., 84 (1978), pp. 125–143.

[22] R. Griffiths, *The dynamics of lava flows.*, Annu. Rev. Fluid Mech., 32 (2000), pp. 477–518.

[23] J. Grotberg, *Pulmonary flow and transport phenomena*, Annual Review Fluid Mech., 26 (1994), pp. 529–571.

[24] ——, *Respiratory fluid mechanics and transport processes*, Annu Rev Biomed Eng., 3 (2001).

[25] L. Hocking, *Spreading and instability of a viscous fluid sheet*, J. Fluid Mech, 211 (1990), pp. 373–392.

[26] C. Huh and L. Scriven, *Hydrodynamical model of steady movement of a solid/liquid/fluid contact line*, J. Colloid Interface Sci., 35 (1971), pp. 85–101.

[27] H. Huppert, *The flow and instability of viscous gravity currents down a slope*, Nature, 300 (1982), pp. 427–429.

[28] O. Jensen, *Self-similar, surfactant driven flows*, Phys. Fluids A, 6 (1994), pp. 1084–1094.

[29] O. Jensen, *The stress singularity in surfactant-driven thin-film flows. part 2. inertial effects*, J. Fluid Mech, 372 (1998), pp. 301–322.

[30] O. Jensen and J. Grotberg, *Insoluble surfactant spreading on a thin viscous film: shock evolution and film rupture*, J. Fluid Mech., 240 (1992), pp. 259–288.

[31] O. Jensen and D. Halpern, *The stress singularity in surfactant-driven thin-film flows. part 1. viscous elements*, J. Fluid Mech, 372 (1998), pp. 273–300.

[32] O. Jensen and S. Naire, *The spreading and stability of a surfactant-laden drop on a prewetted substrate*, J. Fluid Mech., 554 (2006), pp. 5–24.

[33] J. Jerrett and J. de Bruyn, *Fingering instability of a gravitationally driven contact line*, Phys. Fluids A, 4 (1992), pp. 234–242.

[34] L. Kondic, *Instabilities in gravity driven flow of thin fluid films.*, SIAM Review, 45 (2003), pp. 95–115.

[35] L. Kondic and J. Diez, *Pattern formation in the flow of thin films down an incline: Constant flux configuration,*, Phys. Fluids, 13 (2001), pp. 3164–3184.

[36] ——, *Computing three-dimensional thin film flows using contact lines*, J COMPUT PHYS, 183 (2002), pp. 274–306.

[37] I. Langmuir, *The constitution and fundamental properties of solids and liquids.*, J. Am. Chem. Soci., 38 (1916), pp. 2221–2295.

[38] R. Levy and M. Shearer, *The motion of a thin film driven by surfactant and gravity*, SIAM J. Appl. Math., 66 (2006), pp. 1588–1609.

[39] R. Levy, M. Shearer, and T. Witelski, *Gravity-driven thin liquid films with insoluble surfactant: smooth travelling waves*, Eur. J Appl. Math., 8 (2007), pp. 679–708.

[40] C. Marangoni, *On the expansion of a drop of liquid floating in the surface of another liquid*, PhD thesis, Pavia, Italy, 1865.

[41] A. Marmur and M. Lelah, *The spreading of aqueous surfactant solutions on glass*, Chem. Eng. Commun., 13 (1981), pp. 133–143.

[42] O. Matar and S. Troian, *Dynamics and stability of surfactant coated thin liquid films*, Mat. Res. Soc. Symp. Proc., 464 (1997), pp. 237–242.

[43] ——, *Growth of non-modal transient structures during the spreading of the surfactant coated films*, Phys. Fluid A, 10 (1998), pp. 1234–1237.

[44] ——, *The development of transient fingering patterns during the spreading of surfactant coated films.*, Phys. Fluid A, 11 (1999), pp. 3232–3246.

[45] ——, *Spreading of a surfactant monolayer on a thin liquid film: Onset and evolution of digitated structures.*, Chaos, 9 (1999), pp. 141–153.

[46] A. Mavromoustaki, *Long-wave Dynamics of Single- and Two-layer Flows*, PhD thesis, Imperial College of Science, Technology and Medicine, 2011.

[47] A. Mavromoustaki, O. Matar, and R. Craster, *Dynamics of a climbing surfactant-laden film-i: Base-state flow*, J. Colloid Interface Sci., 371 (2012), pp. 107–120.

[48] ——, *Dynamics of a climbing surfactant-laden film-ii: Stability*, J. Colloid Interface Sci., 371 (2012), pp. 121–135.

[49] T. Myers, *Surface tension driven thin film flows*, in The Mechanics of Thin Film Coatings, World Scientific Publ. Co. Pte Ltd., 1996.

[50] ——, *Thin films with high surface tension*, SIAM Review, 40 (1998), pp. 441–462.

[51] C. Navier, *Memoire sur les lois du mouvement des fluids*, Mmoires de l'Acadmie des sciences de l'Institut de France, 6 (1823), pp. 389–440.

[52] A. Oron, S. Davis, and S. Bankoff, *Long-scale evolution of thin liquid films*, Rev. Mod. Phys., 69 (1997), pp. 931–980.

[53] M. Rosen, *Surfactants and interfacial phenomena*, John Wiley and Sons, Inc., 3rd ed., 2004.

[54] L. Schwartz, *Viscous flows down an inclined plane: Instability and finger formation.*, Phys. Fluids S, 1 (1989), pp. 443–445.

[55] L. Scriven, *Dynamics of a fliuid interface*, Chem. Eng. Sci., 12 (1960), pp. 98–108.

[56] L. Shampine and M. Reichelt, *The matlab ode suite*, SIAM J. Sci. Comput., 18 (1997), p. 122.

[57] N. Shuaib, H. Power, and S. Hibberd, *Bem solution of thin film flows on an inclined plane with a bottom outlet*, Eng. Anal. Bound. Elem., 33 (2009), pp. 338–398.

[58] N. Silvi and E. Dussan, *On the rewetting of an inclined solid surface by a liquid*, Phys. Fluids, 28 (1985), pp. 5–7.

[59] M. Spaid and G. Homsy, *Stability of newtonian viscoelastic dynamic contact lines.*, Phys. Fluids, 8 (1996), pp. 460–478.

[60] H. A. Stone, *A simple derivation of the time-dependent convective- difusion equation for surfactant transport along a deforming interface*, Phys. Fluids A, 2 (1990), pp. 111–112.

[61] L. Tanner, *The spreading of silicone oil drops on horizontal surfaces*, J. Phys. D : Appl. Phys., 12 (1979), pp. 1473–1485.

[62] S. Troian, E. Herbolzheimer, and S. Safran, *Model for the fingering instability of the spreading surfactant drops.*, Phys. Rev. Lett., 65 (1990), pp. 333–336.

[63] S. Troian, E. Herbolzheimer, S. Safran, and J. Joanny, *Fingering lnstabilities of driven spreading films*, Europhys. Lett., (1989), pp. 25–30.

[64] E. Tuck and L. Schwartz, *A numerical and asymptotic study of some third-order ordinary differential equations relevant to draining and coating flows*, SIAM Review, 32 (1990), pp. 453–469.

[65] M. R. E. Warner, R. Craster, and O. Matar, *Fingering phenomena associated with insoluble surfactant spreading on thin liquid films.*, J. Fluid Mech., 510 (2004).

[66] G. B. Whitham, *Linear and Nonlinear Waves.*, Wiley, 1974.

[67] H. Wong, D. Rumschitzski, and C. Maldarelli, *On the surfactant mass balance at a deforming fluid interface.*, Phys. Fluids, 385 (1996), pp. 79–99.

[68] X. Xu, *Electrohydrodynamic flow and chaotic mixing inside drops*, PhD thesis, UNIVERSITY OF CALIFORNIA, 2007.